

Design, Synthesis and Evolution of Functional Tripodal Platforms for Single Molecule Devices

Inauguraldissertation

zur

Erlangung der Würde eines Doktors der Philosophie

vorgelegt der

Philosophisch-Naturwissenschaftlichen Fakultät

der Universität Basel

von

Nico Balzer

Basel, 2021

Originaldokument gespeichert auf dem Dokumentenserver der Universität Basel

<https://edoc.unibas.ch>

Genehmigt von der Philosophisch-Naturwissenschaftlichen Fakultät
auf Antrag von

Prof. Dr. Marcel Mayor

Prof. Dr. Oliver Wenger

Prof. Dr. Yoko Yamakoshi

Basel, den 22.06.2021

Prof. Dr. Marcel Mayor

Dekan

Dedicated to

My family

ACKNOWLEDGMENTS

No man is an island and therefore, I would like to thank everyone who has accompanied me during my time at INT and who has contributed to this thesis. I especially would like to thank some people in particular:

At first, I want to express my deepest gratitude to *Prof. Dr. Marcel Mayor* for giving me the opportunity to join his research group, for allowing me to work in the fascinating research field of nanotechnology, for the tremendous support both personally and scientifically during my entire PhD and for his enthusiastic and motivational nature.

Furthermore, I would like to thank *Prof. Dr. Oliver Wenger* for being my second supervisor and for offering his experience and knowledge. I would also like to thank *Prof. Dr. Yoko Yamakoshi* for being my external expert.

I owe much gratitude to *Dr. Michal Valášek* for the very welcoming, inspiring, and motivating environment he established at the INT. Besides appreciating his scientific expertise and experience, I enjoy our daily discussions about both science and everything else. I am deeply grateful for his support and mentorship since the beginning of my scientific journey at INT.

I am very thankful to *Prof. Wulf Wulfhekel*, *Dr. Lukas Gerhard*, *Julian Skolaut* and *Vibhuti Rai* and all other current and former members of the RG Wulfhekel for this fruitful interdisciplinary collaboration. I enjoyed our group meetings and the evaluation of our tripods a lot. Furthermore, I would like to thank Vibhuti and especially Julian for their time explaining me all the (physical) issues we were facing.

I am very thankful to *Prof. Dr. Michael Zharnikov* for measuring and evaluating my SAMs and for sharing his knowledge about self-assembled monolayers.

Happiness is having colleagues who become friends. *Liang*, *Jasmin* and *Tingting*, thank you so much guys for having these wonderful little coffee breaks, spending our free time together, introducing me to foreign languages, cultures, habitats and so much more. You guys are just wonderful, and I am looking forward to seeing you all again.

A big thank is attributed to the lovely people working in the laboratory wing of INT. Especially, the *Panamanians*, *Nithin*, *Sai*, *Asato*, *Shirin*, *Sören*, *Senthil*, *Patrick*, *Rui*, *Camilla* and *Joel*.

Furthermore, I would also like to thank all current and former students of *Prof. Dr. Marcel Mayor* in Basel. I really enjoyed the hiking trips and Christmas parties.

I thank all my current and former colleagues from INT. Especially, I would like to thank *Hagen Sparrenberger* for providing everything needed for the daily work, *Dr. Olaf Fuhr* for measuring my crystals, *Dr. Papri Chakraborty* and *Dr. Marco Neumaier* for letting me use their ESI-TOF on such short notice and *Dr. Stefan Walheim* for introducing me into the field of SAMs.

Finally, I would like to thank my family for their support, motivation and comforting. You are the reason I could start this journey. Last but not least, thank you, *Lena*, for being the stable anchor I could only dream of.

Table of contents

1	Introduction.....	8
1.1	Organic Electronics	9
1.2	From Organic Electronics to Single Molecule Devices	10
1.3	Molecular Contacts with Surfaces – “Molecular Bridges”	14
1.3.1	Types of Surface Decoration	15
1.3.2	Choice of Electrode Material	17
1.3.3	Anchors	20
1.3.4	Structure of the Anchors	25
1.3.5	Linker.....	29
1.4	(Single) Molecular Machines	32
1.4.1	General.....	32
1.4.2	Working Mode of (Molecular) Machines	33
1.4.3	Molecular Rotators on Surfaces.....	35
1.4.4	Azimuthal Molecular Motors on Surfaces	36
1.4.5	Chiral Induced Spin Selectivity – Effect	40
1.5	Luminescence.....	42
1.5.1	General.....	42
1.5.2	Single Molecule Luminescence	45
1.5.3	Self-Decoupling of Chromophores	46
1.5.4	NDI Chromophores for Single Molecule Luminescence.....	47
1.6	Characterisation Methods of the Surface-Molecule Interface.....	52
1.6.1	Microscopy (STM, AFM)	52
1.6.2	Spectroscopy (XPS, NEXAFS)	54
1.6.3	Others (ellipsometry, contact angle)	55
2	Motivation.....	56
3	Results and Discussion	59

3.1	“En Route to Tripodal Functionalised Molecules”	60
3.1.1	Molecular Platform	61
3.1.2	Lorentz Force Molecular Rotor	63
3.1.3	Prochiral Rotor.....	65
3.1.4	Tripodal Chromophores	66
3.1.5	Conclusions of the First-Generation Single Molecule Devices	91
3.2	“Evolution of the Platforms”.....	93
3.2.1	Design and Synthesis of Second-generation Tripodal Structures.....	93
3.2.2	Surface Studies of Second-Generation Tripodal Structures in SAMs	105
3.2.3	Model Compounds for STM studies.....	115
3.2.4	Conclusion of the second-generation platforms	119
3.3	“Tripodal Functionalised Molecules”	121
3.3.1	“Geländer-Type” Rotors	122
3.3.2	Second-Generation Chromophores	131
3.3.3	Conclusion of Second-Generation Functional Units	137
4	Conclusion and Outlook	139
5	Experimental Section	143
5.1	Materials.....	143
5.2	Equipment and Measurements	143
5.3	Experimental Details and Synthetic Procedures	145
6	List of Abbreviations	207
7	References.....	211
8	Appendix.....	225

1 Introduction

This chapter introduces the reader to the topics dealing with this thesis and it is divided into the following parts:

1. Organic Electronics
2. From Organic Electronics to Single Molecule Devices
3. Molecular Contacts with Surfaces – “Molecular Bridges”
4. (Single) Molecular Machines
5. Luminescence
6. Characterisation Methods of the Surface-Molecule Interface

These six parts are further organised into subcategories which include the theoretical background, the historical development of underlying concepts, the scope of the research topics and the latest state-of-the-art technology.

1.1 Organic Electronics

Organic electronics is a branch of modern electronics and deals with the implementation of (conductive) organic molecules or polymers in electronic devices, such as field effect transistors (OFETs), light emitting diodes (OLEDs) or organic solar cells (OSCs). The field of organic electronics is still in its infancy compared to their inorganic counterparts. Nevertheless, consumers are already using organic electronic devices, such as organic light emitting diodes (OLEDs) in their smartphones or in a new generation TVs. Since the first observation of electroluminescence in organic materials by André Bernanose in the early 1950s,^[1,2] it took more than 30 years before Ching Wan Tang and Steven Van Slyke had manufactured an efficient low-voltage OLED-device at Eastman Kodak Company in 1987.^[3] However, such device architectures need further improvements regarding chemical and thermal stability of the flexible substrates.^[4] Likewise, from a chemist's point of view, OLED materials still suffer from short lifetimes, low efficiencies and light output.^[5] It is therefore of fundamental interest to fathom the underlying process of light emission of (single) organic molecules. In general, organic functional materials own enormous potential for future device applications. Amongst many concepts, molecular machines, show very interesting features that might be used in sensors, information technology or even in new types of the functional materials.^[6] The field of synthetic molecular machines was pioneered by the seminal works of J. Fraser Stoddart on molecular shuttles^[7] and Jean-Pierre Sauvages on mechanical interlocked catenanes.^[8] Together with Bernard "Ben" Feringa, who published a breakthrough on light-driven unidirectional molecular rotors in 1999,^[9] they were awarded the Nobel Prize in Chemistry in 2016 "for the design and synthesis of molecular machines".^[6] Although such molecular machines are far from being commercially available, they led to an inspiring contest in April 2017, where the first Nanocar Race competition in Toulouse took place.^[10]

1.2 From Organic Electronics to Single Molecule Devices

Starting with the discovery of conducting polymers by Alan J. Heeger, Alan G. MacDiarmid and Hideki Shirakawa, the interest in organic electronics has been tremendously increased. Their great impact on this field resulted in awarding them the Nobel Prize in Chemistry in 2000 for their work on conductive polymers. One of the main advantages of organic electronics is the possibility to process such organic material on very thin or/and flexible substrates leading to curved monitors, foldable screens or even rollable papers. Regarding the aspects of Green Chemistry,^[11] organic electronics could pay a big attribute to this concept, including the “use of Renewable Feedstocks”, the “Design for Degradation”, “Catalysis”, “Design for Energy Efficient” and not mining rare-earth elements.

However, the origin of organic electronics should not only be traced back to the work by the 2000’s Nobel prize laureates but rather four decades before, namely by Gordon Moore’s statistical empirical *Moore’s Law*.^[12,13] During the “transistor age” he postulated that at stable commercial prices about every 18-24 month the number of transistors per each integrated circuits/chips would double, thus leading to an improved performance of electronic devices. His postulation of linear growth had remained reliable until the 2010s, before it then started to transform into an exponential growth (Figure 1). Following this trend, by about 2030, humankind might transcend biology.^[14]

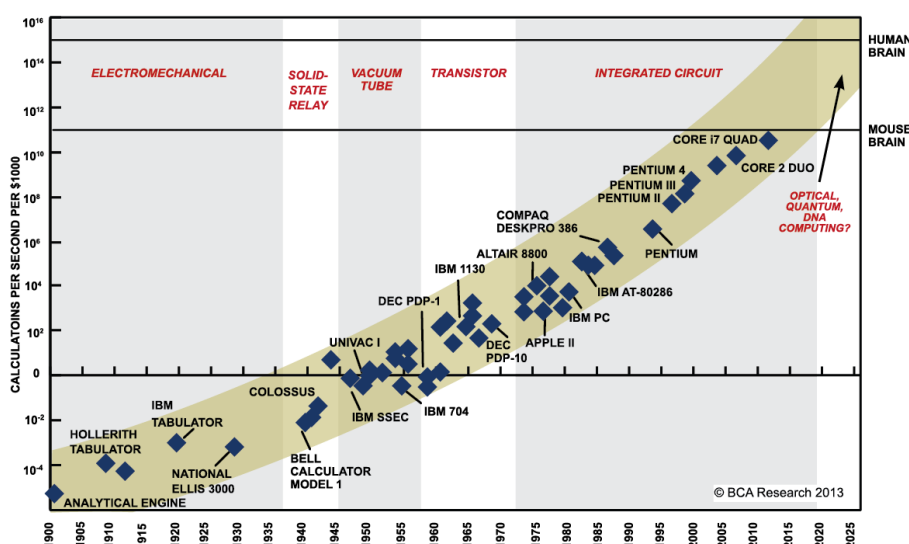


Figure 1. The historical development of electronic devices: it shows the linear growth of the number of components per integrated circuits until the year 2010 and how it transforms into exponential growth, which might extend the human brain by the year 2025. Image taken from Ref.^[15].

According to Moore's law, chip producers try to double the numbers of transistors while keeping the same chip size or even shrinking it. Following this design, at some point it will be too complicated/expensive to reduce the size of the inorganic materials (the widely held opinion is about 50 nm). And by that means, this sets a fundamental limit for the top-down (reducing macroscopic structures) approach of silicon based circuits and starts the beginning of the bottom-up approach (starting from microscopic structures / molecules) using molecular (organic) electronics.^[16] Yet, the concept of the bottom-up approach is not new, because in 1959 it was first introduced by Richard Feynman's seminal talk "*There is plenty of room at the bottom*" at Caltech.^[17] His vision might be considered as the birth of Nanotechnology. It was then in 1974, when Ari Aviram and Mark Ratner theoretically showed that electrical rectification might be possible by single molecules.^[18] The scientific interest in these at-that-time new type of diodes is indicated by several conferences, hosted by either Forrest Carter or Ari Aviram.^[19–22] For several reasons, languishment about this topic took place and only two decades later, Metzger *et al.*^[23] confirmed molecular rectification experimentally in Langmuir-Blodgett films. Since then, molecular (organic) electronics have received a renaissance due to the fact that direct measurements of electronic behaviour of Langmuir-Blodgett monolayers,^[24,25] self-assembled monolayers (SAM)^[26–28] or even single molecules^[29–32] became available by means of scanning probe in microscopy or in sandwiched films between two electrodes.

Another milestone in the history of organic electronics are the inventions by the Sir Fraser Stoddart, Jean-Piere Sauvage and Ben Feringa, who were awarded the Nobel Prize in Chemistry in 2016 "for the design and synthesis of molecular machines".^[6] With their discoveries, they paid a great attribute to organic functional materials. The group of Stoddart was the first to publish a molecular shuttle, which started the emerging field of artificial molecular machinery.^[7] These machines were based on rotaxanes. However, they were not able to overcome the system's equilibrium because they were lacking ratchet mechanism. Later, Stoddart constantly enhanced the design of these shuttles, which then ultimately led to concept of the artificial molecular pumps.^[33] By implementing several stoppers whose energetical barrier can be changed by the oxidation state, they were able to transport macrocycles energetically uphill against the local concentration gradient.^[33] In contrast to rotaxanes, catenanes do not reach steady state, in which work cannot be further done. Therefore, the architecture of catenanes allows a continuously operation of the function, which is an important criterion for molecular motors (see, Chapter 1.4.2). It was Jean-Pierre Sauvage who first controlled the continuous rotary movement of components. By chemical engineering, they demonstrated that molecular design can overcome the system's equilibrium. Showing that one

can artificially control and manipulate different states of the system, molecular machines are interesting candidates for possible devices.^[34]

In solution, however, the molecules are controlled in their “bulk version”, which means that single molecules (such as a single machine in the macroscopic world) cannot be addressed independently. Furthermore, to verify “movement” in molecular machines, one must define a fixed reference, which is an issue in solution. Therefore, the immobilisation of the machines to surfaces is of key interest for understanding and controlling the motion in single molecular machines. Additionally, the surface lowers the degree of freedom of the molecules and forces them into some degree of order.

Ben Feringa (the third of the 2016 Chemistry laureates) mounted his concept of motors which is based on a rotation around a C=C bond triggered by light,^[9] both on a quartz substrate^[35] and on gold (see Figure 2).^[36] Their design consists of a rotor which is connected to the stator *via* an axle and finally bound to the gold surface by thiol-anchors. The rotational unit is a helical chiral alkene. To start the unidirectional rotation, the parent motor absorbs a photon which then results in an isomerisation of the central overcrowded alkene, which leads to a high-energy conformation. Upon heating, the strained motor then relieves into a thermodynamically more favourable conformation. In this way, an irreversible conformational change is provided, and a 180° rotation is performed. Repeating the aforementioned steps, a 360° rotation can be observed.^[36]

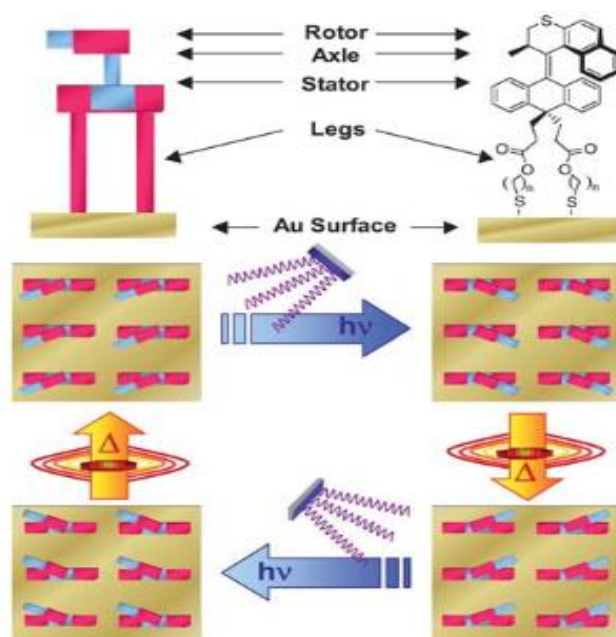


Figure 2. Feringa's rotor mounted on gold. By heating and following radiation, directional motion was achieved. Taken from Ref.^[36]

The aforementioned examples of molecular machines show the potential of molecules to serve as functional units, but mainly are interesting from a scientific point of view. Nevertheless, starting with study of conducting polymers,^[37,38] molecular organic electronics did already enter the market by providing organic light emitting diodes^[3,39] and organic solar cells.^[40] While these devices are based on “large-area”- junctions, yet single molecules are not implemented into commercially available technologies. Only with the tremendous evolution in regard of single molecule characterisation, such as scanning tunnelling microscopy (STM), conducting atomic force microscopy (C-AFM) and scanning tunnelling spectroscopy (STS) it became possible to manipulate single molecules and probe the electronic transport at the single molecule scale. These advances in technology and characterisation further increased the research of single molecule devices for the bottom-up approach. Until now, most of the studies focused on the conductance properties of single molecules.^[41,42] Therefore, well-understood chemical principles can be incorporated into the study of structure-functionality relationships. With single molecule studies, the assumption that defined functionalities can be related to defined structures should be confirmatory since single molecule studies eliminate close interactions between neighbouring units. However, controlling the interface between a solid-state substrate and the decorating molecular functionalised layers is not yet fully understood and therefore of fundamental interest in single molecule science. While the variety of functional units to implement in organic electronics is almost infinite,^[43] this work focuses on the field of single molecular rotors and single molecule luminescence.

To finalise this chapter, organic functional materials are already available. Yet, it still remains challenging to enclose these functional building blocks in between two (or even three) electrodes ensuring successful, stable and suitable contacts in order to enable single molecule functionality.^[42] Therefore, tailor-made molecules are necessary for bridging the functional unit with the electrodes, on which the following chapter will focus.

1.3 Molecular Contacts with Surfaces – “Molecular Bridges”

The ultimate goal of organic electronics is to use molecular assemblies or even single molecules as functional building blocks and to integrate them into electric circuits between macroscopic electrodes, where sufficiently strong binding between the terminal anchoring groups of the bridging functional molecule and the metal electrode is achieved (see Figure 3). Only if this requirement is met, the control over the electronic properties of (individual) molecules becomes possible, which is of paramount importance for molecular electronic devices. Depending on the field of application, molecular engineers need to decide which type of surface decoration is the most suitable one. Furthermore, not only the effect of anchoring groups, but also the choice of electrode material, the entire rigidity and dimension of the molecule, the structure of the molecular linker and the functional unit, as well as accurate measurements of such functional molecules between the macroscopic electrodes are crucial to fulfill requirements for molecular electronic devices.

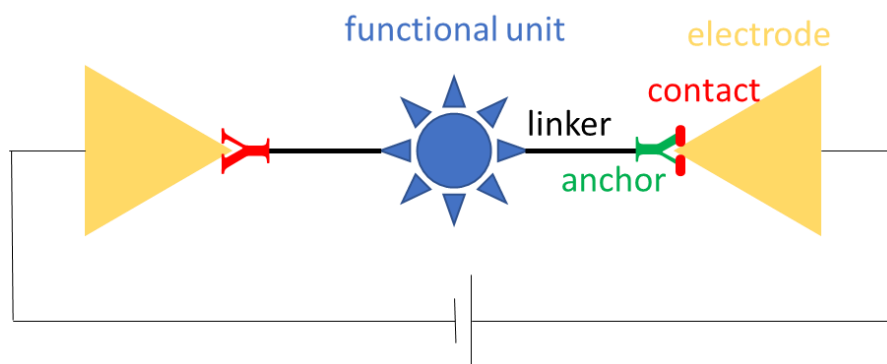


Figure 3. Schematic (experimental) drawing of the functional molecule bridging the macroscopic electrodes: It includes an electrode (yellow), the contact (red) from the anchor (green) to a linker (black) and the functional unit (blue).

1.3.1 Types of Surface Decoration

There are several techniques to modify the surface, namely the non-specific technique, the electrografting technique, the Langmuir-Blodgett (LB) method and the self-assembly monolayer (SAM) approach. For all of surface deposition techniques, the driving force to form the molecular monolayers is that metal surfaces tend to adsorb organic molecule in order to lower the free energy of interface between metal and the ambient environment such as the liquid-solid or the gas-solid interface.^[44] If there is no structured alignment of adsorbed molecules on the surface, this type is called non-specific functionalisation. Electrocrafting is based on the electrochemical reaction between a conductive substrate and the organic anchoring group and has been recently reviewed by D. Bélanger and J. Pinson.^[45] The first method used to organise molecules between two interfaces is the Langmuir-Blodgett technique. In 1917, Irving Langmuir set experimental and theoretical aspects of this concept, for which he was awarded the Nobel Prize in Chemistry in 1932.^[46] A few years later, his apprentice, Katherine Blodgett, transferred a monolayer onto a solid substrate by the vertical deposition method.^[24] The horizontal deposition method was developed later and is called Langmuir-Schäfer technique.^[47] This technique has been intensively used in organic electronics since 1971, when Hans Kuhn first build the LB device for molecular applications.^[48] Key advantages of the LB-method are that both chemisorbed and physisorbed molecules can be used, low-cost and large-area manufacturing and a number of different solid substrates can be used. However, for molecular electronics, the main drawbacks are in the nature of processing: weak contacts (in case of physisorption) and residues of the solvent may restrain. In contrast to the previous LB technique, molecular self-assembled monolayers (SAMs) are based on the spontaneous arrangement of molecules into ordered structures on a solid substrate. This means that no additional stimuli are needed to form the monolayers and the formation of SAMs is of spontaneous and autonomous nature.^[49] Moreover, in such molecular self-assembly, the molecular structure determines the composition of the assembly. The simple processing of SAMs makes them easily manufacturable and therefore interesting for advanced technological applications. From a scientific point of view, SAMs offer unique possibilities to understand fundamentals of the structure-property relationships and self-organisation of molecules on surfaces. Tailor-made molecules for SAMs open up the opportunities to understand the phenomena of competing intermolecular, molecular-substrates and molecule-solvent interactions in terms of ordering, adhesion, corrosion, growth or wetting.^[50] SAMs are

generally manufactured as follows (Figure 4b): A substrate is introduced to an organic solution with the molecule of interest. Optional, previous cleaning methods for the substrate may include flame-annealing, etching, cleaning and rinsing. After incubating the substrate in the solution for a definite period of time, samples are taken out and rinsed copiously to remove the physisorbed molecules. Post-annealing or other techniques may help to improve the quality of the monolayer. Various parameters, such as the temperature, the humidity, the concentration, the annealing or the structure of molecules influence the outcome and open possibilities for further optimisation.

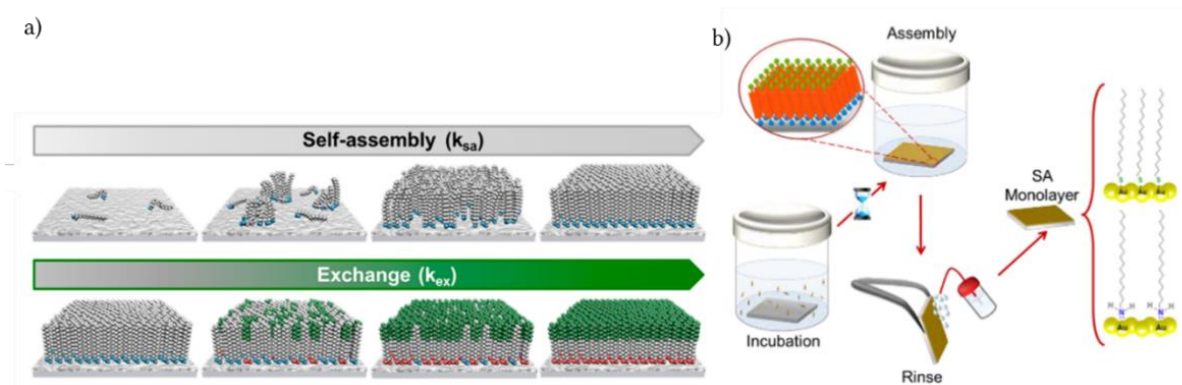


Figure 4. a) SAM formation of alkane thiols on the gold surface (top) and exchanging procedure (down). Image taken from Ref.^[51]. b) An illustrative process of SAM preparation is shown. Image taken and slightly modified from Ref.^[52].

Historically, the most studied SAMs typically consists of molecules with a thiol as an anchoring group, a hydrocarbon chain and a terminal group which may carry a functional unit. All three parts contribute to the formation, however not equally strong. Energetically, the thiolate head group contributes with 50 kcal mol^{-1} , each methylene group of the linker gives about $1\text{-}2 \text{ kcal mol}^{-1}$ while the terminal group has only very little impact on the overall binding energy.^[53] At low concentrations (1 mM), kinetic studies of alkanethiols on Au(111) surfaces showed that in the absorption process onto gold there are two subsequent steps involved: A very fast first one, where most of the surface is already covered with thiols (thiol adsorption, Figure 4a, top).^[28,54,55] The adsorption mechanism is not trivial and is more diverse than pure chemisorption and will be discussed later in Chapter 1.3.3.3.^[54] This first step can be described either by a diffusion-limited model or a 2nd order Langmuir adsorption model.^[54] The following step (orientation ordering) can be termed to surface crystallisation process^[50] and is both significantly slower and highly dependent on the solvent and the chain length.^[54] (Figure

4a, top) One reason might be that the second kinetic step depends on the formation of preordered domains,^[56] which therefore control the rate of adsorption. In this step, the alkyl chains get out of the disordered state into an ordered one. This happens by moving from the physisorbed layers to the gold surface and not from “bulk” solution. The authors believe that alkane thiol addition (or exchange) happens most eagerly at domain edges.^[54,57] Studies indicate that the second step may take several hours.^[58,59] All of the theory above presumes that there was an equilibrium established between surface and solution, and the concentration of organic molecules was high enough to provide a stable equilibrium. Moreover, an advanced technique is the using of mixed self-assembled monolayers consisting of at least two different types of anchoring molecules (Figure 4, bottom). They can be achieved by either parallel adsorption^[60] or by selectively changing the end group^[61] or unsymmetrical substituted disulfides.^[62]

1.3.2 Choice of Electrode Material

The choice of the electrode material plays an important role for the experimental setup as different metal-molecule contacts show different conductance characteristics depending on the work function of the electrode material.^[63–65] Gold (Au)^[66] is commonly used for molecular junctions. But also other metal-based electrodes such as silver (Ag),^[67] platinum (Pt),^[68] palladium (Pd),^[69] copper (Cu)^[70] or even carbon-based materials, such as graphite,^[71] graphene^[72] or carbon nanotubes^[73] could be successfully used. In general, the choice of the electrode material needs to fulfil four main criteria:

1. Chemical inertness to ambient air
2. Good processability
3. Compatibility with organic or biological functional units
4. Suitable work function

Gold is rather inert and reacts neither with atmospheric oxygen nor most of the chemicals. Thus, gold is rather stable at ambient conditions, whereas silver is quite labile. Copper might be interesting from a technical and industrial aspect, but it is even more labile than silver.^[74]

Besides being stable at ambient conditions, gold is malleable (and therefore easy to

pattern) and easy to obtain. Those two facts made gold is the most studied, historically. Although SAMs on d⁶-transition metals might be more suitable for electronic devices,^[75–77] they are still less studied than gold. A huge drawback of these metals are the fluctuating prices making them unreliable for commercial devices.

From a biological point of view, gold is more suitable compatible than other metals. Gold is not toxic to cells and self-assembled monolayers on gold are stable to some extent. In contrast to that, silver (the second most studied substrate for self-assembled monolayers of alkanthiolates) is toxic to cells^[78,79]

For the metal-organic interface, the work function Φ_B of the electrode is of great importance. The work function is the energy which is required to pull out the electron at the Fermi level (E_{Fermi} = half-filled energy levels within the metal conduction level (higher than 0K)) to the vacuum level (Figure 5) and is usually the energy barrier between the valence band (VB) and the conduction band (CB). Frisbie *et al.* developed a series of alkanethiols integrated in a conducting probe atomic force microscopy (CP-AFM) and in this experiment they could connect the contact resistance with the work function of silver, gold, palladium and platinum.^[64] It shows that silver has the lowest work function and therefore should be the metal of choice from an energy level point of view. When talking about single molecule, VB disengage into the highest occupied molecular orbital (HOMO) and the CB to the lowest unoccupied molecular orbital (LUMO), respectively. In general, HOMO and LUMO energies are noted with respect to the Fermi level of the system. While the LUMO energy levels influence the net electronic performance,^[80] the HOMO defines the alignment between the metal's Fermi level and anchoring group.^[81] The energy which is needed to remove an electron from an isolated atom or molecule is called ionisation potential (IP). The IP is thus equal to the energy difference between HOMO and the vacuum level. The energy barrier for capturing electrons in the LUMO level is called electron affinity (EA). In contrast to single molecules, the energy levels of molecular films are much broader, which results in a continuum of the states involved, visualised in Figure 5 on the left side.

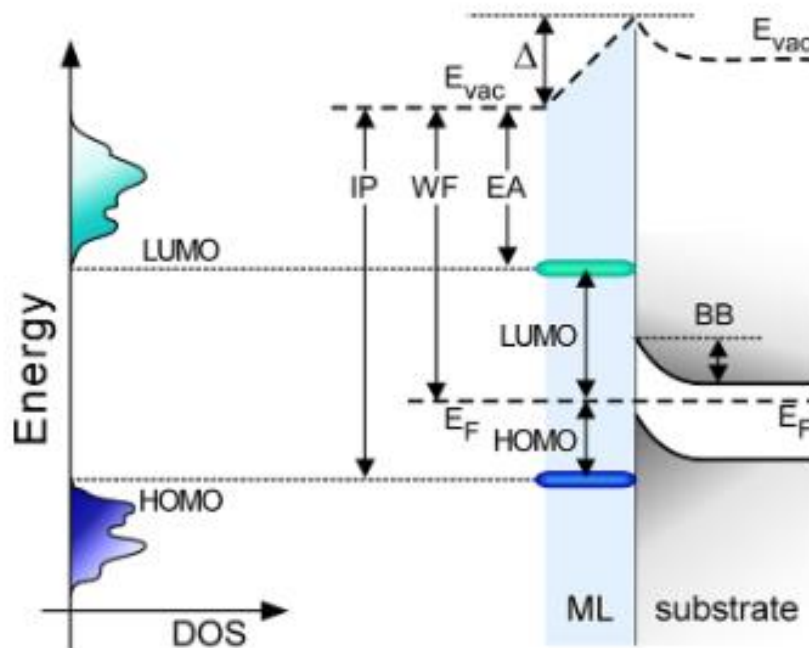


Figure 5. Right side: One-electron energy diagram of the main electrical characteristics in a molecular monolayer (coloured)-substrate interface (grey): It illustrates the ionisation potential (IP), work function (WF) and electron affinity (EA) with respect to HOMO energy level, Fermi level (E_F) and LUMO energy level. Left side: a realistic energy diagram of the density of states (DOS) as a function of energy close to the Fermi level. Taken from Ref.^[80].

It is of key interest in molecular electronics to understand and manipulate the metal-organic interface.^[82,83] The most crucial impact on charge carrier transport is the energy alignment of the frontier molecular orbitals/levels with respect to the Fermi level of the substrate and their overlapping with each other.^[80] This electrode–molecule hybridization Γ can be manipulated by chemical engineering: Varying the molecular adsorption geometries changes the alignment of the molecular energy levels and thus it is crucial for net charge transport. For successful experiments, the molecules must be designed so that the anchoring part of the molecule has a higher affinity to the surface than the rest part of the molecule.

In general, the choice of metal must meet all of the four main criteria mentioned above. Each experiment must be evaluated individually meeting all the requirements for its application. Because of its easy handling and its binding characteristics to thiols, this work focuses on gold as the metallic substrate.

1.3.3 anchors

1.3.3.1 Classification of Adsorption

Depending on the nature of the electrode material and the *anchor* groups, the functional *molecules* can be either *physisorbed* (Figure 6a, (1)) or *chemisorbed* (Figure 6a, (2)).^[84] In general, physisorption (from physical adsorption) is coupling between a molecule and a substrate through van der Waals interactions and thus it has less binding energy /low enthalpy than chemisorption (from chemical adsorption), which is coupling through chemical bonding. Moreover, physisorption is reversible and occurs rapidly because it does not require an activation energy and does not change the nature of the adsorbent. In contrast, chemisorption is not necessarily reversible, needs activation energy and changes the bonds of the adsorbent. Although these two bonding regimes of molecules to a surface have been already described in 1932 by Lennard Jones,^[84] it has only very recently shown experimentally that chemisorption first undergoes physisorption and then induces a strong covalent bond.^[85] If due to repulsive energy the energy barrier is too high to overcome, the molecules remain physisorbed on the substrates (Figure 6b, black line). In case of a lower barrier, the activation energy can be overcome by thermal excitation (Fig. 4b, green line). In case of a very low or no repulsive energy barrier, the molecule will get closer to the surface and thus chemisorbs (Figure 6b red or blue line).

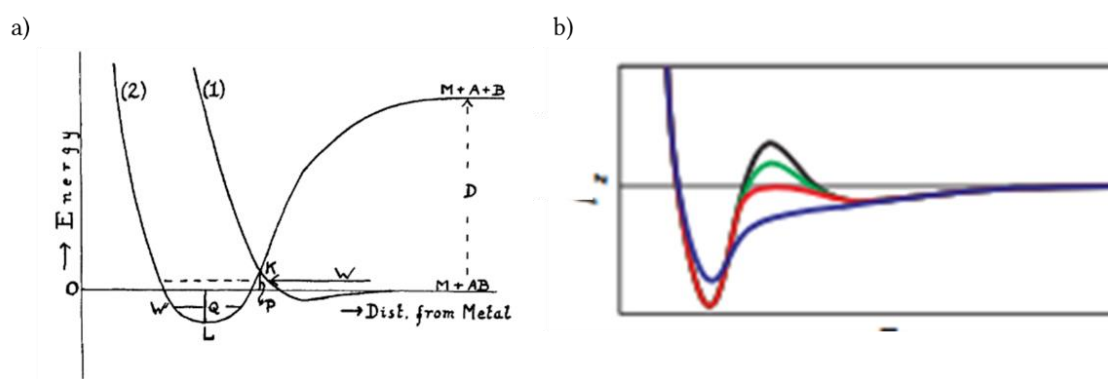


Figure 6. Lennard Jones potential: a) taken from the original publication^[84] and b) showing different activation energy for the transition (green and red curve) from physisorption (black curve) to chemisorption (blue curve), taken from Ref.^[85].

1.3.3.2 State of the Art Surface Anchoring Strategies

For surface decorations, both adsorption approaches are used and involved in different electrode-molecule interactions. On this basis, one can divide the molecular anchors further into four subcategories, namely:

1. dative bonds such as *N*-heterocyclic carbenes^[86], pyridines^[87], nitriles,^[88] isocyanides^[69]
2. the supramolecular approach based on like fullerene^[89], naphthalene diimides^[90] or benzene^[91]
3. electrostatic anchors^[92]
4. pure chemisorbed molecules based such as thiols^[93–95], selenols^[95,96], acetylenes^[97] or amines^[98,99]

As depicted in Figure 7 on (left) a schematic drawing of the mentioned concept is partnered with one example out of many different strategies (right). Note, that numerous anchoring strategies are available, but their explanation would exceed the scope of this introductory chapter. Hence, the undermentioned concepts are presented only briefly to emphasise the advantages and disadvantages that come hand in hand with their use.

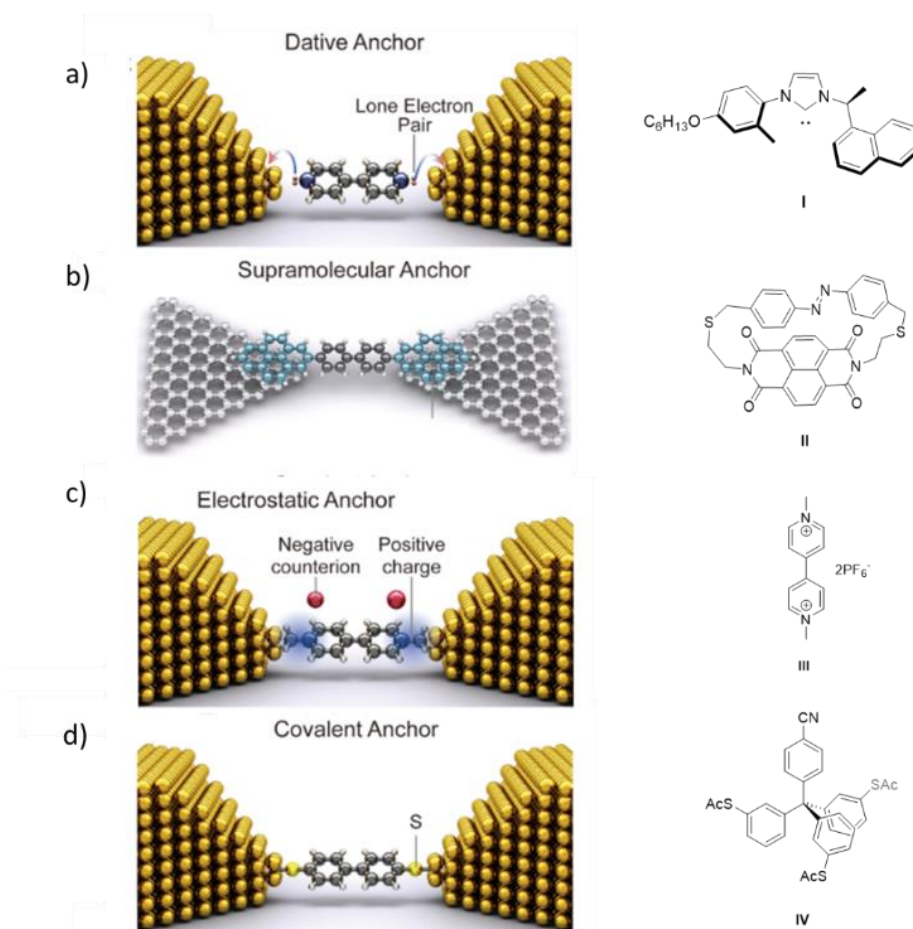


Figure 7. Different approaches for surface modification: On the left side, there is the schematic drawing for a break junction setup and on the right side, one can see an experimental example for the utilisation of the strategy by a) using dative anchors and an NHC-based molecular rotor^[100] b) a physisorption a NDI-derivative Mayor et al.,^[90] c) implementing covalent bonds to the substrate *via* the S-Au-bond of rigid tripodal anchors^[101] and d) creating a break junction through electrostatic anchors^[92]. Image taken and altered from Ref.^[92].

One example for dative bonds, which form strong bonds with gold are N-heterocyclic carbenes.^[86] They are thermally, hydrolytically, chemically, electrochemically and oxidatively stable.^[86] Recently, Fuchs and co-workers have published a unidirectional rotor-based on N-heterocyclic carbene anchors (see Figure 7, molecule **I**).^[100] Despite their stability, a limitation is the lack of spatial control.

The supramolecular approach is based on interactions between the π -system of the aromatic scaffold and the surface. In this case, the molecules are bound to the surface by non-covalent bonds, such as van der Waals' interactions, hydrogen bonds or π -channel

hybridisation. One example for this is the group of cyclophane scaffolds including either naphthalene diimide units (see Figure 7, molecule **II**)^[90] or a Janus-like 3D tectons as anchoring groups.^[91] Mayor *et al.* showed with a naphthalene diimide based cyclophane that it is possible to effectively decouple chromophores from metal surfaces.^[102] Although these cyclophanes are flat on the surface and form densely packed assemblies,^[103] the incorporation of functionality is not trivial.

Recently, it has been reported that electrostatic interactions between protonated pyrazolyl derivatives,^[104] deprotonated imidazoles^[105] and the gold surface form an intact molecule-substrate junction (see Figure 7, molecule **III**). To the best of our knowledge, yet this tactic is limited to break junction techniques.

The fourth another anchoring strategy is based on covalently bond anchors to the substrate. Amongst many examples, the gold-thiol bond is the most prominent one^[53,106] and will be described in detail in the following Chapter 1.3.3.3. If the mounting of functional units requires both lateral and spatial control, rigid tripodal platforms are promising alternatives to thiol alkanes.^[107] One out of many examples of thiol-gold-based anchoring group is the foot structure (see Figure 7, molecule **IV**) of Mayor *et al.*^[101]

1.3.3.3 Gold-Thiol-Anchors

As already mentioned, the most commonly used immobilisation technique is based on covalent bonds between thiol anchoring groups and gold substrates.^[106] The nature of their dominance can be deduced historically. Easy handling, their preparation and the fact that gold binds thiols with a high affinity made thiols the candidates of choice.^[108] The actual nature of the interplay between this couple is still under debate.^[109,110] For a long period, it had been believed that first physisorption occurs and then chemisorption follows. (eq. 1).



Physisorption has been observed with methanethiol and dimethyl disulfide at 5K.^[111,112] However, the process of chemisorption has not been fully understood and is discussed controversially. It has been proposed that the oxidative adsorption is the nature of chemisorption, although without any evidence whether such process undergoes *via* ions, radicals or other species.^[53] Diverse measurement techniques (XPS, IR spectroscopy, mass

spectrometry and electrochemical techniques) show evidence that the Au-S bond is as strong as in thiulates.^[53] However, the state of the thiol-hydrogen bond remains an issue. One hypothesis claims that the single hydrogen atoms form hydrogen.^[113,114] This would result in a thiol-gold covalently-like bond. However, there is also evidence that hydrogen is retained and that the non-chemisorbed nature prevails in gold-sulfur SAMs.^[110] In case of methanethiol, there was no observation for the scission, which results in a non-dissociative adsorption.^[115] Venkataraman *et al.* published a comprehensive study of C₁₂-based alkanes with different anchoring groups in which they claim that the thiol-terminated alkanes do not form chemisorbed gold-sulfur bonds in STM-break junction experiments, whereas in solution they observe covalent bonds.^[110] They postulate that chemisorption requires high-energy surface gold sites.^[110] However, in regards to dissociation energy, the gold-sulfur interface is stronger than the gold-gold-bond (2.1 eV in gold-sulfur vs. 0.8 in Au-Au).^[116]

At saturation coverage, thiols are based on a ($\sqrt{3} \times \sqrt{3}$)R30° lattice (where R means rotated) and exhibit a hexagonal symmetry.^[117] In large aromatic thiols however, more complexity is found. Here, they form disordered aggregates, show π - π - interactions or yield $5 \times \sqrt{3}$ surface reconstructions.^[118] It is discussed that during the formation of Au-S bonds the gold reconstruction is removed. Generally, thiols have the following three different sites to attack (the top, bridge and the hollow site) where sulfur atoms are bound by either one (top), two (bridge) (Figure 8, standard model) or three (hollow site).^[119] Other models involve disulfide bonding (Figure 8, middle) and binding of the thiolate on adatoms.^[120,121] Also polymeric chain structures are discussed, in which monothiolates are bridged in between gold adatoms (Figure 8, right).^[122] In low coverage regimes, it is believed that a formal RS-Au(I)-SR complex is formed, with the bridging gold atom being in the oxidation state of +1.^[123]

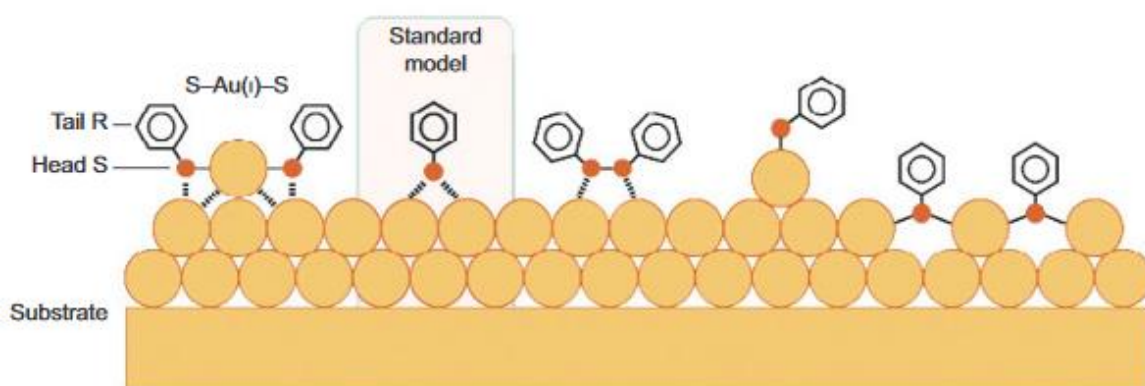


Figure 8. Different adsorption models: the formation of RS-Au(I)-SR complex (left), the standard model, disulfide bonding, binding on an adatom and polymeric structures. Taken from Ref.^[124].

1.3.4 Structure of the Anchors

Most of the aforementioned SAMs are based on monodentate alkanethiols. Hence they anchor through one bond/anchoring group having a tilt angle of about 30° - 35° with respect to the surface normal.^[50,53] One drawback of the monodentate alkanethiols is, that they require neighbouring molecules, which results in steric and/or electrostatic repulsion and a highly densely packed monolayer of functional units. A promising alternative is the utilisation of rigid (multidental) platforms to control the lateral arrangement and the tilting angle. To enforce a suitable orientation of the functional units, either monodental platforms or multidental architectures are needed. Controlling the geometry of the platform is also of great importance^[125] and has to be chosen carefully to suppress unwanted interactions of the functional group with the underlying substrate.^[126]

1.3.4.1 Flat Platforms

Herges *et al.* introduced a flat platform approach which is based triazatriangulenium based derivatives (TATA) (Figure 9, molecule **V**).^[127] They form hexagonally ordered adlayers with various functional units attached to the central carbon atom and their exceptional features result in several applications such as switches^[128], rotors (on trioxatriangulenium, TOTA)^[129,130] or porphyrins standing with and upright orientation.^[131] Given the fact that these platforms can be also modified laterally on the three nitrogen atoms, they show enormous potential to fine tune their properties for of the further applications. Moreover, they might outperform SAMs which are covalently bond to the surface in terms of binding energy.^[132] This can be explained by lateral interactions between the alkyl chains of surrounding platforms.^[133] Another approach of flat platforms is based on the cyclophane scaffold by Mayor and co-workers.^[102,103,134,135] They synthesised a planar chiral asymmetric naphthalene diimide cyclophane upon which they controlled the optical features by different core-substitution (Figure 9, molecule **VI**).^[134] The core-substitution of naphthalene diimides will be discussed later in Chapter 1.5.4. STM experiments showed that cyclophanes are lying flat and forming SAMs on Au(111). Moreover, the self-assembly is driven by the formation of hydrogen bonds between naphthalene core protons and carboxylic oxygen atoms.^[103] The efficient electronic decoupling from the surface^[102] enables them to emit light which has been observed by means of STM.^[135] A similar

strategy was followed by Attias and Charra where they designed a benzene-cyclophane scaffold. ^[91] The lower subunit was extended by stilbene derivatives in order to enable a widespread footprint. The cyclophane is fixed on the *para* positions of the lifted benzene, leaving the *ipso* position free for diverse functionalities.^[136–138] Other approaches involve the application of zinc-phthalocyanines,^[139] bare polyaromatic backbones with bulky side groups as spacing legs, so-called molecular landers^[140] or molecular cages.^[141]

Michl *et al.* bridged two platforms with an altitudinal molecular rotor to achieve a bridge-type functional unit with a tetraarylcyclobutadienecyclopentadienylcobalt complex^[142] as a “tower-stand” and a 9,9,10,10-tetrafluoro-9,10-dihydrophenanthrene as a dipolar rotating unit (Figure 9, molecule **VII**).^[143] They were able to electrically control the flipping of the dipolar rotor.

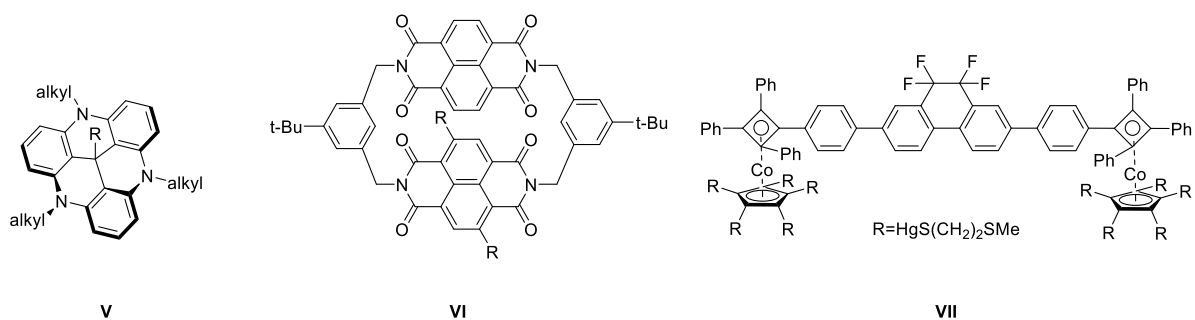


Figure 9. Platform approach used by Herges *et al.* (**V**, left), Mayor *et al.* (**VI**, middle) and by Michl *et al.* (**VII**, right).

1.3.4.2 Multidental Platforms

Another strategy to provide an upright orientation of functionality is the installation of a multipodal architecture. For a stabile configuration, it requires at least three anchoring groups which should not be in line.^[144] The first study reporting the immobilisation of tripodal molecules with a central sp^3 -hybridised carbon atom on surfaces was published by Whitesell and Chang in 1993 (Figure 10, **VIII**).^[145] Compared to the monodentate or bidentate structures, the experiments showed less ordering in SAMs but higher thermal stability, which can be explained by the chelating effect.^[146] The strategy of incorporating a sp^3 hybridised core atom as the centre of the platform remains a predominant strategy, indicated by several concepts

using this approach where C₃-symmetrical tripods bearing either a carbon atom^[147–151] or a silicon atom.^[152,153] The next step in the evolution of rigid multipodal platforms was then taken by Kitagawa *et al.* and their adamantyl framework (Figure 10, **IX**).^[154] The increased rigidity of the adamantyl framework resulted in highly ordered SAMs, which was observed by scanning tunnelling microscopy.^[154,155] When they implement additional phenyl substituents on top of the adamantane, the molecular arrangement on gold decreased. This shows that the functional group has an impact on molecular arrangement on the surface. Note, that even further advanced structures of adamantyl-based structures have been developed.^[156,157] Even more rigidity was introduced by the group of Fukushima *et al.* and their tripodal triptycene derivative (Figure 10, **X**).^[158,159] They focused on the formation of rigid SAMs based on triptycene derivatives. The SAMs of molecule **X** is significantly less ordered than the SAMs based on more flexible triptycene derivate.^[158] They reason, that the increased flexibility leads to an improvement of the orientation of the SAM.^[160] Admittedly, a significant handicap of this triptycene molecule is the absence of the perpendicular functionality.^[158]

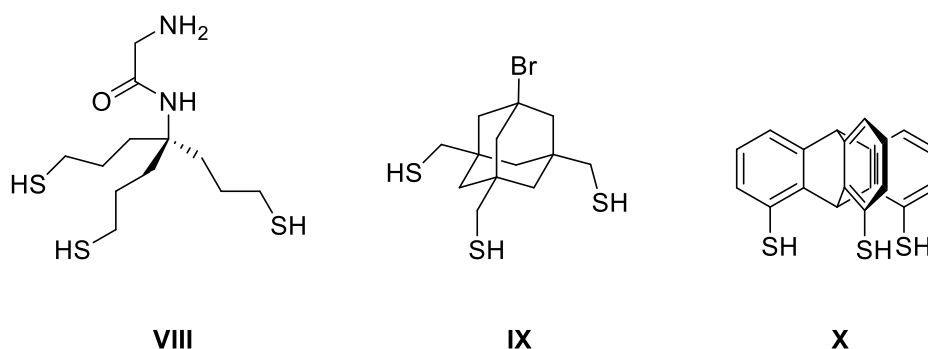


Figure 10. Increasing rigidity in tripodal structures for SAM by molecule **VIII** (synthesised by Whitesell *et al.*)^[145], molecule **IX** (synthesised by Kitagawa *et al.*)^[154] and molecule **X** (synthesised by Fukushima *et al.*)^[158]

Rigid molecular platforms with a tetraphenylmethane scaffold (Figure 11, **XI**, **IV**, **XIII**) enjoy immense popularity and have been reported for various applications.^[161–164] In this molecular setup, three out of four phenyl rings contain anchoring groups, while the fourth one ring opens the possibility of further functionalisation. Optionally, the forth phenyl ring can be replaced by acetylene group.^[150,165] It has been shown that these types of anchors form efficient packing in SAMs due to the lateral stabilisation by van der Waals forces.^[166] Noteworthy, some other

tripodal platforms were synthesised based on boron central atom of subphthalocyanine,^[167] gallium complexes^[168,169] and both ruthenium tripodal complexes^[170] and piano-stool complexes.^[171] Moreover, tetraphenylsilane platforms (Figure 11, **XII**) were employed in order to mount functional units, such as luminescent complexes,^[172] molecular motors,^[173,174] or different chemical switches atop flat surfaces.^[175,176] Given the decreased overlap of valence orbitals between the legs and the central atom (silicon, boron or metals), such scaffolds electronically decouple the functional unit from the underlying surface. The first synthesised tripods were anchored through benzylic thiols^[148,163,164], while aromatic thiols are more rigid.^[101,177] Furthermore, due to the differences in binding energy (74 kJ mol⁻¹ for R-CH₂-S-Au bond vs 46 kJ mol⁻¹ for R-C_{aromatic}-S-Au) the diffusion barrier is lower for arenethiols and thus the mobility on the metal's surface is higher.^[178] Lindner *et al.* highlighted the importance of thiol anchoring position in tetraphenyl scaffold.^[101] While the *para*-substituted (Figure 11, **IV**) anchor forms multilayers, the *meta*-substituted (Figure 11, **XIII**) one develops well-ordered monolayers.^[101] Meanwhile, the single molecule conductance is not influenced by the anchoring position.^[101] This is in contrast to other studies concerning the anchoring position.^[179] They further synthesised a series of molecular tetraphenylmethane derivatives (Figure 11, **IV** n = 1 - 4). On gold, these molecules adsorbed in a periodic lateral arrangement with one acetyl group protruding from the molecular film. By means of the STM-tip, they were able to remove the acetyl groups without causing a significant change in the molecular assembly. The modified molecules were then distinguishable from the parental ones. By varying the length of the molecular spacer, they could control the mesh size of this “molecular graph paper”.^[180]

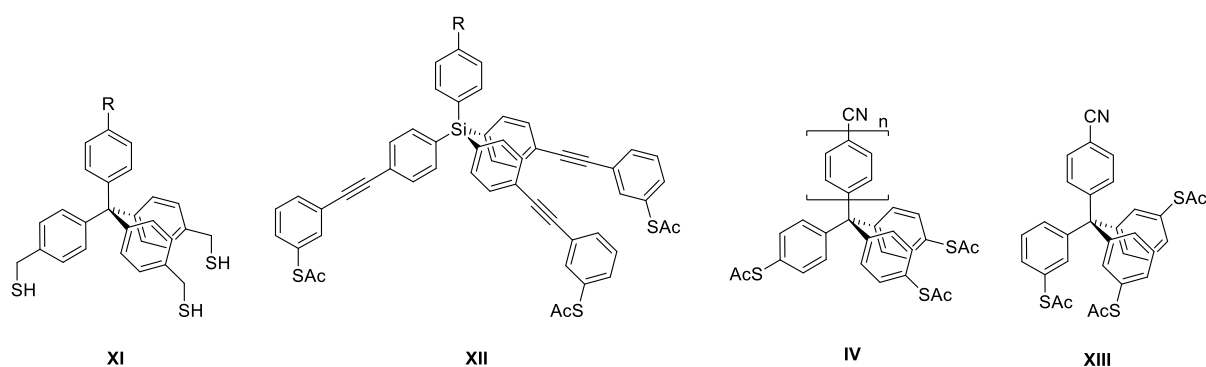


Figure 11. Different tripodal Platforms. Flexible tripodal platform **VIII**, silane based tripodal platform **XII** and two tetraphenylmethane based anchors **IV**^[180] and **XIII**^[180].

Benneckendorf *et al.* introduced four anchoring groups on two sides of triptycene scaffold and obtained an almost perpendicular orientation of the top-part (Figure 12, **XIV**).^[181,182] Inspired by the design of the “Houmuwu-ding” (heaviest piece of bronzeware of the ancient world), Yao and co-workers synthesised a quadripod for non-covalent interfacial coordination assemblies (Figure 12, **XV**).^[183] On an ITO-surface, coated with their SAM, they were able to mount ferrocene or bipyridine Ru complexes and to perform several redox and optical studies.^[183] An entirely new concept was devised by Bryce *et al.*: They split the anchoring task and the conducting pathway within the molecule (Figure 12, **XVI**).^[184] The double sulfanyl-decorated carbazoles are placed on each site of the anchor, while the core benzene-unit enables the conducting.^[184] However, perpendicular arrangement of the mounted units could not be achieved with such system.

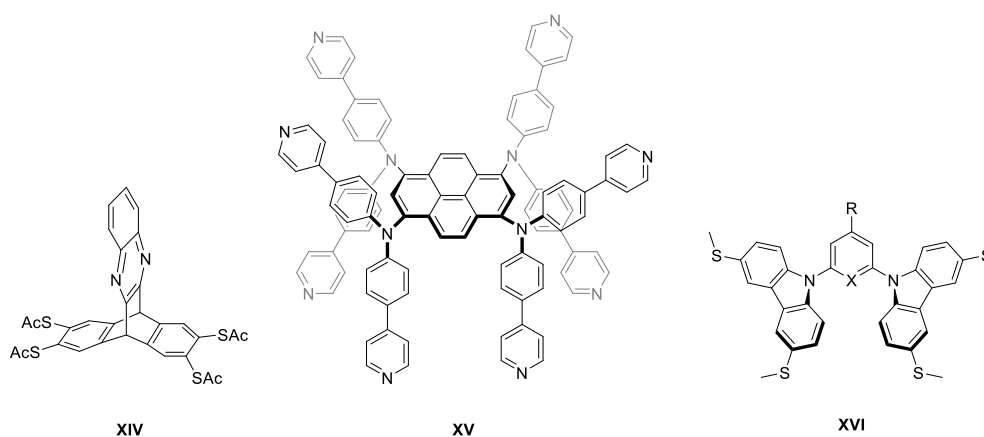


Figure 12. Tetrapodal anchor **XIV** by Benneckendorf *et al.*,^[181,182] quadripod **XV** Yao *et al.*^[183], and the multidentate anchor **XVI** by Bryce *et al.*^[184].

1.3.5 Linker

The design of the entire platform has to be chosen carefully, since the requirements of the functional units vary for different devices. Therefore, molecular engineers must tune the electronic coupling of the frontier orbitals of the molecules with the electronic structure of the substrate. For electronic devices, the electronic coupling must be maximised while in optoelectronic devices, the linker should break the electronic pathway, to efficiently decouple the chromophore from the substrate thus prevent quenching of the excited states. This concept

will be further introduced in Chapter 1.5.3. In tripodal structures, to provide electronic (de)coupling between the functional units and the substrate, controlling the π -conjugation of the entire platform is of key interest.

Note, that while controlling the electronic properties of the anchor, molecular engineers must maintain the rigidity of the entire scaffold and preserving the spatial control of the functional units.

1.3.5.1 Electronic (De)coupling

Early studies of single molecules which enable conductance was done by Reed and Weis and his co-workers.^[185,186] They showed that in a mixed SAM between *n*-dodecanol and an ethyl-substituted benzothioacetate derivative an increased conductance is observed in comparison to the non-mixed thioalkane SAM.^[185] Further conductance experiments of single molecule junctions have been made and lead to a good understanding of conducting mechanism,^[187,188] such as implementing push-pull-systems,^[189] the impact of multicentre bonds,^[190] the influence of chain length of the unsaturated linker^[191] or even integrating an insulating unit.^[192] Generally, the level of (de)coupling correlates with the degree of the conjugation within the entire anchoring group.^[99,193] Venkataraman studied a series of substituted biphenyls with alternated twist angles. With increasing twist angle, the tendency of decrease the conductance was confirmed.^[194] Mayor *et al.* confirmed the same tendency of decreased conductivity with an increased torsion angle.^[193]

Herges and co-workers comprehensively studied a series of surface-catalysed *cis-trans* switching.^[195] By means of azobenzene-functionalised TATA platforms, they observed a gold-catalysed rate acceleration of the switching depending on the level of conjugation. For this, they designed six different derivatives with different conjugation lengths, increased torsion angles and (nearly) insulating units. In case of high π -conjugation, rate acceleration was observed.^[195]

Another approach in which spatial control was preserved while enabling an increased conductance has been published by Mayor and co-workers as depicted in Figure 13 on the left side. By chemical engineering,^[180] they prolonged the π -delocalisation of molecule **IV** to the upright phenyl ring. This led to molecule **XVII**, in which two additional σ -bonds are introduced, with one yielding a fully conjugated system (Figure 13, left, red biphenyl) between

the nitril and the anchoring sulfur.^[149,196] A similar approach has recently been reported by Aso *et al.* as depicted in Figure 13 on the right side.^[150,197] The evolution of the thiophene-based tripodal anchor, first published in 2015,^[197] is marked in red in Figure 13 on the right side. With the one-side π -conjugated 2,2'-bithiophene-naphthyl leg, they accomplish hole-transport from the gold-surface to the functional unit and reported the first conjugated π -channel hybridisation.^[150] In comparison to early reported anchor, the recent one outperforms in term of conductance.^[150,197] Aso *et al.* also developed a π -channel anchor which acts through to LUMO, thus as an electron acceptor.^[147]

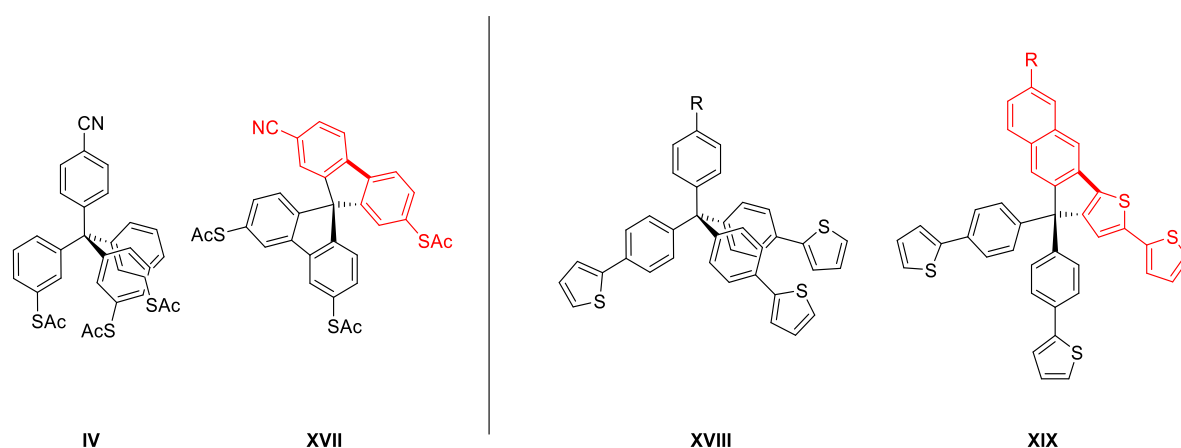


Figure 13. Structural development to increase conductance of tetraphenylmethane based tripod **IV** to spirobifluorene **XVII** by Mayor *et al.* (left side) and **XVIII** to **XIX** by Aso *et al.* (right side).

1.3.5.2 Spatial Control

In comparison to the conductive features of anchoring groups, the control over spatial arrangement of the functional groups at the surface has attracted less attention. Especially in multipodal anchoring strategies, the molecular engineers aim to provide an upright orientation. Furthermore, spatial control of molecular arrangement is also important regarding a defined tilt angle. In single molecule luminescence studies, the presence of various luminescence spectra of self-decoupled tetrapodal perylene diimide show, that the adsorption configuration plays an important role.^[198] Therefore, the control over the tilt angle of the functional unit is inevitable for single molecule devices.

1.4 (Single) Molecular Machines

1.4.1 General

Molecular machines have been present since the origin of life and the variety of this amazing biological protein machinery has been inspiring scientists who try to mimic their features.^[199] Both artificial and biological machines convert energy (electrical, chemical or thermal) into mechanical motion. However, because of their complexity it remains a challenging task to transfer these biological systems *ex vivo*.^[200] As a consequence, scientists try to transfer the knowledge gained from biology in to artificial nanoscale machines which can be operated *ex vivo*. Since nature is still the best chemical architect, man-made artificial machines are much simpler than their biological counterparts. With the outstanding input of the chemists Jean-Pierre Sauvage, Fraser Stoddart and Ben Feringa, tailor-made artificial machines have become accessible. Since then, many different applications of molecular machines have been demonstrated, such as elevators,^[201] shuttles,^[7] or synthesisers^[202] and may allow to build chemical computers, since implementation of functional molecules in logic operations already happened.^[34]

The terminology of molecular machines can be defined as devices which are able to perform a defined function by means of external energy in the molecular scale. Molecular machines and motors are often used as synonyms, however, to use the same terminology from the macroscopic world, a molecular motor converts energy into motion (in nanoscale, the randomness of thermal motion is excluded),^[203] whereas molecular machines usually consist functional units energised by motor components. Ultimately, molecular motors can be used to force systems out of the equilibrium. However, most of these systems have been accomplished in solution and are thus subordinated by Brownian motion and not by gravity and inertia. Such molecular devices must be sufficiently big enough to overcome the random thermal motion. To find a balance between the macroscopic Newtonian motion and the microscopic Brownian motion is one of the most challenging tasks for molecular engineers.^[204,205] To quote R. D. Astumian, molecular machines must “*swim in molasses and walk in a hurricane*”.^[206]

1.4.2 Working Mode of (Molecular) Machines

Molecular machines can be defined by similar characteristics from the macroscopic world^[203]

1. Operation mode
2. Monitoring
3. Time scale
4. Cyclic process
5. Form of motion
6. Form of energy input

To start with the most obvious one, the operation mode determines in which way the molecular machine is designed to operate.

Of course, for controlling and observing the functionality of the molecular machine, the change of chemical or physical property must be measurable.

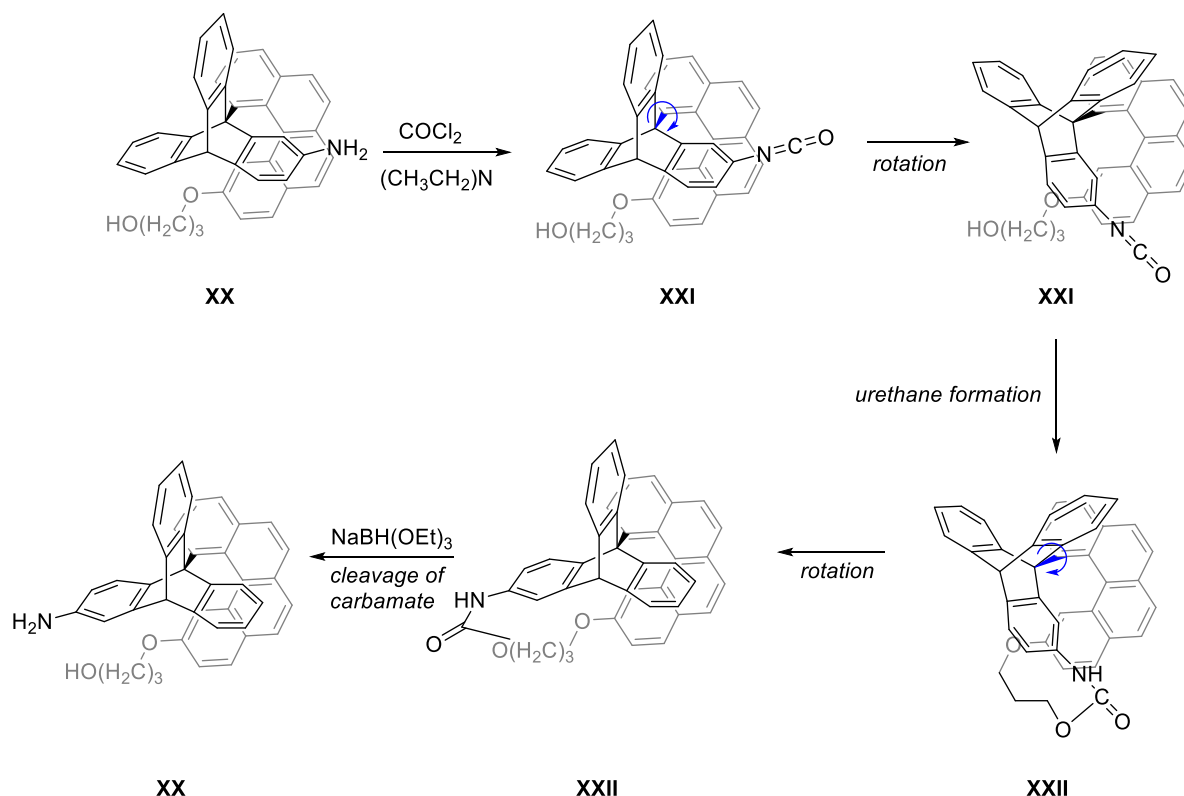
The time scale of motion can range from the almost infinite to the lowest detectable speed limit.

A key feature of molecular machines is the capability of operating in a constant behaviour, which means the motion is *autonomous*. While applying the same external energy source (fuel), the motion should be available and cyclic. Most of the non-electrically powered machines are not *autonomous*; they need different types of external stimuli *e.g.*, different light excitations^[9] and hence the motion is not cyclic.

The form of motion can be deduced from rotations around covalent bonds, by the change in the environment^[7,207] or by forming of new bonds.^[208]

In close connection with motion, the form of external stimuli has a tremendous impact on the system.^[209] Kelly *et al.* introduced a chemically driven molecular system which is illustrated in Scheme 1.^[208] Their approach is based on a triptycene “wheel” and a helicene “brake” molecule **XX**.^[210] With this design, the rotational barrier around the aryl-aryl bond is about 25 kcal mol⁻¹ and thus hampering the spontaneous rotation around this axis. If this rotation is performed without chemical stimuli (*e.g.* external heating), there is no unidirectionality since the barrier of rotation is the same in both directions.^[211] However, unidirectionality was accomplished by chemical stimuli with phosgene and intramolecular reaction to **XXII**. As a result, the sterically constrained conformer **XXII** is formed. This conformer then relaxes *via*

directed rotation into the less constrained one (see Scheme 1, second rotation around the C-C bond (blue), **XXII**). After cleavage of the carbamate, a 120° rotation is completed. One drawback of this approach are side products which are formed by the chemical reactions. Similar approaches based on tricarboxylate^[212] systems or metal complexations^[213] have also been published.



Scheme 1. Chemically induced rotation of the rotor **XX** by Kelly *et al.*^[210]

Thus, electrochemically or photophysically stimuli driven systems have been established to overcome the waste formation.^[34] Prototypes of electrochemically driven motors have been pioneered by Sauvage, Stoddart and lately by Leigh.^[214] The other waste-less fuel is based on photoexcitation which usually involves reversible reactions, such as *cis/trans* isomerisation of $\text{C}=\text{C}$ ^[215] or $\text{N}=\text{N}$ bonds.^[128]

1.4.3 Molecular Rotators on Surfaces

Before Feringa *et al.*, also Tour and his group published a design of molecular rotor on gold surfaces which should be triggered by an external electric field.^[173] So far, only the synthesis and design of such molecular motors has been published, while the proof of concept of this experiment is still missing. In general, surface mounted molecular rotors can be split into two groups: azimuthal rotors having the rotational axis perpendicular to the surface (Figure 14, left) and altitudinal rotors, whose rotation axis is parallel to the surface (Figure 14, right).^[216] Both setups require a stator which provides the mechanical stability. Furthermore, throughout this thesis we will refer to the rotating part as the rotator, the combination of rotator and stator as the rotor and if the motion of the rotor is induced upon electrical stimuli, we will refer to this device as a motor.

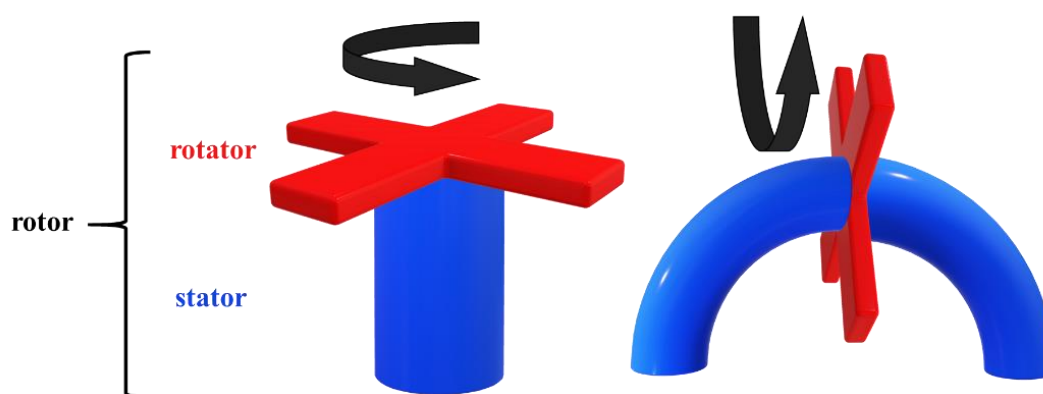


Figure 14. Illustrative azimuthal (left) and altitudinal rotors right).

One of the first altitudinal molecular rotor (Figure 9, **XII**) has been published by Michl *et al.*^[142] Recently, Tour and co-workers controlled single-molecule rotation of a polar molecule placed in between two adamantane “wheels” by changing the tip position.^[217] Yet, the directionality of such “molecular Segway” on the Ag surface is not deduced by the intrinsic features of the molecule but rather by the STM tip itself. Furthermore, the molecule is not covalently bound to the surface and therefore, it even undergoes translation at higher biases.^[217]

In 2011, Sykes experimentally demonstrated that one can rotate azimuthal rotor by electric “fuel”.^[218] When butylmethylsulfide is bound on the surface, a pair of two enantiomers

exists. In their study, thermal induced rotation around the gold-sulfur bond is random, while excitation with the STM-tip prevails a 5% directionality for one enantiomer and an increase in rotation speed for the other enantiomer. They assigned this feature to the intrinsic chirality of the STM tip,^[219] because with achiral tips no measurable difference was observed. Recently, they observed the same behaviour in *N*-methylbutylamine rotors on copper substrates.^[220] Since the findings of Sykes, many groups have studied the rotational behaviour of molecules mounted on surfaces, including the work of Fonin *et al.*^[221] in which the motion of the molecule is not initiated by rotation around a pivot point but instead flips over silver adatoms, which in a macroscopic world can be compared to a Mexican-wave-behaviour. Scientists around Wang were able to manipulate single atoms of tin-phthalocyanine on gold and thus create up to four different rotation axis within one molecular design.^[222] A gear-inspired experiment has recently been published by Moresco and colleagues, which is based on star-shaped pentaphenylcyclopentadiene derivatives.^[223] By manipulating a “driver”, they were able to show that two neighbouring molecules were affected by the original manipulation and followed the direction, just like in trains of gears. An advanced, electrically unidirectional motor was published by Fuchs and co-workers, as shown in Figure 7a.^[100] Based on a *N*-heterocyclic carbene rotor, they were able to show that a symmetric non-chiral rotor shows random rotation, while the modified asymmetric chiral rotor performs unidirectional motion.^[100] Only very recently it was shown, that unidirectional motion of an ethylene unit connected to a chiral Pd₃-Ga₆-Pd₃ cluster can be observed.^[224]

1.4.4 Azimuthal Molecular Motors on Surfaces

In these aforementioned azimuthal motors, the molecular substrates serve as stators and the molecules themselves as rotors. Another approach includes both stator and rotor serving as subunits of the same functional molecule. In 2013, Rapenne, Joachim and Hla designed a piano-stool-like molecular rotor based on a ruthenium cyclopentadienyltris(indazolyl)borate complex (see Figure 15, left) and they deposited it on gold (Figure 15, right).^[171] They claim that almost every tunnelling electron energy transfer can induce a rotation step, indicating that an inelastic electron tunnelling (IET) process is underlying. Short excitation leads to single step rotation, whereas longer manipulation starts a multistep transformation. Given the symmetry

of the molecule, either clockwise or anticlockwise rotation can be expected. Interestingly, placing the STM tip on different positions above the molecule results in different rotation directions. Placing the tip above the phenylene arm of the rotator, clockwise rotation was observed. On the contrary, inducing IET into the ferrocene, anticlockwise motion occurred. Supported by theoretical calculations, for an entire rotation around the axis, 15 local minima (15 potential wells) are to be expected (5 arms + 3 tripodal anchor). Calculations produce a unsymmetric sawtooth-like rotational potential shape which is required for unidirectional rotation.^[225] Computational studies found that the potential energy curves for different LUMOs show reverse direction shapes, which would explain clockwise and anticlockwise rotation. LUMOs lying close to the ruthenium core can be excited through the shortened phenylene arm, while the other LUMO levels lay on the ferrocene sites. To sum up the rotation, the transferred energy by the IET is converted into translational energy (rotation) *via* vibrational relaxations to the ground state.^[171]

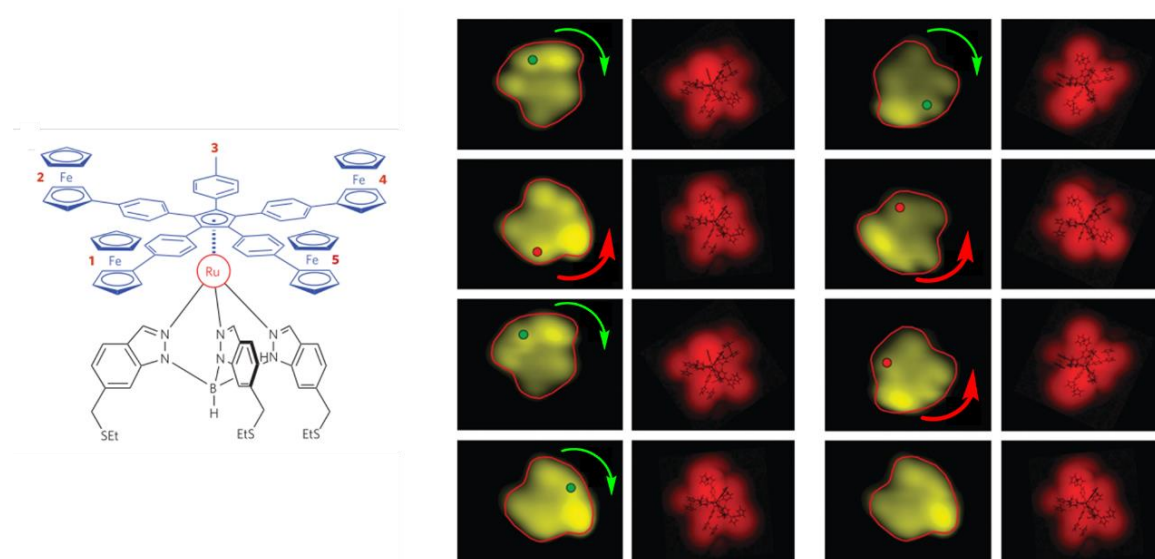


Figure 15. Left: Molecular piano-stool rotor by Rapenne, Joachim and Hla. Right: Clockwise rotation (green arrows) or anti-clockwise (red arrows) motion. Directionality depends on the STM tip position. Image taken and slightly modified from Ref.^[171]

Later, Rapenne and Hla used a precursor from the previous experiments as a chiral molecular propeller which showed unidirectional rotation.^[226] Noteworthy, in this experiment rotator and stator were inverted, where this metallic complex arranges on the surface in reverse order. Therefore, the cyclopentadienyl part serves the stator, while tris(indazolyl)borate complex has

become the rotator. By adsorbing its penta(*para*-bromophenyl)cyclopentadienyl analogue, chirality is dictated and rotation follows accordingly.^[226] Furthermore, they also developed molecular rotor networks based on porphyrine-naphthalocyanine europium double-decker complexes.^[227] As already mentioned, the research group of Herges is also interested in the functionalisation of surfaces. With derivatisation of TATA^[127] and TOTA platforms, they also entered the field of rotation studies of surfaced mounted molecules (Figure 16).^[129] They placed both ethoxy and ethyl moieties on top of TOTA-platform which finally arrange as a hexagon-cluster of 6 individual molecules on the surface (Figure 16, c)-e) + f)-h)). Switching the molecular states is possible even at mild conditions and stoppable if wanted. However, the activation energy of the ethyl-rotator to switch differs in the two structures. This is explained by the stronger binding of the rotator's methylene-protons to the two neighbouring oxygens in Ethyl-TOTA (Figure 16b, see the green marked protons and their interaction to the neighbouring oxygens (red)). The rotation is only observable above a certain voltage, implicating that the rotation is an over barrier process rather than a tunnelling process. The authors show that they could rotate the moieties in a controlled manner. This means that the rotor followed the STM tip. With increasing distance of the tip apex to the rotor, the directionality control was significantly reduced. The total yield of rotation is independent of the tip position.^[129]

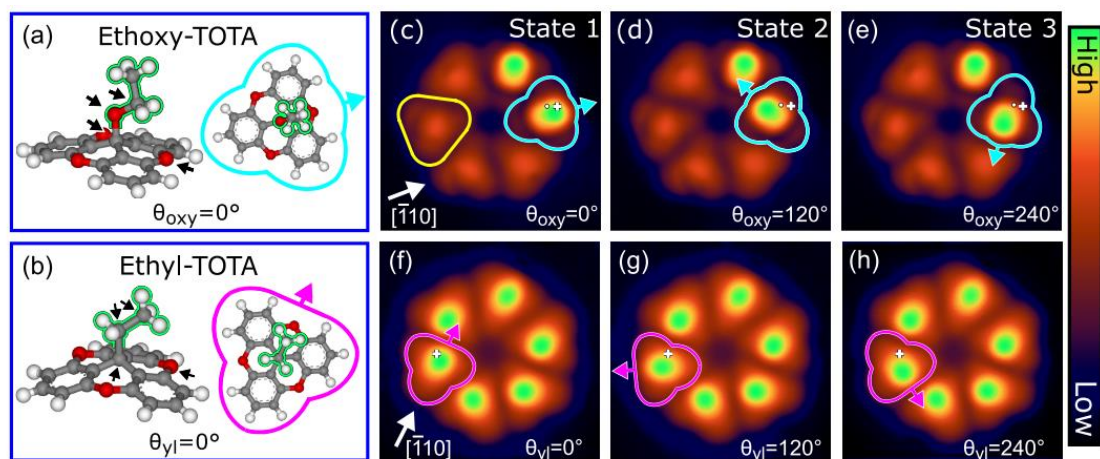


Figure 16. a) Ethoxy-TOTA molecule, b) Ethyl-TOTA molecule, c)-e) rotation states of ethoxy-TOTA, f)-h) rotation states of ethyl-TOTA. Image taken from Ref.^[129]

Our group has recently published tetraphenylmethane derivatives which show promising features towards a molecular rotor (Figure 17a, **III**).^[177] On gold, there are six different metastable conformational isomers which can be deduced to a combination of a rotation of the slightly tilted molecular head group. The internal inversion of the molecular foot is shown in Figure 17b) and c). The rotation of the head group stops at three equivalent local minima, which are separated by 120° (Figure 17d). Another rotation mechanism is based on the change of adsorption geometry by the concerted inversion of the molecular foot around the C-S and C-C bond, which is equivalent to a 60° rotation (See Figure 17b) from even numbers to odd numbers). An energetically equivalent adsorption is shown in Figure 17c). The rotation of the head group (nitrile) is more likely to happen than flipping each “foot-phenyl” simultaneously.

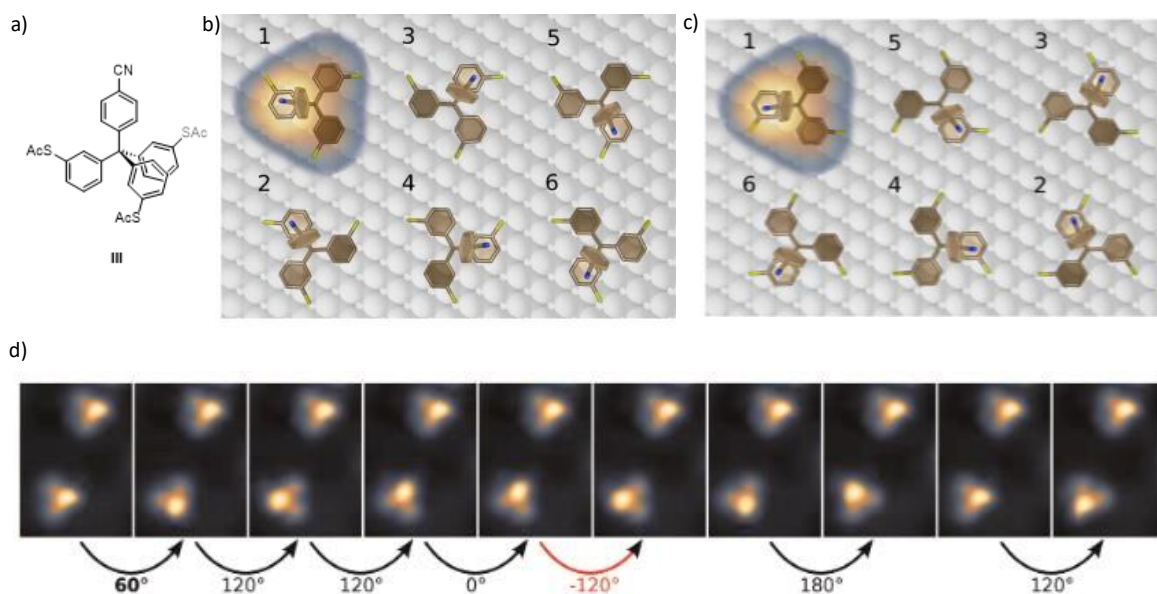


Figure 17. a) Molecular revolver, **III**. b) and c) energetically equivalent adsorption and the illustrative rotation. d) STM images showing the rotation of the molecules. Taken and modified from Ref.^[177]

However, with this first prototype, rotational unidirectionality of the “molecular revolver” was not achieved.^[177] Given the fact that the aforementioned rotors consist as combinations of stators and rotators within the same molecule, to some extent the directionality - if it is observed - is dictated by the geometry of the stator and the resulting ratchet-like mechanism. When being independent of any foot geometry, one needs to utilise the intrinsic characteristics

of the rotator only. One approach transfers the working principle of macroscopic electric motors based on the Lorentz force to the nanoscale. Here, rotational switching is induced by applying a magnetic field that acts on the electrons that pass through the molecular motor. This current then leads to a Lorentz force that forces the rotator to rotate in one direction. Theoretically, by externally reversing the direction of the magnetic field, the rotation direction is expected to change to the opposite.

Another approach is based on the chiral induced spin selectivity (CISS) effect and will be described in the next chapter.

1.4.5 Chiral Induced Spin Selectivity – Effect

Spin filtering of electrons by chiral molecules was first observed by Ray *et al.* almost 30 years ago, when he showed, that the transmission of spin polarised electrons through one enantiomer of stearyl lysine was different than from the other enantiomers.^[228] In order to understand the effect, many experiments have been done including photoelectron transmission measurements of chiral monolayers,^[229] that are chiral molecules adsorbed on a surface, conduction measurements of chiral monolayers^[230] and electrochemistry experiments of chiral molecules.^[231] In general, the CISS effect is the interaction between the electron spin and its momentum with the chiral electronic field of the axis. This interaction results in a generation of preferred electron spin direction within the molecular frame.^[232] In an electrostatic field, the moving electron feels a magnetic field in its rest frame and thus, the electrons spin magnetic momentum interacts with the magnetic field. In light atoms, such as carbon, the spin-orbit coupling is weak and a cumulative effect is necessary.^[233] When the electron moves through the helix, it interacts with single atoms of the helix. Each of it leads to a spin-orbit coupling. Necessarily, the orientations of the orbits must point out in the same directions otherwise, quenching of the effect would occur. In chiral molecules, this situation is given.^[234] The chiral charge distribution of the molecule induces a magnetic field onto the electron in its rest frame. In this frame, when the electron passes the helix, the moving charge distribution of the chiral molecule creates a magnetic field \vec{B} acting on the electron (Figure 18). For a given charge q and spin state σ , the magnetic field \vec{B} is described as

$$\vec{B} = \frac{\vec{v}}{c^2} \times \vec{E}_{chiral}$$

where \vec{v} is the velocity of the electron, c is the speed of light and \vec{E}_{chiral} is the chiral electric field. \vec{E}_{chiral} is defined by the pitch of the helix p , the radius of the helix R and the distance along the helical axis Δz .

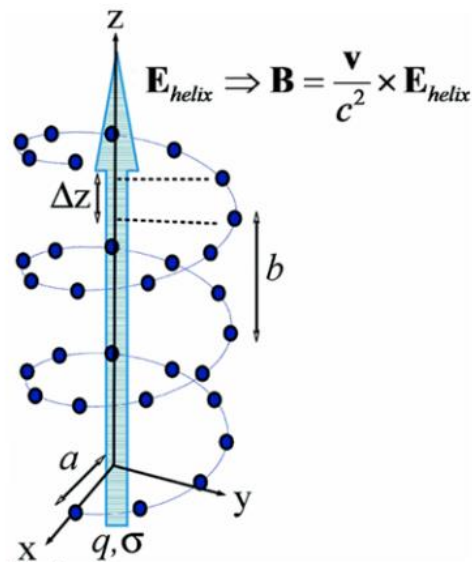


Figure 18. The effective magnet field B , which is generated by the helical electrical field E_{chiral} . With q being the charge and σ being the spin state of the moving electron. E_{chiral} is defined by the pitch of the helix p , the radius of the helix R and the distance between the single components of the helix Δz .

The models explaining the CISS effect are still under debate but they have to agree with observed features, such as the length dependence of the molecule with respect to the spin polarisation effectivity,^[229] temperature independence^[229,230] and the reversibility of spin polarisation between two different enantiomers of the same molecule.^[235] Many theories have been shared by the scientific community,^[233,234,236–238] yet none of them can explain all of the observations. Recent experiments have shown that CISS is not only observed in SAMs but already happens in single molecules.^[239,240] Kumar *et al.* showed that spin polarisation is accompanied by charge polarisation^[241] and later it was demonstrated that upon addition of polarisable units, enhancement of spin polarisation occurs,^[242,243] which leads to the conclusion that spin polarisation must be created within the molecular structure and net electron transfer is not needed. Only recently, Yamamoto *et al.* have combined the chiral induced spin selectivity effect with the molecular rotor approach of Feringa.^[244] Upon external triggering of the molecular rotor, conformation change occurred, which lead to the spin polarisation flip.^[244]

1.5 Luminescence¹

1.5.1 General

The terminology “luminescence” descends from Latin (lumen = light) and was introduced by Eilhardt Wiedemann in 1888 to describe “all those phenomena of light which are not solely conditioned by the rise in temperature”.^[245] To be more precise, luminescence is the spontaneous emission of light by an excited molecule which is not in a thermal equilibrium with its surrounding environment.^[246] Various types of luminescence are known, such as photoluminescence, cathodoluminescence, electroluminescence, chemiluminescence and *etc.* The most important ones for the presented work are electroluminescence and photoluminescence. For the latter one, it is common to distinguish between fluorescence and phosphorescence. Fluorescence is defined as the spontaneous emission of radiation after exciting a molecule with retention of spin multiplicity.^[246] After light irradiation, the electron is excited from the vibronic ground state S_0 to excited vibrational states S_1 or S_2 . Since the spin of the electron must be conserved, the transition usually results in an excited singlet state. The transition probabilities from the vibronic ground states of S_0 into the different vibronic states of S_1 depend on the overlap of the vibronic wave functions (Franck-Codon-principle). Then, in the internal conversion, which is considered the fastest relaxation process, the excited molecule relaxes non-radiatively into the lowest vibronic level of that state (Kasha’s Rule) (Figure 19, orange lines). From the S_1 (or S_n) state, the excited molecule relaxes into the ground state S_0 and can release energy in the form of light. This process is called fluorescence. However, competing relaxation pathways are present, such as internal conversion to the S_0 -state or transferring the electron to potential redox partners. Since some part of the energy for the excitation relaxes non-radiatively, the wavelength of the emitted light is always longer than the excitation light, this difference is named *Stokes* shift. The timescale of the absorption process is within femtoseconds, while the fluorescence occurs in a pico- or nanosecond time scale. In contrast to that, phosphorescence can endure in the timescale of seconds. Phosphorescence is the long-lived luminescence which involves change in the spin multiplicity. This process

¹ Parts of this chapter have been accepted by Chemistry - A European Journal:

N. Balzer, J. Lukášek, M. Valášek, V. Rai, Q. Sun, L. Gerhard, W. Wulfhekel, M. Mayor, *Chem. – A Eur. J.* **2021**, doi: 10.1002/chem.202101264

typically undergoes inter-system-crossing from singlet states to triplet states (Figure 19, blue lines).^[246] Inter system crossing becomes weakly allowed through spin-orbit coupling. From the triplet state (T_1), the excited molecule can relax back to the ground state either by emitting light (phosphorescence) or non-radiatively. However, another spin flip must be overcome. Therefore, the timescale for phosphorescence is much longer than for fluorescence.

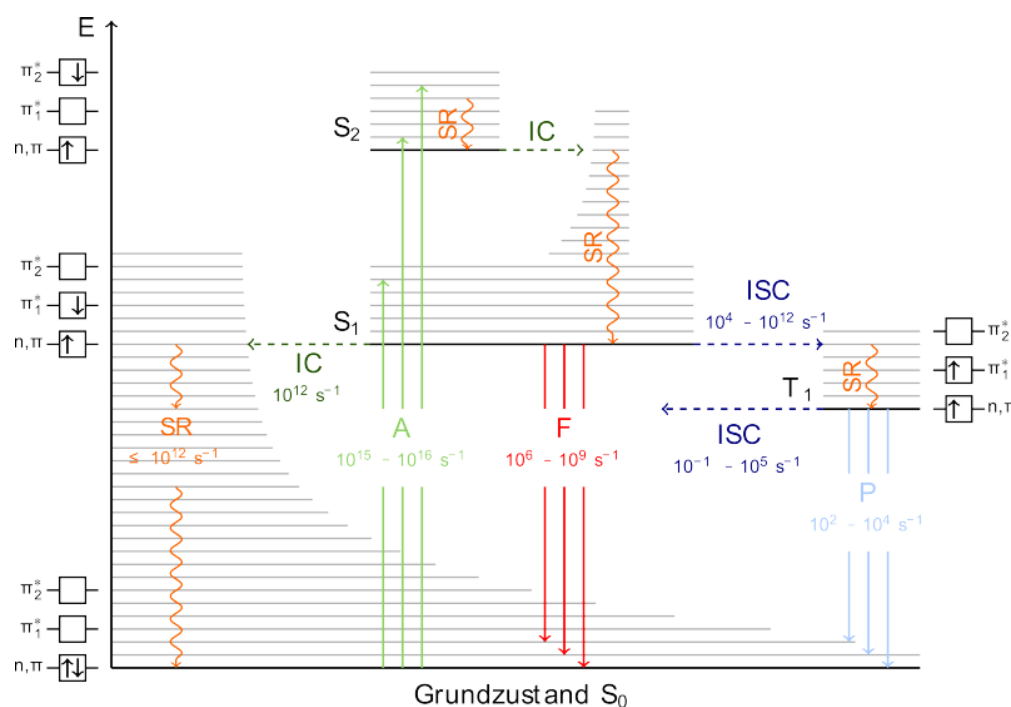


Figure 19. Jablonsky diagram showing ground state S_0 , excited states S_1 and S_2 . After absorption (A), internal crossover (IC) leads to non-radiative decay from vibrationally excited states to S_1 . Fluorescence (F) is observed by radiative relaxation of the excited state to the ground state S_0 . Another pathway runs through inter-system-crossing (ISC), which requires a spin flip of the excited electron. Subsequently, the radiative decay of the excited electron leads to phosphorescence (P). Image taken from Ref.^[247]

In contrast to photoluminescence, electroluminescence is the non-thermal conversion of electrical energy into optical radiation.^[246] Electroluminescence is the concept behind light emitting diodes (LED) and organic light emitting diodes (OLEDs) whose historical development was recently reviewed by Bräse *et al.*^[248] Electroluminescence was first observed by Destriau *et al.* in 1936 from ZnS phosphor powder positioned in between two electrodes.^[249] Due to low efficiencies and low lifetimes of electroluminescence by organic crystals,^[250] research interest in organic light emitting compounds was low at that time and was revived 25 years later than their first observation.^[3,251] Since then, many different organic or hybrid

molecules for electroluminescence have been reported.^[252] In electroluminescence, an electric field needs to be applied to create charge carriers (electrons and holes) within the emitting unit. As shown in Figure 20, after injecting the electron (e^-), a radical anion is formed. Simultaneously, a hole must be created at the anode which forms a radical cation. This newly formed species, named exciton, consists of an electron and a hole, attracting each other by Coulomb forces. If the charge carriers meet in close distance, they will recombine and thus release energy in the form of light. However, only if spin-allowed transitions are present, fluorescence is observed. Recent research in OLED devices focuses on the thermally activated delayed fluorescence (TADF).^[253] Induced by nearby thermal energy, reversed intersystem crossing (RISC) leads to the depopulation of the triplet states and the population of singlet states, which then can relax into the ground states by emitting light. If RISC is present, the emission efficiency of OLEDs increases.

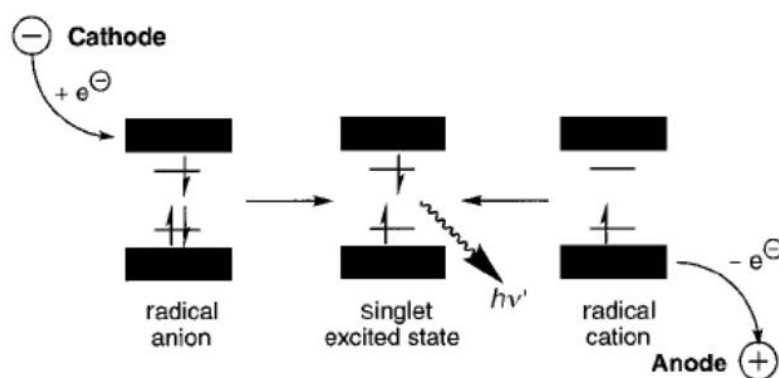


Figure 20. Simplified version electroluminescence. Upon inserting electrons *via* the cathode and holes *via* the anode. Charge recombination from the singlet excited state results in emitting of a photon. Image taken and modified from Ref.^[254].

1.5.2 Single Molecule Luminescence

Fathoming the underlying light emission processes from molecules is not only interesting from a scientific point of view but also a key factor in developing new materials for optoelectronic devices based on organic chromophores. Therefore, single molecule optoelectronic studies are inevitable. A promising approach to study electrically induced light emission and the underlying mechanisms involved in the optoelectronic response with submolecular precision is based on scanning tunnelling microscopy induced luminescence (STML) experiments.^[255–257] In 1971, STML was theoretically proposed by Young.^[258] Around 20 years later, this concept was experimentally shown^[259,260] and in 2003, it was demonstrated that submolecular precision of vibrationally resolved fluorescence was achieved.^[261] In general, STM induced luminescence can be divided into three different regimes according to the tip-sample distance. In each regime, different mechanisms prevail. On the one hand, for large tip-sample distances, voltages higher than 10 V are essential to measure current. In this setup, catholuminescence - that is electron bombardment - can be observed and one advantage of this setup is that no optical-field enhancement by the tip is affecting the luminescence. On the other hand, with small tip-sample distances (in the range of 2 Å), voltages in the mV range are enough to observe measurable currents and ultimately lead to multielectron or hot electron emission pathways.^[262,263] The scope of this work, however, focuses on the tunnelling regime where voltages in the range of 1 V are sufficient enough to observe tunnelling currents in the order of nA. In this regime, STM-induced luminescence can be achieved mainly by two different mechanisms. Firstly, so-called tip-induced plasmons^[257] lead to a mechanism which is comparable to photoluminescence. An inelastic electron tunnelling process induces a direct energy transfer to the electromagnetic modes of the cavity between the tip and sample. This process then excites the molecule which then ultimately relaxes into its ground state by emitting light. In general, plasmons can be defined as oscillations of the free electrons in a metal and in STM experiments (which consist of metal contacts), light emission by plasmon modes are present.^[255] If there are molecules in between the metal contacts (substrate and tip), tip-induced plasmons can dominate or enhance the molecule's luminescence. Calculations revealed that only about 0.1% of the tunnelling electrons leads to photon by tip-induced plasmons.^[264] The second mechanism in the tunnelling regime occurs if the HOMO of the chromophore matches the Fermi-energy of the substrate and if the LUMO is lower than the tip's energy level. Then charge injection forms an electron-hole pair (exciton) that can recombine and thus lead to

electroluminescence (Figure 20). Clearly, the Coulomb interactions between the two charge carriers (holes + electrons) are highly dependent on the charge mobility of the material and in the case of organic molecules, the excitons are localised quite closely, compared to semiconductors.^[265] Furthermore, other pathways for single molecule light emission have recently been discovered, including dipole-dipole coupling, hot electroluminescence, plasmon-exciton coupling and electrofluorochromism at the single-molecule level, respectively.^[266–269]

1.5.3 Self-Decoupling of Chromophores

To enable electroluminescence from single molecules within the scanning tunnelling microscopy setup, one has to face four major issues. On the one hand, the molecule must be stable enough to sustain both charge carriers within the same molecule. On the other hand, the lifetime of this inner salt (one may call it zwitterion) has to be long enough so that the charge carriers can meet to recombine. This leads to the third challenge: If the chromophore is too close to the metal substrate, it will form hybridised electronic states with the surface. This then would result in a non-radiative exciton quenching. In order to prevent this, the emitter must be electronically decoupled from the underlying metal substrate to compete with quenching of the molecule's excited state by the metal's electrons.^[259,261] Common approaches to achieve such isolation of individual chromophores are either based on ultrathin (in)organic insulating layers with large band gaps of several electron volts between the metal surface and chromophores,^[259,261,270,271] or on multi-layered stacks of the chromophore.^[272] Alternatively, less explored strategies to electronically decouple organic emitters from the underlying surface involve either bulky spacer groups within the tailor-made molecule or large multipodal platform.^[107,273] The latter has been recently applied e.g. with a fully symmetric tetrapodal molecule, from which three functional legs served as tripod and the fourth leg was perpendicularly arranged in an upward direction.^[198] The focus of the presented work is on separating the chromophore subunit from the surface with a rigid multipodal anchoring scaffold.^[102,131,163] The modular strategy of electronic decoupling *via* a rigid multipodal platform not only enables the investigation of a variety of chromophores, but also allows to align the chromophore's dynamic dipole vector perpendicular to the surface. This is the fourth key issue which molecular engineers must take into consideration in the design of the single molecule self-decoupled chromophore.^[274]

1.5.4 NDI Chromophores for Single Molecule Luminescence

Amongst others,^[252] various derivatives of naphthalene-1,4,5,8-tetracarboxdiimides (NDIs) are widely used in organic electronics due to their by core substituents tuneable electronic and optical properties, their chemical and photochemical stability,^[275,276] and their favourable electron transport properties.^[277,278] Moreover, OLEDs based on these subunits have been recently reported.^[279,280] Although Vollmann *et al.* first published this type of molecules already in the early 1930s,^[281] it was the group of Würthner who draw anew the attention on NDIs and their core substituted derivatives.^[282] In general, NDI is the smallest member of the rylenediimide family and can be synthesised from naphthalene-1,4,5,8- tetracarboxylic acid dianhydride (NDA). The amide condensation of parental NDA with alkyl or arylamines leads to the core unsubstituted NDIs. These NDI scaffolds with their large electron deficient aromatic system show reversible electrochemical reduction properties to form both, radical anions after one-electron reduction and dianions after two-electron reduction.^[283] To modify their electrical, optical or redox properties, NDI scaffolds can be functionalised at three main positions are the axial position, the shoulder position and the core position, as illustrated in Figure 21.

Functionalisation of the axial *N*-imide positions of NDI mainly influences its solubility^[284] or morphology in thin films,^[285] while having negligible effect on the optoelectronic properties. Modification of the shoulder position significantly influences the optical and electrochemical properties of the molecule. This strategy involves either the exchange of the heteroatom of the imide group^[286] or diagonal utilisation of the core position and shoulder position.^[287] The most prominent strategy to fine-tune the electronic and photophysical properties of NDI is based on the substitution at the 2, 3, 6 and 7 positions of the NDI core with various groups, such as alkyl or arylamino, alkoxy, sulfanyl, cyano, thiophene and different heterocycles.^[275]

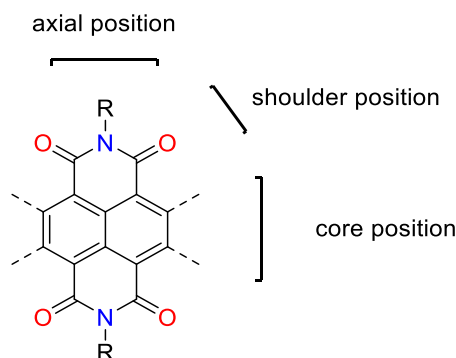
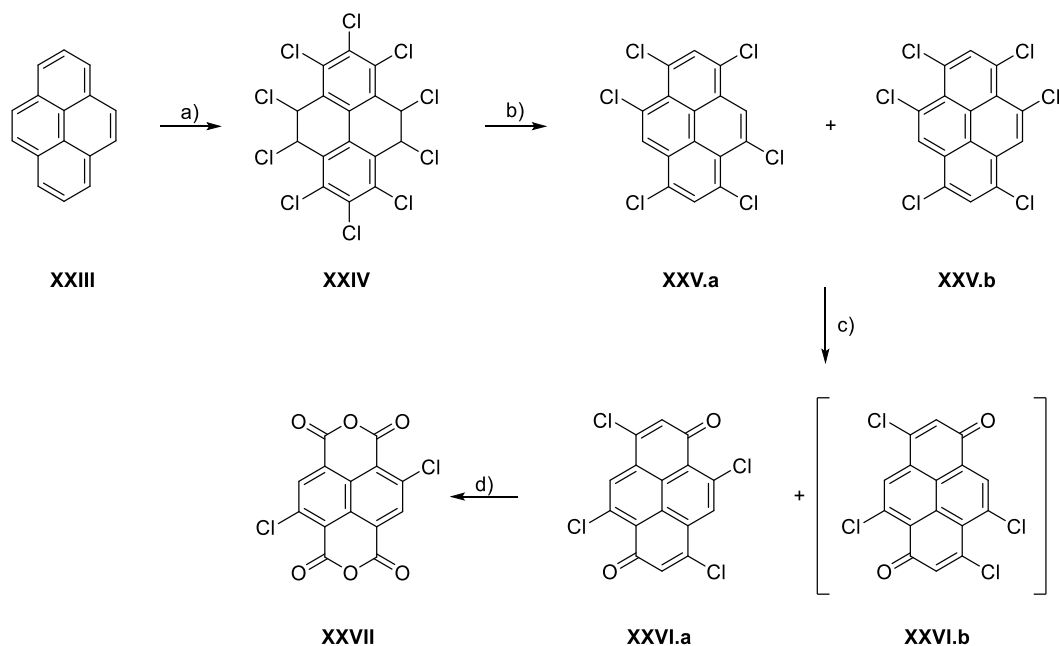


Figure 21. Possible sides for modification of NDI, including axial *N*-imide positions, shoulder positions and core-position.

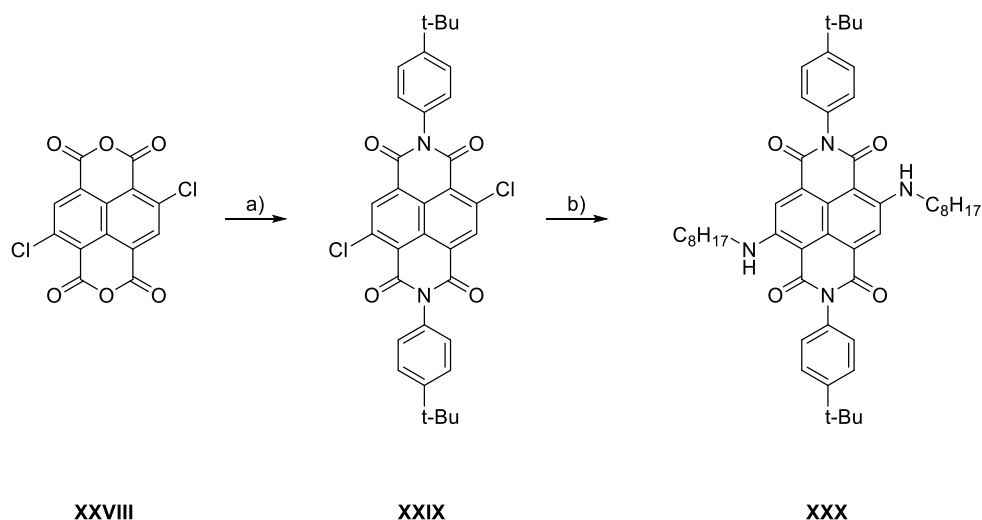
In order to prepare core substituted NDIs, a key precursor is the 2,6-dichloronaphthalene-1,4,5,8-tetracarboxylic anhydride **XXVII**. It was Vollman and co-workers in 1937 who first reported the synthesis of this molecule and some derivatives.^[288] Due to the lack of promising optical features, the research interest in these molecules was low at that time. It was then Würthner *et al.* who modified the synthesis^[283] and reinvestigated the optical features of core-substituted NDIs and thus started the renaissance of these chromophores.^[282] As shown in Scheme 2, Würthner adapted the same approach starting with the chlorination of pyrene. He changed the reaction temperatures, in particular time intervals, and then switched from concentrated nitric acid to fuming nitric acid.^[283] Furthermore, HCl elimination of **XXIV** to yield the two 2,6- and 2,7-dichloro isomers was carried out in ethanolic KOH. Subsequently, precipitation of **XXVIa** was feasible and led to pure isolation of the desired compound. Final oxidation of **XXVIa** to **XXVII** was carried out with fuming nitric acid.^[283] Since their first publication, more strategies for the synthesis of functional naphthalene diimides have been found.^[289]



Scheme 2. Synthesis protocol for **XXX**:^[283] a) $\text{Cl}_{2(\text{g})}$, 1,2,4 trichlorobenzene, b) KOH, EtOH, c) fuming HNO_3 , d) HNO_3 , H_2SO_4 .

With the availability of core-chlorinated NDAs, Würthner then was able to synthesise a variety of core functionalised NDIs.^[282,283] An illustrative example is shown in Scheme 3. In boiling glacial acetic acid, the NDA **XXVIII** is converted into the NDI **XXIX**. A subsequent twofold

nucleophilic aromatic substitution with *n*-octylamine forms the compound **XXX**. Würthner and his co-workers were able to show that their core-substituted NDIs could be used in FRET studies^[282] and had significant higher fluorescence quantum yields than the core-substituted NDIs by Vollmann *et al.* Furthermore, Würthner was able to synthesise and characterise different core substituted NDIs showing a variety of optical and redox properties.^[283]



Scheme 3 . Synthesis protocol for molecule **XXV**.^[283] a) 4-*tert*-butylaniline, glacial acetic acid, 120 °C, b) *n*-octylamine, DMF.

While the LUMO energy level of substituted NDIs only slightly differ, the HOMO energy level can be lifted by electron donating groups and lowered by electron withdrawing groups. Furthermore, electron poor NDIs show tremendous π -acidity and can serve as model compounds for anion- π -interactions^[290] and other applications for NDI have been found.^[276]

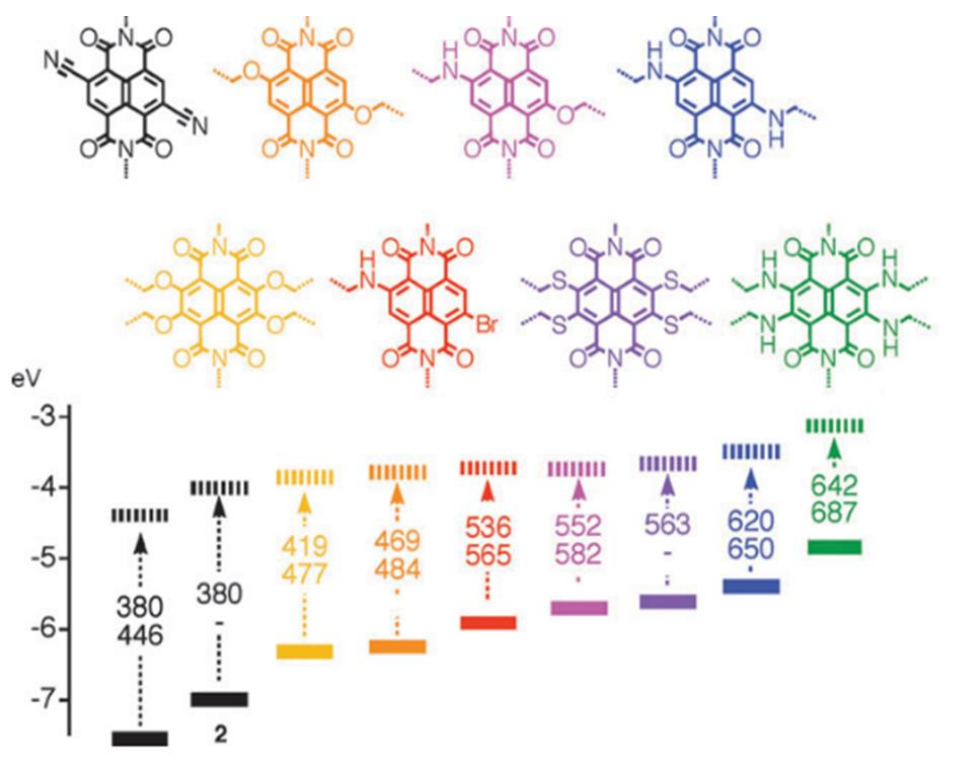


Figure 22. Impact of the core-substitution of NDI on the colour and HOMO/LUMO levels and gaps. Image taken from Ref.^[275].

Therefore, molecular engineers use these positions to fine-tune the HOMO and LUMO energy levels of the NDI-core in order to obtain model compounds with tailor-made optical and electronic properties.^[275,282,283] The ability to change both, colour and redox properties without global structural changes is one of the most attractive characteristics of core-substituted NDIs. Since the 2000s, many groups have developed various strategies to core substitute NDIs with electron donating heteroatoms like S, O or N and thus create push-pull-systems with the electron poor NDI core to modulate the absorption and emission properties of the organic chromophore.^[282,283,289] The colours of a core-substituted NDIs originate from a charge transfer band that moves to the red over the full rainbow spectrum with increasing push-pull character between the core substituent and the NDI core. While photoluminescence properties of NDIs have been extensively studied,^[275] their electroluminescence behaviour is barely studied.^[279,280] Mayor and co-workers designed and synthesised chromophores comprising a cyclophane architectures of NDIs (Figure 7, similar to **II**).^[102,103,134] Immobilisation of the cyclophane NDIs on the surface was achieved by sublimation and led to self-assembled ordered patterns which are driven by hydrogen bonds.^[103] Furthermore, they observed that the molecules formed a staggered conformation which should guarantee self-decoupling of one chromophore from the

surface.^[103] This was then experimentally proven and it revealed vibronic excitations of modes at C=O in STM.^[102] Another approach of Mayor and co-workers comprises of a core-substituted naphthalene diimide chromophore bearing two oligo-*p*-phenylenes (OPE) as linkers and a phenanthrene anchoring group (Figure 23a).^[291] They were able to implement this dye in between two metallic single-walled carbon nanotube electrodes forming a rigid solid-state device.^[73] With this setup, they were able to observe light upon electrical excitation.^[73]

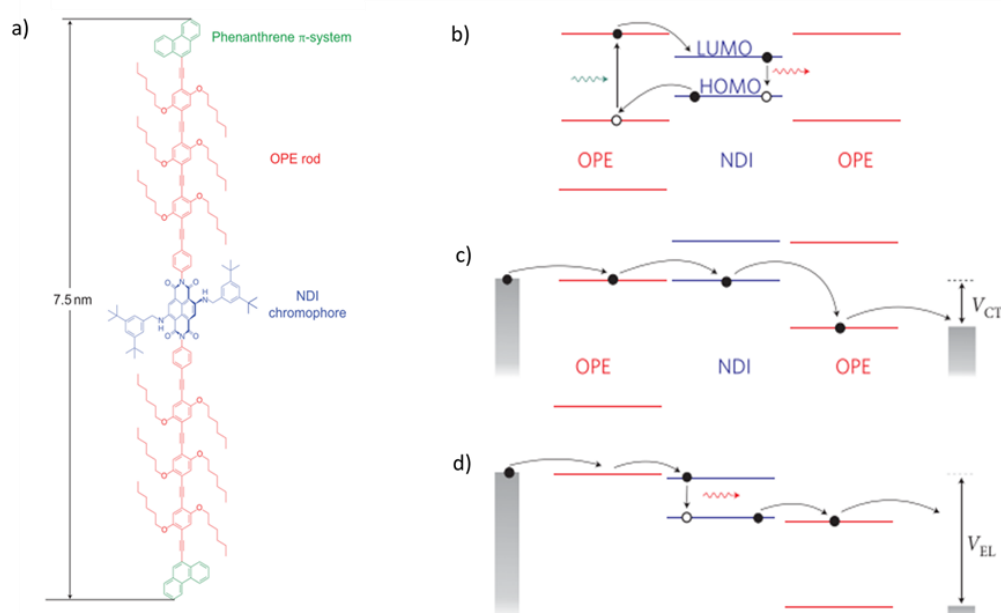


Figure 23. a) The structure of the NDI chromophore in the study of Ref.^[73] and energy levels of the chromophore b) in solution, c) bias <4V and d) bias >4V. Images taken and modified from Ref.^[73].

The design strategy consists of polyaromatic hydrocarbons (PAH) as anchoring groups to enable sufficient interactions between the metallic single-walled carbon nanotube electrodes and the anchoring group. With the number of the oligo-*para*-phenylene units, they were able to provide a long enough rod to electronically decouple the central fluorophore. As the light emitting unit, they chose a series of NDIs.^[291,292] In their study, they obtain both fluorescence (Figure 23b, red arrow) and electroluminescence (Figure 23d, red arrow). After applying a voltage (<4V), charge transfer occurs *via* the pathway shown in Figure 23c. There, the energy levels of the OPE and NDI subunits align. Increasing the voltage bias to >4V, electroluminescence becomes dominant. The two orbitals of the NDI subunits are located between the two rods. Both electrons and holes are injected, and the recombination of the charge carriers lead to electroluminescence, as shown in Figure 23d.

1.6 Characterisation Methods of the Surface-Molecule Interface

Characterisations of the surface-molecule interface are inevitable and many techniques have been employed.^[293] In the following pages, important characterisation methods will be briefly introduced. As aforementioned, thiol-gold-SAMs are reasonably inert and stable at ambient conditions and can be transferred to external setups.

1.6.1 Microscopy (STM, AFM)

Scanning probe microscopies use a tip apex to obtain electronical and topographical information about the surfaces. Among them, scanning tunnelling microscopy (STM)^[294] and atomic force microscopy (AFM)^[295] are the most prominent ones. Binnig and Rohrer were the pioneer physicists of the first STM-device at IBM and were awarded the Noble Prize in Physics in 1986.^[296] In STM, a tunnelling current between the tip and the conductive substrate is observed if the distance between the two is small enough to tunnel but high enough for the potential barrier to restrain conductance. The tunnelling current is highly dependent on the distance between the tip and the surface. Therefore, topographical or electronical changes of the surface can be translated into a 2D picture. Thus, the STM-image is a convolution of topographic and electronic contributions. Generally, the sharp tip is made of tungsten by electrochemical etching or gold. A setup of STM requires a piezoelectric scanning unit to control vertical and lateral movement of the tip, a *x-y*-scanner, a vibration isolation (due to the exponential correlation of height and tunnelling current) and an analyser. If the difference between tip and surface is less than one nanometre, electrons will move from the Fermi level of the tip into the HOMO of the samples (in positive mode) or *vice versa* (in negative mode). STM measurements can be done in two different modes: constant height mode (CHM) or constant current mode (CCM). In CHM, the tip stays at a constant height profile and records the corresponding tunnelling current, whereas in CCM, the current stays constant and the change of the height profile is recorded. With the same setup scanning tunnelling spectroscopy

(STS) is also available.^[297] With that, the local density of states can be recorded and in particular it is interesting for single molecule conductance measurements. In contrast to STM, where mainly information about topography is obtained, the voltage in STS is not constant. Like STM, STS can be operated in two different modes: current-voltage mode and current-distance mode. In the first one, at a defined distance between surface and sample, the correlation between bias voltage and current is measured to obtain insight of the electronic properties, such as HOMO and LUMO energy levels.^[298] In the current-distance mode, the bias voltage is fixed and the distance is recorded (as a function of tunnelling current). With this setting, information about local barrier height can be collected. Moreover, STM-tips can be used to manipulate and contact the sample in a controlled manner. Therefore, STM can be used to induce catalysis,^[299] rotation or for optoelectronics devices and play a major role in organic electronics.^[32,187]

In contrast to STM/STS, in AFM the forces (*e.g.*, attractive, repulsive, magnetic, electrostatic) between tip and surface are measured. Hereby, the tip is mounted onto a cantilever and scans over a sample.^[300] Since there are no electrons involved, AFM can picture the topography of insulating layers. AFM can be operated in several modes, such as contact mode, non-contact mode, tapping mode or conductive mode. The latter one requires a conducting tip and can collect both topography and electronic features of the sample. In the contact mode, the cantilever deflections are recorded, which results from mechanical, repulsive forces between the tip and the sample. Unlike in non-contact mode, the cantilever oscillates in the attractive regime and the analyser measures change of the resonant frequency of the cantilever. As indicated by the name, the cantilever taps the surface in swinging fashion. This mode gains insight into the phase shift of the resonance frequency of the cantilever in the close contact area.

1.6.2 Spectroscopy (XPS, NEXAFS)

These techniques detect emitted electrons and therefore require ultra-high-vacuum (UHV) (to provide a reasonable mean free path of the electrons). Moreover, the instruments mainly settle in facilities which can provide synchrotron radiation for high resolution/sensitivity. In case of X-ray photoelectron spectroscopy (XPS), the theory is based on the photoelectric effect in which photoelectrons are emitted after the exposure of the material to X-ray radiation. The electrons' ability to be emitted from the material decays exponentially with layer thickness and thus is surface sensitive. If the energy is high enough, core electrons can be emitted and the binding energy (E_{bind}) of the photoelectrons can be calculated from their kinetic energy (E_{kin}), work function Φ , and the used photon energy E_{photo} (eq. 2).

$$E_{\text{bind}} = E_{\text{photo}} - (E_{\text{kin}} + \Phi) \quad (2)$$

The binding energy depends on the original orbitals they were released from. Therefore, it provides information about the chemical bonds involved near the surface. The most informative peak in XPS for SAM characterisation is the S 2p – peak. As shown in Figure 24, it consists of three different components, which are termed C1 (at 161 eV), C2 (at 162 eV) and C3 (at 163-164 eV). Also peaks at higher binding energies might be observed, and they indicate oxidised S species.^[301,302] C1 (Figure 24, green line) is attributed to atomic sulfur, either from being decomposed or by impurities.^[293,303] The main peak is the C2 (Figure 24, red line) component and stems from chemisorbed sulfur through a S–bond.^[304,305] Unbound thiols can be attributed to the C3 (Figure 24, blue line) peak, which highly depends on the quality of the SAM. Moreover, disulfide species may be another reason for this peak.^[306] Another technique is the near edge X-ray absorption fine structure (NEXAFS) which provides information about the valence and conduction bands at surfaces and therefore it offers information about the involved electronic states. The radiation photons are linearly polarised and can be manipulated. Depending on the orientation with respect to the surface, signals from specific orbitals can be enhanced or erased. Thus, this technique gathers insight on the molecular orientation of orbitals

at the surface. In comparison mode, this technique allows to identify unknown species or structures.

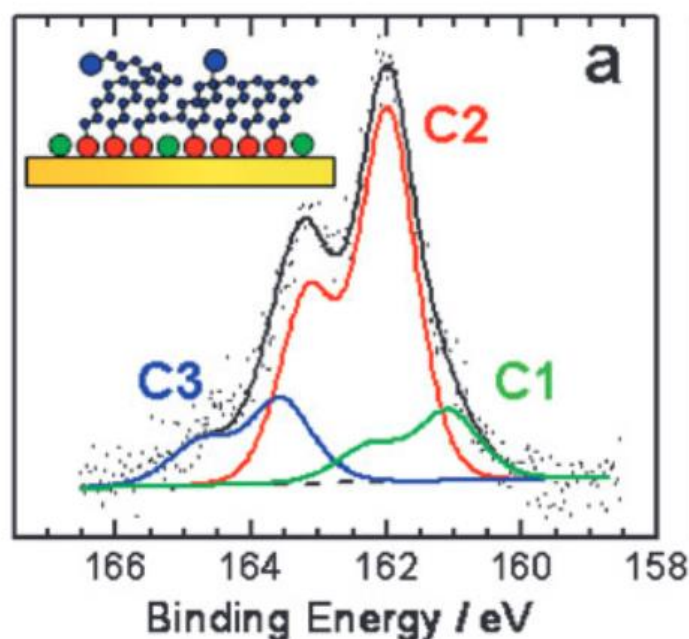


Figure 24. Inset of alkane thiolates and an exemplary S 2p XPS spectra of a thiolate on Au(111). C1 represents atomic sulfur (green), C2 corresponds to thiolate (red) and C3 comes from physisorbed molecules (or free SH) (blue). Image taken from Ref.^[53].

1.6.3 Others (ellipsometry, contact angle)

Ellipsometry is another optical tool for thin film characterisation by measuring the change of polarisation. It gives information about composition, roughness, thickness and other material characteristics. The polarisation of the incident radiation (normally linear or circular polarised light) is changed elliptically upon interaction with the surface. The angle of the setup should be close to the Brewster angle.^[307]

The contact angle Θ is the result of the thermodynamic equilibrium between surface-liquid and liquid-air interface. It results from a certain surface energy which varies upon interatomic and intermolecular forces. The bigger the contact angle is, the lower the interactions between surface and solid are. Contact angle measurements only give information about the macroscopic characteristics of the SAMs, yet it is an easy technique to check the quality and reproducibility of the SAMs.

2 Motivation

According to Moore's law, chip producers try to double the number of transistors on chips while keeping the same size or even shrinking it. Following this design, at some point it will be too complicated to reduce the size of the inorganic materials (the widely held opinion is about 50 nm). By that means, this sets a fundamental limit for the top-down (reducing macroscopic structures) approach and thus starts the beginning of the bottom-up approach (starting from microscopic structures / molecules) using molecular (organic) electronics.^[16] Inspired by Richard Feynman's seminal talk "*There's Plenty of Room at the Bottom at Caltech*", the idea of a bottom-up approach was born and thus the concept of single molecule devices rose.^[17] Unimolecular electronics is believed to be a potential technology in further shrinking the devices to the nanoscale. This would ultimately result in denser packed components in electronic devices providing faster circuitry, computing and higher resolution in screens. In order to pave the future for molecular devices, such as memory elements,^[308] single molecule switches,^[309] the smallest OLED, molecular spintronics^[310] or others,^[311] fundamental understanding of the involved processes is inevitable. Hence, this work is dedicated to the interdisciplinary research of single molecular devices^[16] particularly in the field of unidirectional motion of single molecule motors and single molecule electroluminescence. In order to enable single molecule functionality, controlling the interface between a solid-state substrate and the decorating molecular functionalised layers is of fundamental interest in nanotechnology. Based on previous results of our group,^[101,177] a rigid, tripodal scaffold is chosen to be the platform, on which a free acetylene was installed onto the sp^3 hybridised carbon. This triple bond serves as a linker and allows us to modularly assemble various functional units *via* Sonogashira coupling. With this design strategy, we intend to provide a rigid, covalently bonded anchor to the Au(111) surface providing an upright orientation of the protruding functionality.^[40] Furthermore, we also aim to effectively self-decouple the functional units from the surface. These tripodal molecules with acetyl protected anchoring groups can be efficiently deprotected either *in situ*^[40,41] upon binding to the gold surface or chemically by cleaving agents.^[42]

The first type of single molecule devices involved molecular motors. Hereby, the design of the rotor should enable three main characteristics:

1. Perpetual 360° rotation
2. driven by biases
3. unidirectional motion

The last one is of key interest when it comes to understanding the chiral induced spin selectivity (CISS) effect. If the electrons are transferred a spin torque by the chiral molecule, directed motion is to be expected due to the law of conservation of momentum. However, the involved mechanism of CISS is widely debated. We aim to contribute to the understanding of this effect by combining the theory with experiment. The chiral molecules needed for this approach are based on so-called “Geländer-type”-molecules. They can be defined as molecular assemblies where the longer part of the molecule wraps around the shorter one creating a “Geländer-type” helix. While at elevated temperatures these molecules are prochiral, deposited on surfaces these architectures should provide stable-enough helical chiral structures at low temperatures.^[312]

The second type of single molecular devices covers single molecule electroluminescence. NDIs are particular appealing chromophores for the development of model compounds to investigate single molecule electroluminescence due to their synthetic accessibility, tuneable photophysical properties, reversible electrochemistry,^[313,314] ground- and excited state stability, and structural integrity. To the best of our knowledge, only few studies have been published so far.^[73,135] Therefore, this work focuses on the synthesis of a series of different NDIs with the aim to fathom the underlying light emission processes in single molecule devices.

After the successful synthesis of both the tripodal platforms and the functional units, we assemble them by cross-coupling reactions. Finally, the functional molecules’ eligibilities as single molecule devices are measured by means of STM. However, this thesis not only focuses on single molecule devices but also utilises the functional molecules to deposit them on large-area substrates to form self-assembled monolayers with functionality.

It should be noted that the stabilisation of the functional tripodal molecules on metallic surfaces is a subtle balance which is attributed both to the lateral van der Waals interactions *e.g.* between flat delocalised π -systems and to the chelate effect of the tripodal scaffolds. Therefore, one has to consider the competing binding energies of the two potential anchoring sites of functionalised tripods, namely the functional unit-surface interface and the degree of chelation

via thiolate anchors of the molecular tripod in a commensurate order to the gold surface. If the interactions between functional unit and surface are larger than the energy gained by the foot structure, the molecules will be lying flat on the surface.^[180] Hence the molecular platform will be adjusted and optimised, if needed.

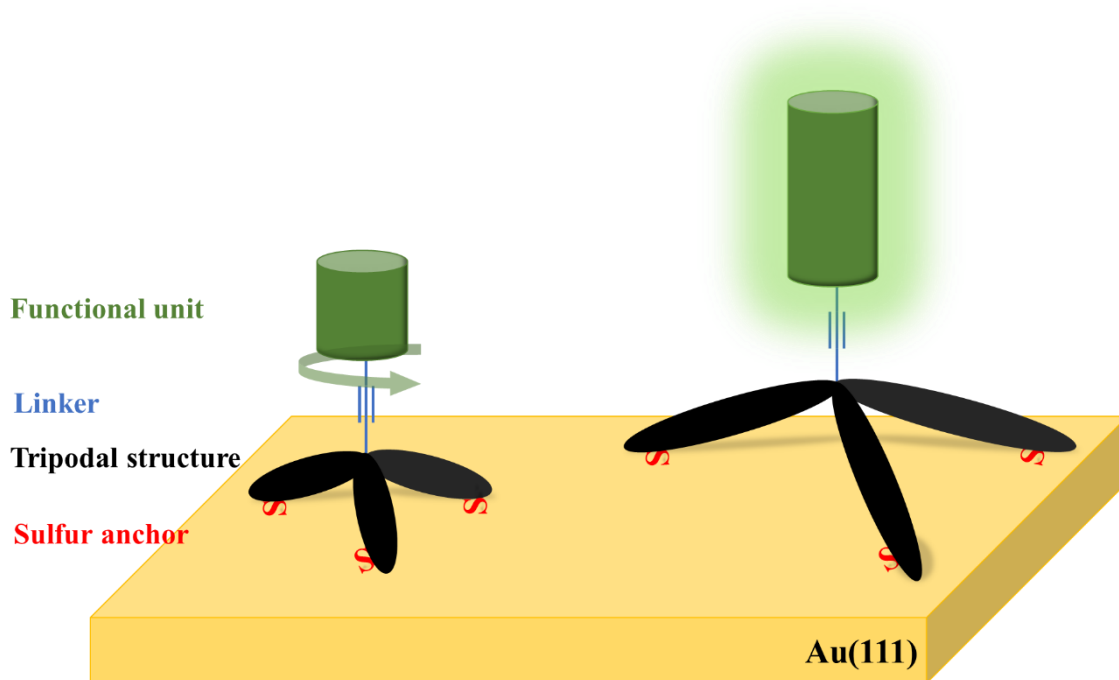


Figure 25. Illustrative design of the functionalised tripods. Functional unit (green, either rotor or light emitting chromophore) mounted on the tripodal structure (black) *via* the triple bond linker (blue). The functionalised tripods are bound to the gold surface through three sulfur anchors (red).

3 Results and Discussion

The following chapter describes the design synthesis, performance and the evolution of tripodal functional molecules deposited on the gold surface. The chapter is divided into three main parts:

1. *“En Route to Tripodal Functionalised Molecules”*
2. *“Evolution of the Platforms”*
3. *“Tripodal Functionalised Molecules”*

3.1 “En Route to Tripodal Functionalised Molecules” ¹

In this subchapter, the design and synthesis of the first-generation **Ph-Tpd** molecular platform based on a triphenylpropyne scaffold is described. Subsequently, we present the design strategy and synthesis of two molecular rotors **Ph-Tpd-Rot_{LF}** and **Ph-Tpd-Rot_C**, whose surface behaviour has been investigated and discussed.

Furthermore, the design, synthesis, optical, electrochemical and spectroelectrochemical features of (core-substituted) NDIs are presented as well as their eligibility as single molecule emitters. All first-generation functional units are depicted in Figure 26.

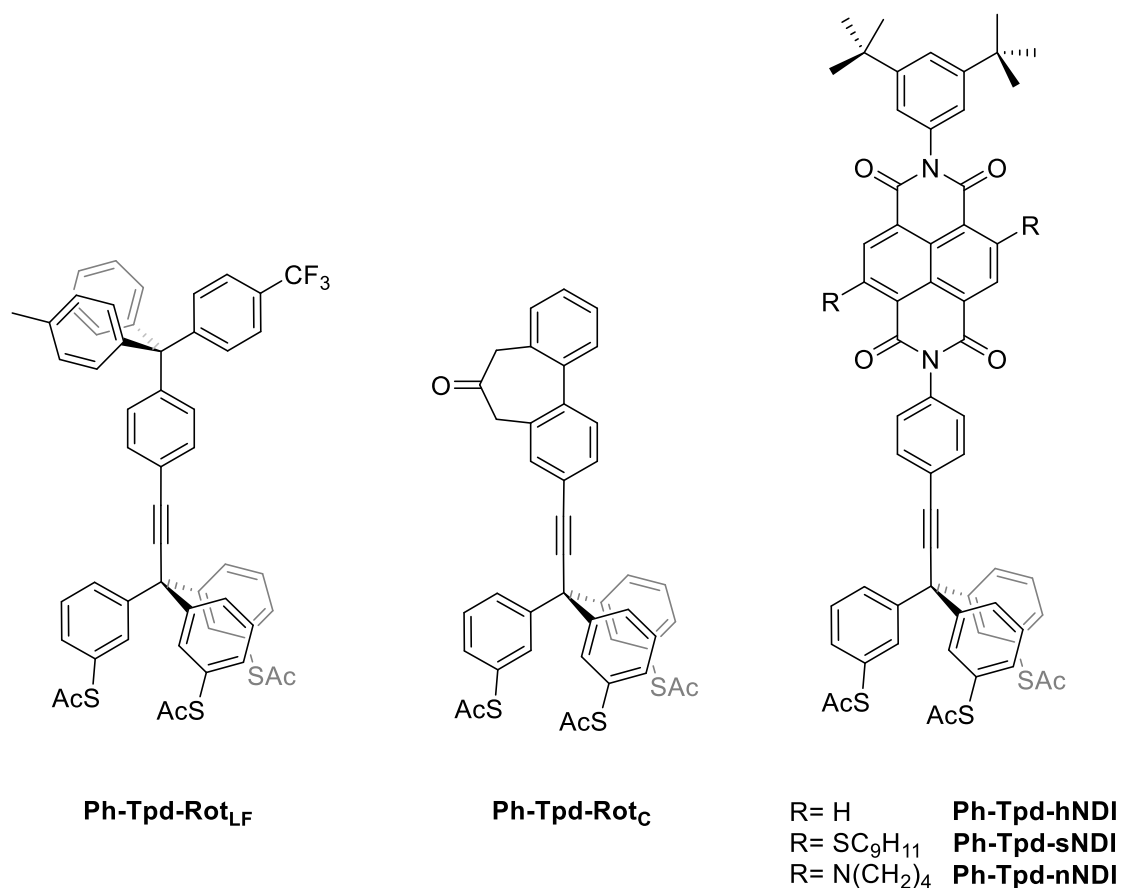


Figure 26. First-generation functional units **Ph-Tpd-Rot_{LF}**, **Ph-Tpd-Rot_C**, **Ph-Tpd-hNDI**, **Ph-Tpd-sNDI** and **Ph-Tpd-nNDI**.

¹ Large parts of this chapter have been accepted by Chemistry - A European Journal: N. Balzer, J. Lukášek, M. Valášek, V. Rai, Q. Sun, L. Gerhard, W. Wulfhekel, M. Mayor, *Chem. – A Eur. J.* **2021**, doi: 10.1002/chem.202101264

3.1.1 Molecular Platform

The design of the first-generation tripodal platform is based on a triphenylpropyne derivative as shown in Figure 27.^[101,161,163] Introducing a triple bond on the sp^3 -hybridised carbon atom of the tripodal platform is expected to provide the compactness required for STM based investigations and enables to modularly develop the structure *via* Sonogashira coupling chemistry. Note, that a comparable foot structure based on a tetraphenylmethane scaffold has been recently used in single molecule light emission experiments by Hou *et al.*, but significant differences are expected in the sturdiness of the tripod-Au(111)-interface arrangement due to the used benzylthiol anchor groups.^[163] In the presented tripod design, the aromatic thiol anchors at the *meta*-positions allow direct connections to the gold substrate avoiding additional flexibility due to CH_2 linkers. Our intention is to improve both the electron transport and the rigidity of the spatial arrangement, hopefully controlling an upright orientation of the molecular rods on the gold substrate. Throughout this work, we will refer the molecules comprising this particular foot structure as **Ph-Tpd-{functional unit}**.

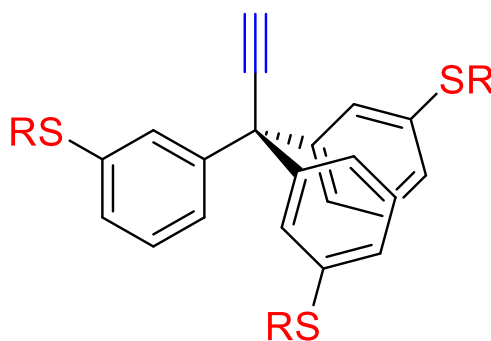
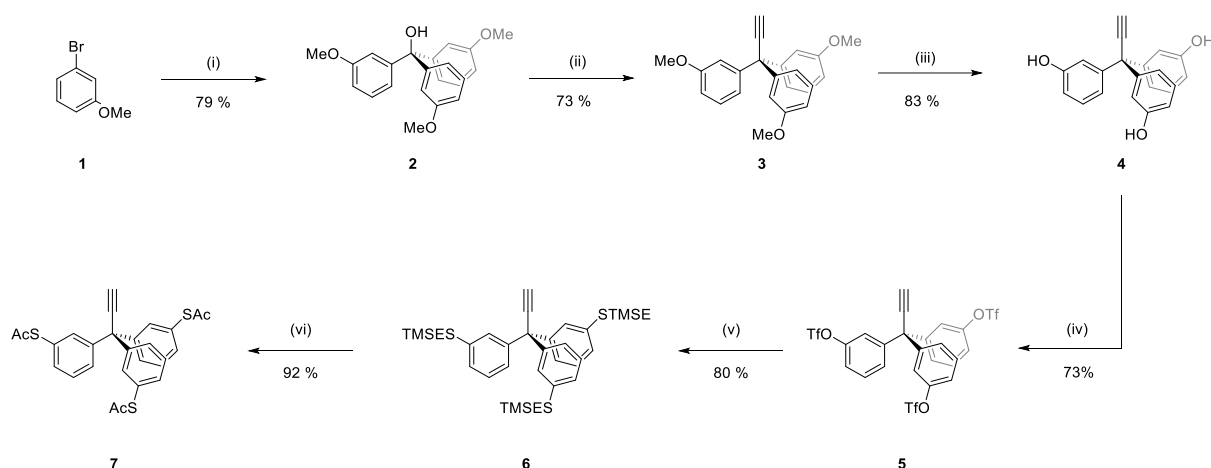


Figure 27. Design of the molecular platform **Ph-Tpd** including the triple bond (blue) which allows functionalisation *via* Sonogashira reaction, the rigid tripodal platform (black) and acetate masked aromatic thiol anchors at the *meta*-positions (red)

3.1.1.1 Synthesis of the Platform

The synthesis of the tripodal platform started with the lithiation of *meta*-bromoanisole at -78 °C and the subsequent threefold nucleophilic attack on diethyl carbonate gave triphenylmethanol **2** in 79% yield. Using acetyl chloride, compound **2** was then converted into its chlorinated analogue, which is prone to hydrolysis during the work-up. Therefore, we collected this trityl chloride without any further purification and treated it with ethynylmagnesium bromide in toluene at elevated temperatures to afford compound **3** with acceptable yields. This synthetic approach of 3,3,3-tris(3-methoxyphenyl)propyne (**3**) was previously reported by Garcia-Garibay *et al.*^[315] While the demethylation of **3** with commonly used Lewis acids, such as BBr₃, would require an additional protection of the triple bond to avoid its borylation,^[316] a method originally published by Feutrill and Mirrington involving sodium ethanethiolate in DMF as demethylation agent afforded the desired product **4** in 83% yield.^[317] The following step was the triflation of triol **4** with triflic anhydride to yield triflate **5** in 73%. In the next step, the thiol anchor groups were introduced in their TMS-ethyl-protected form. The triflate **5** was converted by the C–S cross-coupling reaction with 2-(trimethylsilyl)ethanethiol in the presence of palladium catalyst and Xantphos ligand to the desired product **6** with a yield of 80%. Subsequent transprotection of the thiols in **6** was performed using AgBF₄ and acetyl chloride in dichloromethane to afford the desired thioacetate **7** in very good yield of 92%.^[196] Unfortunately, the thioacetate groups did not provide the stability required for the Sonogashira coupling reactions disqualifying the modular plan of decorating the platform in the last step with functional units. As second best alternative, the 2-(trimethylsilyl)ethyl protected derivative **6** was used for the assembly between functional units and platform, followed by a final transprotection step to get the target molecules as thioacetates.



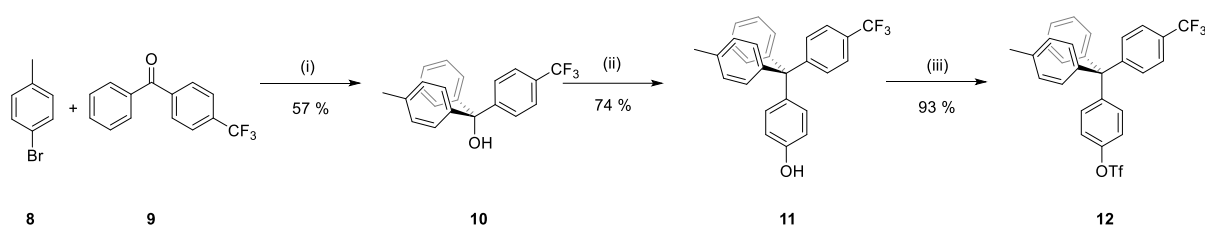
Scheme 4. Synthesis of the tripodal platforms. Reaction conditions: i) *n*-BuLi, (CH₃CH₂O)₂CO, THF; ii) AcCl, toluene; BrMgCCH, toluene; iii) sodium ethanethiolate, DMF; iv) Tf₂O, NEt₃, DCM; v) 2-(trimethylsilyl)ethanethiol, Xantphos, Pd₂(dba)₃, dioxane; vi) AgBF₄, AcCl, DCM.

3.1.2 Lorentz Force Molecular Rotor

The design of the presented molecular rotor is based on a dipolar triphenylmethane rotator, which is linked to the tripodal stator. One of the three phenyl rings bears a trifluoromethyl group to induce a dipole moment within the molecule. Upon applying an electric field, the dipole allows us to address the molecules and thus creating an electric field controlled (unidirectional) rotor. The other two phenyl rings of the rotator differ in the substitution in the *para* position, so that distinction between the two of them becomes possible by means of the STM tip. Originally, we planned to use only a triple bond as a linker between the rotator and the stator. The synthesis of such compound however, turned out to be more difficult than expected, which then resulted in a slight modification of the entire rotor. Hence, we enlarged the rotator to a tetraphenyl scaffold **12** with one phenyl ring bearing a pseudohalogen. This modification enables the assembly of tripodal platform **6** with the rotator-part *via* Sonogashira protocol. The synthetic route is outlined in Scheme 5 and 6.

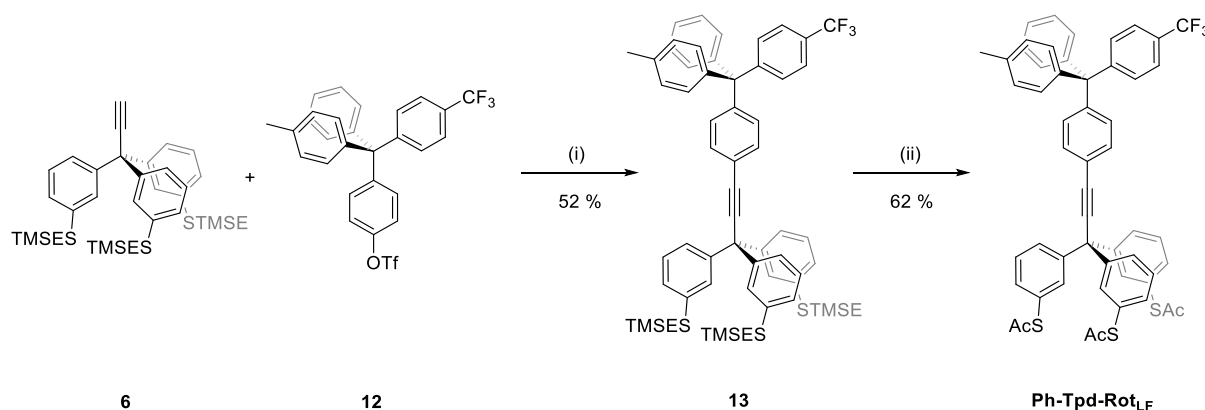
3.1.2.1 Synthesis of the Lorentz Force Molecular Rotor

To create the tripodal scaffold **10**, *para*-bromotoluene was first lithiated by *n*-BuLi at -78 °C and then reacted with the unsymmetric ketone **9** to afford compound **10** in 57% yield. As the alkynylation of compound **10** was not successful (see compound **3**), we changed the strategy and used an acid catalysed Friedel-Crafts reaction to obtain the phenol **11** in moderate yield. Subsequent reaction of tetraphenylmethane **11** with triflic anhydride afforded the corresponding triflate **12** in 93% yield.



Scheme 5. Synthetic approach to molecule **12**. Reaction conditions: i) *n*-BuLi, THF; ii) phenol, HCl, toluene; iii) Tf₂O, NEt₃, DCM.

The final assembly of tripodal platform **6** and triflate **12** *via* Sonogashira cross-coupling reaction gave compound **13** in 52% yield. An excess of triflate **12** was used to ensure that, all of the tripodal platform **6** was converted as the separation of the starting material **6** from the product **13** is troublesome due to their similar R_f values. The following transprotection of the thiols of **13** with acetyl chloride and AgBF₄ gave the desired rotor **Ph-Tpd-Rot_{LF}** in 62% yield.



Scheme 6. Synthetic approach to **Ph-Tpd-Rot_{LF}**. Reaction conditions: i) CuI, Hünig's base, Xantphos, Pd₂(dba)₃, dioxane; ii) AcCl, AgBF₄, DCM.

The surface behaviour of the dipolar rotor **Ph-Tpd-Rot_{LF}** is currently under investigation by means of our home-built UHV-STM setup at 5K.

3.1.3 Prochiral Rotor¹

The synthesis of the prochiral rotor **Ph-Tpd-Rot_C** (see Figure 28a) is shown in Figure S 1 and was performed by Dr. Jan Lukášek. The design of this prochiral rotator consists of the **Ph-Tpd** foot structure **6** and a helical biphenyl, interlinked by propan-2-one at the 2,2' positions of the biphenyl. The detailed description of each reaction step is not discussed in this thesis. After dissolving in DCM, **Ph-Tpd-Rot_C** was then sprayed on an Au(111) surface. After the deposition, the samples were transferred to the UHV chamber and annealed at 150 °C. The purpose of this annealing process is twofold, residues of the solvent is removed and the deprotection of thioacetate groups to the corresponding Au-thiolates is promoted at elevated temperatures. The deposition method has been developed in 2014 and has been published.^[196] The detailed procedure is described in the experimental section. The molecules were characterised at low temperatures (5 K) in our homebuilt STM setup.

As seen in Figure 28b, the molecules form unordered islands on the surface, indicating that the adsorption geometry of the molecules does not permit long-range order. This in turn implies, that the adsorption geometry is not uniform and hence several different adsorption configurations are present on the surface. To our delight, isolated single molecules are observed with a blossom-like pattern, as shown in Figure 28c. However, the molecular footprint of these “blobs” significantly exceeds the expected radius of the foot geometry. While a diameter between 0.7 and 1 nm (see Table 6) for each single molecule is to be expected, here we observe diameters ranging from 3.3 to 4.6 nm. Taking the apparent height of the molecular rotor **Ph-Tpd-Rot_C** of about 1.5 nm into consideration, we assume the molecules are lying flat and being anchored through only one of the thiolates. Rotating around this newly formed pivot point, diameters at the 3 nm scale are likely to be observed. Unfortunately, it is not possible to detect isolated rotational states of **Ph-Tpd-Rot_C** and we assume that a blossom-like shape represents the superposition of the overlapped individual rotation states.

¹ The molecule **Ph-Tpd-Rot_C** has been synthesised by Dr. Jan Lukášek. The results are discussed to further emphasise the eligibility of the **Ph-Tpd**-platform. STM-measurements were conducted by Julian Skolaut and analysed by Julian Skolaut, Dr. Lukas Gerhard and Prof. Dr. Wulf Wulfhekel.

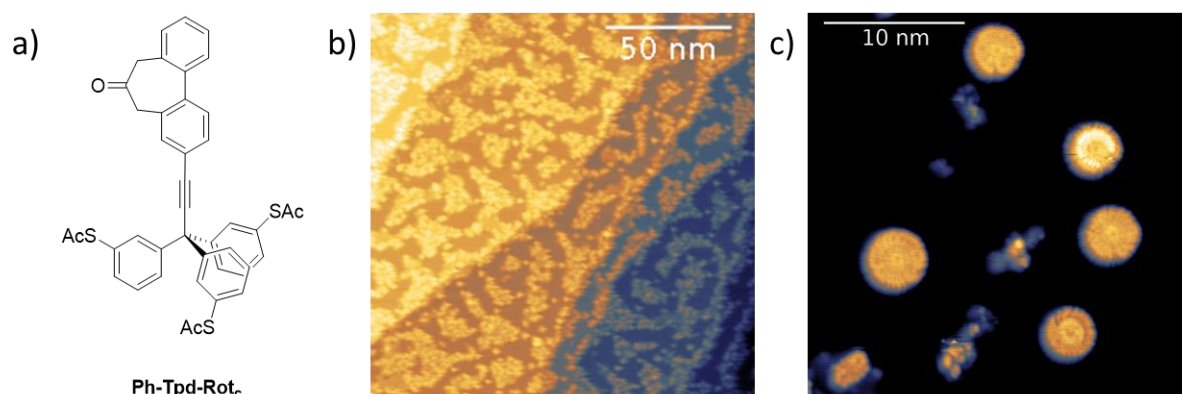


Figure 28. a) Molecular structure of **Ph-Tpd-Rot_c**. b) unordered islands of **Ph-Tpd-Rot_c**. Sample bias: 1 V, tunnelling current 13 pA. c) single molecules of **Ph-Tpd-Rot_c**. Sample bias: 1.5 V, tunnelling current 8 pA.

3.1.4 Tripodal Chromophores

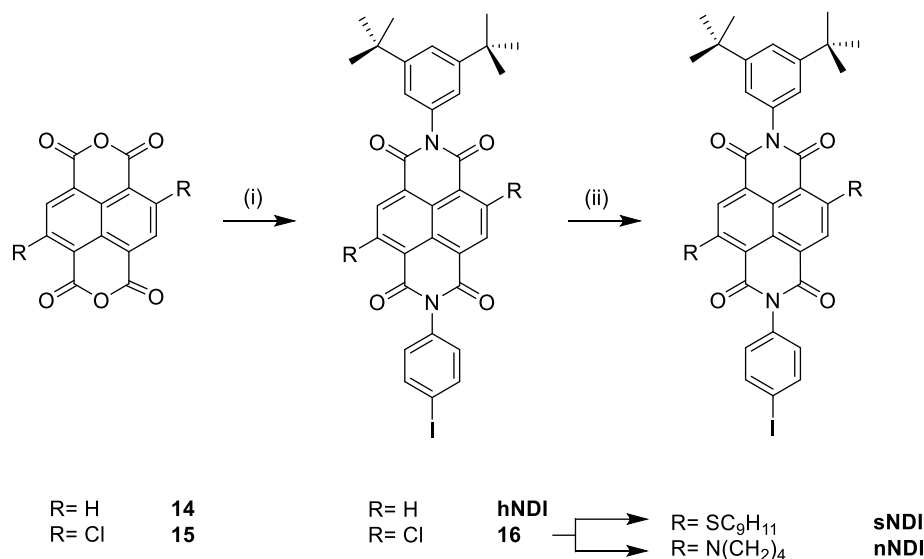
3.1.4.1 Synthesis of Tripodal Chromophores

As this thesis is also dedicated to single molecular emitters, another series of tripodal architectures consisting of NDI emitters mounted on the tripodal platform has been developed, displayed in Scheme 8. NDI derivatives **hNDI**, **sNDI** and **nNDI** (with h/s/n representing the (hetero)atom directly connected to the NDI core) suitable for their assembly with the tripodal platform were synthesised as shown in Scheme 7. The molecule 2,6-dichloronaphthalene-1,4,5,8-tetracarboxylic acid dianhydride **15** was prepared in four reaction steps by following a literature procedure.^[281] The twofold amide condensation with two different aniline derivatives to obtain asymmetric naphthalene-1,4,5,8-tetracarboxdiimides turned out to be more challenging than expected. In the case of unsubstituted **hNDI**, the classical step-by-step approach was followed to obtain **hNDI** with an overall yield of 43%. Unfortunately, in the case of 2,6-dichlorinated NDI **15**, this approach was not successful because such disubstituted-core derivatives are more soluble in organic solvents and prone to nucleophilic substitutions at the 2 and 6 position, resulting in considerable material loss due to a number of core-substituted NDIs as side products. As an alternative, a one-pot reaction with an equimolar stoichiometric ratio of both anilines was performed, expecting a statistical distribution of all possible products.

To our delight, the desired NDI derivative **16** was isolated as a yellow powder in 39% yield with an optimised procedure. In particular, the reaction temperature was decreased to room temperature from initially 100 °C and the anilines were deactivated by stirring for 30 minutes in acetic acid prior their addition to the dianhydride **15**. For the amide condensation, aniline derivatives were chosen carefully so that one of those has the iodine moiety attached in the *para*-position to further interlink the NDI chromophore with the tripodal platform **6** via Sonogashira protocol, while the second one bears two *tert*-butyl groups in the *meta*-positions providing both, the solubility required for further processing and the rigidity favouring STM experiments. Although NDI solubility could have also been increased by using (long and branched) alkyl chains, their flexibility and bulkiness could handicap the arrangement of the target molecules upright on the metallic surface. Although benzylic core substituted NDIs are known to be more fluorescent than their phenyl counterparts,^[292] 2,4,6-trimethylthiophenol and pyrrolidine were selected as substituents because benzylic substituents might be more prone to degradation in the final transprotection step. Core-functionalisation of **16** with 2,4,6-trimethylthiophenol *via* nucleophilic aromatic substitution reaction gave a red **sNDI** in 69% yield. Methyl groups in the *ortho*-positions of 2,4,6-trimethylphenyl substituent are increasing its steric hindrance and thus prevent their further substitution under harsh conditions in the final transprotection step. Initially, carbazoles were considered as amino substituents, however their reactivity in S_NAr reaction with **16** was too low and did not lead to the desired product. Moreover, primary alkyl amines as NDI-core substituents were avoided because particular decay mechanisms were suggested for substituents containing an α -proton next to the heteroatom. In particular, their fluorescence might be quenched either by electron transfer into the SOMO (former HOMO) of the chromophore, or by the formation of intramolecular hydrogen bonds between the α -proton and the closed carbonyl group, resulting in a radiation less decay of the excited state.^[282,292] Therefore, pyrrolidine was used for the substitution of **16** in the 2 and 6 positions to obtain **nNDI** in almost quantitative yield as a blue solid. As already indicated by the colour change of all three NDIs, the electron donating character of substituents is also observed in ¹H-NMR spectra, which is associated with a general upfield shift of the NDI-core protons with an increasing number of electron donating groups (see Figure S 2 - Figure S 4).

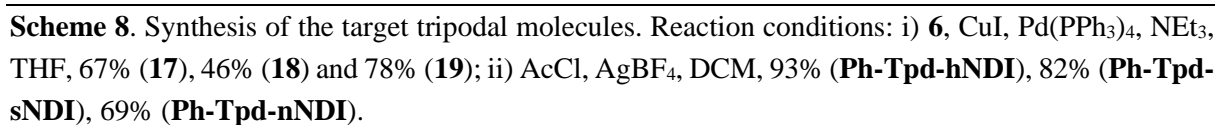
Comparing the chemical environment of the NDI-core protons, core-substitution with 2,4,6-trimethylthiophenol results in a chemical shift of 8.04 ppm and 8.01 ppm for the NDI core protons, while substitution with pyrrolidine leads to a chemical shift of the core protons to 8.43

ppm and 8.40. The unsubstituted **hNDI** core protons show the most deshielded chemical shift of 8.84 ppm.



Scheme 7. Synthesis of NDI chromophores. Reaction conditions: i) 3,5-di-*tert*-butylaniline, *p*-iodoaniline, AcOH, 43% (39% for compound **16**); ii) for **sNDI**: 2,4,6-trimethylthiophenol, K_2CO_3 , 69%; for **nNDI**: pyrrolidine, K_2CO_3 , 99%.

The final assembly of the target molecules **Ph-Tpd-hNDI**, **Ph-Tpd-sNDI** and **Ph-Tpd-nNDI** is outlined in Scheme 8. After successful isolation of all NDIs, Sonogashira reaction was used to couple **hNDI**, **sNDI** and **nNDI** respectively with the modular platform **6** to afford precursors **17-19** in 67%, 46% and 78% yield, respectively. THF was used as co-solvent for the Sonogashira cross-coupling reaction because of poor solubility of the NDI-precursors in neat amines (NEt_3 , etc.). Final transprotection of the thiols in **17-19** was successfully performed using AgBF_4 and acetyl chloride in dichloromethane to afford the desired thioacetate masked target structures **Ph-Tpd-hNDI**, **Ph-Tpd-sNDI** and **Ph-Tpd-nNDI** in good yields. Note, that the acetyl protected target molecules in solution at ambient conditions are only moderately stable. Therefore, solvent evaporation must be carried out at room temperature, otherwise thiol deprotection and subsequent polymerisation to *e.g.* disulfides was observed. Also, long retention times on column chromatography leads to a significant decrease in isolated yield. The introduction of the tripodal structure had no impact on the electronic structure of the NDI chromophore, as very comparable photophysical properties and chemical shifts of the NDI-cores were observed for precursors and target structures (see Figure S 5 for **hNDI**, **17**, **Ph-Tpd-hNDI**, Figure S 6 **sNDI**, **18**, **Ph-Tpd-sNDI** and Figure S 7 for **nNDI**, **19**, **Ph-Tpd-nNDI**).^[318]



The crystals suitable for X-ray diffraction analysis were obtained by the slow diffusion of ethanol into a DCM solution of **Ph-Tpd-sNDI**. The crystal data and structure refinement are summarised in Table 1 and visualised in Figure 29. **Ph-Tpd-sNDI** crystallise in the monoclinic crystal system in $P2_1/c$ space group. However, as indicated by the “Goodness of fit on F^2 ”, the quality of this crystal structure is rather low. As shown in Figure 29, the foot structure is not clearly resolved, resulting in an overlay of two different arrangements of one of the molecular legs. Furthermore, the tilt angle of the NDI unit is about 174° and thus not perpendicular to the foot structure. The distance from the sp^3 -carbon of the foot structure to the outmost centroid between the two *tert*-butyls of the NDI is measured to be 20.85\AA . The 2,4,6 trimethylsulfanyl

69

core substitution arranges in a way that the π -system of the sulfanyl core shields the proton of the NDI core.

Table 1. Crystal data and structure refinement for **Ph-Tpd-sNDI**

Formula weight	1349.70
Temperature/K	150
Crystal system	monoclinic
Space group	P2 ₁ /c
a/Å	27.2663(3)
b/Å	11.54380(10)
c/Å	25.4108(2)
α /°	90
β /°	94.1490(10)
γ /°	90
Volume/Å ³	7977.26(13)
Z	4
$\rho_{\text{calc}}/\text{cm}^3$	1.124
μ/mm^{-1}	1.057
F(000)	2848.0
Crystal size/mm ³	0.28 × 0.26 × 0.03
Radiation	GaK α (λ = 1.34143)
2 Θ range for data collection/°	5.654 to 123.988
Index ranges	-35 ≤ h ≤ 35, -15 ≤ k ≤ 12, -33 ≤ l ≤ 27
Reflections collected	159465
Independent reflections	19009 [R_{int} = 0.0411, R_{sigma} = 0.0213]
Indep. refl. with $I \geq 2\sigma(I)$	15068
Data/restraints/parameters	19009/0/978
Goodness-of-fit on F^2	1.751
Final R indexes [$I \geq 2\sigma(I)$]	R_1 = 0.1041, wR_2 = 0.3611
Final R indexes [all data]	R_1 = 0.1176, wR_2 = 0.3688
Largest diff. peak/hole / e Å ⁻³	2.02/-0.70

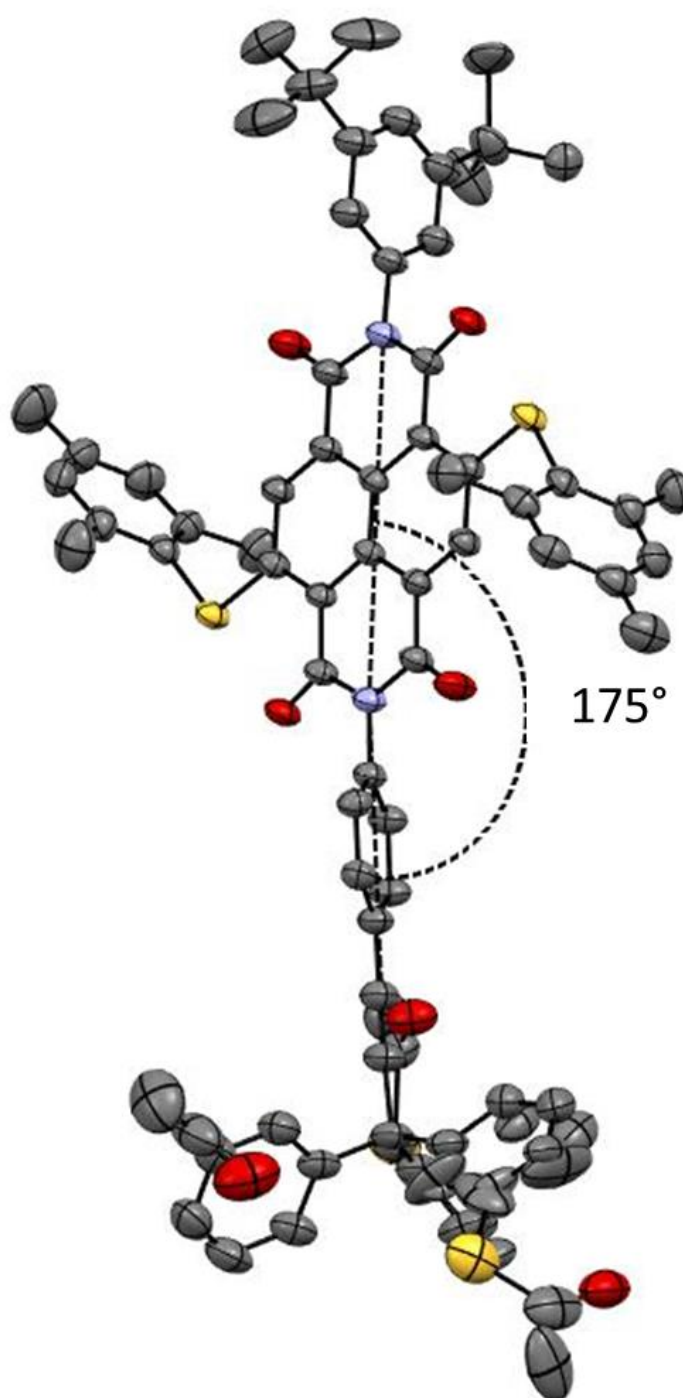


Figure 29. Solid state structure of **Ph-Tpd-sNDI** determined by single-crystal X-ray diffraction (50% probability of thermal ellipsoids)

3.1.4.3 Spectrophotometric Studies of the Tripodal Chromophores

UV-Vis absorption and fluorescence spectra of the molecules were recorded in dichloromethane with a concentration of about 25 μM , as shown in Figure 30 and summarised in Table 2. The absorption and emission properties of **Ph-Tpd-hNDI**, **Ph-Tpd-sNDI** and **Ph-Tpd-nNDI** noticeably depend on the core substitution. Absorption bands can be divided into three different parts. The central absorption bands at around 350 nm, which show the π - π^* transition and their vibrational fine structure of the three different chromophores, barely differ upon substitution, which is in accordance with the literature.^[282] Moreover, the peaks in the UV region (~ 300 nm) do not significantly change upon core-substitution, whereas they are missing in unsubstituted **Ph-Tpd-hNDI**.^[283] The rise of a new charge-transfer band in the visible region, which is introduced by and strongly depending on the push-pull character of the core-substitution is associated with the colours. Whereas unsubstituted **Ph-Tpd-hNDI** is pale yellow in DCM solution, **Ph-Tpd-sNDI** is red ($\lambda_{\text{max}} = 524$ nm) and **Ph-Tpd-nNDI** is blue ($\lambda_{\text{max}} = 602$ nm). The remarkable bathochromic shift in the absorption maxima of the amino substituted NDI **Ph-Tpd-nNDI** can be related to the stronger electron donating effect (+M-Effect) of the pyrrolidine substituent on the frontier molecular orbitals of the NDI core.^[292] In case of **Ph-Tpd-nNDI**, this intramolecular charge transfer can be hindered by mono protonation with HCl or even switched off by total protonation and reversibly restored.^[319] The absorption maxima at 524 nm with a shoulder at 492 nm (**Ph-Tpd-sNDI**) and at 602 nm with a shoulder at 558 nm (**Ph-Tpd-nNDI**) are quite broad.^[319] In contrast to previous reports, our 2,4,6-trimethylphenylsulfanyl core-substituted NDI chromophore **sNDI** shows fluorescence at 557 nm with a broad emission band,^[73,292] however the quantum yield is very low and cannot be reproducibly measured. For pyrrolidine core-substituted **Ph-Tpd-nNDI** the emission maximum is observed at 627 nm. The *Stoke* shift, that is the difference between the absorption and emission maxima, is 33 nm for the **Ph-Tpd-sNDI** chromophore and 25 nm for **Ph-Tpd-nNDI** chromophore.^[275] The emission intensity and the fluorescence quantum yield significantly decreases from **Ph-Tpd-nNDI** to **Ph-Tpd-sNDI** and no fluorescence has been observed for unsubstituted **Ph-Tpd-hNDI** derivative.

Table 2. UV-Vis absorption and emission characteristics of **Ph-Tpd-hNDI**, **Ph-Tpd-sNDI** and **Ph-Tpd-nNDI** in dichloromethane at ambient temperature.

Molecule	λ_{abs} [nm] (ϵ [Lmol ⁻¹ cm ⁻¹])	λ_{em} [nm]
Ph-Tpd-hNDI	360 (24995), 381 (26976)	n.d.
Ph-Tpd-sNDI	297 (50638), 357 (10053), 370 (10620), 524 (19231)	557
Ph-Tpd-nNDI	298 (32790), 349 (9600), 365 (11463), 602 (17376)	627

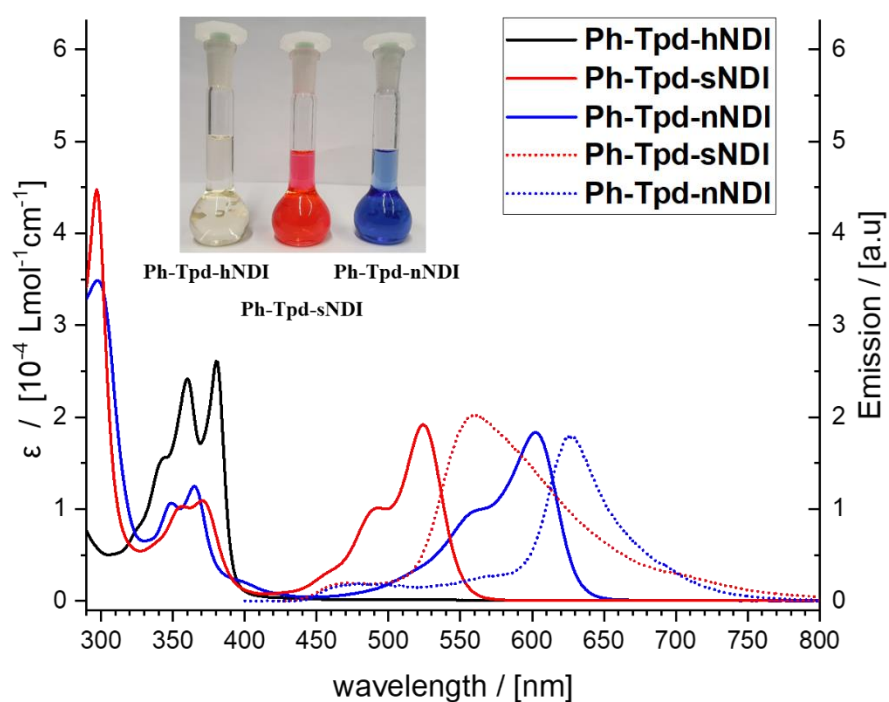


Figure 30. UV-Vis absorption spectra (solid line) of **Ph-Tpd-hNDI** (black), **Ph-Tpd-sNDI** (red), **Ph-Tpd-nNDI** (blue) and normalised emission spectra (dotted line). Recorded in dichloromethane with a concentration of 25 μM at ambient temperature. A photograph of **Ph-Tpd-hNDI** (left), **Ph-Tpd-sNDI** (middle) and **Ph-Tpd-nNDI** (right) solutions in dichloromethane is shown in the inset.

3.1.4.4 Electrochemical Properties of the NDIs

Cyclic voltammetry (CV) in dichloromethane vs. ferrocene/ferrocenium (Fc/Fc^+) was conducted to further investigate the influence of core substitution upon the electrochemical properties of all chromophores **hNDI**, **sNDI** and **nNDI** (see Figure 31, Table 3 and Figure S 8, shown in the appendix). The half-wave potential values $E_{1/2}$ were calculated as the arithmetical mean of the anodic and the cathodic peak potentials. To calculate the LUMO energy levels (against vacuum), the onset reduction potentials $E_{\text{onset}}^{\text{red1}}$ versus the Ag/Ag^+ reference electrode of each NDI were taken and subtracted from the Fc/Fc^+ standard (using -4.8 eV). It is assumed that the redox potential of Fc/Fc^+ has an absolute energy level of 4.8 eV to vacuum.^[320] The HOMO energy is determined from the LUMO level minus the HOMO/LUMO gap, which is available from absorption spectra at the long wavelength absorption edge ($E_{\text{gap}}^{\text{opt}} = 1240/\lambda^{\text{onset}}$).^[321] Such determination of optical as well as electrochemical band gap from peak values is mainly based on the detailed quantum chemical calculations of Brédas *et al.* who found a linear correlation between ionisation potential and oxidation potential and also between electron affinity and reduction potentials.^[322] Note, that small differences between the optical HOMO/LUMO gap and the electrochemical gap are expected not only because of the intrinsic experimental uncertainties but also because charged molecules are compared to neutral ones.^[323]

All three NDIs show two reversible reduction processes, implying the formation of radical anions and dianions, which are separated by 0.34 V, 0.43 V and 0.48 V for **nNDI**, **hNDI** and **sNDI** respectively. In case of **nNDI**, the electron donating core substitution, namely pyrrolidine, results in destabilising the radical anion and shifting the reduction to the more negative potentials. A gradual shift of the reduction potentials to more negative values for the core substituted NDIs reveals a direct relationship between the electron-donating properties of the core substituents and the electrochemical properties of NDIs. Additional irreversible oxidation waves are observed for **nNDI** at around +0.6 and +0.8 V vs Fc/Fc^+ (see Figure S 8 in the appendix). To prevent irreversible oxidations, the CV was carried out only in the cathodic region. Thus, both **hNDI** and **sNDI** chromophores were also measured between -2 V and 0 V. The amino substituted **nNDI** chromophore shows reduction potentials at -1.43 and -1.77 V that are in the same range as previously observed for the similar amino core-substituted NDIs.^[318,319,324] The LUMO energy estimated from the CV is -3.37 eV resulting in the HOMO energy level of - 5.31 eV, which is comparable to previously reported results.^[319] However,

each of the two anodic and cathodic peak potential pairs differ for about 0.3 V. Electrode films of some newly formed species as an explanation for these broad peaks can be excluded, since the experiments were carried out with freshly cleaned electrodes and are reproducible over several measurements. As seen from the cyclic voltammograms in Figure 31, the sulfanyl core substitution in **sNDI** decreases the electron donating character compared to the amino derivative **nNDI**. Hence, the reduction potential values (-1.14 and -1.62 V) of **sNDI** are shifted towards more positive potentials, corresponding to a LUMO energy level of -3.72 eV and a HOMO energy level of -5.96 eV. The obtained values are comparable with previously published results on alkylsulfanyl and arylsulfanyl core-substituted NDIs.^[290,325] Within this series, the core-unsubstituted compound **hNDI** exhibits the most positive reduction potentials of -1.10 and -1.53 V. Comparing the **sNDI** and **hNDI** chromophores, the donating character of the arylsulfanyl group is clearly observed in the second reduction $\text{NDI}^{\cdot-}/\text{NDI}^{2-}$ but significantly less in the first reduction $\text{NDI}/\text{NDI}^{\cdot-}$. This suggests that arylsulfanyl as a core substituent destabilises the dianion more than the radical anion. The LUMO energy level of **hNDI** is calculated to be -3.80 eV, which results in the HOMO energy of -6.97 eV. The HOMO-LUMO optical gaps were calculated from the onset of the lowest energy absorptions to approximate the HOMO energies and the obtained values are listed in Table 3.

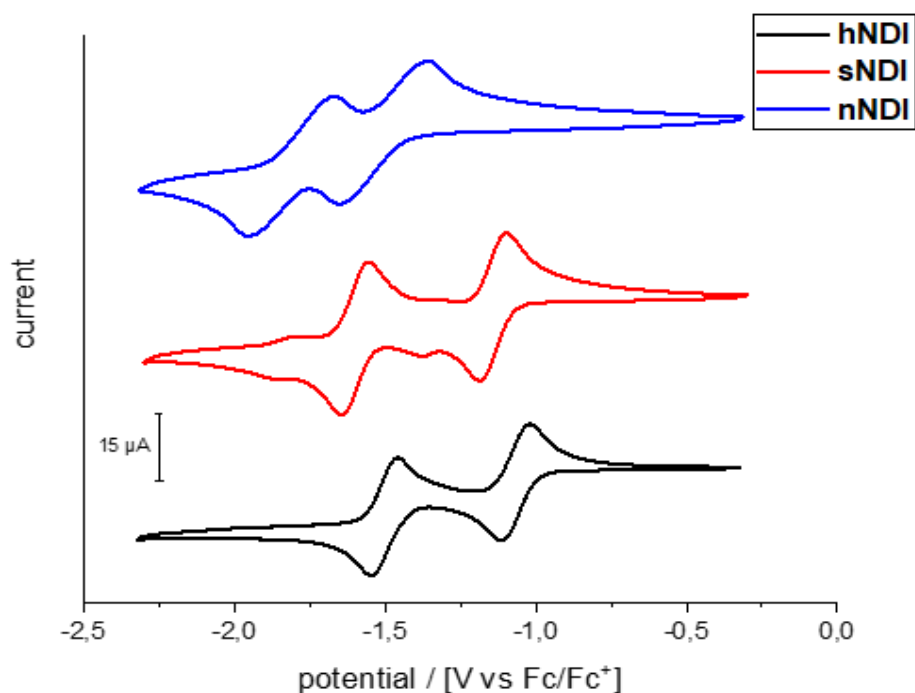


Figure 31. Cyclic voltammograms in the cathodic region of **hNDI** (black), **sNDI** (red) and **nNDI** (blue) recorded in dichloromethane containing 0.1 M solution of Bu_4NPF_6 as the supporting electrolyte. Fc/Fc^+ was used as an internal reference. Scan rate 100 mVs^{-1} .

Table 3. Electrochemical potentials, energy levels and bandgaps of all NDI chromophores. Redox potentials $E_{1/2}$ were obtained by the arithmetical mean of anodic and cathodic peaks. The LUMO energies (for Fc/Fc^+ standard against vacuum) were calculated from the onset of reduction waves using the empirical equation: $E_{\text{LUMO}} = (-4.8 \text{ eV} - E_{\text{onset}}^{\text{red1}})$. The optical band gap was calculated from the onset of the lowest energy absorption as follows: $E_{\text{gap}}^{\text{opt}} = 1240/\lambda^{\text{onset}}$ and $E_{\text{HOMO}} = E_{\text{LUMO}} - E_{\text{gap}}^{\text{opt}}$.

Chromophore	$E_{1/2}^{\text{red1}}$	$E_{1/2}^{\text{red2}}$	E_{LUMO}	$E_{\text{gap}}^{\text{opt}}$	E_{HOMO}
hNDI	-1.10 V	-1.53 V	-3.80 eV	3.17 eV	-6.97 eV
sNDI	-1.14 V	-1.62 V	-3.72 eV	2.24 eV	-5.96 eV
nNDI	-1.43 V	-1.77 V	-3.37 eV	1.94 eV	-5.31 eV

3.1.4.5 Spectroelectrochemistry of the NDIs

After obtaining the reduction potentials by cyclic voltammetry, the transient UV-Vis spectra of the charged species of **hNDI**, **sNDI** and **nNDI** were studied. Due to the decreased lifetime of the charged species in DCM, the solvent was changed to DMF. For the spectroelectrochemical analysis, a quartz electrochemical cell was used with a platinum gauze working electrode. In each spectroelectrochemical measurement, the neutral NDI was recorded as a reference (Figure 32-Figure 34, black line). To reduce to the first anion, constant potential that commensurate with the first anodic potential were chosen as the applied voltages until full saturation was observed. Then, the spectra were recorded and are presented as blue lines in Figure 32-Figure 34. For the reduction to the dianion, constant potential that commensurate with the second reduction potentials was applied and the obtained spectra are presented in Figure 32 and Figure 33 as red curves. In the case of **nNDI**, reduction and subsequent measurement of the dianion's optical features was not possible.

Regardless of the substitution, the twin peaks between 360 and 380 nm decrease upon reduction and totally vanish in the case of the dianion. As shown in Figure 32, new sharp peaks arise at 474 and 605 nm for the colourless **hNDI**, while the two highest peaks at 360 and 381 nm decrease dramatically, establishing an isosbestic point at 391 nm. New broad peaks at 703 and 786 nm arise, which can be assigned to the D₀-D₁ electronic transition.^[326] In solution, the radical anions are intensely orange coloured. Further reduction to the pinkish dianion abrogates the double peak features between 360 and 381 nm. A new broad peak at 541 nm rises, whereas the other peaks at 474, 605 and 703 nm diminish. These findings are shown in Figure 32 and are in agreement with other non-substituted NDIs.^[314]

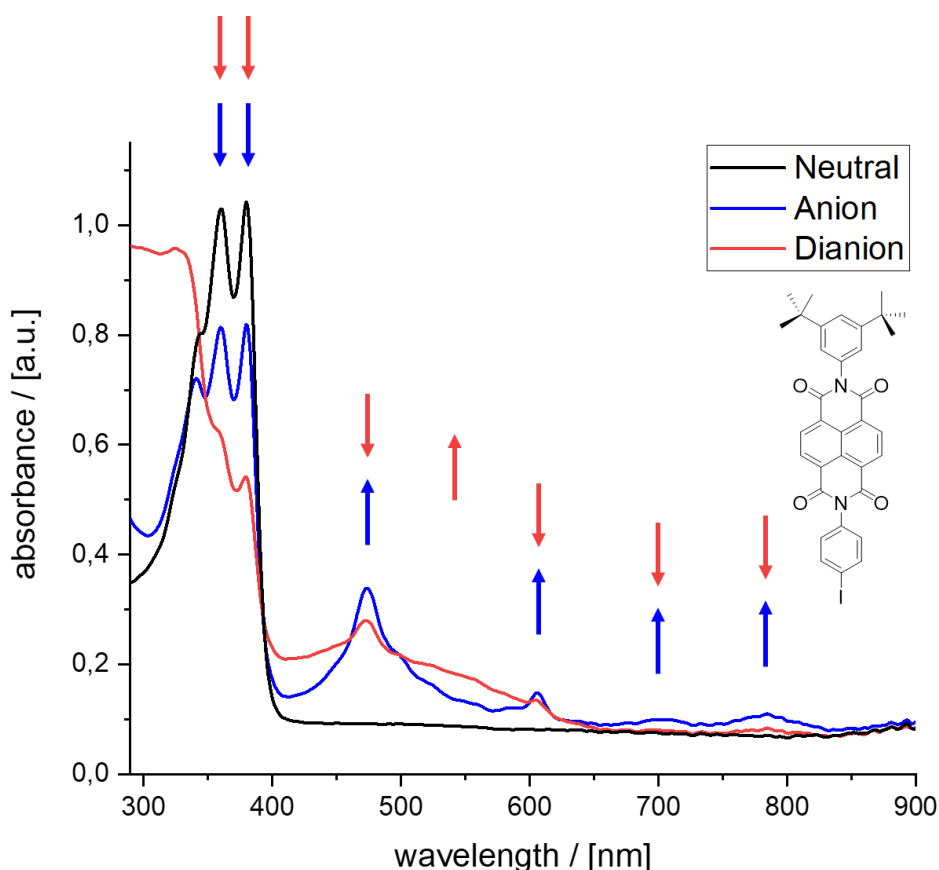


Figure 32. Spectroelectrochemical analysis of **hNDI** recorded in DMF containing 0.1 M solution of Bu_4NPF_6 as the supporting electrolyte. The neutral form is plotted in black, the anion in blue and the dianion in red.

In Figure 33, the spectroelectrochemical analysis of **sNDI** is shown. Upon reduction, the sulfanyl core substituted **sNDI** shows a broad peak at 506 nm which can be attributed to the intramolecular charge transfer, yet no significant shift of the peak is observed. Similar to the radical anion of **hNDI**, new broad peaks arise for **sNDI** at 636, 755 and 844 nm. Compared to **hNDI**, these new peaks are bathochromically shifted by 31, 52 and 58 nm, respectively. After reduction to the dianion, the characteristic double peaks between 357 and 370 nm are disbanded, while the overall peaks decrease. In general, reduction of the **sNDI** does not tremendously change the UV-Vis absorption characteristic of this chromophore. A conclusion could be drawn, that the reduction is chemically decoupled from the core and thus is localised at the N,N' -positions of the **sNDI** and not at the core. However, no similar observation has been published so far and would need further investigations.

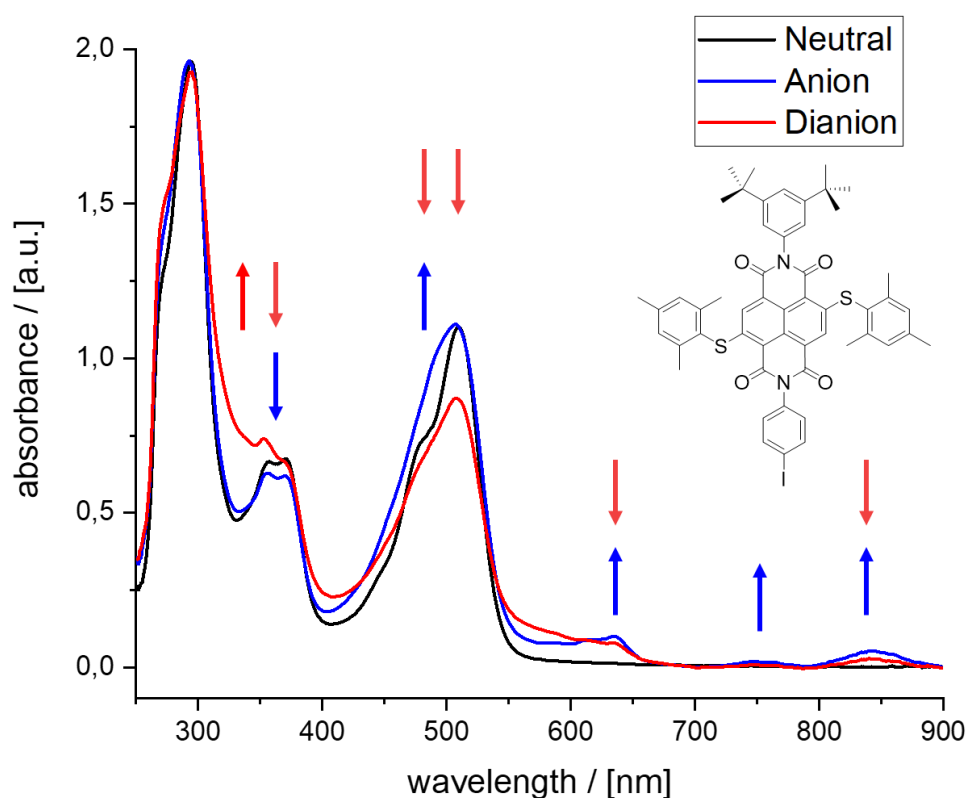


Figure 33. Spectroelectrochemical analysis of **sNDI** recorded in DMF containing 0.1 M solution of Bu_4NPF_6 as the supporting electrolyte. The neutral form is plotted in black, the anion in blue and the dianion in red.

The spectroelectrochemical analysis of **nNDI** and its anion is visualised in Figure 34. After reduction, the intensity of the $S_0 - S_1$ transition is decreased and the absorption maximum is hypsochromically shifted to 554 nm, exactly located at the shoulder of the parental **nNDI**'s $S_0 - S_1$ transition. Noteworthy, the broad peaks (observable for **hNDI** and **sNDI**) above 600 nm are not present in the **nNDI** anion absorption spectrum. However, a new peak arises at 402 nm. Similar to **sNDI**, the characteristic double-peak of the $\pi-\pi^*$ transition and the vibrational fine structure is disbanded and additionally, hypsochromically shifted. The parental peak at around 300 nm is shifted to shorter wavelengths and its fine structure changed as well. Compared to a similar pyrrolidine core-substituted NDI, the rise of a new peak at around 690 nm is not observed.^[319] For **nNDI**, it was not possible to obtain a UV-Vis spectra of the dianion in DMF.

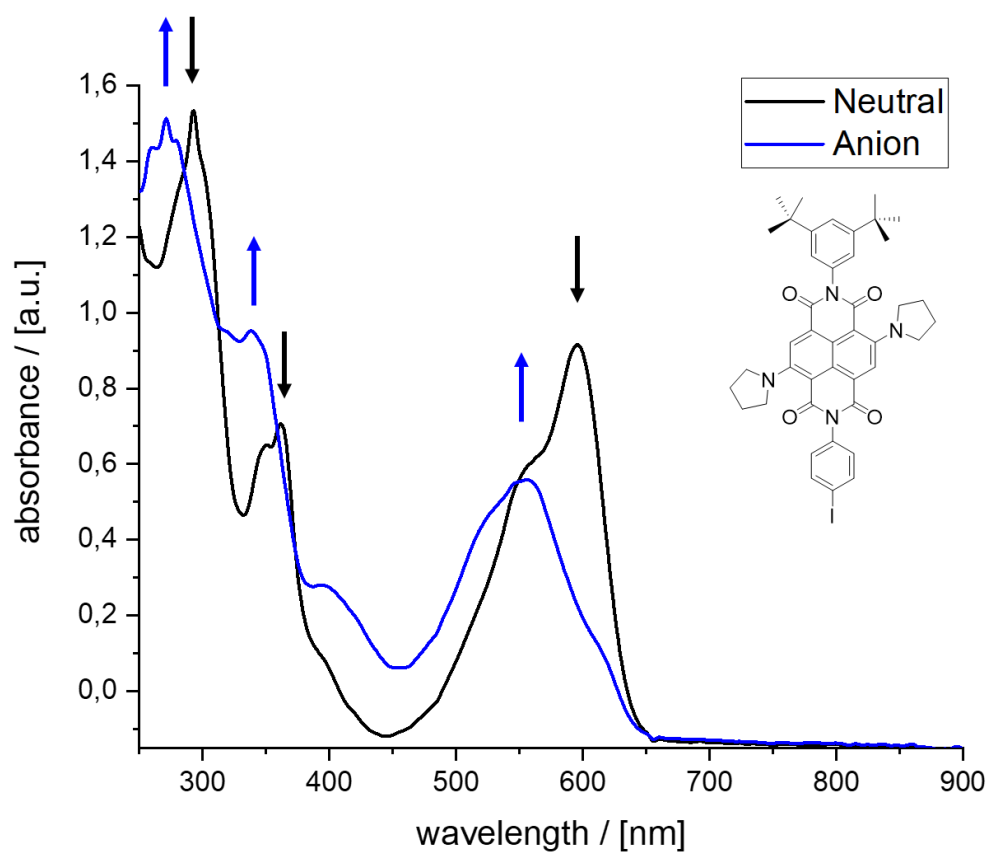


Figure 34. Spectroelectrochemical analysis of **nNDI** recorded in DMF containing 0.1 M solution of Bu_4NPF_6 as the supporting electrolyte. The neutral form is plotted in black, the anion in blue.

3.1.4.6 STM-Induced Luminescence (STML)¹

The surface behaviour of all three tripodal molecules bearing NDI chromophores was investigated using STML at 5 K in UHV. Spray deposition, of about 1 μL of **Ph-Tpd-hNDI** solution ($c \sim 1 \text{ mg/mL}$, for details see the Experimental Section) with a post annealing temperature of 100 $^{\circ}\text{C}$ leads to the formation of unordered islands of about 0.3 nm in height (see Figure 35a). This height indicates that the molecules are not adsorbed as intended but rather adsorb flat on the metal surface. While the islands seem to be composed of identical objects with clear substructure, the lack of any long-range order makes an assignment of the molecular adsorption impossible. When the STM tip is placed above these islands, plasmonic light emission which is characteristic for noble metal nanogaps,^[257] is partially or fully suppressed and the molecular layer merely acts as a dielectric layer that lowers the emission intensity.^[327] At some positions, molecular clusters of more than 1 nm in height protrude from the molecular islands (see Figure 35b). STM images of these clusters typically show white streaks and abrupt changes in the apparent height from one horizontal scan line to the next. These are signs of instability of the tunnel junction and can be explained by multilayers of **Ph-Tpd-hNDI** molecules of unknown orientation or by standing molecules in a less stable configuration as compared to the ordered monolayer. On these clusters and in the close vicinity, some light emission spectra are clearly different from a plasmonic light emission. We recorded 2500 photon spectra at different positions across the two clusters as depicted in Figure 35b. At most positions, the photon spectra are similar to the grey spectrum as shown in Figure 35c recorded at the position indicated by the grey cross in Figure 35b, with a broad peak centred around 1.5 eV. While the precise energy of the plasmonic resonance might shift depending on the exact position and the shape of the tip apex,^[255,328] the FWHM of about 300 meV indicates a plasmonic origin. About 200 out of 2500 spectra recorded on this area have a clearly different appearance and exhibit one or more sharper peaks of 30 to 100 meV FWHM to which we therefore tentatively assign a molecular origin. Six examples of such photon spectra are shown in Figure 35c (coloured photon spectra). The peak position ranges from 1.5 eV to 2.05 eV within the measurement on the area shown in Figure 35b. The quantum yield, that is the number of photons emitted per tunnelling electron, ranges from 1×10^{-4} to 1×10^{-3} for an applied sample bias of -2.5 V. Neither the spectral shape nor the quantum yield can be definitely related to the position where the spectrum has been recorded (that is the topography) and small displacements

¹ STML-measurements were conducted by Vibhuti Rai and analysed by Vibhuti Rai, Dr. Lukas Gerhard and Prof. Dr. Wulf Wulfhekel.

of the STM tip may lead to drastic variations of the photon spectrum (compare, for example, the grey and the dark blue spectra in Figure 35c). Still, at fixed positions, the junction is stable enough to perform extended measurements.

This allows to record photon spectra as a function of the applied sample bias that is as a function of the energy of the tunnelling electrons. Figure 35d shows such spectra recorded at the position marked by the red cross in Figure 35b. In this experiment, light emission sets in for a sample bias above +1.8 V and below -2 V with photon energies of less than 1.7 eV. For low currents and low temperatures, the high energy edge of a photon spectrum of plasmonic origin is expected to be limited by the energy provided by the tunnelling electrons: $eV = h\nu$. However, the threshold values for light emission observed in Figure 35d are clearly higher than the high energy edge of the photon spectra, which is a clear sign of molecular contribution to the light emission. In addition, both peaks emerge at the same bias voltage, which indicates that the redshifted peak can be attributed to the same molecular transition with an additional excitation of a molecular vibration,^[261,329] $eV = h\nu + \hbar\omega$. Indeed, most photon spectra recorded on the unordered clusters of **Ph-Tpd-hNDI** show a series of peaks with a typical spacing of about 160 meV (see also Figure S 9c in the appendix), in full agreement with a recent study on tetrapodal perylene diimides (PDIs) on Au(111).^[198] Rarely, light emission above the quantum threshold has been observed, even at low currents, which is an indication for intramolecular up-conversion (see also Figure S 9d in the appendix).^[330]

The combination of our highly efficient photon collection setup^[256] and an efficient conversion process in the molecular junction results in unusually high count rates observed for **Ph-Tpd-hNDI**. The spectrum recorded at 2.5 V and 5.2 pA shown in Figure 35d corresponds to 1.3×10^{-3} photons counted per tunnelling electron, which is, to the best of our knowledge, about one order of magnitude higher than the highest external quantum yields reported so far.^[255,331] After correction by the detector efficiency, this results in an internal quantum yield of about 6×10^{-3} .

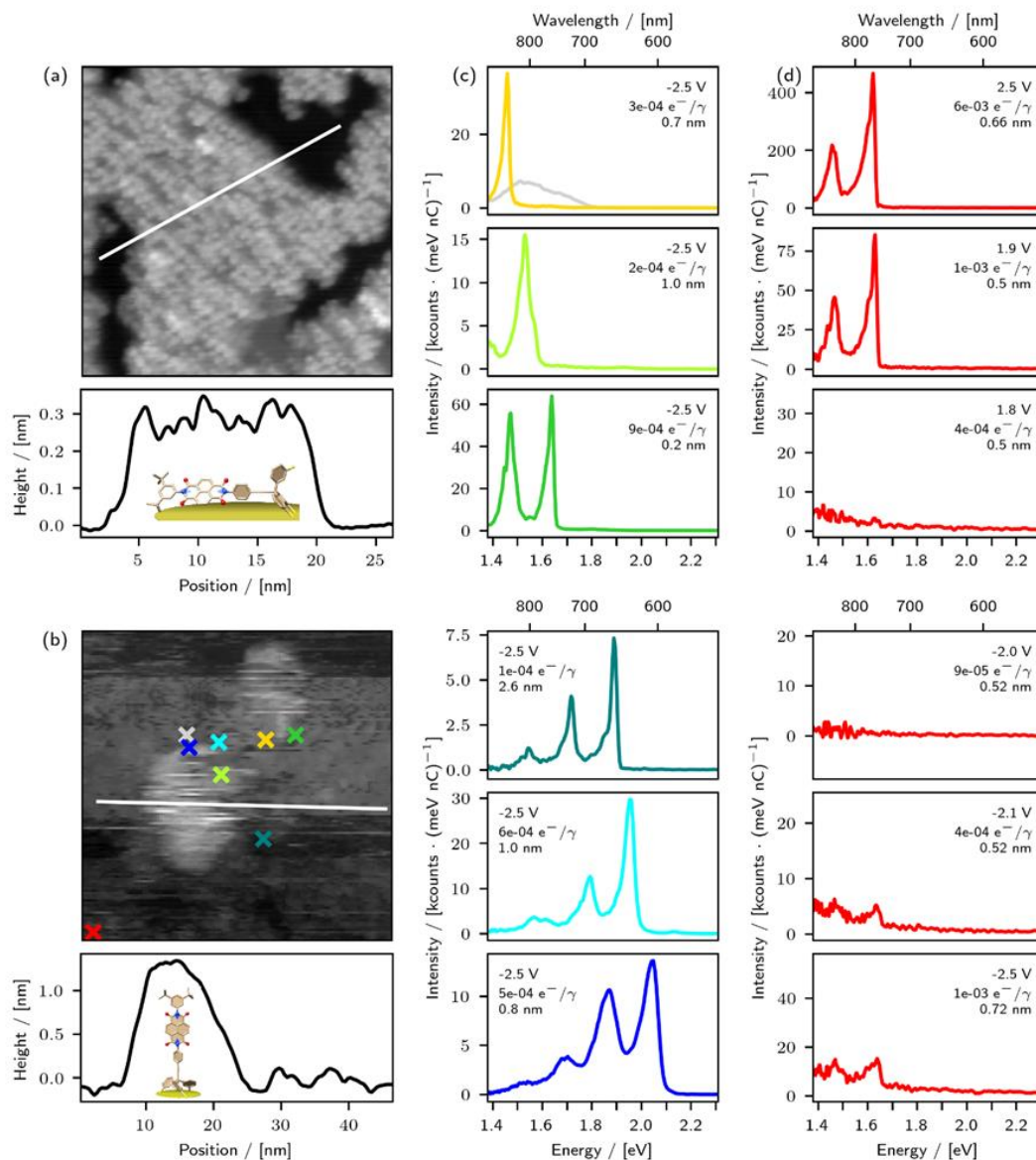


Figure 35. Light emission from unordered clusters of **Ph-Tpd-hNDI**. (a) Typical island structure of **Ph-Tpd-hNDI** with clean areas of Au(111) in between (black areas). The cross section taken along the white line reveals an apparent height of the island of about 0.3 nm. Molecular model in the proposed orientation is not to scale. Sample bias: 1.8 V, tunnelling current: 5 pA. Width of scan frame is 30 nm. (b) Two cluster of **Ph-Tpd-hNDI** (bright areas) with an apparent height of 1.2 nm (see cross section along the white line) above the island (darker areas). Sample bias: -2.3 V, tunnelling current: 5 pA. Width of the scan frame is 50 nm. Molecular model in the proposed orientation is not to scale. (c,d) Photon spectra recorded at the positions indicated by the corresponding crosses in (b). The applied sample bias, the internal quantum yield (count rate corrected for detector efficiency) and the vertical z-position of the tip are indicated in each panel. Tunnelling current is 130 pA in (c) and 5 pA in (d), integration time is 2 s.

After annealing the **Ph-Tpd-hNDI** sample for a second time, at 180 °C, ordered island structures form. Figure 36a shows a typical island which exhibits a monoclinic lattice structure with a unit cell (red lines) of 2.7 nm × 4.04 nm ($\alpha = 53^\circ$) = 8.6 nm². The apparent height of about 0.3 nm of these islands (see cross section along the white line in Figure 36a) is similar to that of the unordered ones discussed above and indicates that the **Ph-Tpd-hNDI** molecules adsorb in a horizontal configuration. In comparison, at similar voltages, a naphthalene diimide cyclophane “double decker” has been reported to show an apparent height of about 0.7 nm.^[135] Although the precise adsorption configuration is difficult to infer from the topographic image, we suggest a pairwise alignment as outlined in Figure 36b so that each bright blob corresponds to one molecule. This would result in an area of 4.3 nm² covered per molecule.

Similar to the unordered flat islands, plasmonic light emission is strongly suppressed when the tip is placed on top of the ordered islands. Figure 36c shows examples of photon spectra with the tip placed above Au(111) (red curve) and placed above the molecular island (black curve). While there are expected small intensity variations superimposed to a broad plasmonic spectrum in both curves, sharp peaks of molecular origin as described in Figure 35c are absent.

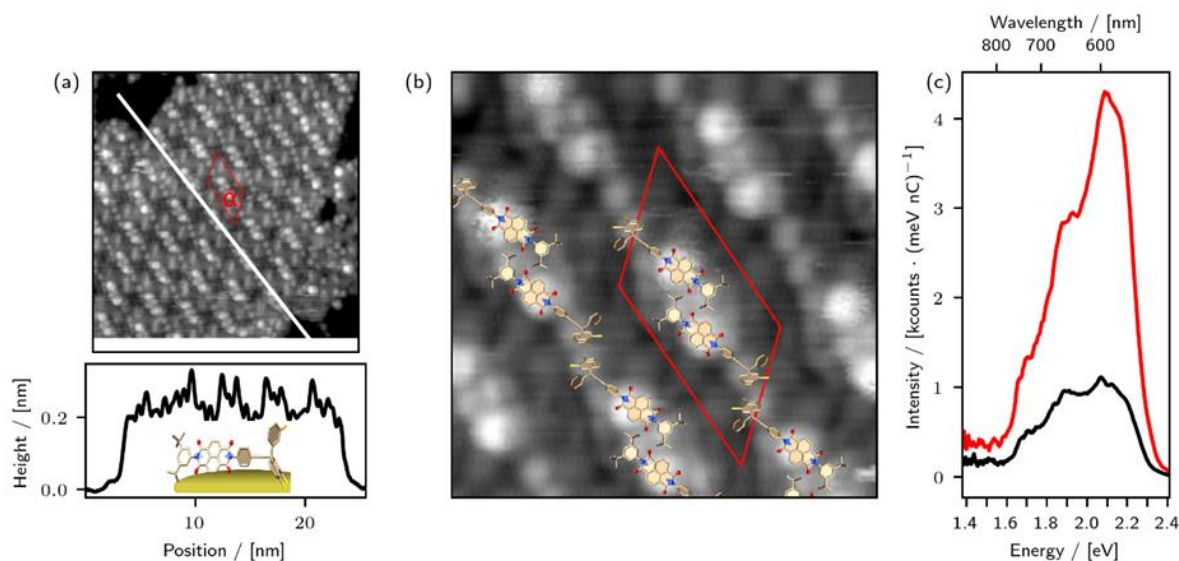


Figure 36. Ordered structure of **Ph-Tpd-hNDI**. (a) Ordered island of **Ph-Tpd-hNDI** with a unit cell indicated in red. Black areas correspond to the empty Au(111) surface. The cross section taken along the white line shows an apparent height of about 0.3 nm. Molecular model not to scale. Sample bias: 2.1 V, tunnelling current 9 pA, scan width: 22 nm. (b) Close-up scan of an ordered island with the unit cell indicated in red and molecular models of **Ph-Tpd-hNDI** superimposed to scale in the suggested adsorption configuration. Sample bias: -2.1 V, tunnelling current 5 pA, scan width: 8 nm. (c) Typical photon spectra recorded on the ordered islands (black) and the nearby Au(111) surface (red). Sample bias: 3 V, tunnelling current 140 pA, integration time: 2 s.

Ph-Tpd-nNDI also forms unordered islands of about 0.3 nm in apparent height at a post annealing temperature of 100 °C, suggesting that also for these molecular complexes the horizontal arrangement is preferred (see Figure 37). In this horizontal arrangement, the optical activity of the chromophore is expected to be quenched and indeed no molecular features in the photon spectra were observed. Formation of clusters consisting of molecules in more upright configurations were not observed.

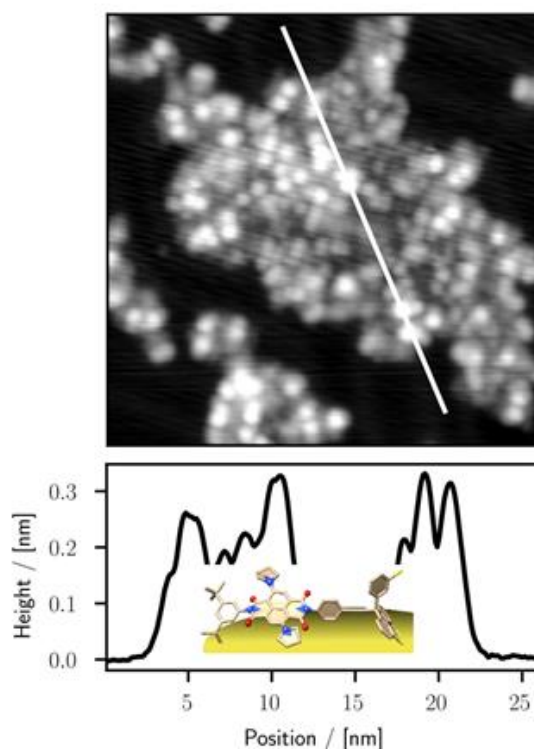


Figure 37. Unordered island of **Ph-Tpd-nNDI** with cross section along the white line. Molecular model (put model of **Ph-Tpd-nNDI**) not to scale. Sample bias -1.9 V, tunnelling current 2 pA, scan width 27 nm.

Similar to **Ph-Tpd-hND** and **Ph-Tpd-nNDI**, the sulfanyl-core-substituted variant **Ph-Tpd-sNDI** forms unordered islands of about 0.3 nm in apparent height as is shown in Figure 38a at a post annealing temperature of 100 °C. In addition, these islands act as a dielectric that reduces light emission from the decay of local gap plasmons, similar to Figure 38c. While we cannot exclude formation of clusters at 100 °C, we only observed such clusters of increased height after annealing a second time, to 180 °C. Figure 38b shows an example of a cluster that exceeds the surrounding island by 0.2 to 0.4 nm in apparent height. With the STM tip placed above these clusters, we observe light emission with pronounced peaks, very similar to Figure 35c.

The photon spectra also show two peaks that are typically separated by about 160 to 170 meV, which can be explained by energy transfer to the C-N stretch mode of the NDI core. Apparently, the local surrounding has a significant influence on both the electroluminescence efficiency and the energy of the emitted light. In agreement with the recent study on PDI tripodal molecules,^[198] the molecular configuration seems to be easily influenced by the nearby tip which hampers reproducibility of STML experiments. The wavelength shift of the substituted NDI molecules compared to the unsubstituted chromophore as it is observed in our PL measurements, does not translate to a shift of the electroluminescence photon spectra of the molecules deposited on the Au(111) surface.

Similar to **Ph-Tpd-hNDI**, **Ph-Tpd-sNDI** forms well-ordered islands at elevated post-annealing temperatures of 180 °C (see Figure 38d). The apparent height of 0.3 nm suggests that these islands are composed of flat-lying molecules, which is in agreement with the absence of any molecular signature in the photon spectra on these islands. A close-up scan of an ordered island shown in Figure 38d reveals a rich sub-molecular structure. We propose an adsorption configuration similar to the case of **Ph-Tpd-hNDI** (presented in Figure 37): Molecular pairs arrange in chains with the foot group pointing towards the next pair (see Figure 38e). Molecules of adjacent chains are mirrored. A closer look at the edges of the molecular island shows one quarter of the unit cell as the smallest unit, which confirms the hypothesis of pairwise adsorption (see also Figure S 9d in the appendix). In this rather tightly packed configuration, the unit cell with an area of $3.3 \text{ nm} \times 5.0 \text{ nm}$ ($\alpha = 47.6^\circ$) = 12.2 nm^2 contains 4 molecules (= 3.05 nm^2 per molecule).

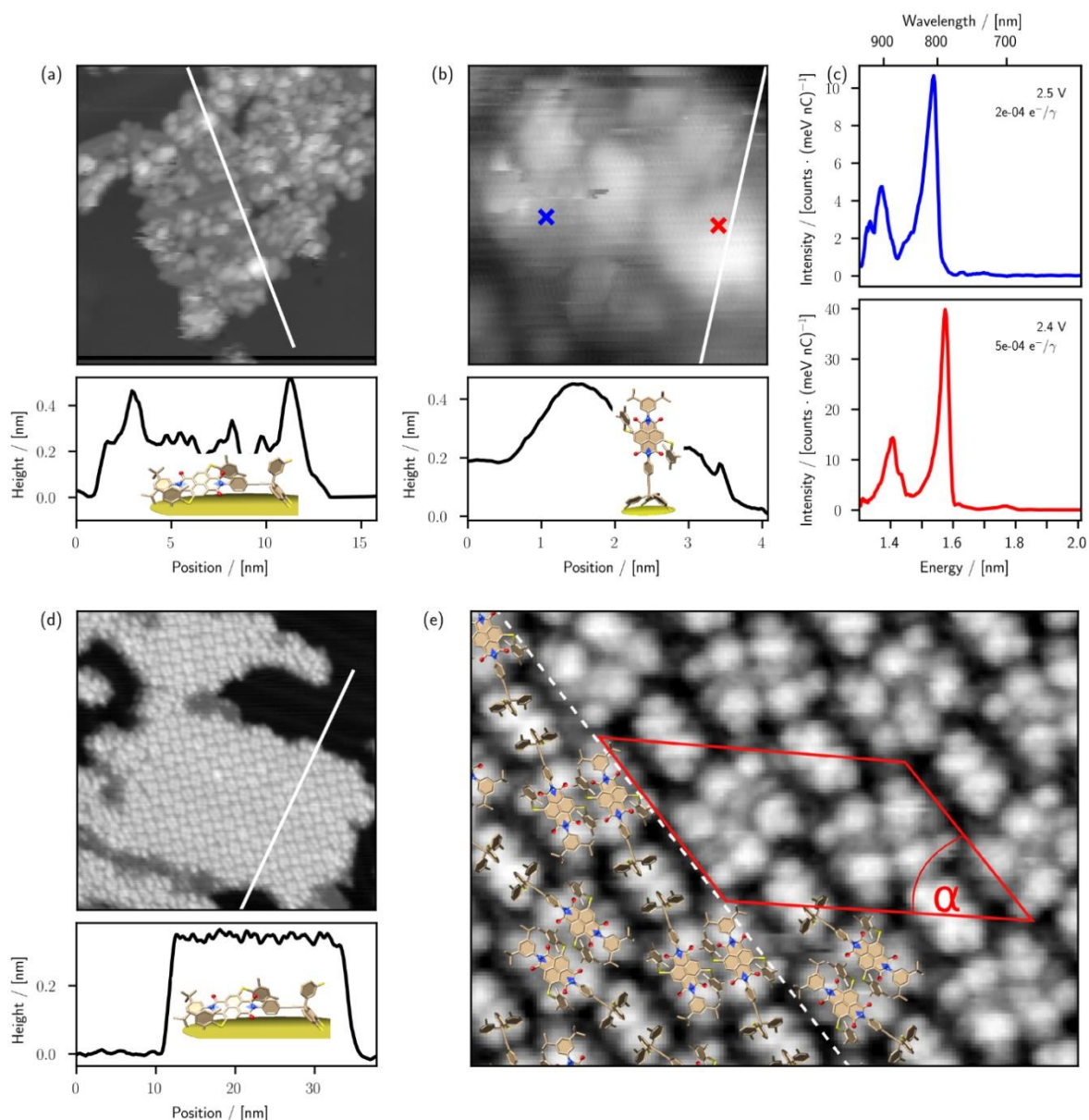


Figure 38. Adsorption and electroluminescence of **Ph-Tpd-sNDI**. (a) Unordered island structure of **Ph-Tpd-sNDI**. The cross section taken along the white line shows a typical height of 0.3 to 0.4 nm. Molecular model not to scale. Sample bias: -1.4 V, tunnelling current 2 pA, scan width: 15 nm. (b) Unordered cluster of **Ph-Tpd-sNDI** with a maximal apparent height of 0.4 nm above the surrounding island (see cross section along the white line). Molecular model not to scale. Sample bias: 2.4 V, tunnelling current 5 pA, scan width: 4 nm. (c) Typical photon spectra recorded at the positions indicated by the blue and red crosses in (b). Sample voltages of 2.5 and 2.4 V, tunnelling currents of 27 pA and integration times of 4 s were used. (d) Molecular model not to scale. Sample bias: 1.8 V, tunnelling current 3 pA, scan width: 43 nm. (e) Close up scan of an ordered island with molecular models superimposed to scale. Adjacent rows are mirrored and translated along the dashed white line. The red line indicates a possible unit cell. Sample bias: 2.6 V, tunnelling current 8 pA, scan width: 10 nm.

3.1.4.7 **Ph-Tpd-sNDI** as a Memory-in-Pixel Display¹

As described in the previous chapter, after annealing at 180 °C, most of the **Ph-Tpd-sNDI** chromophores lie flat and arrange couples of opposite orientations (Figure 38e). Interestingly, this pairwise adsorption configuration of the molecules allows a controlled manipulation by applying positive sample bias voltage above 2.5 V. This switching is reproducible, reversible and allows us to write “INT” on a monolayer, as shown in Figure 39. Due to its reversibility, this setup can be classified as a molecular “magnetic painting board” and thus is an evolution of our previous reported “molecular graph paper”.^[180]

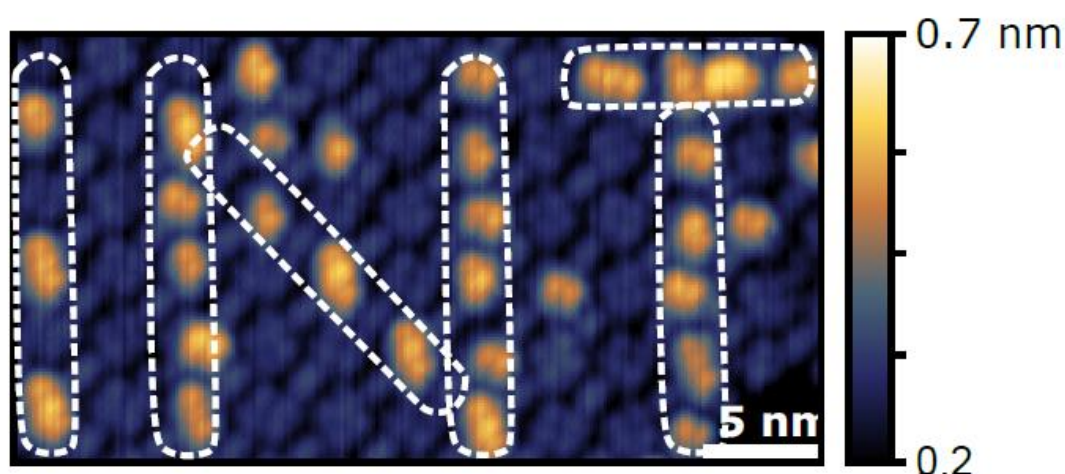


Figure 39. Molecular magnetic painting board on Au(111) decorated with **Ph-Tpd-sNDI**. Applying voltages >2.5V, controlled switching of individual molecules allow to write the letters “INT”. Sample bias: 2.5 V, tunnelling current 3 pA.

More importantly, the switching process is not only limited to the writing ability but also it elevates some of the molecules to a level successfully decoupling them from the surface. Therefore, quenching the emission by the substrate is suppressed and light emission is enabled as shown in the blue emission spectra of Figure 40b. In this way, we create a fluorescent molecular “memory-in-pixel” (MIP) display with single molecular resolution. MIP display technology is characterised by its ultra-low power consumption. The energy reduction

¹ STML-measurements were conducted by Vibhuti Rai and analysed by Vibhuti Rai, Dr. Lukas Gerhard and Prof. Dr. Wulf Wulfhekel.

Large Parts of this Chapter have been submitted to *Angewandte Chemie*: Vibhuti Rai, Lukas Gerhard, Nico Balzer, Michal Valášek, Christof Holzer, Liang Yang, Martin Wegener, Carsten Rockstuhl, Marcel Mayor and Wulf Wulfhekel

compared to other techniques is significantly reduced, because each pixel has a memory of its state and thus no additional energy is required for maintaining its state.

At ~1.88 eV, the photon spectrum exhibits a sharp peak which is labelled as X^+ . By addressing different areas of the monolayer, the recorded emission spectra change significantly. Therefore, the emission of the molecules strongly depends on the tip position. In Figure 40a, an excerpt of a **Ph-Tpd-sNDI**-decorated surface is shown, while in Figure 40b the corresponding light emission spectra of molecules at defined positions (indicated by different colours) are displayed. When the tip is placed above gold, the typical surface plasmons of gold are observable. On the contrary, the plasmon emission can be suppressed, when placing the tip over the flat lying molecule monolayer (pink position). Hence, the molecules are capable of forming a dielectric layer. The emission spectra of the optically active molecules significantly differ from the photoluminescence recorded in solution. While in solution the emission maximum is set at $\lambda_{max}^{em} = 557$ nm (see Figure 30, red line), the peak at ~1.88 eV in the photon spectrum corresponds to 660 nm (Figure 40b, blue line). There is reason to believe, that the luminescence is not dedicated to a neutral species but rather a charged one. Comparing the absorption spectra of the radical anion of **sNDI** (Figure 33, blue line) and by adding a Stokes shift of about 33 nm, which we observed for the neutral **sNDI**, an emission wavelength of 669 nm is to be expected. This would fit well to the observed emission X^+ . In strong contrast to the anion hypothesis, calculations reveal that cationic dimers of **Ph-Tpd-sNDI** would be stable enough to emit at 1.88 eV. Given the fact, that the molecules only emit at negative biases, which create positively charged molecules, further supports the theory of cationic dimers. Additionally, such switching and subsequent light emission is only observed in the pairwise adsorption configuration. We then investigated the differential conductance $(dI/dU)/(I/U)$ which correlates to the local density of states and hence gives information about the electronic structure of the involved orbitals. The flat lying **Ph-Tpd-sNDI** exhibits a broad peak ~ 1.11 V and after switching it, this peak is significantly sharper and centred at 1.24 and 1.29 V. The observed switching is not only present in the apparent height profiles of the involved molecules but is also accompanied by a change in the electronic decoupling of the corresponding orbitals. We speculate that this orbital is the LUMO. Furthermore, at negative sample biases, only the fluorescent chromophores exhibit a peak at 2.11 V which we tentatively assign the HOMO. Therefore, both HOMO and LUMO must be electronically decoupled from the surface in order to enable light emission. Although we cannot exclude direct charge-injection induced molecular excitation mechanism,^[332] we assume that the molecules' excitation can be

explained by an direct energy transfer *via* plasmons, since the critical sample bias of the onset of X^+ emission coincides with itself. ^[268,333,334] Based on the experiments, we interlink the emission band X^+ to a direct energy transfer as shown in Figure 40c. ^[268,335] The peaks at the lower energy region can be clarified as vibrational satellites of the X^+ . ^[261,272,329] At high-enough bias, the HOMO of the **Ph-Tpd-sNDI** is higher than the electrochemical potential of the tip E_T . Then, an electron is transferred from the HOMO to the tip, resulting in a charged state of the dimer. In the charged species, the LUMO level is expected to be 1.9 eV above the HOMO. By an inelastic tunnelling electron process (Figure 40c, (1)), an excited plasmon is formed, which then ultimately excites the molecule see Figure 40c, (2)). By radiative decay, the excited molecule then emits a photon. In this way, we not only created a “memory-in-pixel” display but proofed the concept of manipulating the luminescence of single molecules by varying their level of decoupling from the surface.

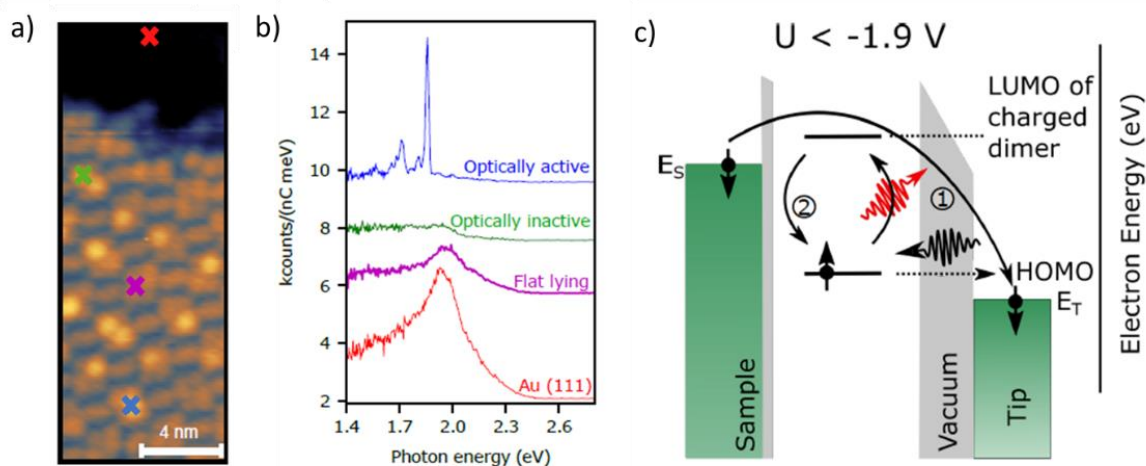


Figure 40. a) **Ph-Tpd-sNDI** decorated Au(111) surface. The image was recorded with a sample bias of -2.3 V and tunnelling current 2 pA. The coloured crosses indicate the tip positions at which the b) photon spectra are recorded. c) Illustrative mechanism of the light emission.

3.1.5 Conclusions of the First-Generation Single Molecule Devices

To conclude the Chapter 3.1, a tripodal platform **Ph-Tpd** based on a triphenylpropyne scaffold was developed. It consists of three acetyl-protected thiol anchors in the *meta*- position of phenyl legs and ethynyl linker allowing a modular assembly of several functional units *via* Sonogashira protocol. The initially designed platform **7** with thioacetate anchors is not stable under cross-coupling conditions, therefore the best alternative is the 2-(trimethylsilyl)ethyl protected derivative **6**.

After slight modification of the original design, the dipolar rotator **Ph-Tpd-Rot_{LF}** was synthesised in 5 steps.

Furthermore, a series of three different core-substituted NDI were developed and their photochemical, electrochemical and spectroelectrochemical characteristics were studied. While the synthesis of **hNDI** was straightforward, the synthesis of precursor **16** was quite troublesome. By using an equimolar stoichiometric ration of both anilines in a one-pot reaction, the yield was increased to almost 40%. Subsequent core-substitution by either 2,4,6-trimethylthiophenol or pyrrolidine afforded the chromophores **sNDI** and **nNDI**.

After the assembly of the functional with the molecular platform **6**, final transprotection step yielded the target molecular rotors **Ph-Tpd-Rot_C** and **Ph-Tpd-Rot_{LF}**, as well as the single molecule light emitters **Ph-Tpd-hNDI**, **Ph-Tpd-sNDI** and **Ph-Tpd-nNDI** as thioacetates. Except for **Ph-Tpd-Rot_{LF}**, all of them have been deposited on the Au(111) surface using the standard deposition method. Subsequent studies of their surface behavior helped us to evaluate the eligibility of both the molecular platform and the functional units.

The molecular rotor **Ph-Tpd-Rot_C** lies flat on the surface and is bound to the gold surface *via* one anchoring group. This newly formed pivot point allows the molecule to rotate, however not in an upright orientation. Admittedly, controlling of the rotation is not possible and not unidirectional. Since the rotating unit is most probably lying flat on the surface, an evaluation of the rotator's eligibility for unidirectional rotation cannot be proven with certainty.

Similar to **Ph-Tpd-Rot_C**, the NDIs mounted on the phenyl tripodal foot structure tend to mainly adsorb in a horizontal configuration as suggested by their arrangement in flat islands. Both **Ph-Tpd-hNDI** and **Ph-Tpd-sNDI** arrange in a close-packed pairwise fashion and form islands with a long-range lateral order upon annealing to 180 °C. At some positions, these molecules

form clusters with apparent height clearly exceeding those of the surrounding islands. According to the apparent height, these clusters compose of multilayers of horizontally aligned molecules or a single layer of upright oriented molecules in a less stable configuration. The lateral size clearly suggests that these clusters are composed of several molecules. These clusters of molecules show sharp peaks in photon spectra, which are clearly distinct from the plasmonic light of the same tip. Extensive low temperature UHV-STML studies of these molecules deposited on Au(111) by spray deposition technique revealed that only a minority of the tripodal chromophores form clusters, which show luminescence, while the majority of the chromophores are lying flat on the gold substrate. By applying positive bias voltages, the pairwise aligned **Ph-Tpd-sNDI** molecules can be reversibly and reproducibly switched into a new configuration resulting in an increase of the apparent height. This switching enables self-decoupling of the chromophore and upon applying negative bias, some of the switched molecules show sharp emission peaks which significantly differ from the photoluminescence recorded in solution. Supported by calculations, we assume that a positively charged dimer is formed which can be excited by plasmon. This excited state of positively charged dimers then decays radiatively by re-emitting a photon. Thus, the surface decorated with **Ph-Tpd-sNDI** can be classified as a “memory-in-pixel” display. While the initial design of the tripodal foot architecture is not providing upright orientated chromophores, the record high electroluminescence yields of up to 6×10^{-3} in the STML experiment showcase the potential of the presented NDIs as efficient emitters.

As a general conclusion, the functional units do not require further structural improvement whereas the tripodal platform needs to enlarge. Hence, the next chapter describes how to increase the feet geometry in order to guarantee the perpendicular orientation of the functional units with respect to the metallic substrate.

3.2 “Evolution of the Platforms”

As the **Ph-Tpd** platform requires an enlargement of the molecular footprint to guarantee an upright orientation of the functional units, this chapter describes the evolution of the enlarged second-generation tripodal structures **Bp-Tpd** and **Tol-Tpd**. Furthermore, in this chapter we present both (HR-)XPS studies based on the second-generation platforms and STM investigations of tolane-based symmetrical model compounds.

3.2.1 Design and Synthesis of Second-Generation Tripodal Structures

The design strategy of the second-generation platforms involves an enlargement of the molecular footprint, while preserving the triple bond on the triphenylpropyne scaffold. In Figure 41, the retrosynthetic approach is shown. We designed a triphenylpropyne scaffold comprising a halogen atom at each *para*-position of the phenyl ring (Figure 41, blue X). This design enables us to connect any “molecular leg” onto the scaffold *via* cross-coupling such as Sonogashira reaction or Suzuki reaction. By the design of the “molecular leg”, we preserve the aromatic thiol anchors at the *meta*-positions. This modular approach allows us to easily develop a library of extended molecular platforms with variation only in the architecture (length, nature of bonds, connectivity, *etc.*) of the molecular legs. After the successful synthesis of the second-generation platforms, we studied and optimised the formation of SAMs on the gold surface of the different platforms by means of laboratory XPS, high resolution XPS (HR-XPS) and X-ray absorption fine structure (NEXAFS) spectroscopy. To measure the tilting angle of the platforms by means of NEXAFS spectroscopy, the installation of a nitrile group with the orientation of the upstanding axis is required. For this purpose, three *para*-benzonitrile functionalised platforms **Ph-Tpd-CN**, **Bp-Tpd-CN** and **Tol-Tpd-CN** (see Figure 41) have been synthesised and the subsequent study of the self-assembly features of these functionalised platforms is discussed.

Increasing molecular footprint

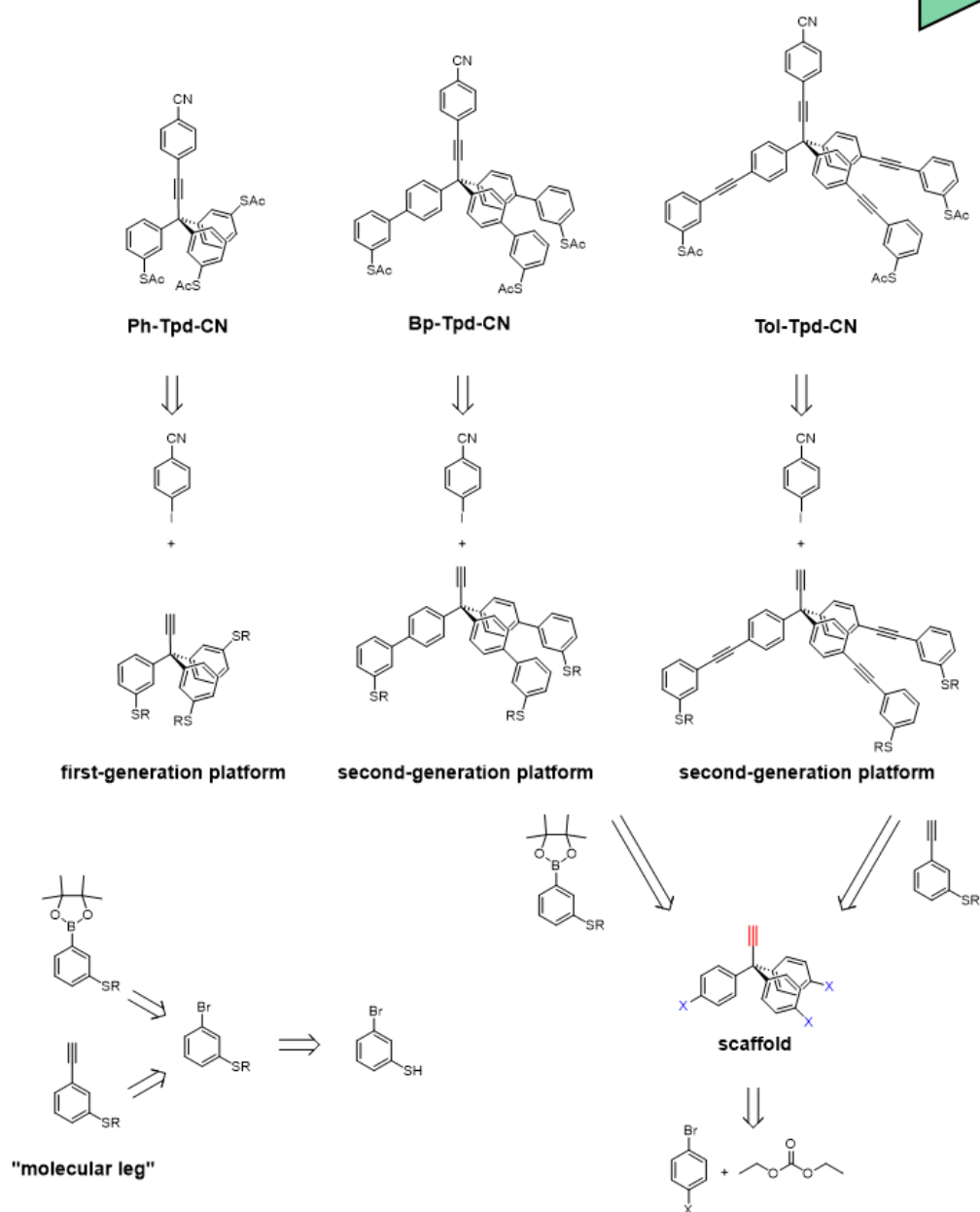
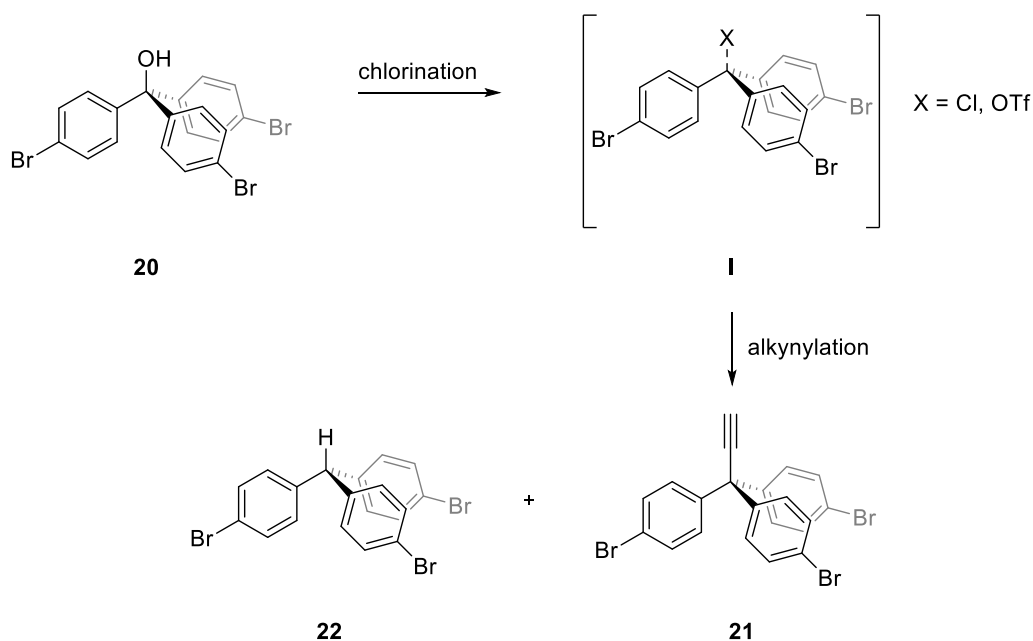


Figure 41. Increasing of the molecular footprint of the tripodal structures. Retrosynthetic analysis of the target molecules **Ph-Tpd-CN**, **Bp-Tpd-CN** and **Tol-Tpd-CN** including the design of the first and second-generation platforms as well as the molecular legs and the key scaffold bearing a triple bond (red) and the (pseudo)halogen X (blue and light blue).

3.2.1.1 Synthesis of the Scaffold

The synthesis of a triphenylpropyne scaffold fulfilling all the criteria mentioned above is inspired by the synthesis of molecule **6** presented in Chapter 3.1.1. By modification of a literature procedure, the synthetic route started with the mono-lithiation of *p*-dibromobenzene with *n*-BuLi (0.9 eq) at -78 °C.^[101] The lithiated species was then reacted with diethyl carbonate (0.25 eq) to yield the desired triphenyl methanol **20** in 92% yield, as shown in Scheme 11. To our delight, this reaction is scalable up to grams. The synthesis of triphenylpropyne **21** has been previously published by Hashmi *et al.*^[336] However, their synthetic strategy involves cyanation of the sp³-carbon, subsequent reduction to aldehyde and its final conversion to the triple bond *via* Bestmann-Ohira method. Despite their synthetic effort, they did not show the successful isolation of the product and used it for following reaction without further purification.^[336] To avoid their multistep synthesis, we developed a new single-step approach based on chlorination of the triphenyl methanol **20** and the subsequent ethynylation, as depicted in Scheme 9. The alkynylation however, turned out to be more challenging than expected. As a result, we changed both the chlorination and the alkynylation reagents. As this reaction involves two consecutive steps, we investigated each step individually by GC-MS analysis. As illustrated in Scheme 9, we first tried to optimise the formation of the (chlorinated) key intermediate **I** (Scheme 9, **I**) and then its subsequent conversion into the alkyne **21**.



Scheme 9. Chlorination and subsequent alkynylation of triphenylmethanol **20** to afford triphenylpropyne **21**. X = Cl or OTf.

Chlorination of **20** with acetyl chloride was not feasible under the conditions established for the synthesis of molecule **3** (Table 4, entry 1+ 2). We therefore varied the nucleophilic reagent such as an excess of $\text{HCl}_{(\text{aq})}$ (Table 4, entry 3-9), SOCl_2 (Table 4, entry 12) or use triflation with triflic anhydride (Table 4, entry 10+11). Although the key intermediate **I** was formed with both thionyl chloride and triflic anhydride, subsequent alkynylation was not possible. The approach of weakening the C-O bond with Lewis acids such as BF_3 , BCl_3 , and BBr_3 followed by the alkynylation with ethynylmagnesium bromide did not lead to the product, but exclusively to the triphenylmethane **22** as a by-product (Table 4, entry 13 and Table 5, entry 5). Among all the reagents we used, only aqueous hydrochloric acid provided reasonable results. We therefore studied the effect of solvents such as toluene (Table 4, entry 3+9), diethyl ether (Table 4, entry 4), tetrahydrofuran (Table 4, entry 5) and dichloromethane (Table 4, entry 6+7). It turned out that DCM was the most promising one. Also, increasing the temperature and reaction time did not improve the formation of key intermediate **I** either (Table 4, entry 8+9). As a result, chlorination of compound **20** in dichloromethane and hydrochloric acid was the most promising approach to form the key intermediate **I** as shown in Table 4.

Table 4. Reaction attempts for reacting molecule **20** to intermediate **I**, with different reagents, under different reaction times and temperatures. The ratio is determined by the peak intensities of the GC-MS chromatogram. *not possible for alkynylation

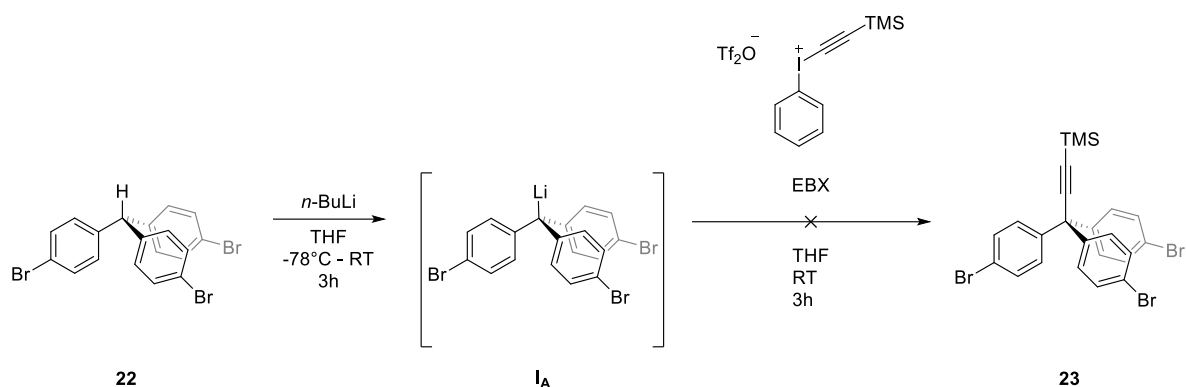
entry	solvent	reagents	rct. time [min]	Tem- pera- ture	ratio 20 : I : 22
1	toluene	AcCl	240	60 °C	only 20
2	DCM	AcCl	240	25 °C	only 20
3	toluene	HCl	5	25 °C	20 : 1 : 1
4	diethyl ether	HCl	5	25 °C	5 : 1 : 1
5	THF	HCl	5	25 °C	10 : 4 : 1
6	DCM	HCl	5	25 °C	1 : 9 : 3
7	DCM - dis- tilled	HCl	5	25 °C	1 : 9 : 3
8	DCM	HCl	120	60 °C	1,5 : 2 : 1
9	toluene	HCl	120	60 °C	20 : 1 : 1
10	NEt ₃	Tf ₂ O	25	25 °C	1: 1 : 2,5*
11	NEt ₃	Tf ₂ O	120	25 °C	1 : 1 : 1 *
12	NEt ₃	SOCl ₂	120	25 °C	1 : 1 : 1 *
13	DCM	BX ₃ X=F, Cl, Br	30	0 °C	only 22

Prior the subsequent alkynylation, residual HCl_(aq) must be removed. For that, phases were separated, and the organic solvent was then removed under reduced pressure at 50 °C. With the aforementioned chlorination conditions (Table 4, entry 6 and 7), different alkynylation methods were performed as shown in Table 5. While the choice of solvent and reaction temperature between 40 °C-60 °C has almost no impact (Table 5, entry 1-3) on the yield, the source of the ethynylmagnesium bromide is of great importance. It turned out, that the commercially available ethynylmagnesium bromide by *Sigma Aldrich* (Table 5, entry 7) gave the highest yield. Also, neither lithium acetylides (Table 5, entry 4) nor *in situ* formed sodium acetylides (Table 5, entry 6) did lead to the formation of the desired triphenylpropyne scaffold.

Table 5. Reaction attempts of the alkynylation of intermediate **I**, with different alkynylation reagents, reaction times, temperatures and the yields. The yields are estimated from the peak intensities of the GC-MS chromatogram.

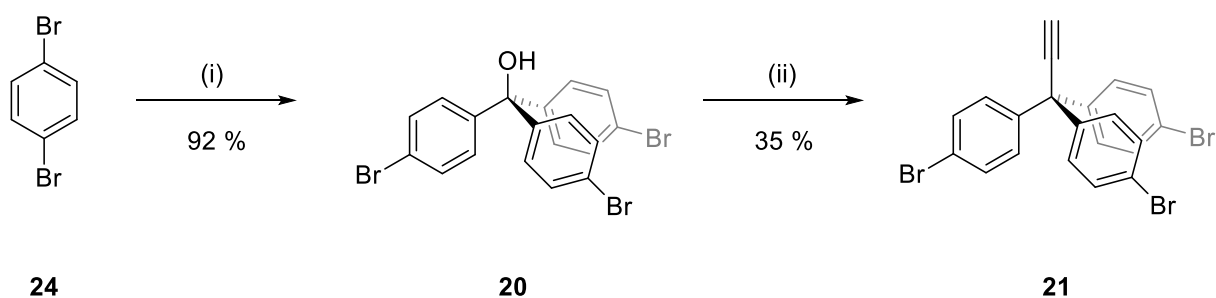
entry	solvent	reagent to synthesise I	alkynylation reagent	rct. time [min]	tempera- ture	yield of 21 by GC-MS
1	toluene	HCl	HC≡CMgBr (Acros Organics)	240	60 °C	5 %
2	THF	HCl	HC≡CMgBr (Acros Organics)	240	60°C	5 %
3	THF	HCl	HC≡CMgBr (Acros organics)	240	screening to 60°C	5 %
4	THF	HCl	TMS-C≡CLi	240	-78°C to 25°C	-
5	DCM	BF ₃	HC≡CMgBr (Acros Organics)	240	-78°C to 25°C	-
6	THF	HCl	TMS-C≡CNa	240	60°C	-
7	THF	HCl	HC≡CMgBr (Aldrich)	240	60°C	35 %

In another approach, we tried to reuse the undesired tris(*meta*-bromophenyl)methane **22** by deprotonation and subsequent alkynylation with a hypervalent iodine compound **EBX**. Using *n*-BuLi, we were able to deprotonate compound **22** to form the anion **I_A** which was indicated by the colour change of the solution from colourless to deep red. After quenching the reaction with deuterated water, investigation of such mixture by GC-MS mass spectroscopy evidenced the successful deprotonation of the compound **22**. Unfortunately, only organometallic bases such as *n*-BuLi are strong enough to deprotonate tris(*meta*-bromophenyl)methane **22**, which led to the inevitable competing reaction of lithium-halogen exchange. Subsequent quenching of the trityl anion with the hypervalent iodine **EBX** was not successful.^[337]



Scheme 10. Synthetic approach towards compound **23** *via* deprotonation and subsequent alkynylation.

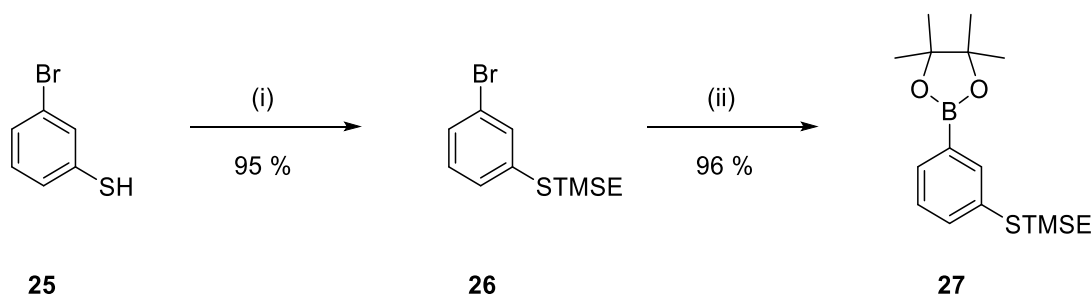
To sum up, in a high yielding and multigram scale reaction, we were able to synthesise the triphenylmethanol **20**. After screening the reaction conditions for compound **21**, we optimised the reaction yield up to acceptable 35%, as shown in Scheme 11.



Scheme 11. Synthetic approach to building block **21**. Reaction conditions: i) $n\text{-BuLi}$, $(\text{CH}_3\text{CH}_2\text{O})_2\text{CO}$, THF; ii)a: HCl, DCM; b: $\text{HC}\equiv\text{CMgBr}$, THF.

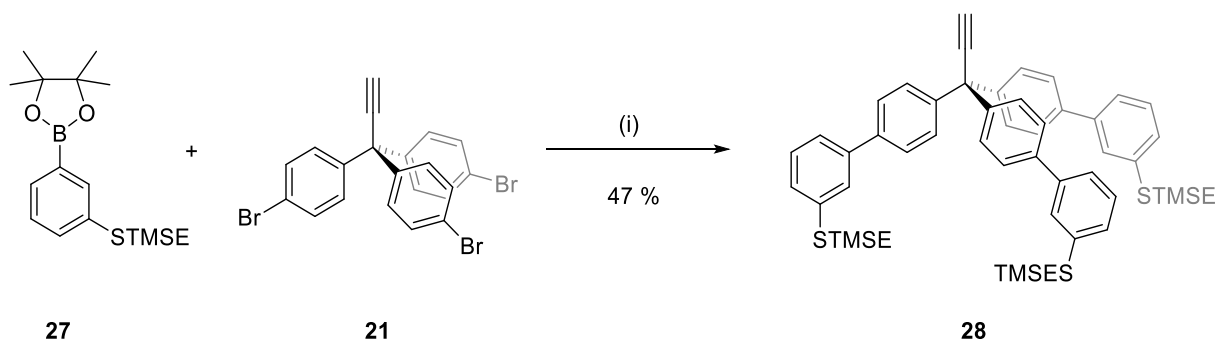
3.2.1.2 Synthesis of the Second-Generation Platforms

The synthesis of the boronic ester **27** has been published by our group and is outlined in Scheme 12.^[196] In a radical reaction, *meta*-bromothiophenol **25** was converted to 3-[2-(trimethylsilyl)ethylsulfanyl]phenylacetylene **26** with vinyltrimethylsilane and the radical initiator azobisisobutyronitrile (AIBN) with high yields.^[196] Subsequent reaction to the boronic ester **27** can be performed in two different ways. On the one hand, lithiation of the compound **26** followed by quenching with 2-isopropoxy-4,4,5,5-tetramethyl-1,3,2-dioxaborolane (ⁱPrOBpin) led to the corresponding pinacol boronic ester **27** in 35% yield. On the other hand, the Miyaura-borylation of compound **26** with bis(pinacolato)diboron in the presence of PdCl₂(PPh₃)₂ afforded the desired boronic ester **27** in very high yields.



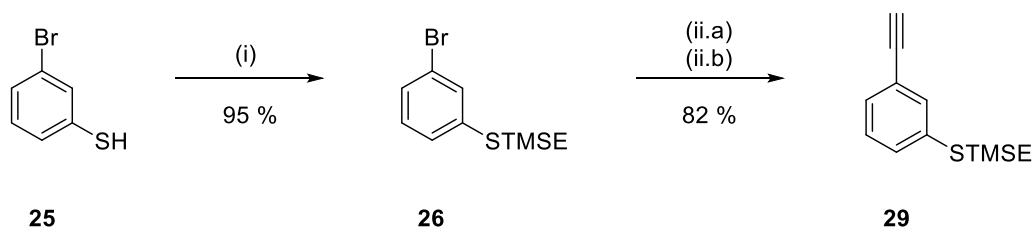
Scheme 12. Synthetic approach to the building block **27**. Reaction conditions: i) vinyltrimethylsilane, AIBN, neat; ii) PdCl₂(PPh₃)₂, B₂Pin₂, KOAc, dioxane.

With both building blocks in hand, we assembled triphenylpropyne scaffold **21** with the boronic ester **27** *via* Suzuki cross-coupling to afford the extended tripodal platform **28** in moderate yield (Scheme 13). For this extended platform we will use the abbreviation **Bp-Tpd-{functional unit}**.



Scheme 13. Synthetic approach to biphenyl tripodal platform **28**. Reaction conditions: i) $\text{PdCl}_2(\text{dppf})$, K_2CO_3 , DMF.

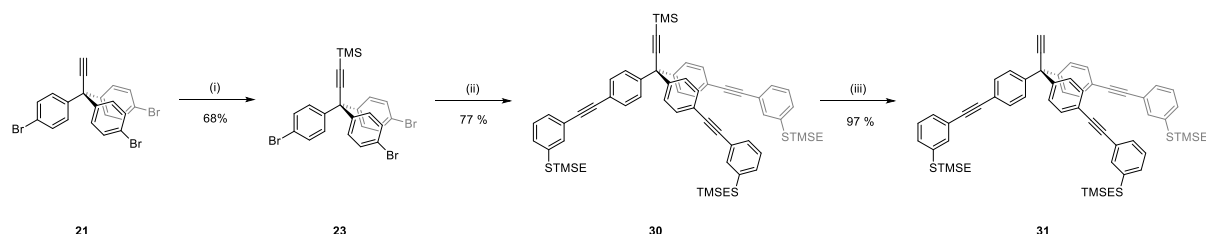
The second extended platform (Scheme 15, compound **31**) contains an additional phenylacetylene unit in between the scaffold and the anchoring group. As shown in Scheme 14, we synthesised the phenylacetylene derivative **29** from compound **26**. After the introduction of trimethylsilylacetylene *via* Sonogashira protocol, and subsequent cleavage of the TMS protecting group, the *meta* substituted phenylacetylene **29** was afforded in high yield.



Scheme 14. Synthetic approach to compound **29**. Reaction conditions: i) vinyltrimethylsilane, AIBN, neat; ii.a) $\text{Pd}(\text{PPh}_3)_4$, CuI , NEt_3 , TMS-acetylene; ii.b) MeOH , K_2CO_3 .

By coupling of the triphenylpropyne scaffold **21** with phenylacetylene **29**, we obtained the tripodal platform **31** in three reaction steps in moderate yield. Given the architecture of the molecular legs, we will refer to the tolane containing tripodal derivatives of **31** as **Tol-Tpd-{functional unit}**. As shown in Scheme 15, it is important to protect the free acetylene of **21** with TMS in order to prevent its homo-coupling during the Sonogashira reaction. In the presence of palladium catalyst and phenylacetylene **29**, the TMS-decorated tripodal scaffold **23** was converted to the tolane-based extended platform in its TMS-protected form with acceptable yields. Noteworthy, due to larger difference in the R_f – values of the side products, purification of **30** should be done before cleaving off the TMS group, since separation of the

side product by means of column chromatography is more difficult after removal of the TMS-group. Starting from the key intermediate **21**, the tolane-based tripod **31** was synthesised in three reaction steps with an overall yield of 45%.



Scheme 15. Synthetic approach to tolane based tripodal platform **31**. Reaction conditions: i) EtMgBr, TMS-Cl, THF; ii) **29**, Pd(PPh₃)₄, CuI, NEt₃; iii) MeOH, K₂CO₃

With the successful synthesis of the three different platforms **6**, **28** and **31**, we established a library of various tripodal platforms and studied their eligibility for surface functionalisation. We then visualised their foot geometry and calculated the resulting area underneath the platform – the molecular footprint. In the case of the phenyl tripodal **Ph-Tpd**, the distances between the sulfur atoms amounts 6.0 Å. Depending on the choice of the fixed point, i.e., the sulfur atom of the anchoring group or the most distant hydrogen atom located at the *para*-position, the radius of the smallest platform **Ph-Tpd** is either 3.5 Å (sp³-central carbon – sulfur distance) or 5.1 Å (sp³-central carbon – hydrogen distance). Using the equation 3.1, the area of the footprint is calculated to be 88.2 Å² or 120.8 Å² (equation 3.2), respectively.

$$Area(C-S) = \pi (R + 1.85\text{\AA})^2 \quad (3.1)$$

$$Area(C-H) = \pi (R + 1.10\text{\AA})^2 \quad (3.2)$$

In both equations, the van der Waals radii of the corresponding atoms (Batsanov: sulfur \triangleq 1.85 Å² and hydrogen \triangleq 1.10 Å²) were taken into account.^[338] The sulfur-sulfur distances in the extended platform **Bp-Tpd** is calculated to be 13.0 Å and the radius from the sp³-central carbon to the sulfur atoms is 7.4 Å, while the distance to the most distant hydrogen atoms is 9.1 Å. Hence, the area underneath the molecular footprint can be calculated with equations 3.1 and 3.2 to 265.9 Å² or 326.9 Å² respectively. Compared to the other two platforms, both the sulfur-

sulfur distances and the molecular footprint of the tolane containing platform **Tol-Tpd** exhibit the highest values, which are 16.8 Å between the sulfur atoms, and 9.8 Å from the sp³-central carbon to the sulfur or 11.3 Å from the sp³-central carbon to the outmost hydrogen atom. The calculated results of the molecular footprints are summarised in Table 6.

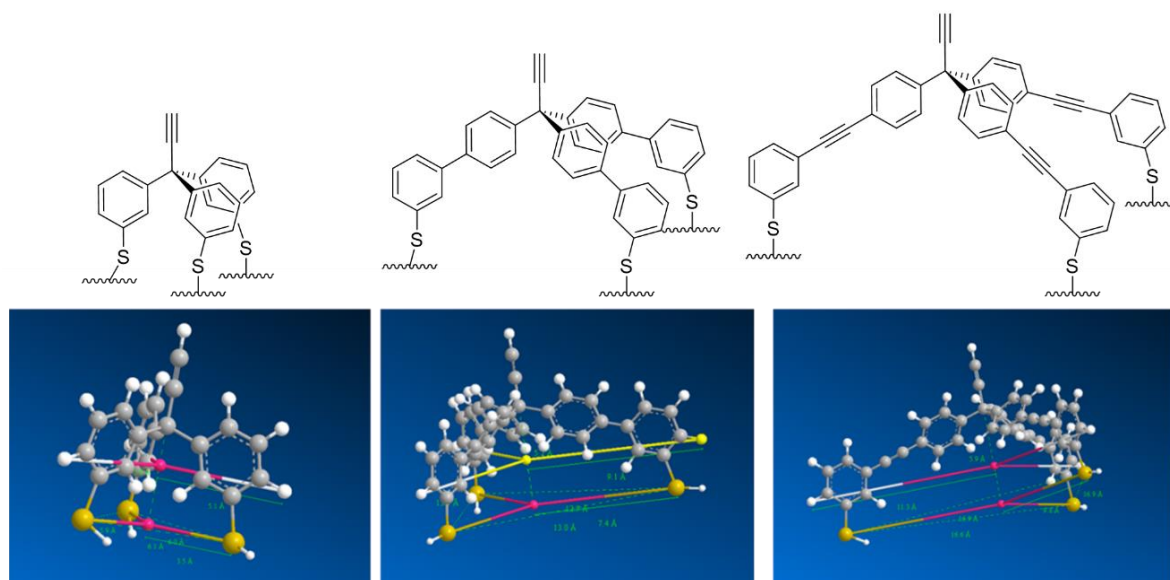


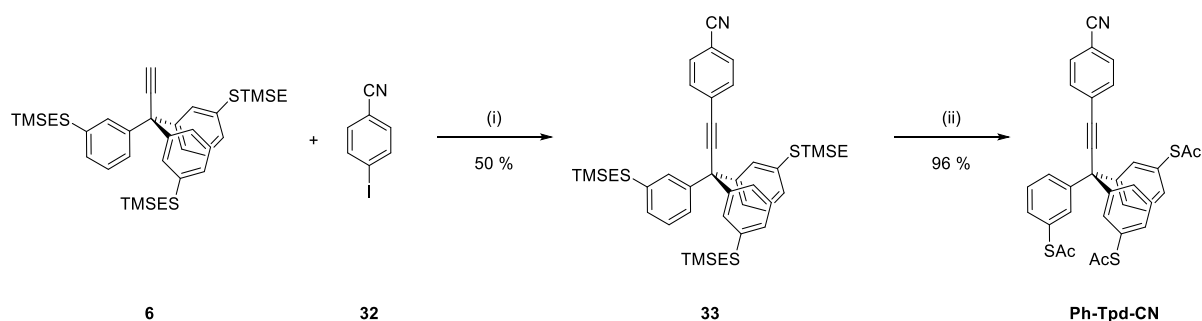
Figure 42. Top: Schematic drawing of **Ph-Tpd**, **Bp-Tpd** and **Tol-Tpd**. Bottom: 3D-Models after MM2 optimisation including key distances within the molecule. Calculated with Chem3D.

Table 6. Key features of the molecular footprint of **Ph-Tpd**, **Bp-Tpd** and **Tol-Tpd**. Distances were calculated with Chem3D after MM2 optimisation.

	Ph-Tpd	Bp-Tpd	Tol-Tpd
S-S distance	6.0 Å	13.0 Å	16.8 Å
radius _(c-s)	3.5 Å	7.4 Å	9.8 Å
area _(c-s)	88.2 Å ²	265.9 Å ²	422.7 Å ²
radius _(h-s)	5.1 Å	9.1 Å	11.3 Å
area _(h-s)	120.8 Å ²	326.9 Å ²	483.1 Å ²

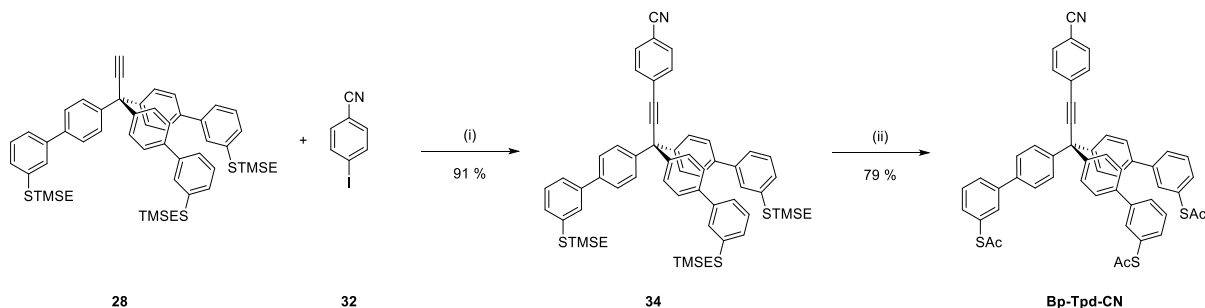
3.2.1.3 Synthesis of Second-Generation Functional Tripods as SAMs

For the study of SAM formation of our three tripodal platforms, the *para*-benzonitrile-functionalised platforms **Ph-Tpd-CN**, **Bp-Tpd-CN** and **Tol-Tpd-CN** have been synthesised. The synthetic approach towards the first functionalised platform **Ph-Tpd-CN** is based on a Sonogashira protocol. In triethylamine, *para*-iodobenzonitrile **32** was coupled with platform **6** in moderate yield and subsequent transprotection of the thiols (introduced in Chapter 3.1.1) afforded the desired thioacetate protected platform **Ph-Tpd-CN** in high yield as shown in Scheme 16.



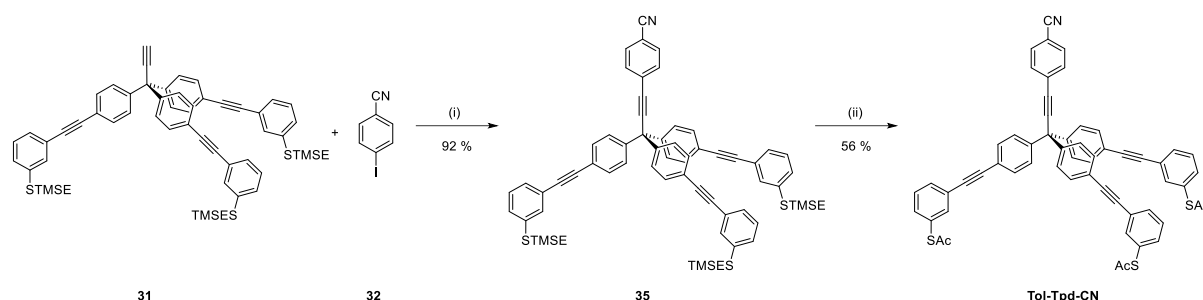
Scheme 16. Synthetic approach to **Ph-Tpd-CN**. Reaction conditions: i) CuI, Pd(PPh₃)₄, NEt₃; ii) AcCl, AgBF₄, DCM

Similarly, under the standard Sonogashira protocol, *para*-iodobenzonitrile **32** was coupled with the extended platform **28**, which resulted in compound **34** in 91% yield. As shown in Scheme 17, the subsequent transprotection gave the desired thioacetate **Bp-Tpd-CN** in high yields.



Scheme 17. Synthetic approach to **Bp-Tpd-CN**. Reaction conditions: i) CuI, Pd(PPh₃)₄, NEt₃; ii) AcCl, AgBF₄, DCM

Using the previous conditions for both the Sonogashira reaction and the transprotection step, **Tol-Tpd-CN** was isolated in moderate yield.



Scheme 18. Synthetic approach to **Tol-Tpd-CN**. Reaction conditions: i) $\text{Pd(PPh}_3)_4$, CuI , NEt_3 ; ii) AcCl , AgBF_4 , DCM

3.2.2 Surface Studies of Second-Generation Tripodal Structures in SAMs¹

The samples for the SAM characterisation were freshly prepared for each new series. Hereby, freshly annealed gold-coated silicon wafers were immersed in a solution of the tripodal molecules **Ph-Tpd-CN**, **Bp-Tpd-CN** and **Tol-Tpd-CN**. The thickness of gold layers varied between 100 and 200 nm. To find the most suitable conditions, different immersing times (1h and 18h), cleaving agents (MeOH only, NH_3 , NEt_3), temperatures ($25\text{ }^\circ\text{C}$ and $50\text{ }^\circ\text{C}$) and concentrations (0.1 mM and 0.01 mM) were tested. Prof. Dr. Michael Zharnikov and M.Sc Andika Asyuda measured and evaluated the samples. The first and fourth series was measured by means of HR-XPS and NEXAFS spectroscopy, while the second and third series was carried out with laboratory X-ray photoelectron spectroscopy by Prof. Dr. Michael Zharnikov at the University of Heidelberg.

¹ The SAMs were measured and evaluated by Professor Dr. Michael Zharnikov and M.Sc Andika Asyuda

3.2.2.1 XPS-Studies

In our first series, two samples of each **Ph-Tpd-CN**, **Bp-Tpd-CN** and **Tol-Tpd-CN** were prepared. Based on our previous preparation method of SAMs of tetraphenylmethane tripods,^[101] we diluted the molecules in a mixture of methanol/THF (3:1, v/v) and used a 1 M solution of ammonia in methanol as cleaving agent. The overall concentration was set to be 0.1 mM and the gold-coated samples were immersed overnight. After taking them out of the vial, the substrates were then thoroughly rinsed with dry MeOH and THF to wash off all residues. For each molecule, one SAM was post-annealed at 135 °C for 90 minutes under argon conditions. In Figure 43a, the Au 4f-HR-XPS of **Ph-Tpd-CN**, **Bp-Tpd-CN** and **Tol-Tpd-CN** are shown. Only the spectra of **Ph-Tpd-CN** exhibits the characteristic peak of the gold surface. It indicates that only **Ph-Tpd-CN** forms monolayers, whereas **Bp-Tpd-CN** and **Tol-Tpd-CN** grow multilayers. The Au 4f spectra of the post-annealed **Ph-Tpd-CN** shows a discernible higher peak compared to the non-annealed one, suggesting that the high temperature treatment results in a smaller layer thickness. Because of strong self-attenuation of the signal within this energy range, the difference in a layer thickness is less observable in the C 1s spectra.^[339] The main peak at ~284 eV in this spectra can be assigned to the aromatic scaffold while the small shoulder at ~286 eV verifies the presence of the nitrile group.^[340] The intensity of the N 1s signal (see Figure 43c) is more pronounced in the post-annealed SAM compared to the other. This is in agreement with the layer thickness observed from the Au 4f spectrum. Comparing the O 1s spectra of the two different SAMs of **Ph-Tpd-CN**, a remarkable difference is pronounced: the intensity of the O 1s signal is significantly lower in the post-annealed sample, indicating that the quality of the SAM is drastically increased by the post-annealing process. In the S 2p spectra of the multilayers of **Bp-Tpd-CN** and **Tol-Tpd-CN** the peaks in the region over 166 eV can be assigned to oxidised sulfur species. For the two extended platforms, the characteristic thiolate doublet feature between ~162.0 eV and ~163.6 eV is absent. This means that there are either no thiolates or the thiolates close to the surface are not accessible, which is another indication for the formation of multilayers. In contrast to that, the S 2p spectra of **Ph-Tpd-CN** exhibit peaks that correspond to the superposition of physisorbed material (or free thiols) and surface bound thiolates. For both samples of **Ph-Tpd-CN**, the ratio between physisorbed material and thiolate is estimated to be 1:2. Comparing the intensities of the S 2p spectra, the signals of **Ph-Tpd-CN** SAMs are significantly lower than for **Bp-Tpd-CN** and **Tol-Tpd-CN**-based self-assembled monolayers, explained by the increased number of sulfur moieties in multilayers compared to the monolayer.

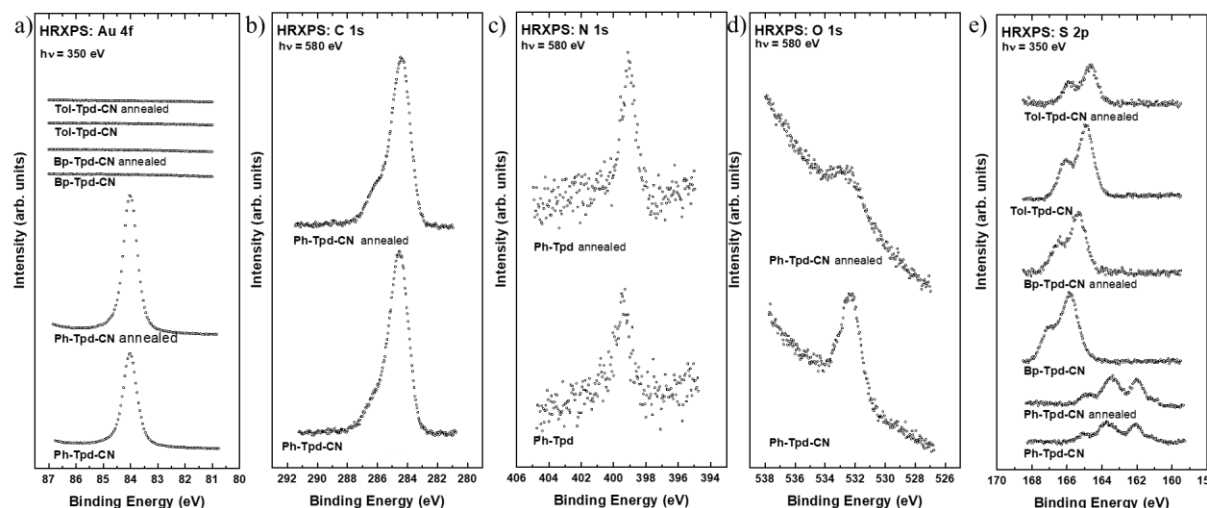


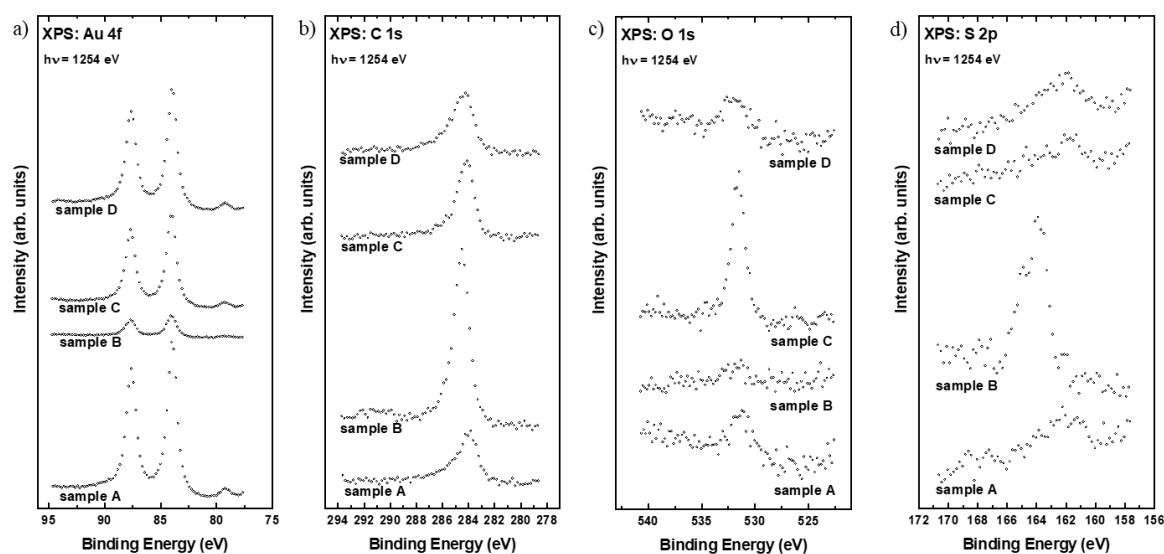
Figure 43. HR-XPS study of the 1st series. a) HR-XPS spectra of Au 4f of **Ph-Tpd-CN**, **Bp-Tpd-CN** and **Tol-Tpd-CN**. HR-XPS spectra of **Ph-Tpd-CN** of b) C 1s, c) N 1s, d) O 1s and e) the HR-XPS spectra of S 2p of **Ph-Tpd-CN**, **Bp-Tpd-CN** and **Tol-Tpd-CN**.

The first series of SAM studies of **Ph-Tpd-CN**, **Bp-Tpd-CN** and **Tol-Tpd-CN** revealed that, in order to promote monolayers, the preparation conditions must be optimised. We therefore started a second series on **Bp-Tpd-CN** aiming to prevent the formation of multilayers. Within this study, we varied the cleaving agents, immersion temperatures and times. For all experiments, we substantially decreased the concentration by one order of magnitude to get an overall concentration of 0.01 mM. At first, we tried to promote the cleavage of thioacetates only in MeOH and THF at elevated temperature (Table 7, sample A). As the second and third alternative, ammonia was used as the cleaving agent, while immersing the sample at room temperature for either 18 hours (Table 7, sample B) or 1 hour (Table 7, sample C). As the fourth option, triethylamine was tested as a cleaving agent. In this trial, the sample was immersed at room temperature overnight as well (Table 7, sample D).

Table 7. Overview of the preparation conditions for the 2nd-series of XPS studies.

entry	molecule	cleaving agent	temperature	time	concentration
<i>sample A</i>	Bp-Tpd-CN	none	50 °C	18 h	0.01 mM
<i>sample B</i>	Bp-Tpd-CN	NH ₃	25 °C	18 h	0.01 mM
<i>sample C</i>	Bp-Tpd-CN	NH ₃	25 °C	1h	0.01 mM
<i>sample D</i>	Bp-Tpd-CN	NEt ₃	25 °C	18h	0.01 mM

As indicated in Figure 44a, all attempts feature reasonably thinner layers compared to the results of **Bp-Tpd-CN** in the first study. The use of ammonia leads to the formation of the thickest layer, especially in sample B. Furthermore, an increased peak at ~164 eV is observed, suggesting that thiolate-bonding is not predominant. With shorter immersion times in ammonia-conditions, a significant amount of oxygen is still present. Conclusively, ammonia is not a suitable candidate for cleaving the thioacetate of our tripodal structures. Both samples A and D show promising characteristics in the Au 4f spectra, defined peaks in the C 1s spectra and small or almost no peaks in the oxygen XPS spectra. Concerning the S 2p spectra, however, immersing at elevated temperatures might form some oxidised sulfur species which is indicated by peaks >167 eV. Admittedly, it is difficult to validate whether these peaks are trustworthy or a result of a low resolution of the laboratory XPS. Nevertheless, for the following series, we chose the conditions of sample D as the best one.

**Figure 44.** XPS study of the 2nd series. XPS spectra of **Bp-Tpd-CN** of a) Au 4f, b) C 1s, c) O 1s and d) S 2p. The used conditions for these samples are listed in Table 7.

In the third series, we then applied the most promising conditions of the second series on **Ph-Tpd-CN**, **Bp-Tpd-CN** and **Tol-Tpd-CN**. By comparing the results of sample D of the second series with sample B of the third series, the reproducibility of our protocol is verified. Furthermore, in a control experiment, increasing the concentration (Table 8, sample D) promotes the formation of unbound or weakly bound material, as seen in Figure 45b. In general, all three molecules show reduced layer thickness when compared to the first series (compare Figure 43a and Figure 45a), indicating that the quality of the SAMs has been significantly improved by decreasing the concentration and by changing the cleaving agent. Furthermore, preliminary experiments show that for **Ph-Tpd-CN**, 77% of sulfur bonds correspond to thiolates. Unfortunately, for the extended platforms **Bp-Tpd-CN** and **Tol-Tpd-CN** thiolates prevail only 40% and 38%, respectively. Note, that these results are based on a low resolution XPS and should be considered tentatively. Therefore, high resolution XPS measurements are inevitable.

Table 8. Overview of the preparation conditions for the 3rd-series of XPS studies.

entry	molecule	cleaving agent	temperature	time	concentration
<i>sample A</i>	Ph-Tpd-CN	NEt ₃	25 °C	18 h	0.01 mM
<i>sample B</i>	Bp-Tpd-CN	NEt ₃	25 °C	18 h	0.01 mM
<i>sample C</i>	Tol-Tpd-CN	NEt ₃	25 °C	18 h	0.01 mM
<i>sample D</i>	Ph-Tpd-CN	NEt ₃	25 °C	18 h	0.1 mM

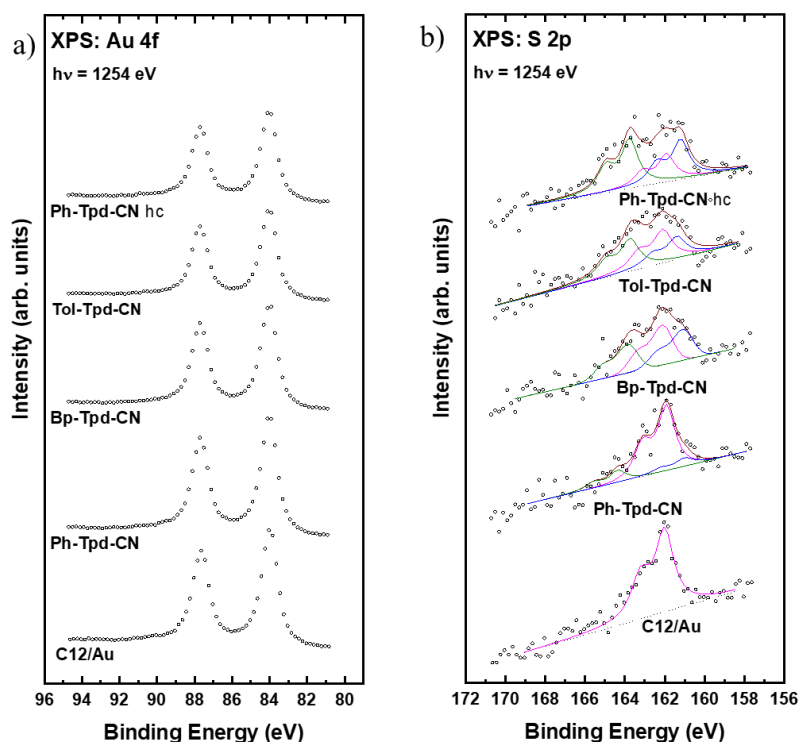


Figure 45. XPS study of 3rd series. XPS spectra of **Ph-Tpd-CN**, **Bp-Tpd-CN** and **Tol-Tpd-CN** and for higher concentration (hc) of **Ph-Tpd-CN** of a) Au 4f and b) S 2p.

We then verified the preliminary results of the third series with the HR-XPS at BESSY (Berlin) by reproducing the SAMs with the same preparation conditions mentioned in Table 8. The corresponding HR-XPS spectra of the model compounds **Ph-Tpd-CN**, **Bp-Tpd-CN** and **Tol-Tpd-CN** are displayed in Figure 46. To our delight, in all SAMs the typical Au 4f peaks at ~84 eV are present, indicating that monolayers are formed. The C 1s and N 1s spectra confirm that in all SAMs, the adsorbed molecules contain both aromatic carbons and nitriles. In the oxygen spectra, small peaks are observable, especially in the case of the two extended platforms. We assume that these peaks correspond to the residual thioacetates of the parental **Bp-Tpd-CN** and **Tol-Tpd-CN**, respectively. The existence of oxidised sulfur species can be excluded, because the corresponding signals are not observed in the S 2p spectra. Since there are still acetate masked thiols present in the monolayer, we consider that the extended platforms are not bound to the Au surface through all three anchoring groups. This assumption is further supported by the results gained from the S 2p spectra, as shown in Figure 46e. Upon fitting the characteristic peaks of atomic sulfur, physisorbed materials and thiolates to the data, it is calculated that

~60% of thiols are bound covalently to the surface for in smallest platform **Ph-Tpd-CN**, while ~31% of the peaks can be attributed to physisorbed species. Regarding the extended platforms **Bp-Tpd-CN** and **Tol-Tpd-CN**, only 35% and 34% of the peaks can be assigned to thiolates. For these two SAMs, the most prominent peak in the S 2p spectra is attributed to physisorbed material. Therefore, it is difficult to estimate the adsorption orientation of the model compounds. Noteworthy, the preliminary results of the third series fit well with the HR-XPS experiments.

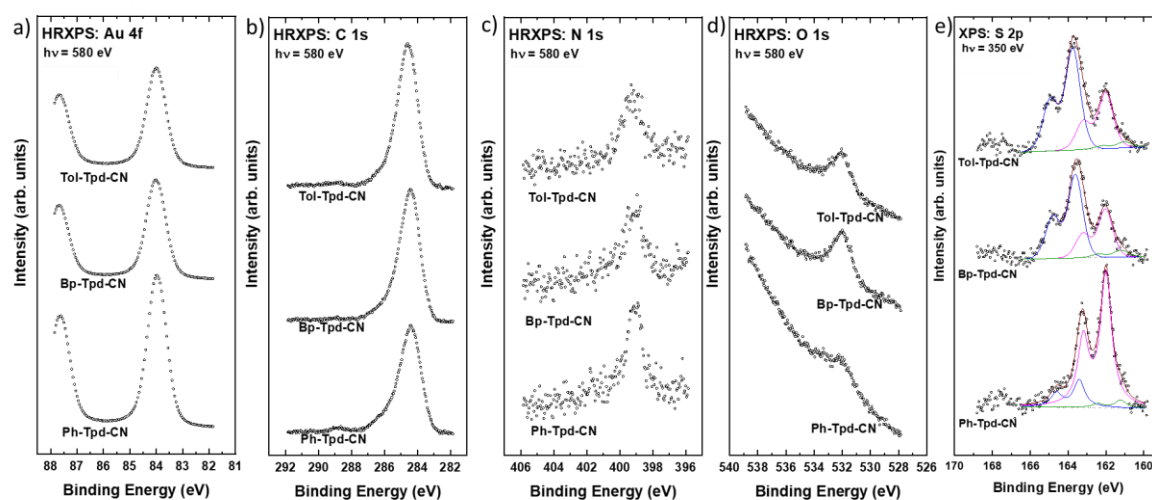


Figure 46. HR-XPS study of the 4th series of **Ph-Tpd-CN**, **Bp-Tpd-CN** and **Tol-Tpd-CN**. HR-XPS spectra of a) Au 4f, b) C 1s, c) N 1s, d) O 1s and e) of S 2p with calculated fits

For further studies, the preparation procedure needs to be improved in order to create SAMs with all anchoring groups covalently bound to the gold surface. The superiority of the smallest platform **Ph-Tpd-CN** might be due to its spatial geometry. Independent of the adsorption configuration, **Ph-Tpd-CN** roughly occupies the same cubic volume on the surface. If all adsorbed molecules are tilted during the formation of the SAM, they still have the space to find an upright orientation in the second step of the SAM formation. Therefore, this would allow the system a significant higher degree of freedom, compared to the extended platforms. In contrast to the smallest one, in **Bp-Tpd-CN** and **Tol-Tpd-CN** the adsorption geometry is highly dependent on the first contact. In a gedankenexperiment, in which we assume full coverage of the surface during the first step of SAM formation, flat lying or tilted extended platforms do not have enough space to transform into the upright orientation. Even if the upright orientation is thermodynamically favoured, there will not be enough space to bind the

third anchor to the surface as soon as the neighbouring molecule is too close. Therefore, the orientation is already determined during the first step of SAM formation and cannot be changed during the second step.

In the next series, we need to decrease the sample concentration to provide the individual molecule more space to find an upright orientation before a second molecule occupies the area. Another strategy to improve the quality of SAMs made from the extended platforms is by reducing the concentration of the cleaving agent. Furthermore, we will study the growth of the SAMs by means of *in situ* ellipsometry measurements. With that setup we can survey the growth rate and hence we might find the perfect conditions to prepare monolayers and prevent the formation of multilayers. To the best of our knowledge, the study of multident SAM growth is rarely discussed in the scientific community and hence these experiments could contribute to understand the mechanism of SAM formation with multiple anchors.

3.2.2.2 NEXAFS studies

Additional information about the SAMs of **Ph-Tpd-CN**, **Bp-Tpd-CN** and **Tol-Tpd-CN** were obtained by means of NEXAFS spectroscopy and the results are displayed in Figure 47. The data were measured using an X-ray with incident angle of 55°, which is called the “magic angle”. This particular setup represents the electronic structures of unoccupied orbitals excluding any orientation effects.^[341]

All three NEXAFS C-K-edge spectra (see Figure 47a-c) are dominated by the characteristic absorption structure of phenyl rings at ~285 eV (π_1^*).^[342] Comparing the peaks, the intensity clearly depends on the molecular legs of the tripodal foot structure. While for **Ph-Tpd-CN** and **Tol-Tpd-CN** the intensity is located at close to 3 A.U, the signal of biphenyl containing **Bp-Tpd-CN** is increased, which is in agreement with other observations of biphenyl containing molecules.^[342] Furthermore, the spectra of **Bp-Tpd-CN** exhibit the π^* resonance of the nitrile group at ~287 eV, whereas they are hidden in the other two spectra.^[340]

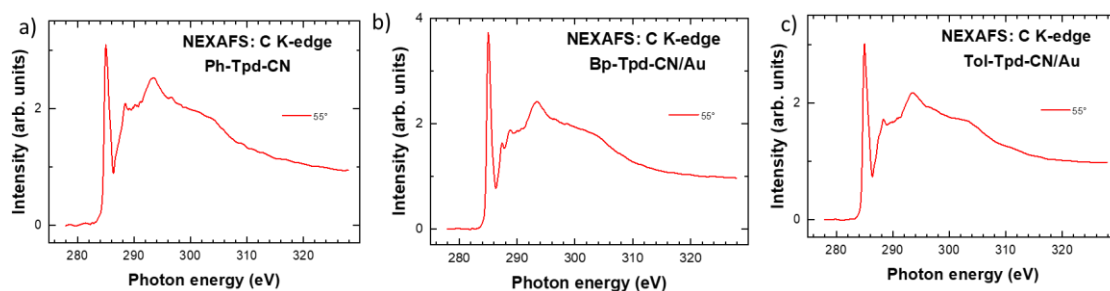


Figure 47. C-K-edge NEXAFS spectra of a) **Ph-Tpd-CN**, b) **Bp-Tpd-CN** and c) **Tol-Tpd-CN**. Data were obtained at an X-ray angle of 55°.

In contrast to the C K-edge NEXAFS spectra, the nitrile moiety is discernible in the N K-edge NEXAFS spectra, as shown in Figure 48. This underlines that the monolayers comprise the featured series of **Ph-Tpd-CN**, **Bp-Tpd-CN** and **Tol-Tpd-CN**. The specific double resonance of benzonitrile at ~399 eV and ~400 eV are dominating the spectra which is in agreement with previously reported benzonitrile terminated SAMs.^[340,343] The double resonance originates from the conjugation between π^* -orbitals of the nitrile group and adjacent phenyl ring.^[344] One orbital (π_1^* , ~399 eV) is then oriented normal to the phenyl ring's plane and the other one becomes (π_2^* , ~400 eV) oriented parallel to the plane of the adjacent phenyl ring.^[345]

The difference between the NEXAFS spectra of the normal angle (90°) and the NEXAFS spectra obtained from the grazing (20°) incident angle are shown in Figure 48 (at the bottom). These data give information about the orientations of the CN-groups within the SAMs. The intensity of the resonance strongly depends on the orientation and reaches its maximum if the orientation of the electric field vector matches with the transition dipole moment of the molecule.^[341] On the contrary, it becomes zero when it is normal to the transition dipole moment. Given the structure of **Ph-Tpd-CN**, **Bp-Tpd-CN** and **Tol-Tpd-CN**, we expect an upright orientation of the benzonitrile if the molecules are anchored through all three thiols. Hence, positive signals in the difference-spectra indicate upright orientations, whereas negative signals suggest down tilt. To our delight, all three tripodal platforms exhibit positive signals, meaning that the nitrile group is pointing to the ambient. Given the fact that the thiolate bonds are not the dominant ones, especially in the case of the extended platform, it is highly unlikely that the tilt angle is close to 90°. Moreover, the signal to noise ratio in this spectrum cannot be neglected disqualifying authentic statements.

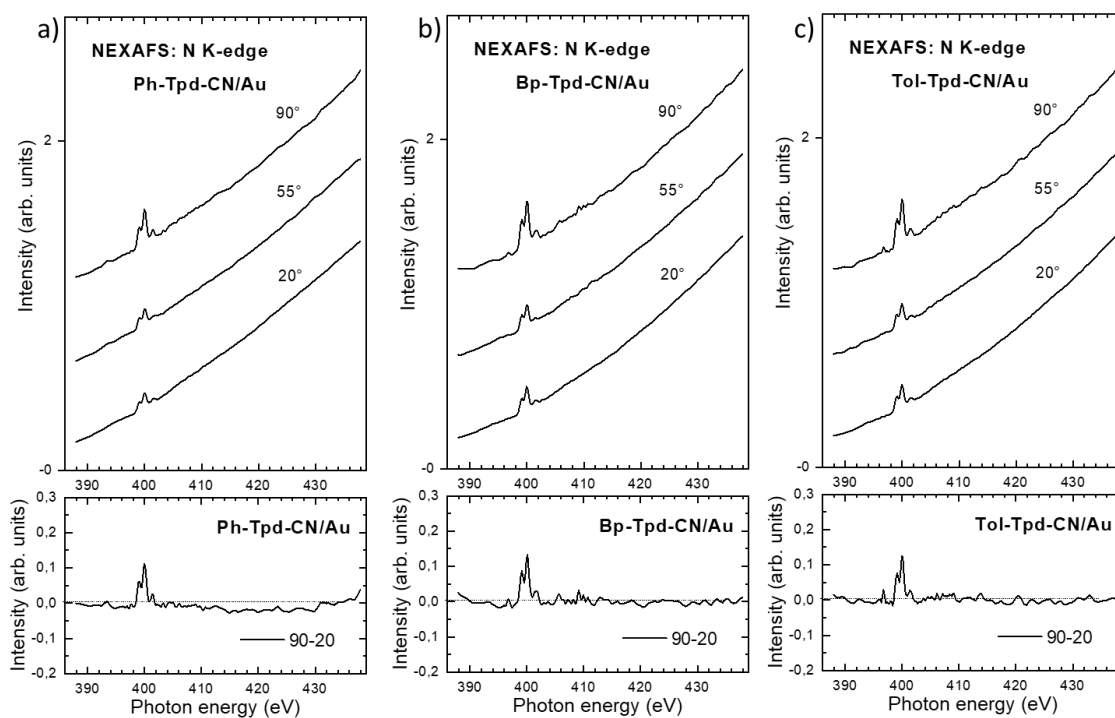


Figure 48. Top: N K-edge NEXAFS spectra at different X-ray incident angles of a) **Ph-Tpd-CN**, b) **Bp-Tpd-CN** and c) **Tol-Tpd-CN** Bottom: Difference N-K-edge NEXAFS spectra of a) **Ph-Tpd-CN**, b) **Bp-Tpd-CN** and c) **Tol-Tpd-CN**.

3.2.3 Model Compounds for STM studies

In order to improve the eligibility of the extended tripodal platforms **Bp-Tpd** and **Tol-Tpd**, the understanding of the surface behaviour of these extended platforms is required. To facilitate the study of the characteristics of the underlying foot geometry by means of STM, it is beneficial to reduce the complexity of the molecules. As shown in Figure 49, we designed two fully symmetrical compounds. By coupling either boronic ester **27** or phenylacetylene **29** to a *para*-substituted tetraphenylmethane, we obtained the two model compounds. In contrary to the parental tripods **Bp-Tpd** and **Tol-Tpd**, we replaced the acetylene linker with an additional fourth leg. With this symmetrical approach, we aimed to minimise the possible configurations on the surface, as each configuration leads to the same adsorption geometry. With this approach, we gain information about the binding configuration of the platform. Hence, these symmetrical model compounds allow a simplified study of the corresponding foot structures.

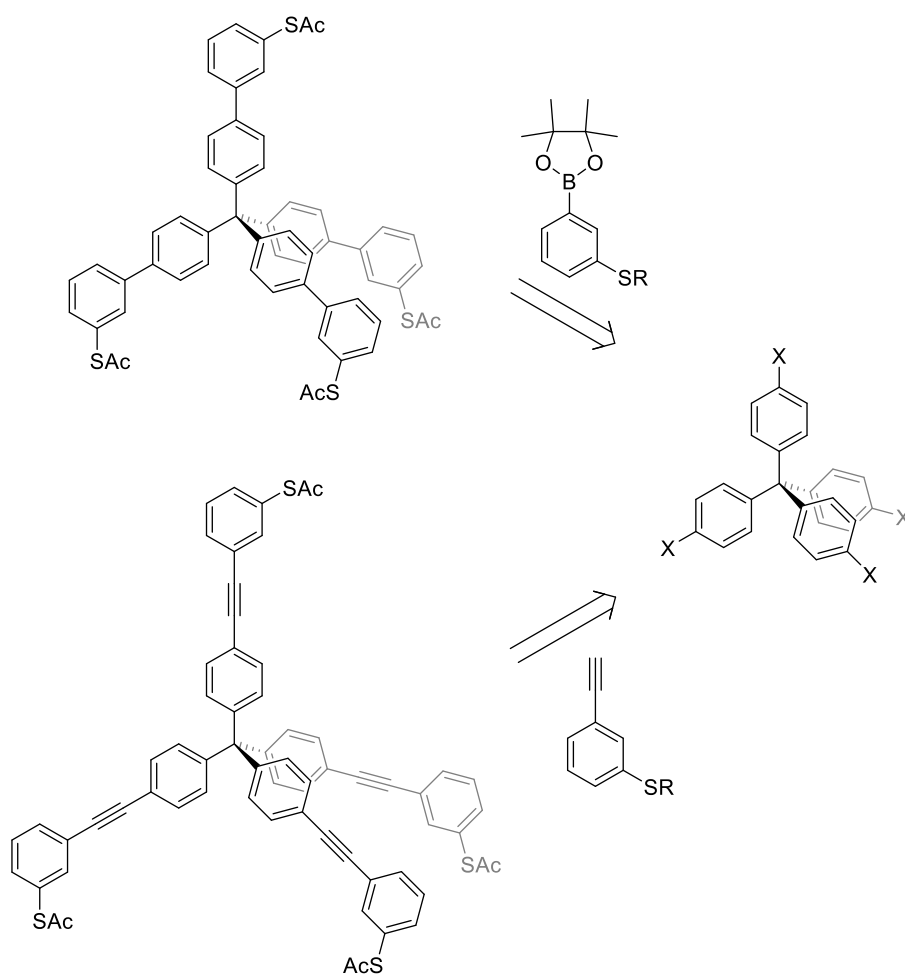
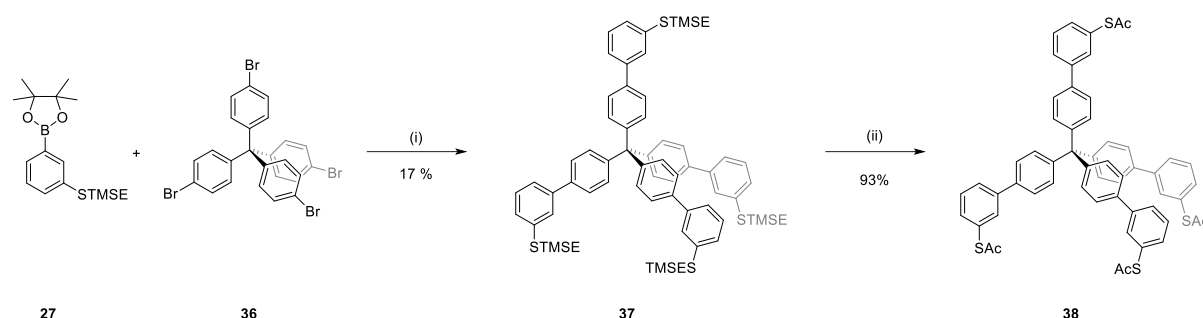


Figure 49. Retrosynthetic analysis of two fully symmetrical model compounds.

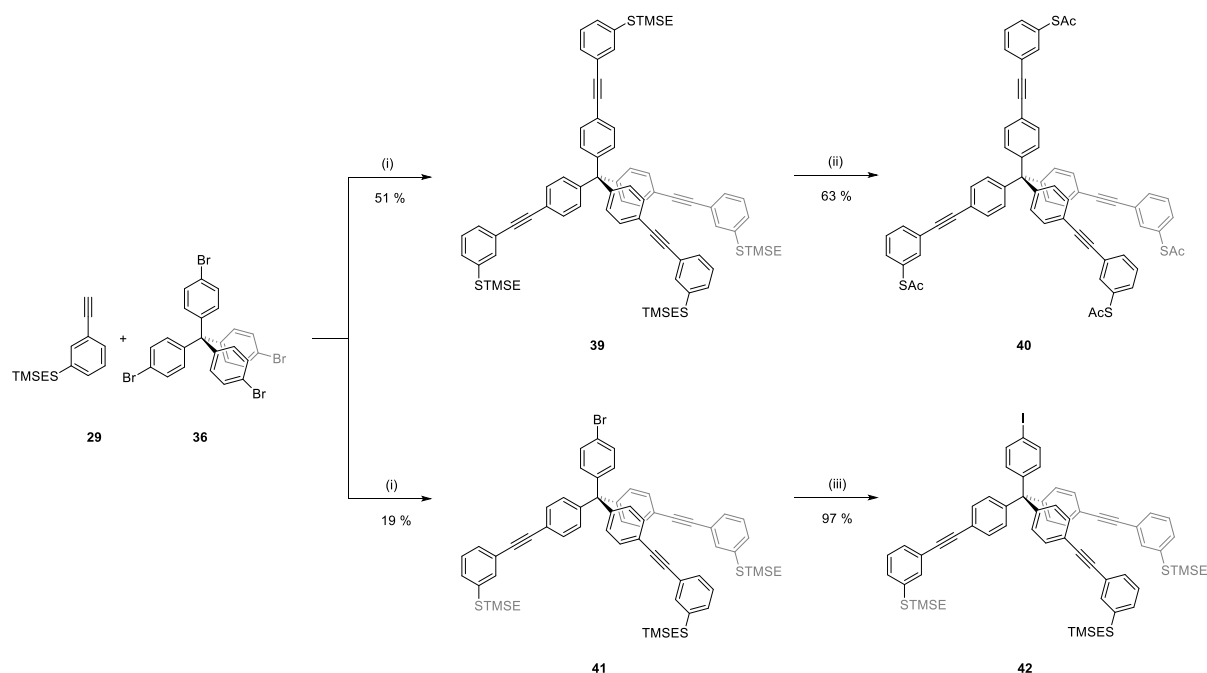
3.2.3.1 Synthesis

The synthesis of fully symmetrical model compound **38** started with the Suzuki reaction between the boronic ester **27** and tetrakis(*para*-bromophenyl)methane **36** and provided the desired compound **37** in 17% yield. The final transprotection step, gave the desired model compound **38** in high yield.



Scheme 19. Synthetic approach to compound **38**. Reaction conditions: i) Pd(dppf)Cl₂, K₂CO₃, THF/H₂O; ii) AcCl, AgBF₄, DCM.

The synthesis of the extended tolane-based model compound **40** started with Sonogashira reaction between the phenylacetylene **29** and compound **36** and afforded the symmetrical model compound **40** in moderate yield. Moreover, we were able to isolate the triple reacted tolane-based platform **41** of the Sonogashira reaction, as shown in Scheme 20. This molecule might be interesting as an additional extended platform. To increase its reactivity for cross-coupling reactions, we are interested in its iodinated form **42**. Hence, we tried to slightly modify the approach by replacing the starting compound **36** with tetrakis-(*para*-iodophenyl)methane. Unfortunately, the iodinated tetraphenyl compound was almost insoluble and thus side reactions such as the Glaser coupling of the triple bond were much faster than the desired Sonogashira reaction. In order to prepare the iodinated species **42**, we therefore applied the copper(I) catalysed aromatic Finkelstein reaction for the halogen exchange of tripod **41** to the iodinated tripod **42** in almost quantitative yield.^[346] Noteworthy, the reaction was carried out under microwave radiation because the published conditions were not sufficient to provide the desired product.



Scheme 20. Synthetic approach to compounds **40** and **42**. Reaction conditions: i) $\text{PdCl}_2(\text{dppf})$, K_2CO_3 , THF/ H_2O ; ii) AcCl , AgBF_4 , DCM; iii) CuI , NaI , 1,2-diaminocyclohexane, dioxane, microwave

3.2.3.2 Performance of the Model Compounds **38** and **40** in STM-studies¹

After successful isolation of the fully symmetrical model compound **40** bearing four tolane legs, the molecules were dissolved in DCM and subsequently deposited on Au(111). At low temperatures (5 K), the molecules were characterised in our homebuilt STM setup. As seen in Figure 50a, deposition of molecules **40** leads to islands with long-range order. The presence of islands with a high degree of order indicates that the adsorption geometries of the molecules resemble. We assume that the yellow “blob” in Figure 50b represents a single molecule of the symmetrical compound **40**. With a diameter of ~ 3 nm, this blob is slightly bigger than the calculated value of the tolane-platform, but still within a reasonable size range. Furthermore, the appearance as a round object without distinguishable states indicates that molecule is not rotating around any newly formed pivot point but rather rotates around an intramolecular axis. This assumes that the single molecule is bound to the surface through three anchors. The hypothesis is further fortified by the close-range adsorption configuration visualised in Figure

¹ STM-measurements were conducted by Julian Skolaut and analysed by Julian Skolaut, Dr. Lukas Gerhard and Prof. Dr. Wulf Wulfhekel

50c. It seems that the predominant order comprises pairs of molecules. The proposed adsorption configuration is illustrated by the superposition of two molecules **40** in Figure 50c. The pairing of the two molecules might be a result of affecting interactions between the two protruding head groups. The possibility to use these molecules as a “molecular graph paper” is currently under investigation.^[180] In general, the presence of both long-range order and individual molecules makes the tolane-based platform a promising candidate for the spraying technique and hence a fertile platform to carry the perpendicular functionality.

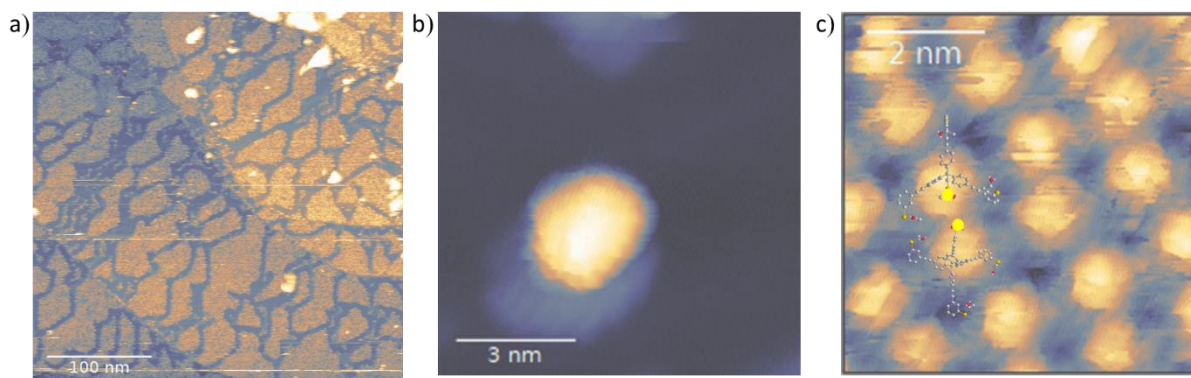


Figure 50. STM-images of molecule **40** show a) ordered islands (sample bias: 2.2 V, tunnelling current 10 pA), b) single molecule (sample bias: 2 V, tunnelling current 8 pA) and c) superimposed pairwise configuration with the acetyl groups pointing towards each other (Sample bias: 1.5 V, tunnelling current 6 pA).

The surface behaviour of the biphenyl model compound **38** is currently under investigation by means of our home-built UHV-STM.

3.2.4 Conclusion of the second-generation platforms

To conclude, the second-generation tripods **Bp-Tpd** and **Tol-Tpd** were designed, synthesised and their surface behaviour on gold has been studied. The molecular footprint of the first-generation tripod was enlarged, leading to an increased mechanical stability of the platform. In general, a library of three tripodal anchors with a terminal alkyne moiety for further functionalisation has been developed and successfully isolated, as illustrated in Figure 51.

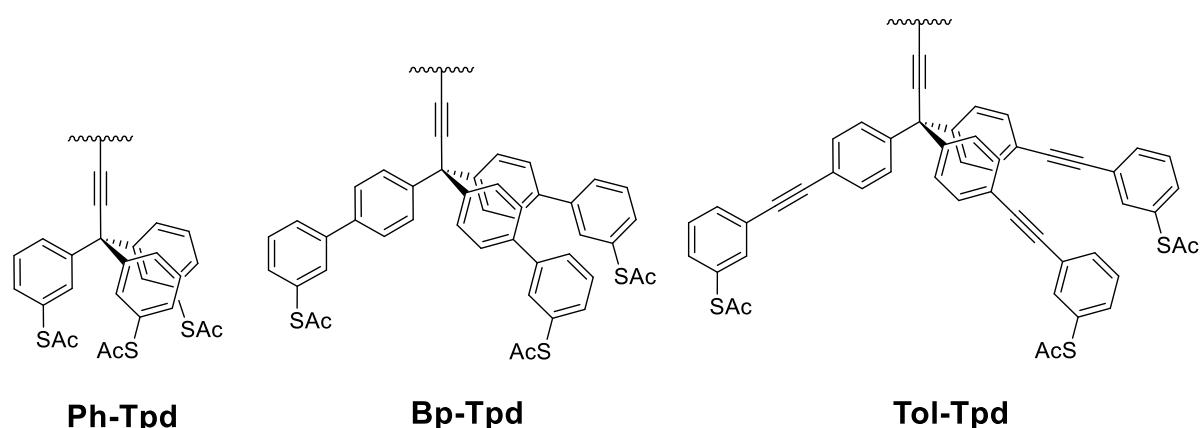


Figure 51. Library of the available tripodal platforms.

The synthesis of the crucial precursor **21** was more troublesome than expected. We therefore investigated the two consecutive synthetic steps and optimised them individually. As a result, the yield of **21** was increased to 35%. After establishing the modular key precursor **21**, we synthesised the second-generation platforms **28** and **31**.

To spectroscopically study the molecular orientation of these newly designed tripods in the SAM, the platforms **6**, **28** and **31** were coupled with *para*-iodobenzonitrile. Presence of sp-hybridised nitrogen at the terminal position enabled us to measure the orientation of such platforms with respect to the surface by means of NEXAFS. For these measurements, an optimised protocol for the formation of self-assembled monolayers of **Ph-Tpd-CN**, **Bp-Tpd-CN** and **Tol-Tpd-CN** has been developed. Unfortunately, the HR-XPS measurements did not confirm the anchoring through all three thiolates. Hence, the preparation method requires further improvement to enhance the quality of ordered SAMs. By comparing the two extended platforms, it is difficult to favour one over the other, since the surface behaviour is quite similar. To study the surface behaviour of single molecules of the extended tripodal platforms, we

designed and synthesised the fully symmetrical model compounds **38** and **40**. STM experiments prevailed a long-range order of the tolane based model compound **40** on gold. This indicates that the molecules adsorb in a structured manner. Moreover, single molecules could be observed with a diameter close to the calculated one. These findings make the tolane based architectures **Tol-Tpd** predestined tripodal platform for the functional units presented in Chapter 3.1.

3.3 “Tripodal Functionalised Molecules”

This chapter focuses on the design and synthesis of the second-generation molecular devices. With the combined results of the previous Chapter 3.2, we selected the tolane-based platform **31** as the tripod of choice for its further functionalisation *via* Sonogashira cross-coupling protocol.

The first part of this chapter describes the design, synthesis and deposition on Au(111) of molecular rotors and the subsequent study of their electrical induced rotation by means of the STM-tip. As shown in Figure 52, a “Geländer-type” prochiral rotator is mounted on the tripodal platform **31**.

The second part then focuses on the synthesis of the second-generation tripodal emitters based on the chromophores **nNDI** and **sNDI**, which are already introduced in the previous Chapter 3.1.4. After deposition on the Au(111), the surface behaviour of the second-generation tripodal chromophores as well as their light emission properties as single molecule emitters have been studied.

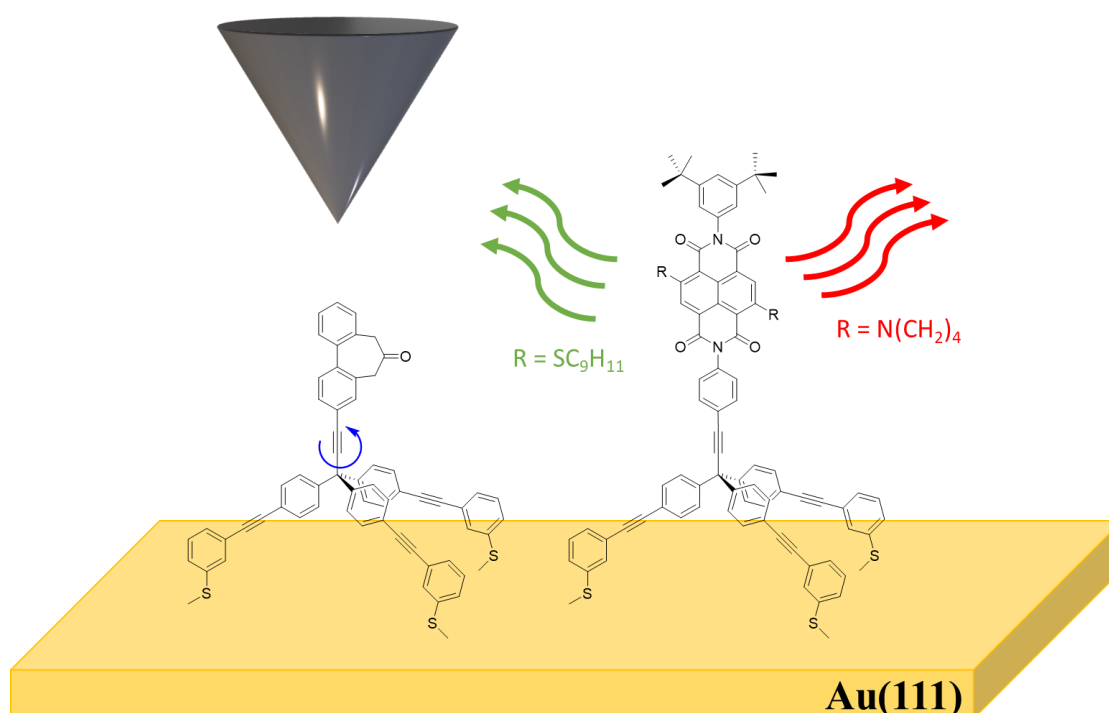


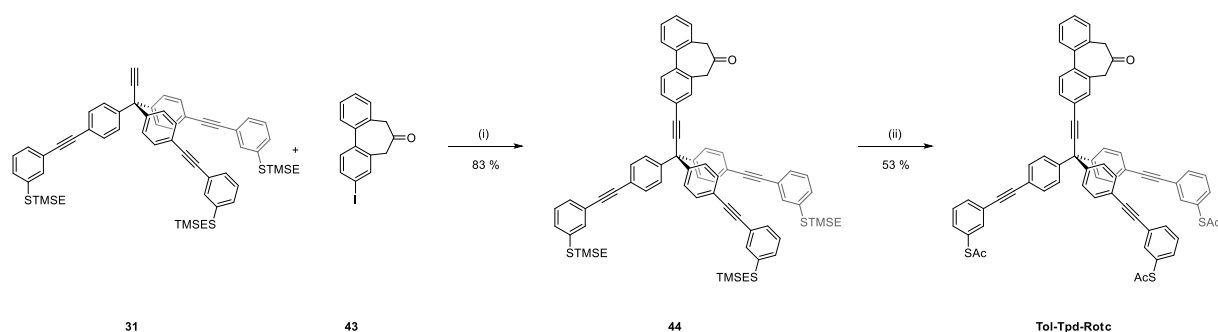
Figure 52. Target structures **Tol-Tpd-Rot_C** and **NDI** mounted on the **Tol-Tpd** platform. The STM tip (black) induces rotation of the molecular rotor **Tol-Tpd-Rot_C**

3.3.1 “Geländer-Type” Rotors

3.3.1.1 Design and Synthesis of “Geländer-Type” Rotors

The synthetic strategy toward the pro-helical tripodal scaffold **Tol-Tpd-Rot_C** is outlined in Scheme 21. The “Geländer-type” rotator **43** was synthesised by Dr. Jan Lukášek and the synthetic approach is outlined in Figure S 1. The design of this rotator is based on the so-called “Geländer”-molecules in which a (chiral) helix wraps around a biphenyl moiety. At low temperatures (5 K), the activation barriers of 2,2’-(propane-1,3-diyl)-bridged biphenyls atropisomers were found to range from 45 kJ/mol to 55 kJ/mol, which equals 466-570 meV.^[312] Compared to the thermal energy at 5 K ($k_bT = 0.42 \text{ meV} \approx 0.04 \text{ kJ/mol}$), these architectures should provide stable helical structures and hence should be suitable candidates for surface studies of single-molecule helical scaffolds. If higher atropisomerisation energy barrier is required, prolongation of the alkyl-bridge by one methylene unit would increase the barrier to some extent.^[347]

Initially, 2,2’-alkyl-bridged biphenyl (see, Figure S 1, **S6**.) was planned to serve as the first helical rotator. However, in our preliminary experiments, it turned out that its precursor – that is the 2,2’-ketone-bridged biphenyl – is easier to track by means of STM. Therefore, we did not reduce the ketone to the alkyl moiety, but mounted compound **43** directly on the tripodal platform **31** *via* Sonogashira protocol in 83% yield (see Scheme 21). Following the standard transprotection method, the thioacetate protected **Tol-Tpd-Rot_C** was isolated in 53% yield.



Scheme 21. Synthetic approach for molecule **Tol-Tpd-Rot_C**. Reaction conditions: i) CuI, Pd(PPh₃)₄, NEt₃; ii) AcCl, AgBF₄, DCM.

3.3.1.2 Performance of the Geländer-Type Rotor¹

After the successful synthesis of **Tol-Tpd-Rotc**, the molecules were dissolved in DCM and subsequently deposited on Au(111) with the standard procedure as described in previous chapters. On the surface, the molecules adsorb both in ordered islands and as isolated single molecules, as shown in Figure 53a. The presence of ordered structures indicates that the adsorption configurations of neighboring molecules resemble. Therefore, we assume most of the molecules are either lying flat or standing upright. With a diameter of ~2.6 nm of the bright blobs, as indicated in Figure 53b, the size of the molecule is within the expected range, but we cannot verify the molecular orientation since both adsorption configurations (upright or flat) result in similar diameters. The blob's round shape suggests that the molecule rotates and does not permanently remain in one state. Due to the absence of distinguishable states as we observed for **Ph-Tpd-Rotc** (see Figure 28c), we exclude the rotation around one single Au-S bond. Therefore, the rotator moves along an internal axle, which is either the triple bond of the linker or one of the molecular legs.

By means of STM measurements, we are able to track three different rotational states. When the tip is placed over the off-centre of the molecule, the observed tunnelling current depends on the headgroups' states. As shown in Figure 53c, three distinguishable states A, B and C are observed. Given the architecture of this foot geometry and rotator, in a ratchet like energy landscape, three individual states are to be expected. Over a period of 10 minutes, 204 switching processes can be observed. Almost 60% of these switches stem from the switching from state A over B to C, while ~40% rotate in the opposite direction. This ratio of ~ 3:2 with one direction dominating over the other suggests, that the motion is not random but rather governed by internal features. However, we are neither able to identify the single states by topography nor able to assign the three states to individual configuration states. Additionally, the observation of different states was not reproducible throughout this sample.

¹ STM-measurements were conducted by Julian Skolaut and analysed by Julian Skolaut, Dr. Lukas Gerhard and Prof. Dr. Wulf Wulfhekel

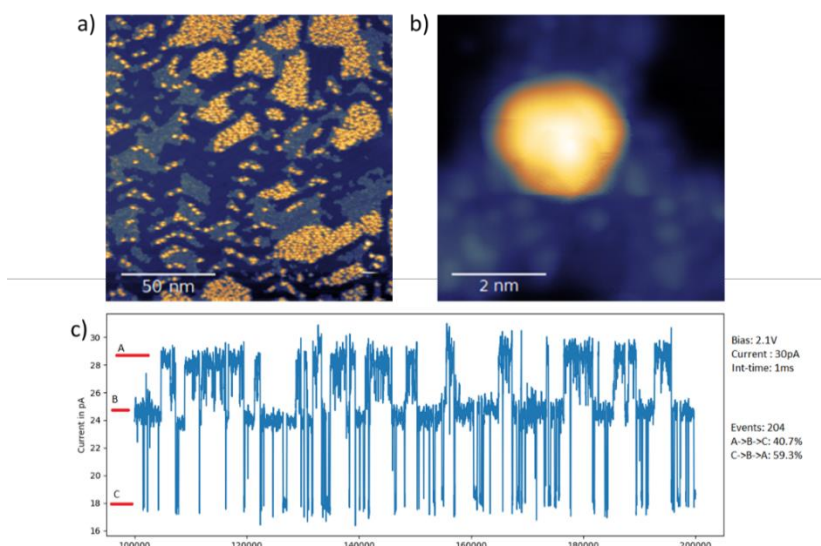


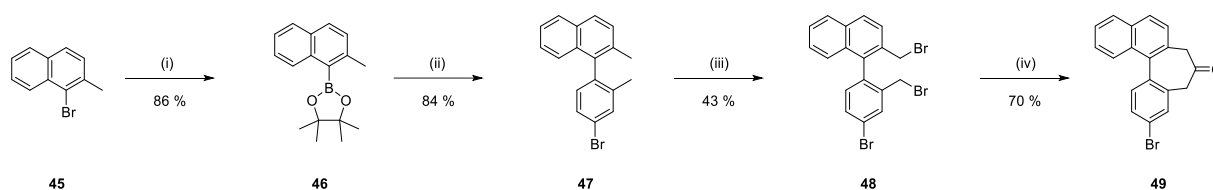
Figure 53. Topography map of a) ordered islands of **Tol-Tpd-Rot_C** (sample bias: 1.5 V, tunnelling current 30 pA); b) single molecules of **Tol-Tpd-Rot_C** (sample bias: 1.5 V, tunnelling current 30 pA); c) long-time current measurement with three rotational states A, B, and C.

Based on the results presented above, we thus have first evidence that such molecules rotate in a preferential direction. Yet, we do not know whether the molecule rotates around the triple bond linker or around one of the molecular legs. Therefore, we cannot claim with certainty whether the molecular is anchored *via* all three legs or not. To conclude, the design of the rotator must be adjusted so that we can recognise the rotational states by means of the STM.

3.3.1.3 Design and Synthesis of an Extended Chiral Rotor **Tol-Tpd-Rot_C**

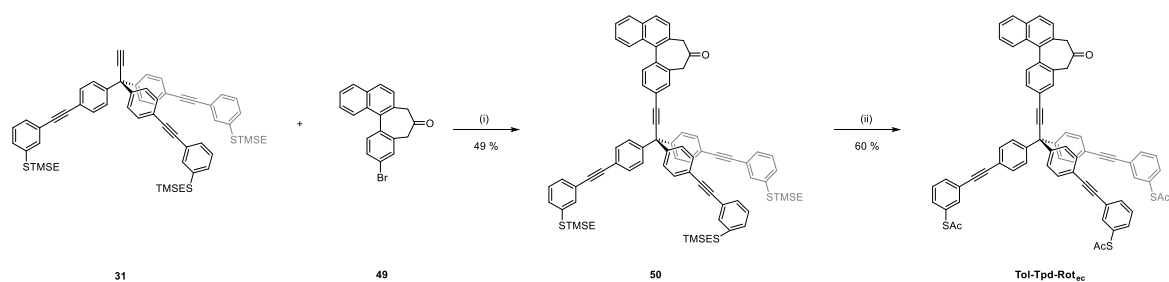
Due to the difficulty of distinguishing between different states of the rotating unit, we extended the headgroup of the molecular rotor. With this approach, we aimed to extend the rotator by an additional phenyl ring, so that it becomes easier for the experimental physicists to observe defined states of the rotator by means of the STM. Therefore, the new headgroup retained the biphenyl part which is linked in the 2,2' positions with propan-2-on-1,3-diyl, whereas the top phenyl part was extended to a naphthyl group. The synthetic approach of the proposed rotator **49** is shown in Scheme 22. Here, we chose a different strategy compared to the synthesis of molecule **43**. The Miyaura borylation of the commercially available 1-bromo-2-

methylnaphthalene **45** provided the corresponding boronic ester **46** in high yield.^[348] The Suzuki reaction of the boronic ester **46** with 2-methyl-4-bromo-iodobenzene gave the strained compound **47** in a high yield. Inspired by a similar bromination strategy,^[349] in a radical reaction with *N*-bromosuccinimide (NBS) as the bromination reagent and AIBN as a free-radical initiator, “benzylic bromination” of two methyl groups in the positions 2,2’ of **47** provided the compound **48** in 43% yield. In this radical reaction, acetonitrile was chosen as solvent and the temperature of 95 °C provided the highest yield. Noteworthy, it is important to check the reaction progress *via* GC-MS in order to find the right balance between monobromination, formation of the desired product **48** and over-bromination. To achieve the propan-2-on-1,3-diyl bridge in **49**, an additional carbon atom was introduced by an intramolecular cyclization reaction of the tribromide **48** using *para*-tosylmethyl isocyanide (TosMIC). Under base-mediated PTC reaction conditions utilising TBAB as the phase catalyst, the desired cyclic ketone **49** was isolated in 70% yield.



Scheme 22. Synthetic approach to compound **49**. Reaction conditions i) bis(pinacolato)diboron, Pd(PPh₃)₂Cl₂, DMF; ii) 2-methyl-4-bromo-iodobenzene, Pd(PPh₃)₄, Cs₂CO₃, DMF; iii) NBS, AIBN, MeCN; iv) a) TBAB, NaOH, TosMIC, H₂O/DCM; b) HCl, H₂O/DCM.

After isolation of the rotator **49**, we then mounted it onto the extended tripodal platform **31** *via* Sonogashira reaction. For this cross-coupling reaction, THF was needed as a co-solvent due the poor solubility of the compound **49** in neat amines. Subsequent, transprotection of **50** gave the desired extended, pro-helical molecular rotor **Tol-Tpd-Rot_{ec}** with a yield of 29% over the final two steps.



Scheme 23. Synthetic approach to molecule **Tol-Tpd-Rot_{ec}**. Reaction conditions: i) Pd(PPh₃)₄, CuI, NEt₃, THF; ii) AcCl, AgBF₄, DCM.

3.3.1.4 Performance of Tol-Tpd-Rot_{ec}¹

With our spraying technique, **Tol-Tpd-Rot_{ec}** was deposited on the Au(111) surface. As presented in Figure 54, the molecules do not show long range order. Hence, we assume that the molecules do not have a uniform adsorption geometry and therefore various adsorption configurations are present. Interestingly, by extending the outmost phenyl group to a naphthyl group, the adsorption behaviour of these tripodal rotors changes significantly. It seems that in its extended version, the increased energy gain by the π interactions between the rotator and the surface hinders the molecules to align in an upright orientation.

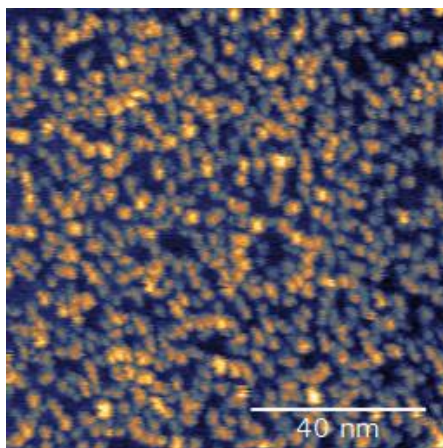
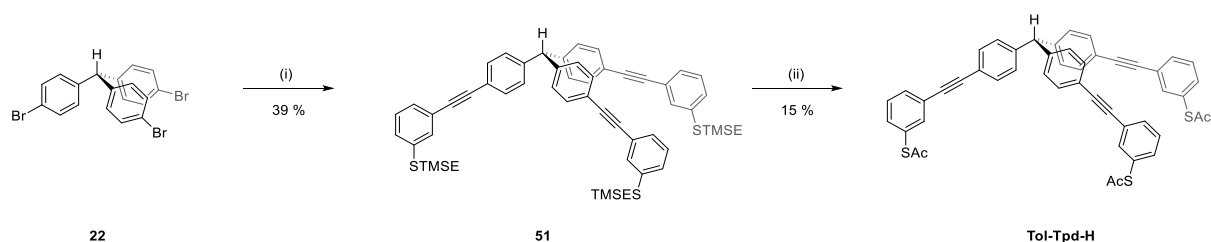


Figure 54. Topography map of unordered islands of **Tol-Tpd-Rot_{ec}**. Sample bias: 1.5 V, tunnelling current 30 pA.

¹ STM-measurements were conducted by Julian Skolaut and analysed by Julian Skolaut, Dr. Lukas Gerhard and Prof. Dr. Wulf Wulfhekel

3.3.1.5 Mixed Deposition of Foot Structure and the Molecular Rotor¹

Assuming that the interaction between the π -system of the molecular rotor **Tol-Tpd-Rot_c** and the gold surface is stronger than the triple binding of the molecular foot structure, we tried a different approach of surface decoration by creating mixed layers of the molecular rotor **Tol-Tpd-Rot_c** and a newly designed, non-functionalised foot structure. As the parental tripod **Tol-Tpd** contains a free triple bond, it is highly likely that it undergoes unwanted side reaction on the gold surface.^[350–352] Therefore, we used the tris(*para*-bromophenyl)methane **22** which was isolated as a side product during the preparation of the tripodal platforms **28** and **31**. In a triple Sonogashira reaction, we coupled phenyl acetylene **29** with the triphenylmethane scaffold **22** in neat triethylamine. After that, transprotection of the TMS-ethyl protected thiols to the corresponding thioacetates gave the target molecule **Tol-Tpd-H** in 15% yield.



Scheme 24. Synthetic approach to **Tol-Tpd-H**. Reaction conditions: i) **29**, Pd(PPh₃)₄, CuI, NEt₃; ii) AcCl, AgBF₄, DCM.

Bearing only a proton and three tolane legs on the sp³-carbon, this molecule should be more suitable for this experiment than platform **31**.

As shown in Figure 55a, molecules of **Tol-Tpd-H** form well-ordered islands. They are closely packed, suggesting that the adsorption configuration is similar throughout all molecules. The apparent height and the diameters of these molecules are in accordance with the estimated values and more importantly, the inner structures of individual molecules barely differ. Superimposing the molecular structures onto the image (see Figure 55b), it seems that the molecules arrange themselves in a gearwheel-like order. In this configuration, each molecular leg points towards the bay region formed by three neighbouring molecules. Comparing the

¹ STM-measurements were conducted by Julian Skolaut and analysed by Julian Skolaut, Dr. Lukas Gerhard and Prof. Dr. Wulf Wulfhekel

surface decorated with **Tol-Tpd-H** (Figure 55a) and the surface decorated with **Tol-Tpd-Rot_c** (Figure 55c) we have found that the lattice parameters are almost the same. Furthermore, we measured different apparent height profiles for the different types of molecules while observing the same diameters of the molecular footprint. We therefore believe that molecules are standing upright.

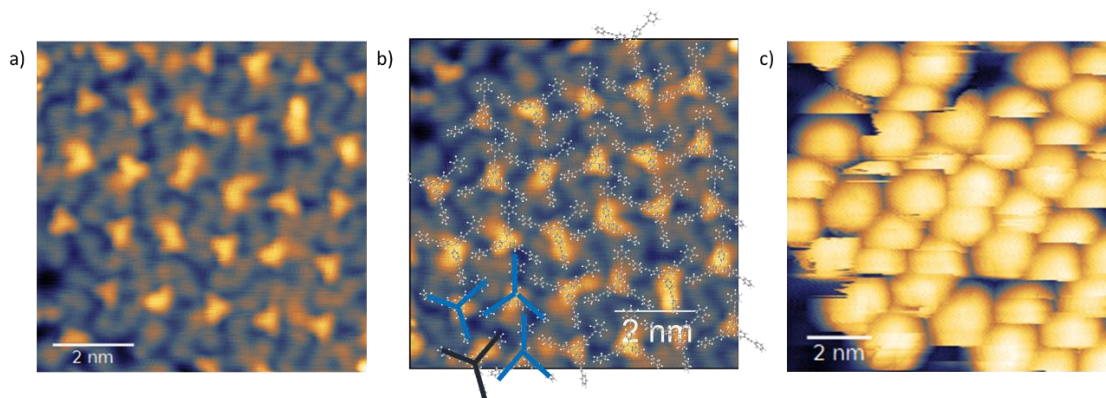


Figure 55. Topography map of a) ordered islands of **Tol-Tpd-H** (sample bias: 1.5 V, tunnelling current 50 pA); b) superimposed molecules of **Tol-Tpd-H** and the molecular leg (black) pointing towards the bay area created by three neighbouring molecules (blue); c) ordered islands of **Tol-Tpd-Rot_c** (sample bias: 1.5 V, tunnelling current 10 pA)

In the next step, we then deposited the rotor **Tol-Tpd-Rot_c** and the non-functionalised platform **Tol-Tpd-H** onto the surface with the standard spraying technique. The ratio was set to be 1:3 between the rotor and the dummy compound. To our delight, **Tol-Tpd-Rot_c** is incorporated into the ordered islands of **Tol-Tpd-H** as shown in Figure 56. The two structures are evidently distinguishable by their topography. This further strengthens the assumption that both molecules adsorb *via* all three thiols, while the functional head group is perpendicular to the gold surface. Based on the results of this experiment, we are sure that we have successfully designed and synthesised a tripodal platform which can provide upright-orientated functional units.

In our future work, we will apply this method to the extended chiral platforms **Tol-Tpd-Rot_c** and aim to confirm and reproduce the increased quality of such mixed self-assembled monolayers.

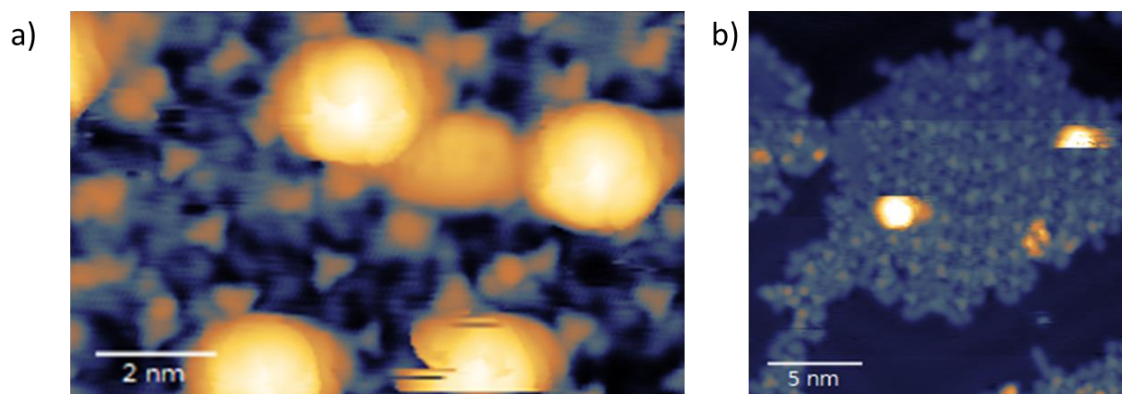


Figure 56. Topography map of ordered islands of the co-deposition of **Tol-Tpd-H** and **Tol-Tpd-Rotc** in different scales. a) sample bias: 0.7 V, tunnelling current 20 pA and b) sample bias: 1.5 V, tunnelling current 30 pA.

After the confirmation of an upright orientation, we then focused on the rotational behaviour of **Tol-Tpd-Rotc** embedded in ordered islands of **Tol-Tpd-H**. In a first experiment, on a fixed position over the off-centre of the molecule, we applied a positive bias (2 V) and recorded the corresponding tunnelling current at a fixed tip-sample distance. The results are shown in Figure 57. Over a period of 20 minutes, we have observed 1514 different switching motions of which 690 rotate in the $A \rightarrow B \rightarrow C$ direction, while 824 switches rotate oppositely. Furthermore, we have identified 24 full rotations of the $A \rightarrow B \rightarrow C \rightarrow A$ system and 69 full rotations in the opposite direction. This results in a ratio of almost 24:69 suggesting that the $C \rightarrow B \rightarrow A$ direction is favoured over the other under these conditions. Compared to **Tol-Tpd-Rotc** which was not embedded in ordered islands, these experiments are reproducible over the vast majority of the single molecules.

In the next experiment, we then applied negative bias (-1.9 V) and recorded again the corresponding tunnelling current. In negative bias, we observe 22 rotations of the $A \rightarrow B \rightarrow C$ system and 9 for the $C \rightarrow B \rightarrow A$ direction. Hence, we have found that the $A \rightarrow B \rightarrow C$ direction is predominant with a ratio of 22:9. In both experiments, a ratio of around 7:3 is observed, which clearly suggests that one of the directions is favoured independent of the applied bias. Currently we are investigating the involved states. As the distinction cannot be deduced by visualised different orientations of the headgroup, we are currently trying to link the states of the positive bias to the states we observe in the negative bias.

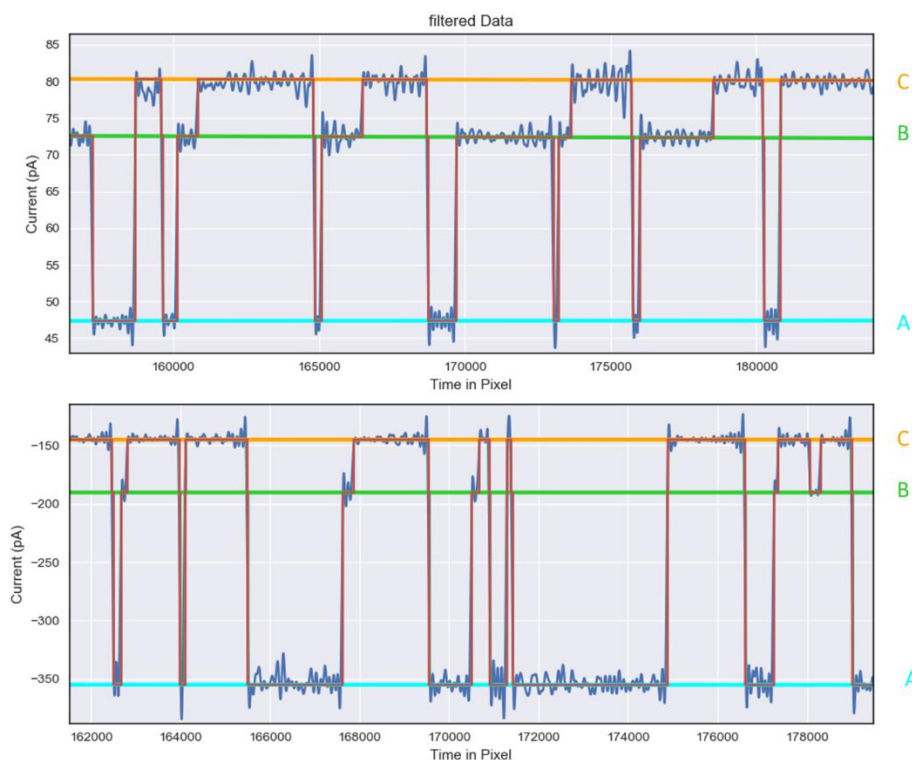


Figure 57. Long-time current measurement with $U > 0$ V (top) and $U < 0$ V (bottom)

If we assume that the assigned states A, B and C correlate in both experiments, this would mean that we could manipulate the directionality of the rotors by applying opposite biases. However, it is speculative to discuss the origin of the observed favoured directionality without being able to assign the three states with certainty. Hence, we are not able to link the rotational behaviour to either the CISS effect or a foot structure implied energy ratchet landscape. Therefore, a new design of the rotator must be developed. However, with the findings of Chapter 3.3.1.4, it is not trivial to design a rotator that is still perpendicular to the surface while having an enlarged structure. There future experiments will focus on the design to enable easily distinguishable states of the rotations.

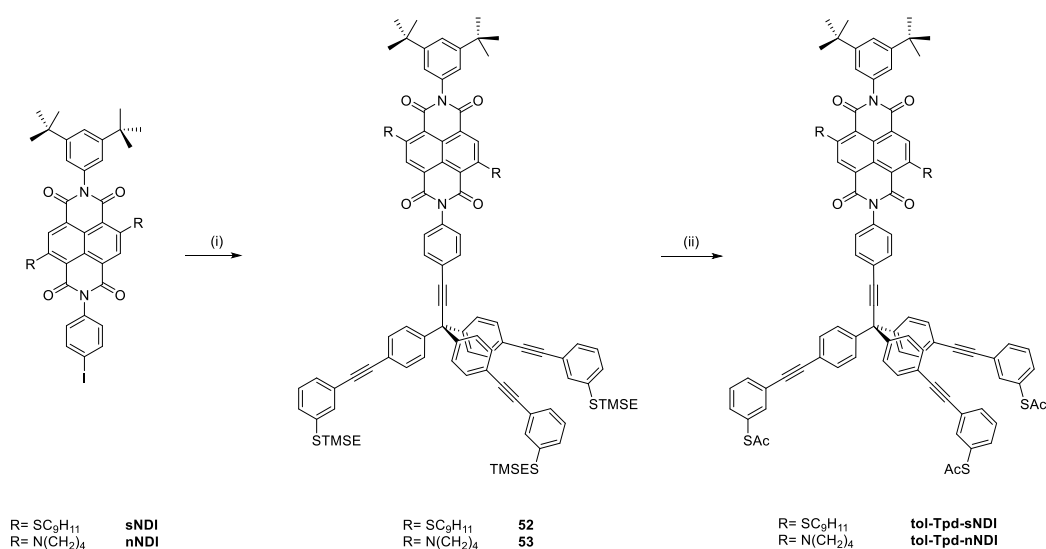
Nevertheless, to the best of our knowledge, we are the first to report that a molecular motor consisting of a stator and a rotator can be rotated continuously and with a preferred directionality without changing the tip position.

3.3.2 Second-Generation Chromophores

3.3.2.1 Synthesis of Second-Generation Chromophores

As mentioned in the previous Chapter 3.1.4.6, most of the NDIs mounted on the phenyl-based platform are lying flat. Therefore, it is of key interest to find foot structures which provide an upright orientation of the mounted chromophores. Here we describe the assembly between the extended tripodal platform **31** and **sNDI** or **nNDI**.

Under Sonogashira conditions, we mounted **sNDI** on the tolane-based tripodal platform **31** in 74% yield. Due to the poor solubility of **sNDI** in neat amines, THF was used as a co-solvent. The subsequent transprotection of compound **52** afforded the desired target molecule **Tol-Tpd-sNDI** in 62% yield. Similar to compound **52**, we mounted **nNDI** on the tolane based tripodal platform **31** in 71% yield. With **nNDI** being poor soluble in neat amines as well, we also used THF as a co-solvent. The transprotection of TMS-ethyl protected thiolate **53** to the corresponding thioacetate afforded the desired target molecule **Tol-Tpd-nNDI** in 76% yield. As expected, both the emission and the absorption spectra of **Tol-Tpd-sNDI** and **Tol-Tpd-nNDI** in solution show similar characteristics compared to their parental **sNDI** and **nNDI** structures (see Figure S 6 for **sNDI** and **Tol-Tpd-sNDI** and Figure S 7 for **nNDI**, **Tol-Tpd-nNDI**).



Scheme 25. Synthetic approach to target molecules. Reaction conditions: i) **31**, CuI, Pd(PPh₃)₄, NEt₃, THF, 74% (**52**), 71% (**53**); ii) AcCl, AgBF₄, DCM, 62% (**Tol-Tpd-sNDI**), 76% (**Tol-Tpd-nNDI**).

3.3.2.2 Self-Assembled Monolayers of Second-Generation Chromophores

Preliminary studies of the second-generation platforms **Tol-Tpd-sNDI** and **Tol-Tpd-nNDI** focuses on the self-assembled monolayer formation of these compounds. For this purpose, Prof. Dr. Michael Zharnikov measured high resolution XPS at BESSY and the corresponding HR-XPS spectra are displayed in Figure 58. The SAMs were prepared according to the conditions we developed for the HR-XPS study of the nitrile containing tripods in the previous Chapter 3.2.2. Additionally, after overnight immersion, the samples were sonicated in MeOH, THF and NEt₃ for 15 min. We expected this post-immersion treatment to complete the cleavage of the remaining thioacetates.

Both samples exhibit the characteristic peaks in the Au 4f spectra (see Figure 58a), suggesting that monolayers or thin multilayers were formed. Comparing these two signals, the peak is significantly stronger for **Tol-Tpd-sNDI** than for **Tol-Tpd-nNDI**. Hence, we can conclude that **Tol-Tpd-nNDI** forms multilayers while **Tol-Tpd-sNDI** forms monolayers. The C 1s spectra of both samples show that carbon-containing molecules are adsorbed on the surface. In the S 2p spectra of the two samples, significant differences are observable. While almost no thiolates are observable for **Tol-Tpd-nNDI**, both thiolates (at ~162 eV) and physisorbed material (at ~163 eV) are found in the case of the sulfur core-substituted chromophore **Tol-Tpd-sNDI**. Furthermore, a shoulder at ~164.3 eV can be attributed to the C-S-C bond of the NDI core-substitution. The strong signal at 163.1 eV can be explained as the overlap of unbound material and the C-S-C bond. Since these are preliminary data, the more detailed assignment will be done as soon as the preparation method has been further improved.

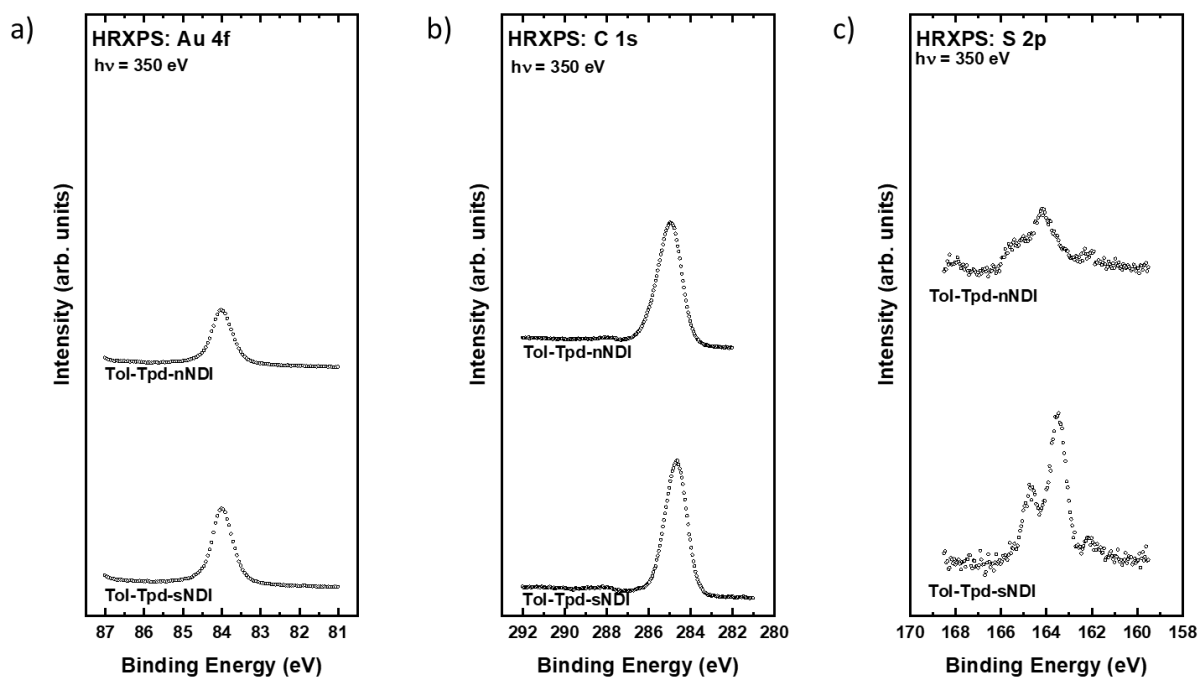


Figure 58. HR-XPS of SAMs of **Tol-Tpd-sNDI** and **Tol-Tpd-nNDI** showing the spectra of a) Au 4f, b) C 1s and c) S 2p.

To conclude the preliminary data, we assume that **Tol-Tpd-nNDI** does not form monolayers with an upright orientation of the chromophores. In contrast to that, **Tol-Tpd-sNDI** forms monolayers with thiolates bound to the Au(111) surface. However, a considerable amount of the anchors remains unbound or physisorbed and thus, the preparation method must be improved in order to increase the quality of obtained SAMs.

3.3.2.3 Surface behaviour and Luminescence of Second-Generation Chromophores

After the successful isolation of **Tol-Tpd-sNDI** and **Tol-Tpd-nNDI**, we subsequently studied the surface behaviour of these molecules by means of STML at 5 K in UHV. The molecules were deposited with our spraying technique. Noteworthy, the molecules decompose during the annealing process at 180 °C. Hence, we only annealed the molecules at 100 °C. Note, that for the first-generation chromophores, high annealing temperature is required in the first place to activate the molecule to emit light. In contrast to the first-generation chromophores, the NDIs

mounted on the extended platform appear as single round blobs as displayed in Figure 59. This suggests that the molecules are standing upright and are not lying flat, as we observed in the previous Chapter 3.1. Compared to the height profiles of the first-generation chromophores, a significant increase in the apparent height of the second-generation chromophores is observed. Juxtaposing **Tol-Tpd-sNDI** and **Tol-Tpd-nNDI**, both samples exhibit a similar apparent height. Since the core-substitution has no impact on the apparent height of the molecules, this finding is in accordance with the theory of upstanding molecules. Noteworthy, the apparent height does not represent the actual height profile and thus the information should be considered tentatively. As shown in Figure 59a, the full width at half maximum of **Tol-Tpd-sNDI** and **Tol-Tpd-nNDI** resemble. Additionally, the diameter of the molecular footprint is close to 3 nm in both structures, indicating that the adsorption geometries equal. Moreover, by comparing the diameters of all second-generation functional tripods (that are all functionalised **Tol-Tpd** foot structures), we notice that the molecular footprints are akin with values ranging from 2.6 nm to 3 nm. This strengthens the hypothesis, that all of the molecules are adsorbed through three anchoring groups ultimately leading to an upright orientation of the functional units.

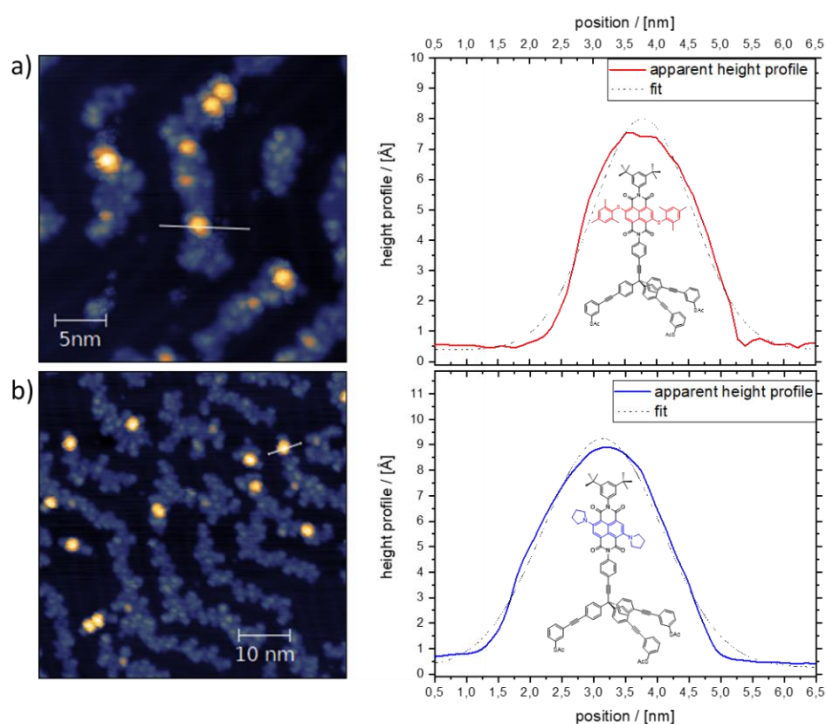


Figure 59. a) Left: Topography map of single molecules of **Tol-Tpd-sNDI**. Right: apparent height profile taken along the white line in the topography map. Sample bias: -1.5 V, tunnelling current 2 pA. b) Left: Topography map of single molecules of **Tol-Tpd-nNDI** and right: the apparent height profile taken along the white line topography map. Sample bias: 2 V, tunnelling current 2 pA.

After studying the topography of these two samples, we focused on the optical features of single molecules. When the STM tip is placed above the molecule, the molecules emit light at a bias of 2.28 V for **Tol-Tpd-sNDI** and 1.97 V for **Tol-Tpd-nNDI**. To our delight, **Tol-Tpd-sNDI** exhibits a sharp peak which perfectly matches the λ_{em}^{max} of the parental chromophore, as shown in Figure 60a. With the peak having its maximum at 551 nm for **Tol-Tpd-sNDI**, we can exclude the plasmonic peak of gold.^[257] The emission spectrum of **Tol-Tpd-nNDI** recorded by means of STML is displayed in Figure 60b. In contrast to the presence of several peaks in the emission spectra of **Tol-Tpd-sNDI**, the pyrrolidine core-substituted **Tol-Tpd-nNDI** exhibits one main peak at 633 nm which ideally fits to the emission spectra we obtained from the solution.

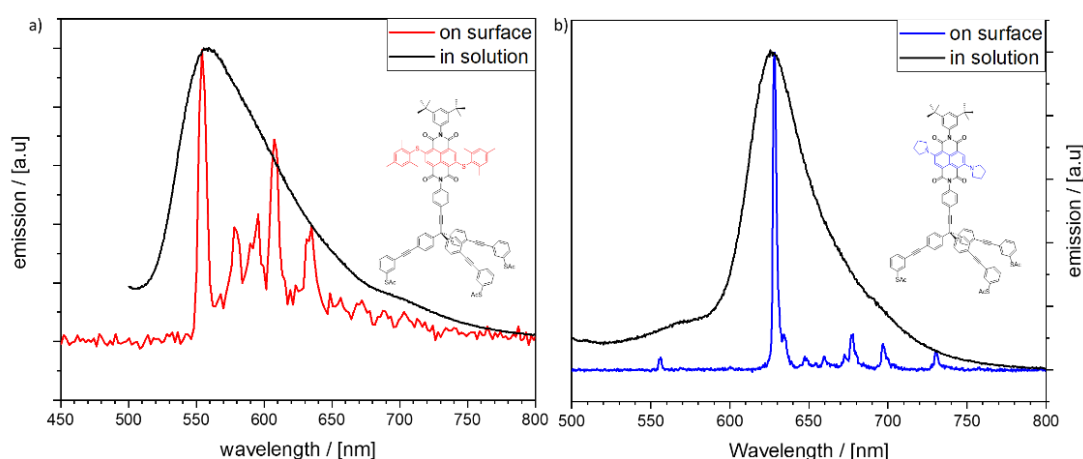


Figure 60. Emission spectra of a) **Tol-Tpd-sNDI** (black line, in solution (DCM); red line, on surface) and b) **Tol-Tpd-nNDI** (black line, in solution (DCM); blue, on surface)

To the best of our knowledge, we are the first to report that well defined and reproducible emission spectra could be recorded from single molecule chromophores which are efficiently decoupled from the metallic surface. Furthermore, the emission spectra do not drastically change neither by varying the tip position nor by switching to another single molecule. Therefore, the recorded spectra only depend on the intrinsic properties of the molecule. This further indicates that the adsorption geometries of the single molecules barely differ and thus maintaining similar surface configuration.

We then studied the nature of the light emission process. Under this purpose, the photon spectra at different sample biases were recorded to find the threshold needed to promote luminescence of the molecules. Both chromophores do not emit light at negative biases. As shown in Figure 61, the emission starts at 2.26 V for **Tol-Tpd-sNDI** and at 1.97 V for **Tol-Tpd-nNDI** respectively. These biases for the onset of the luminescence in both chromophores matches the energy of their wavelengths very closely. This indicates that the luminescence is based on a inelastic energy transfer by plasmons, comparable to the mechanism described in the previous Chapter 3.1.4.7.^[268] Hence, we exclude a mechanism based on electroluminescence at this voltage regime. By applying higher voltages, we intended to induce electroluminescence, as we reported previously.^[73] Unfortunately, increasing the bias to over 4 V leads to desorption of molecules. Therefore, we are not able to induce electroluminescence neither from **Tol-Tpd-sNDI** nor from **Tol-Tpd-nNDI** tripodal molecules.

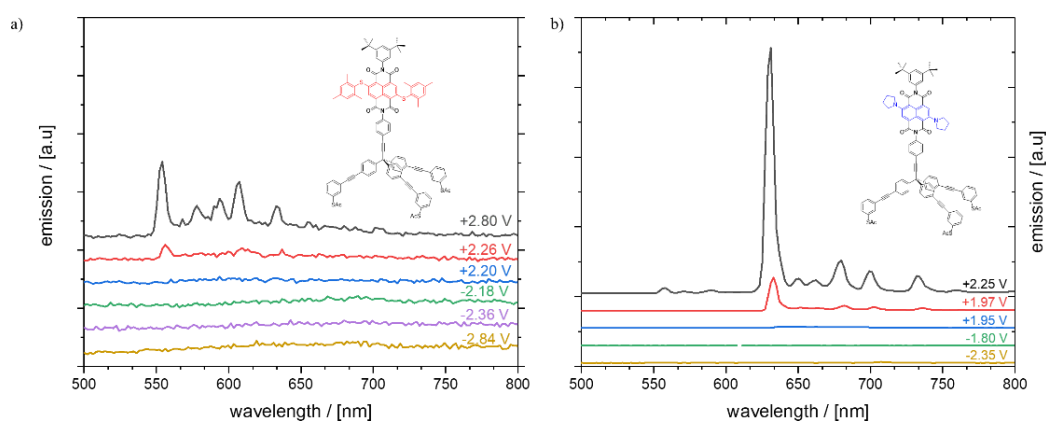


Figure 61. Photon spectra at different sample biases for a) **Tol-Tpd-sNDI** and b) **Tol-Tpd-nNDI**.

3.3.3 Conclusion of Second-Generation Functional Units

In conclusion, the second-generation tolane-based platform was successfully coupled with various functional units *via* cross-coupling protocol. After transprotection of the thiols and subsequent studies of these molecules on gold surface, we assume that except for **Tol-Tpd-Rot_c**, all other functional tripods (**Tol-Tpd-Rot_c**, **Tol-Tpd-H**, **Tol-Tpd-sNDI** and **Tol-Tpd-nNDI**) are anchored through all three anchoring groups and thus are orientated perpendicular to the surface. This assumption is based on the fact that the molecular footprints of the tripodal functional units resemble. Moreover, an increase of the apparent height of such extended functional tripods compared to the first-generation ones suggests, that these tripodal molecules stand upright. Furthermore, our first attempts to prepare mixed monolayer of functionalised tripods and tripodal dummies not only helped us to verify the surface configuration but also have shown that functionalised units can be embedded and diluted successfully on gold. For enlarged functional units, which tend to adsorb flat on the surface, this co-deposition might be a promising approach to force a perpendicular orientation of the functional unit. We can thus conclude, that our designed tripodal **Tol-Tpd** platform with three anchoring thiols allows us to modularly assemble various functional units with a defined and reproducible surface configuration for single molecule devices. Future work will focus on the improvement of SAM preparation of such extended platforms, in order to profit from large ordered arrays for molecular devices.

Moreover, two types of rotators were designed and synthesised. The molecular rotor **Tol-Tpd-Rot_c** has shown, that single molecules rotate in a preferential direction with ratio of 6:4. One full cycle consists of three different states, which we can observe by three different tunnelling currents. However, we have not been able yet to assign the different states to specific configurations. Therefore, we designed a new rotator by enlarging the headgroup of the rotator to naphthyl, with the intention to facilitate the tracking of different rotational states by means of the STM tip. In a six-step synthesis, we afforded the extended tripodal rotor **Tol-Tpd-Rot_c**. Unfortunately, the extended rotor tends to lie flat on the surface probably due to the greater attraction of its extended aromatic rotator with the substrate and its larger volume, disqualifying it for single molecule studies. Another way to ensure the dilution of functional molecules and force their perpendicular arrangement on the surface is to use tripodal dummy molecules with the intention to embed (large) functional units within the ordered islands of the dummy

compound. To our delight, this approach has confirmed exactly the expected outcome as we observed the protruding functional molecules from the ordered monolayer. Subsequent study of the rotational behaviour of the functional units have shown that the rotor rotates in a preferred direction. Noteworthy, the rotation is observable in both positive and negative biases. We are currently focusing on the assignment of the rotational states. If the rotation directionality is changing by varying the bias polarity, this would be pioneering work of bias dependent directionality of rotors and could provide information to further understand the chiral induces spin selectivity (CISS) effect.

Additionally, with core-substituted NDIs mounted on the extended tripodal platform, we have been able to record defined and reproducible emission spectra of single NDI chromophores on gold. We postulate that the molecules adsorb in the designed fashion and thus we have provided a platform which effectively self-decouples the chromophores from the surface. To our delight, the emission spectra only vary upon the core-substitution of the NDI chromophore. In both NDIs, the emission spectra in solution perfectly match the one we have recorded on the gold surface. Hence, we can assign the emission to the intrinsic features of the chromophores. Supported by the photon spectra at different sample biases, we assume a plasmon induced luminescence. Unfortunately, electroluminescence has not been observed since the molecules desorb from the surface at high biases which are required to induce electroluminescence. Therefore, in the future work we will focus on the design of chromophores, which allow electroluminescence at lower biases.

4 Conclusion and Outlook

In summary, the presented work is dedicated to the interdisciplinary research of single molecular devices and focuses on unidirectional motion of single molecule motors and light emission of single molecule chromophores on the gold substrates. Hereby, the design of tripodal molecular architectures was described, the synthesis was optimised, their eligibility as molecular platforms for single molecular functionality has been evaluated and the evolution of tripods based on triphenylpropyne unit were shown. An extended tolane-based, rigid tripodal platform **Tol-Tpd** provides a stable stator for single molecule devices. The eligibility of such extended tripodal platforms providing an upright orientation of functional units on gold has been proven for single molecule motors and single molecule light emitting devices.

In the first Chapter 3.1, the synthesis of the first-generation platform **Ph-Tpd** based on a triphenylpropyne scaffold with three acetyl-protected thiol anchors in the *meta*- position was described. The implementation of an alkyne linker allowed a modular approach to decorate the rigid tripodal platforms with various functional units *via* Sonogashira coupling chemistry. We then synthesised molecular rotors **Ph-Tpd-Rot_{LF}** and **Ph-Tpd-Rot_C**. After the successful synthesis of the three different core-substituted NDIs **hNDI**, **sNDI** and **nNDI**, we studied their optical, photophysical and spectroelectrochemical properties. After their successful assembly with the phenyl-based platform, we obtained the tripodal chromophores **Ph-Tpd-hNDI**, **Ph-Tpd-sNDI** and **Ph-Tpd-nNDI**. The self-assembly features of **Ph-Tpd-Rot_C**, **Ph-Tpd-hNDI**, **Ph-Tpd-sNDI** and **Ph-Tpd-nNDI** were analysed after spray deposition on Au(111) surfaces by low-temperature ultra-high-vacuum STM. Unfortunately, none of them adsorbs in a vertical configuration with respect to the surface. Therefore, we assume that maximum two anchoring groups are covalently bound to the surface while the third one is protruding away. Some kind of rotation has been observed for **Ph-Tpd-Rot_C**, however, the molecule rotates around a newly formed external pivot point suggesting that the molecule is anchored to gold *via* one binding group.

While tripodal chromophore **Ph-Tpd-nNDI** forms unordered islands, both **Ph-Tpd-hNDI** and **Ph-Tpd-sNDI** molecules arrange in islands with a long-range lateral order upon annealing to 180 °C. Also, both of them arrange in a close-packed pairwise fashion. These molecules show the ability to align in clusters with an increased apparent height indicating that these clusters

compose of multilayers of horizontally aligned molecules. Taking our previous results from Chapter 3.3.2.3 into account, we can exclude a single layer of upright oriented molecules. However, a minority of the tripodal chromophores form clusters, which are able to emit light. Further investigation enabled us to switch pairs of **Ph-Tpd-sNDI** reversibly and reproducibly into a configuration which then can emit light by applying negative biases. Supported by theoretical calculations, we assume that a cationic dimer is formed, whose excited states relax back into the ground state radiatively. Given their possibility to switch and emit light, we can define surfaces decorated with **Ph-Tpd-sNDI** as memory-in-pixel displays. Combining the information we gathered of all **Ph-Tpd**-based functional units, we have concluded that the phenyl-based platform **Ph-Tpd** must be enlarged, in order to promote a perpendicular orientation of the functional units with respect to the metallic substrate.

Therefore, in the following **Chapter 3.2** we focused on increasing the feet geometry of tripodal structures, finally obtaining the biphenyl-based tripodal platform **Bp-Tpd** and the tolane-based tripodal platform **Tol-Tpd**. The synthesis of the key precursor **21** turned out to be more challenging than expected. By screening the reaction conditions and its newly formed products, we were able to optimise the reaction protocol. With its modularity, we were able to functionalise such key precursor **21** to prepare numerous extended tripodal platforms by cross-coupling reactions with different structural motifs. In fact, this strategy has been used to create biphenyl-based tripodal platform **28** and the tolane-based tripodal platform **31**.

With the three different tripodal platforms in hand, we then have investigated their behaviour to form ordered self-assembled monolayers. For such study, we coupled all three different platforms with *para*-benzonitrile derivative to obtain nitrile groups as termini for our spectroscopic investigations. This design enabled us to investigate the molecular configuration of **Ph-Tpd-CN**, **Bp-Tpd-CN** and **Tol-Tpd-CN** tripods. A protocol for the preparation of SAMs consisting of these molecules has been established, but still needs some further improvement. For that, we aim to study the kinetic of SAM growth by means of *in situ* ellipsometry. In the case of the extended platforms, HR-XPS measurements have revealed that, anchoring through all three anchors is not favoured with the current preparation method, whereas the smaller platform **Ph-Tpd** has shown significantly better results. To understand the adsorption behaviour of extended tripodal platforms by means of UHV-STM experiments, we synthesised the fully symmetrical tetraphenylmethane **40**. STM experiments have prevailed a long-range order, indicating that these molecules adsorb in a structured manner and form a monolayer. Furthermore, single molecules have been observed with a size diameter which is

in accordance with our expectations. In total, a library of three different functionalised tripodal architectures has been developed with the tolane-based platform **Tol-Tpd** showing promising results.

The third Chapter 3.3 highlighted the synthesis of the second-generation functional units. Using the tolane-based platform **Tol-Tpd**, functional units for single molecule rotation and single molecule light emitting devices were presented.

To enable single molecule rotation, we mounted the prochiral rotator (“Geländer type molecule”) onto the tolane based tripodal platform. **Tol-Tpd-Rot_C** rotates in a preferential direction with ratio of 6:4. However, the quality of the measurement highly depends on each individual single molecule and thus the results are not reproducible. Additionally, we are not able to assign the different states to the corresponding configurations, yet. In a multistep reaction, we then enlarged the headgroup of the rotator, aiming to facilitate the tracking of individual states of the molecule by means of the STM-tip. Unfortunately, this extended tripodal rotor **Tol-Tpd-Rot_{ec}** lies flat on the surface, which hampers their use as single molecule surface motors. After that, we developed a tripodal dummy **Tol-Tpd-H** with the intention to spray a mixture of **Tol-Tpd-H** and **Tol-Tpd-Rot_C** onto the gold surface to dilute the concentration of functional units and achieve their perpendicular arrangement. It has been shown, that **Tol-Tpd-Rot_C** is embedded into ordered islands of **Tol-Tpd-H**, which provides the functional units a perfect environment deploying the directed motion of the rotator. The observed directed rotation is present in both positive and negative biases. Currently we are trying to assign the observed rotational states at both biases in order to evaluate whether the directionality of the rotation changes by changing the polarity of the applied bias. However, we assume that changing of the bias polarity leads to unidirectional rotation, which would be pioneering work and could contribute to understanding the chiral-induced spin selectivity (CISS) effect.

In the second part of the Chapter 3.3 core-substituted NDI chromophores **nNDI** and **sNDI** mounted on the extended tripodal platform **Tol-Tpd** have been described. After spray deposition of **Tol-Tpd-sNDI** and **Tol-Tpd-nNDI**, we have recorded defined and reproducible emission spectra of single molecules on the gold surface. These emission spectra only differ upon the core-substitution of NDI chromophore indicating that only the intrinsic features of the molecules dominate the luminescence characteristics. To the best of our knowledge, this is for the first time when chromophores mounted on rigid tripodal platforms are effectively

decoupled from the metallic surface and emit light after their excitation. The fact that emission spectra of **Tol-Tpd-sNDI** and **Tol-Tpd-nNDI** recorded on the surface perfectly resemble with the ones we obtained in solution, supports a plasmon induced photoluminescence mechanism. This theory is further supported by the photon spectra at different sample biases. Since the molecule desorb at high biases, electroluminescence has not been observed, yet. Hence, our future work will focus on the design of new chromophores which enable electroluminescence at lower biases.

To conclude, the parental tripodal platform **Ph-Tpd** has been successfully enlarged resulting in the tolane based tripod **Tol-Tpd**. This architecture provides for a vast majority of different functional units an upright orientation on gold. Moreover, it enables efficient self-decoupling of chromophores, which leads to surface mounted single molecule emitters. The prochiral motor **Tol-Tpd-Rotc** exhibits directional rotation on the surface at low temperatures. We are currently investigating whether this behavior is attributed to the CISS effect.

Future work will focus on the improved preparation of SAMs, especially for the second-generation platforms **Bp-Tpd** and **Tol-Tpd**. By investigating the growth of SAMs by means of *in situ* ellipsometry, we aim to understand the underlying mechanism of SAM formation of multidental anchors. With such improved preparation protocol, we will be able to decorate large areas of metallic surfaces with our self-decoupled chromophores, and thus possibly create organic light-emitting devices. Furthermore, the mixed deposition method will be further utilised with the aim to incorporate even larger functional units onto the tripodal structures while preserving the perpendicular orientation.

5 Experimental Section

5.1 Materials

All starting materials and reagents were purchased from commercial suppliers *Alfa Aesar* (Karlsruhe, Germany), *Sigma-Aldrich* (Schnelldorf, Germany), *TCI Chemicals Europe* (Zwijndrecht, Belgium), *Merck* (Darmstadt, Germany) and used without further purification. Solvents utilised for crystallisation, chromatography and extraction were used in technical grade. Anhydrous tetrahydrofuran and dichloromethane were taken from MBraun Solvent Purification System equipped with drying columns. Triethylamine was dried and distilled from CaH₂ under nitrogen atmosphere. TLC was performed on silica gel 60 F254 plates, spots were detected by fluorescence quenching under UV light at 254 nm and 366 nm. Column chromatography was performed on silica gel 60 (particle size 0.040–0.063 mm).

5.2 Equipment and Measurements

All NMR spectra were recorded on a Bruker Avance 500 spectrometer at 25 °C in CDCl₃, CD₂Cl₂ or MeOD. ¹H NMR (500 MHz) spectra were referred to the solvent residual proton signal (CDCl₃, δ_{H} = 7.26 ppm; CD₂Cl₂, δ_{H} = 5.32 ppm; MeOD, δ_{H} = 3.31 ppm). ¹³C NMR (126 MHz) with total decoupling of protons were referred to the solvent (CDCl₃, δ_{C} = 77.16 ppm; CD₂Cl₂, δ_{C} = 53.84 ppm; MeOD, δ_{C} = 49.00 ppm). UV-Vis-NIR absorption spectra were recorded with a Cary 5000 Scan spectrophotometer in a 1 cm quartz cell at ambient temperature (excitation coefficient ϵ is given below in units of L mol⁻¹ cm⁻¹). Fluorescence spectra were measured with a Varian Cary Eclipse Fluorescence spectrometer at room temperature in a 1 cm quartz cell. The molecules **sNDI**, **18**, **Ph-Tpd-sNDI**, **52** and **Tol-Tpd-sNDI** were excited at 370 nm and both excitation and emission slits were set to 20 nm. The molecules **nNDI**, **19**, **Ph-Tpd-nNDI**, **53** and **Tol-Tpd-nNDI** were excited at 366 nm and both excitation and emission slits were set to 10 nm. EI MS spectra were recorded with a Thermo Trace 1300-ISQ GC/MS instrument (samples were dissolved in dichloromethane or introduced directly using direct injection probes DIP, DEP) and m/z values are given along with their relative intensities (%) at an ionising voltage of 70 eV. High-resolution mass spectra were recorded with either a

Bruker Daltonics (ESI microTOF-QII) mass spectrometer or a SYNAPT™ G2 Mass Spectrometry (ESI-TOF). IR spectra were recorded with a Nicolet iS50 FT-IR spectrometer under ATP mode. Analytical samples were dried at 40–100 °C under reduced pressure (10^{-2} mbar). Melting points were measured with a Büchi Melting point M-560 apparatus and are uncorrected. Elemental analyses were obtained with a Vario MicroCube CHNS analyser. The values are expressed in mass percentage. Cyclic voltammetry (CV) experiments were carried out with a Gamry potentiostat, connected to a C3 standard electrochemical cell. Glassy carbon was used as the working electrode, a platinum wire as the counter electrode and Ag/AgNO₃ as the reference electrode. Ferrocene was used as an internal standard and was added after each series of measurements. The junction potential was corrected to the reference electrode afterwards. The molecules (0.1 mM) were dissolved in 0.1 M solution of Bu₄NPF₆ as an electrolyte in DCM and the solution was purged with argon for 10 minutes before taking the measurement. Scan rate of the CV measurements was 100 mVs⁻¹ and all experiments were performed under ambient conditions at room temperature. For spectroelectrochemical measurements, a BWTEK light source was additionally installed. The measurements were carried out in a quartz electrochemical cell with the structure of a cuvette (width of 1 mm) with a platinum counter electrode and a platinum working electrode (mesh). The molecules were dissolved in 0.1 M solutions of [NBu₄][PF₆] in dry DMF or MeCN. Concentration of the sample solutions were varied, to reach an absorption value = 1.

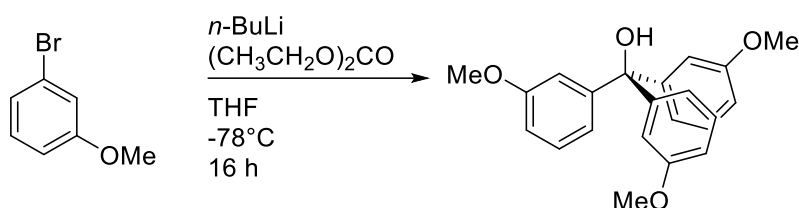
All STM measurements were performed in a homebuilt STM at about 4.4 K in UHV (10^{-10} mbar). This STM is equipped with a photon collection system that allows to analyse light that is emitted from the tunnel junction.^[256] All photon spectra were corrected for the energy-dependent detector efficiency (see SI, Figure 34a). Electroluminescence count rates are normalised by energy resolution and charge injected (labelled as counts per meV and nC). A clean Au(111) substrate was prepared by argon sputtering at 1.5 kV and subsequent annealing to about 500 °C. Molecules were dissolved in dichloromethane (c ~ 1 mg/mL) and sprayed through an aperture onto the cleaned gold surface by using a spray-technique, thoroughly described before.^[196] After deposition, samples were transferred into the ultra-high vacuum (UHV) and were annealed at 100 °C in order to promote deprotection of the thiol anchoring groups and to facilitate ordered arrangements of the molecules. **Ph-Tpd-hNDI**, **Ph-Tpd-sNDI**, and **Ph-Tpd-nNDI** were annealed at 180 °C in a second step.

A suitable crystal was measured on a Stoe StadiVari diffractometer. During the data collection, the crystal was kept at -123.15 °C. The software used was Olex2^[353] and the structure was solved with the ShelXT^[354] structure solution program by Intrinsic Phasing and refined with the ShelXL^[355] refinement package by Least Squares minimisation.

5.3 Experimental Details and Synthetic Procedures

2,6-Dichloronaphthalene-1,4,5,8-tetracarboxylic acid dianhydride **15** was synthesised in four reaction steps by following a literature procedure.^[281]

Tris(3-methoxyphenyl)methanol **2**^[315]



Under argon, *m*-bromoanisole (4.1 mL, 32.1 mmol, 1.0 eq) dissolved in dry THF (80.0 mL). After cooling down to -78 °C, *n*-BuLi (20.1 mL, 32.1 mmol, 1.0 eq) was added dropwise and the mixture was stirred for 60 minutes at this temperature. Then, diethyl carbonate (1.28 mL, 10.6 mmol, 0.33 eq) was slowly added the reaction mixture was stirred overnight and allowed to reach room temperature. The reaction was quenched with NH₄Cl solution (10%, 70 mL) and the aqueous phase was extracted with DCM (3 × 50 mL). The combined organic layer was washed with brine and dried with MgSO₄. After filtration and evaporation of all volatiles, the crude product was purified by flash chromatography on silica gel (hexane/EtOAc = 4:1, R_f = 0.33). 2.2 g (79%) of the title compound was afforded as a white solid.

M.P: 122 °C

¹H NMR (500 MHz, CDCl₃) δ [ppm] = 7.23 – 7.20 (m, 3H, Ar-H), 6.91 – 6.87 (m, 3H, Ar-H), 6.85 – 6.79 (m, 6H, Ar-H), 3.75 (s, 9H, CH₃), 2.85 (s, 1H, OH)

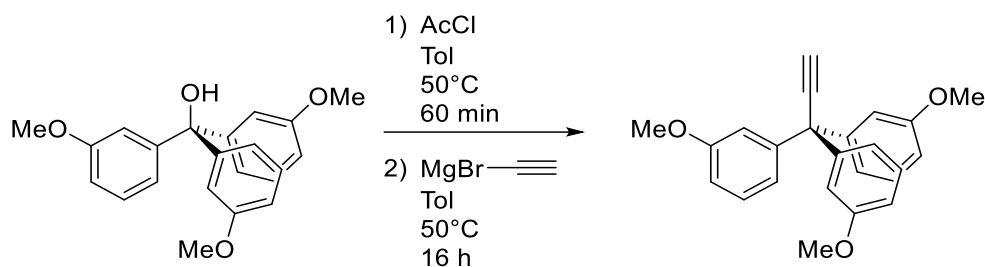
¹³C NMR (126 MHz, CDCl₃) δ [ppm] = 159.4 (C), 148.4 (C), 129.0 (CH), 120.6 (CH), 114.1 (CH), 112.6 (CH), 82.0 (C), 55.3 (CH₃)

EI MS m/z (%) : 350.12 (M⁺, 36), 243.10 (54), 135.06 (100)

FTIR (ATR): $\tilde{\nu}$ [cm⁻¹] = 3454 (m, ν (OH)), 3000 (w), 2959 (w, ν_{as} (CH₃)), 2936 (w), 2834 (w, ν_{sym} (CH₃)), 1604 (m), 1583 (m), 1480 (m), 1465 (w), 1449 (m), 1433 (m), 1344 (w), 1317 (m), 1290 (m), 1234 (m, ν_{as} (=C_{Ar}-O-C)), 1195 (m), 1163 (m), 1146 (m), 1059 (m, ν_{sym} (=C_{Ar}-O-C)), 1032 (m), 996 (w), 968 (m), 952 (m), 894 (w), 883 (w), 875 (m), 851 (w), 805 (w), 770 (m), 705 (m), 698 (m), 609 (w), 578 (w), 559 (w)

The compound was synthesised according to a literature procedure.^[315]

3,3,3-Tris(3-methoxyphenyl)propyne **3**^[315]



Under argon, in an oven dried Schlenk-flask, 3,3,3-tris(3-methoxyphenyl)methanol **2** (2.2 g, 6.3 mmol, 1.0 eq) was suspended in dry toluene (40.0 mL) and stirred for 60 minutes at 50 °C. Then, acetyl chloride (4.5 mL, 62.8 mmol, 10.0 eq) was added dropwise (5 minutes) and the reaction mixture was stirred for 60 minutes under these conditions. After evaporation of the volatiles, the oily crude product was redissolved in dry toluene (50.0 mL), followed by the addition of ethynylmagnesium bromide at 50 °C. The mixture was stirred at this temperature overnight. The reaction was quenched with water (10.0 mL), separated and the aqueous phase was extracted with ethyl acetate (3 × 20.0 mL). The combined organic layer was washed with brine and dried over MgSO₄. Purification by flash chromatography on silica gel (hexane/EtOAc = 10:1, R_f = 0.31) gave 1.7 g (73%) of 3,3,3-tris(3-methoxyphenyl)propyne **3** as a colourless oil.

¹H NMR (500 MHz, CDCl₃) δ [ppm] = 7.21 – 7.18 (m, 3H, Ar-H), 6.91 – 6.87 (m, 3H, Ar-H), 6.84 – 6.73 (m, 1H, 6H, Ar-H), 3.74 (s, 9H), 2.70 (s, 1H)

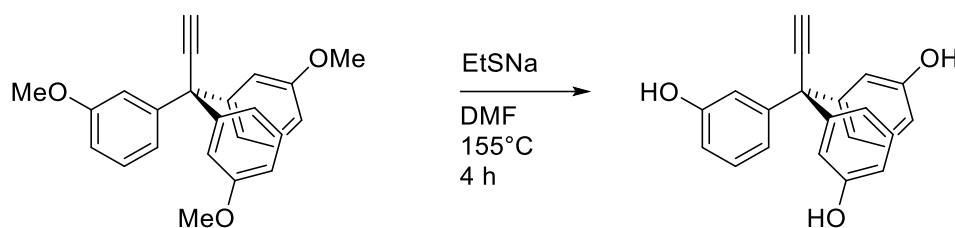
¹³C NMR (126 MHz, CDCl₃) δ [ppm] 159.4 (C), 146.2 (C), 129.0 (CH), 121.8 (CH), 115.6 (CH), 112.2 (CH), 89.6 (C), 73.7 (CH), 55.7 (C), 55.3 (CH₃)

EI MS m/z (%): 358.21 (M⁺, 100), 251.11 (25)

FTIR (ATR): $\tilde{\nu}$ [cm⁻¹] = 3281 (m, $\nu(\equiv\text{CH})$), 3000 (w, $\nu(=\text{CH})$), 2957 (w, $\nu(=\text{CH})$), 2937 (w), 2909 (w, $\nu_{\text{sym}}(\text{CH}_3)$), 2833 (w), 1597 (m), 1582 (m), 1483 (m), 1463 (m), 1450 (m), 1431 (m), 1316 (m), 1290 (m), 1241 (m, $\nu_{\text{as}}(=\text{C}_{\text{Ar}}-\text{O}-\text{C})$), 1186 (w), 1148 (m), 1094 (w), 1049 (m, $\nu_{\text{sym}}(=\text{C}_{\text{Ar}}-\text{O}-\text{C})$), 997 (w), 966 (w), 877 (w), 854 (w), 769 (m), 697 (m), 644 (w)

The compound was synthesised according to a literature procedure.^[315]

3,3,3-Tris(3-hydroxyphenyl)propyne **4**



Under argon atmosphere, 3,3,3-tris(3-methoxyphenyl)propyne **3** (2.4 g, 6.7 mmol, 1.0 eq) and sodium ethanethiolate (6.76 g, 80.4 mmol, 12.0 eq) were dissolved in dry DMF (100 mL) and subsequently heated up to 155 °C. The dark red reaction mixture was stirred for 4 hours while the progress was monitored by TLC. After completion of the reaction, all volatiles were removed under reduced pressure. The slurry was redissolved in DCM (50 mL) and acidified by 2 M HCl_{aq} until the pH value reached pH ~ 4. Separating the layers was followed by washing the organic phase with water (3 × 20 mL) and brine (20 mL). After removal of the solvent, the yellow oil was redissolved in diethyl ether (10.0 mL) and the crude product was precipitated by adding of hexane (50 mL). After filtration and evaporation of all volatiles, the crude product was purified by flash chromatography on silica gel (hexane/EtOAc/formic acid = 2:1:0.02, R_f = 0.31). After drying, 1.75 g (83%) of **4** was isolated as a white solid.

M.p. = 210 °C (decomposition);

¹H NMR (500 MHz, MeOD) δ [ppm] = 7.10 - 7.07 (m, 3H, Ar-H), 6.74 - 6.73 (m, 6H, Ar-H), 6.68-6.65 (m, 3H, Ar-H), 3.03 (s, 1H, ≡CH)

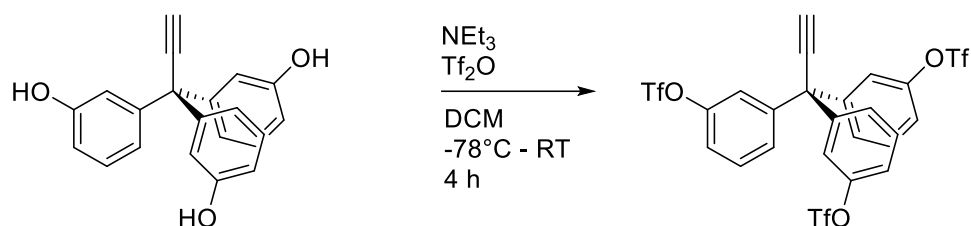
¹³C NMR (126 MHz, MeOD) δ [ppm] = 156.0 (C), 147.8 (C), 129.7 (CH), 121.7 (CH), 117.5 (CH), 114.7 (CH), 90.9 (C), 74.6 (CH), 56.5 (C)

FTIR (ATR): $\tilde{\nu}$ [cm⁻¹] = 3349 (bs, ν(OH)), 3297 (vw, ν(≡CH)), 3054 (w), 3025 (w, ν(=CH)), 1591 (m), 1537 (m, ν(C=C)), 1492 (s), 1450 (s), 1325 (m), 1235 (s), 1164 (m), 1144 (m), 997 (w), 891 (w), 974 (w), 825 (m), 811 (m), 788 (s), 778 (s), 697, (m), 648 (m), 637 (m)

EI MS *m/z* (%): 316.1 (26, [M]⁺), 281.1 (22), 207.0 (100)

Anal. calcd for C₂₁H₁₆O₃ (316.36): C, 79.73; H, 5.10. Found: C, 79.17; H, 5.09

3,3,3-Tris[3-(trifluoromethanesulfonyl)phenyl]propyne **5**



Under argon atmosphere, 3,3,3-tris(3-hydroxyphenyl)propyne **4** (532 mg, 1.7 mmol, 1.0 eq) was dissolved in dry DCM (50.0 mL) and cooled down to -78°C before freshly distilled triethylamine (4.2 mL) was added. After the reaction was stirred for 30 min at this temperature, triflic anhydride (1.7 mL, 10.1 mmol, 6.0 eq) was slowly added and the dark red mixture was stirred for additional 3 h to reach room temperature. The reaction was quenched with NH_4Cl solution (10%, 10 mL) and the aqueous phase was extracted with DCM (3×10 mL). The combined organic layer was washed with brine and dried with MgSO_4 . After filtration and evaporation of all volatiles, the crude product was purified by flash chromatography on silica gel (hexane/EtOAc = 15:1, R_f = 0.23). After drying, 0.87 g (73%) of compound **5** was isolated as a colourless oil.

^1H NMR (500 MHz, CDCl_3) δ [ppm] = 7.47 - 7.44 (m, 3H, Ar-H), 7.28 - 7.25 (m, 6H, Ar-H), 7.15 - 7.14 (m, 3H, Ar-H), 2.89 (s, 1H, $\equiv\text{CH}$)

^{19}F NMR (471 MHz, CDCl_3) δ [ppm] = -72.8

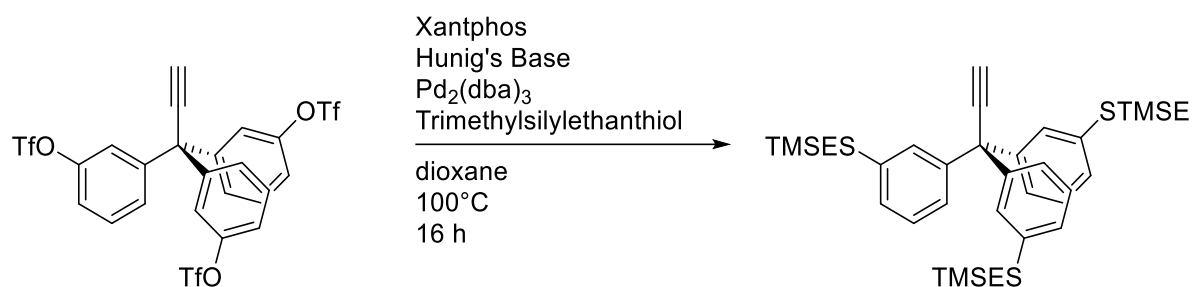
^{13}C NMR (126 MHz, CDCl_3) δ [ppm] = 149.8 (C), 145.7 (C), 130.5 (CH), 128.7 (CH), 122.2 (CH), 121.1 (CH), 118.8 (q, J = 321.1 Hz, CF_3), 86.4 (C), 76.3 ($\equiv\text{CH}$), 55.0 (C)

FTIR (ATR): $\tilde{\nu}$ [cm^{-1}] = 3296 (w, $\nu(\equiv\text{CH})$), 1606 (w), 1582 (w), 1483 (m), 1422 (m), 1249 (m), 1207 (m), 1137 (m), 986 (w), 968 (w), 916 (w), 890 (w), 861 (m), 801 (m), 778 (w), 760 (w), 753 (w), 694 (w), 655 (w), 607 (w), 572 (w), 512 (w)

ESI (+) HRMS calcd for $\text{C}_{24}\text{H}_{13}\text{F}_9\text{O}_9\text{S}_3\text{Na}$: 734.9470 $[\text{M} + \text{Na}]^+$, found m/z 734.9492

Anal. calcd for $\text{C}_{24}\text{H}_{13}\text{F}_9\text{O}_9\text{S}_3$ (712.52): C, 40.46; H, 1.84. Found: C, 40.25; H, 1.99

3,3,3-Tris{3-[2-(trimethylsilyl)ethylsulfanyl]phenyl}propyne **6**



Under inert conditions, in an oven dried Schlenk flask, compound **5** (165 mg, 0.2 mmol, 1.0 eq), $\text{Pd}_2(\text{dba})_3$ (12 mg, 12 μmol , 0.05 eq) and Xantphos (13 mg, 23 μmol , 0.1 eq) were dissolved in dry dioxane (2.5 mL) and flushed with argon for 30 min. Then, the reaction mixture was heated up to 100 °C and stirred for 20 minutes, before Hünig's base (0.3 mL, 2.1 mmol, 9.0 eq) was added and the mixture was stirred for another 40 minutes. Subsequently, 2-(trimethylsilyl)ethanethiol (0.8 mL, 1.4 mmol, 6.0 eq) was added and stirred overnight. The reaction mixture was quenched with water, separated, and the aqueous phase was extracted with DCM (3 \times 10 mL). The combined organic layer was washed with brine and dried over MgSO_4 . After filtration and evaporation of all volatiles, the crude product was purified by flash chromatography on silica gel (hexane/EtOAc = 60:1, R_f = 0.32). After drying, 124 mg (80%) of compound **6** was isolated as a colourless oil.

^1H NMR (500 MHz, CDCl_3) δ [ppm] = 7.23 - 7.17 (m, 9H, Ar-H), 7.00 - 6.98 (m, 3H, Ar-H), 2.87 - 2.84 (m, 6H, CH_2), 2.70 (s, 1H, $\equiv\text{CH}$), 0.88 - 0.84 (m, 6H, CH_2), 0.00 (s, 27H, CH_3)

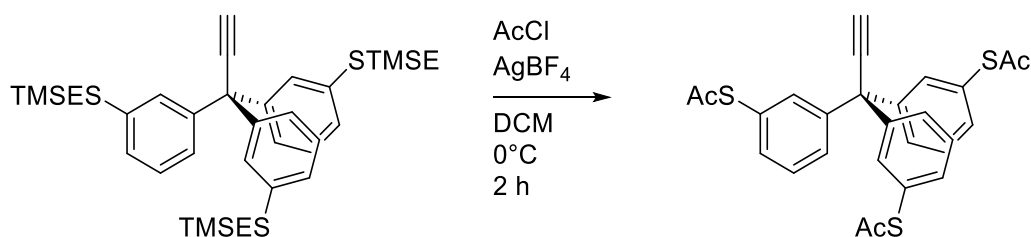
^{13}C NMR (126 MHz, CDCl_3) δ [ppm] = 145.0 (C), 137.5 (C), 129.0 (CH), 128.5 (CH), 127.3 (CH), 126.4 (CH), 89.1 (C), 74.1 (CH), 55.5 (C), 29.3 (CH_2), 16.8 (CH_2), -1.6 (TMS)

FTIR (ATR): $\tilde{\nu}$ [cm^{-1}] = 3310 (m, $\nu(\equiv\text{CH})$), 3058 (m, $\nu(=\text{CH})$), 2954 (m, $\nu_{\text{as}}(\text{CH}_3)$), 2917 (m, $\nu_{\text{as}}(\text{CH}_2)$), 2882 (m, $\nu_{\text{sym}}(\text{CH}_3)$), 2853 (m), 1583 (m, $\nu(\text{C}=\text{C})$), 1475 (m), 1408 (m), 1249 (m), 1162 (m), 1105 (w), 1088 (w), 1010 (w), 846 (bw), 785 (w), 753 (w), 722 (m), 696 (m), 648 (w)

ESI (+) HRMS calcd for $\text{C}_{36}\text{H}_{52}\text{S}_3\text{Si}_3\text{Na}$: 687.2431 [$\text{M} + \text{Na}$] $^+$, found m/z 687.2583

Anal. calcd for $\text{C}_{36}\text{H}_{52}\text{S}_3\text{Si}_3$ (665.25): C, 65.00; H, 7.88. Found: C, 65.31; H, 7.51

3,3,3-Tris[3-(acetylsulfanyl)phenyl]propyne **7**¹



A solution of compound **6** (196 mg, 0.3 mmol, 1.0 eq) in dry CH₂Cl₂ (19.6 mL) was cooled to -78 °C before acetyl chloride (1.96 mL) was added in one portion. After 15 minutes, AgBF₄ (287 mg, 1.5 mmol, 5.0 eq) was added as a solid. The reaction mixture was allowed to reach room temperature and stirred for additional 2 hours. Then the milky solution was cooled down to ~ -7 °C, diluted with CH₂Cl₂ (30 mL) and quenched with crashed ice. The crude product was extracted with CH₂Cl₂ (3 × 25 mL), combined organic fractions were washed with H₂O (25 mL), dried with MgSO₄ and filtered. After filtration and evaporation of all volatiles at room temperature, the crude product was purified by flash chromatography on silica gel (hexane/EtOAc = 3:1, R_f = 0.34). After drying, 132 mg of compound **7** was isolated in 92% yield as a white solid.

M.p. = 40 °C (decomposition)

¹H NMR (500 MHz, CD₂Cl₂) δ [ppm] = 7.42-7.35 (m, 12H, Ar-H), 2.92 (s, 1H, ≡CH), 2.40 (s, 9H, CH₃);

¹³C NMR (126 MHz, CD₂Cl₂) δ [ppm] = 193.8 (CO), 145.3 (C), 135.3 (CH), 133.9 (CH), 130.3 (CH), 129.4 (CH), 129.0 (C), 88.3 (C), 75.6 (≡CH), 55.5 (C), 30.4 (CH₃)

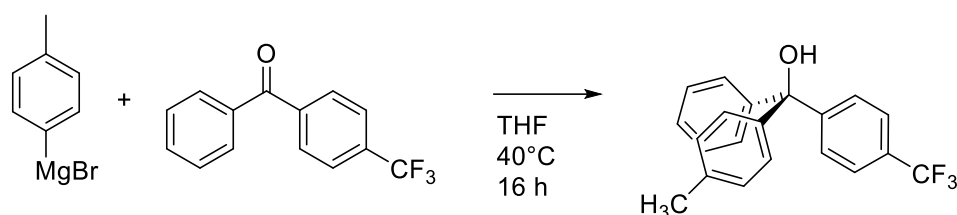
FTIR (ATR): $\tilde{\nu}$ [cm⁻¹] = 3247 (m, $\nu(\equiv\text{CH})$), 3049 (w, $\nu(=\text{CH})$), 2950 (m, $\nu_{\text{as}}(\text{CH}_3)$), 2922 (m, $\nu_{\text{as}}(\text{CH}_2)$), 2854 (m, $\nu_{\text{sym}}(\text{CH}_2)$), 1706 (s, $\nu(\text{C}=\text{O})$), 1584(m), 1469 (m), 1412 (m), 1351 (m) 1304 (w), 1112 (m), 998 (w), 947 (m), 889 (w), 793 (m), 736 (w), 723 (m), 694 (m), 647 (w), 613 (m), 522 (w), 508 (w)

ESI (+) HRMS calcd for C₂₇H₂₂S₃O₃Na: 513.0623 [M + Na]⁺, found m/z 513.0778

Anal. calcd for C₂₇H₂₂S₃O₃ (490.65): C, 66.10; H, 4.52. Found: C, 66.37; H, 4.41

¹ Synthesis by Dr. Jan Lukášek. Analysis by Nico Balzer.

Compound 10



Under argon, 4-(trifluoromethyl)benzophenone (2.0 g, 8.0 mmol, 1 eq) was dissolved in dry THF (8 mL) and heated up to 40 °C, before *p*-tolylmagnesium bromide (1.9 mL, 9.6 mmol, 1.2 eq) was added dropwise. The mixture was then stirred for 16 hours at this temperature. The reaction mixture was quenched with water, separated, and the aqueous phase was extracted with DCM (3 × 10 mL). The combined organic layer was washed with brine and dried over MgSO₄. After filtration and evaporation of all volatiles, the crude product was purified by flash chromatography on silica gel (hexane/EtOAc = 10:1, *R_f* = 0.33) to afford 1.56 g (57%) of the title compound as a colourless oil.

¹H NMR (500 MHz, CDCl₃) δ [ppm] = 7.58 (d, ³J=8.3 Hz, 2H, Ar-H), 7.47 (d, ³J=8.2 Hz, 2H, Ar-H), 7.37 – 7.30 (m, 3H, Ar-H), 7.29 – 7.25 (m, 2H, Ar-H), 7.15 – 7.11 (m, 4H, Ar-H), 2.79 (s, 1H, OH), 2.36 (s, 3H, CH₃)

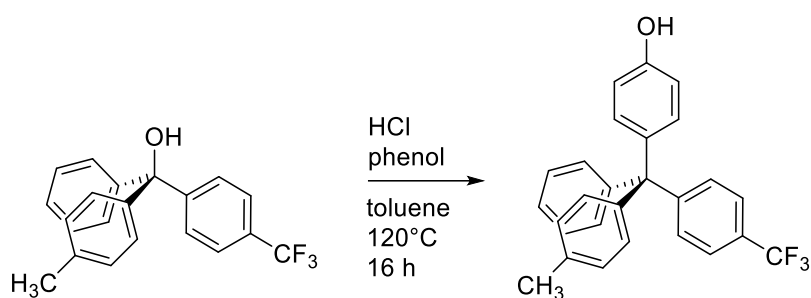
¹³C NMR (126 MHz, CDCl₃) δ [ppm] = 150.9 (C), 146.4 (C), 143.5 (C), 137.6 (C), 129.4 (q, J = 33 Hz, C), 129.0 (CH), 128.30 (CH), 128.29 (CH), 127.95 (CH), 127.92 (CH), 127.7 (CH), 124.3 (q, J = 277 Hz, CF₃), 125.0 (q, J = 4 Hz, CH), 81.8 (C), 21.2 (CH₃)

¹⁹F NMR (471 MHz, CDCl₃) δ = -62.43

FTIR (ATR): $\tilde{\nu}$ [cm⁻¹] = 3461 (w, ν (OH)), 3059 (w), 3028 (w), 2924 (w, ν_{as} (CH₃)), 1618 (w), 1511 (w), 1492 (w), 1447 (w), 1409 (m), 1323 (s), 1164 (m), 1122 (m), 1113 (m), 1067 (m), 1016 (m), 899 (w), 835 (m), 814 (m), 795 (w), 775 (w), 755 (m), 701 (m), 691 (w), 652 (w), 611 (w), 526 (w)

EI MS *m/z* (%) : 342.0 (M⁺, 10), 265.1 (39), 197.1 (93) 173.0 (100)

Compound 11



Triphenylmethanol derivative **10** (500 mg, 1.5 mmol, 1 eq) and phenol (1.37 g, 14.6 mmol, 10 eq) were dissolved in toluene (8 mL) and HCl_{aq} (4 mL) and heated up to 120 °C and stirred for 90 hours. After cooling down to room temperature, the reaction mixture was quenched with Milli-Q water and diluted with ethyl acetate (40 mL). The phases were separated, the aqueous phase was extracted with ethyl acetate (3 × 20 mL) and the combined organic layer was washed with brine and dried over MgSO₄. After filtration and evaporation of all volatiles, the crude product was purified by flash chromatography on silica gel (hexane/EtOAc = 13:1, R_f = 0.33) to afford 454 mg (74%) of the title compound as a white solid.

M.p. = 152 °C

¹H NMR (500 MHz, CDCl₃) δ [ppm] = 7.69 (d, ³J = 8.4 Hz, 2H, Ar-H), 7.54 (d, ³J = 8.3 Hz, 2H, Ar-H), 7.47 – 7.43 (m, 2H, Ar-H), 7.42 – 7.36 (m, 3H, Ar-H), 7.29 – 7.22 (m, 6H, Ar-H), 6.94 – 6.89 (m, 2H, Ar-H), 4.98 (s, 1H, OH), 2.52 (s, 3H, CH₃)

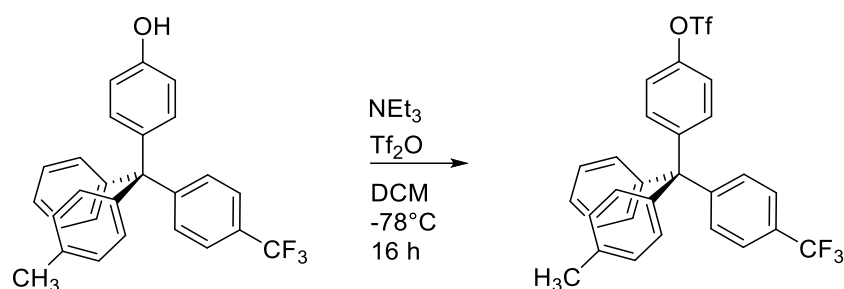
¹³C NMR (126 MHz, CDCl₃) δ [ppm] = 153.8 (C), 151.5 (C), 146.6 (C), 143.5 (C), 138.8 (C), 135.9 (C), 132.4 (CH), 131.4 (CH), 131.1 (CH), 131.0 (CH), 128.5 (CH), 128.1 (q, J = 38 Hz, C), 127.8 (CH), 126.3 (CH), 124.5 (q, J = 4 Hz, CH), 124.4 (q, J = 272 Hz, CF₃), 114.6 (CH), 64.1 (C), 21.0 (CH₃)

¹⁹F NMR (471 MHz, CDCl₃) δ = -62.32

FTIR (ATR): $\tilde{\nu}$ [cm⁻¹] = 3332 (m, ν (OH)), 3054 (w), 3025 (w, ν_{as} (CH₃)), 2162 (w), 1612 (w), 1600 (w), 1508 (m), 1493 (w), 1444 (w), 1411 (w), 1327 (m), 1297 (w), 1255 (w), 1242 (w), 1193 (w), 1181 (w), 1162 (m), 1113 (m), 1070 (m), 1018 (m), 821 (m), 808 (m), 795 (w), 755 (m), 723 (w), 703 (m), 682 (w), 649 (w), 637 (w), 609 (w), 592 (w), 571 (w), 539 (w), 525 (m), 501 (w)

EI MS m/z (%) : 418.3 (M⁺, 35), 141.2 (67), 327.2 (31), 273.2 (100)

Compound 12



Under Schlenk conditions, compound **11** (350 mg, 0.8 mmol, 1 eq) was dissolved in dry DCM (14 mL) and cooled down to -78°C before freshly distilled triethyl amine (0.70 mL, 5.0 mmol, 6 eq) was added. After the reaction was stirred for 30 min at this temperature, triflic anhydride (0.3 mL, 1.7 mmol, 2 eq) were slowly added and the dark red mixture was stirred overnight and allowed to reach room temperature. The reaction was quenched with ammonium chloride and the aqueous phase was extracted with DCM ($3 \times 10\text{ mL}$). The combined organic layer was washed with brine and dried over MgSO_4 . After filtration and evaporation of all volatiles, the crude product was purified by flash chromatography on silica gel (hexane/EtOAc = 20:1, $R_f = 0.07$) to afford 0.43 g (93%) of the title compound as a white solid.

M.p. = 149°C

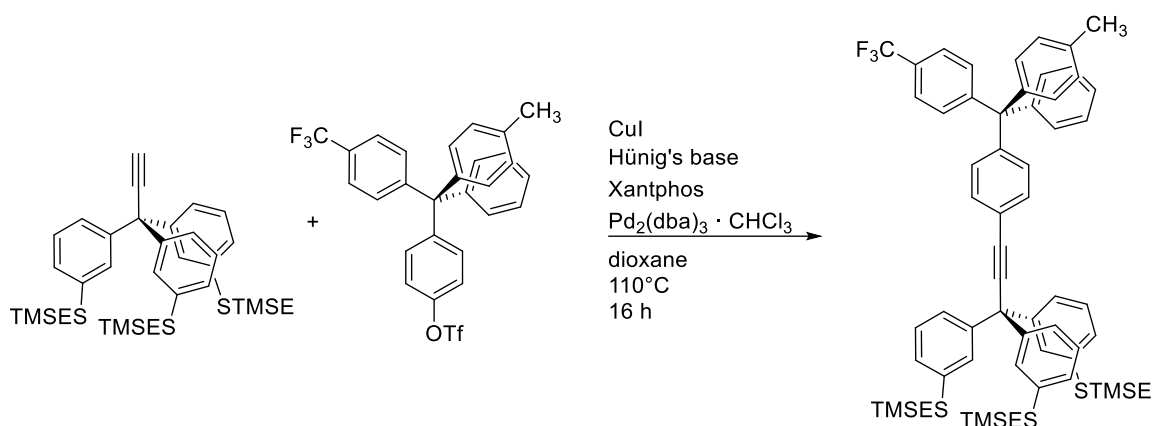
^1H NMR (500 MHz, CDCl_3) δ [ppm] = 7.52 (d, $^3J = 8.4\text{ Hz}$, 2H, Ar-H), 7.34 – 7.27 (m, 6H, Ar-H), 7.25 – 7.21 (m, 1H, Ar-H), 7.19 – 7.13 (m, 4H, Ar-H), 7.11 – 7.07 (m, 2H, Ar-H), 7.04 – 7.00 (m, 2H, Ar-H), 2.33 (s, 3H, CH_3)

^{13}C NMR (126 MHz, CDCl_3) δ [ppm] = 150.4 (C), 147.8 (C), 147.0 (C), 145.6 (C), 142.5 (C), 136.5 (C), 132.9 (CH), 131.3 (CH), 130.9 (CH), 130.8 (CH), 128.8 (CH), 128.6 (q, $J = 32\text{ Hz}$, C), 128.1 (CH), 126.7 (C), 124.8 (q, $J = 4\text{ Hz}$, CH), 124.3 (q, $J = 272\text{ Hz}$, CF_3), 120.6 (CH), 118.9 (q, $J = 315\text{ Hz}$, CF_3), 64.5 (C), 21.0 (CH_3)

^{19}F NMR (471 MHz, CDCl_3) δ = -62.46, -72.91

FTIR (ATR): $\tilde{\nu}$ [cm^{-1}] = 3027 (w), 2926 (w, $\nu_{\text{as}}(\text{CH}_3)$), 2162 (w), 1618 (w), 1509 (w), 1496 (m), 1446 (w), 1424 (m), 1412 (m), 1326 (s), 1250 (m), 1210 (m), 1166 (m), 1137 (s), 1115 (s), 1069 (m), 1035 (w), 1016 (m), 915 (w), 884 (m), 830 (m), 810 (m), 796 (w), 780 (w), 751 (m), 739 (m), 724 (m), 703 (m), 681 (w), 649 (w), 635 (w), 625 (w), 605 (m), 574 (m), 525 (w), 504 (w), 411 (w)

Compound 13



Under inert conditions, in an oven dried Schlenk-flask, compound **12** (130 mg, 236 μmol , 1 eq), $\text{Pd}_2(\text{dba})_3 \cdot \text{CHCl}_3$ (9 mg, 9 μmol , 0.05 eq), Xantphos (10 mg, 18 μmol , 0.1 eq) and CuI (3 mg, 18 μmol , 0.1 eq) were dissolved in dry dioxane (1 mL) and flushed with argon for 30 min. After that, the reaction mixture was heated up to 110 $^\circ\text{C}$ and Hünig's base (0.3 mL, 1.6 mmol, 9 eq) was added. Then, compound **6** (120 mg, 181 μmol , 1 eq) was diluted in dioxane (1 mL) and cannulated into the reaction mixture. The dark red reaction mixture was stirred overnight before the reaction was quenched with ammonium chloride and separated. The aqueous phase was extracted with (3 \times 10 mL) ethyl acetate. The combined organic layer was washed with brine and dried over MgSO_4 . Purification by flash chromatography (hexane/DCM = 20:1, R_f = 0.23) yielded 70 mg (52%) of the desired compound **13** as a colourless oil.

^1H NMR (500 MHz, CDCl_3) δ = 7.50 (d, 3J = 8.5 Hz, 2H, Ar-H), 7.41 – 7.33 (m, 4H, Ar-H), 7.28 (s, 3H, Ar-H), 7.27 – 7.24 (m, 2H, Ar-H), 7.23 – 7.14 (m, 11H, Ar-H), 7.10 – 7.04 (m, 4H, Ar-H), 7.04 – 7.01 (m, 3H, Ar-H), 2.89 – 2.83 (m, 6H, CH_2), 2.33 (s, 3H, CH_3), 0.88 – 0.84 (m, 6H, CH_2), -0.04 (s, 27H, CH_3)

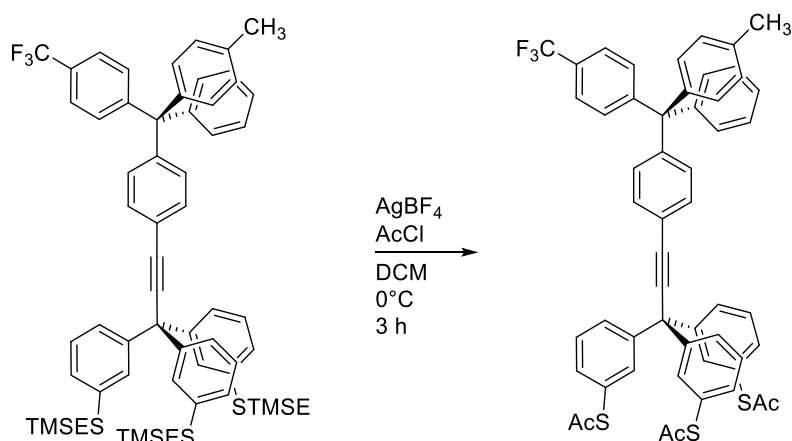
^{13}C NMR (126 MHz, CDCl_3) δ [ppm] = 150.7 (C), 146.5 (C), 145.8 (C), 145.5 (CH), 142.7 (C), 137.5 (CH), 136.0 (C), 131.3 (CH), 131.0 (CH), 130.92 (CH), 130.88 (CH), 130.8 (CH), 128.9 (CH), 128.6 (CH), 128.9 (CH), 128.2 (q, J = 30 Hz, C), 128.1 (CH), 127.8 (CH), 127.1 (CH), 126.4 (CH), 126.3 (C), 124.5 (q, J = 4 Hz, CH), 124.2 (q, J = 277 Hz, CF_3), 121.1 (C), 95.0 (C), 85.3 (C), 64.6 CH_3 , 56.0 CH_3 , 29.2 (CH_2), 20.9 (CH_3), 16.6 (CH_2), -1.8 (CH_3)

^{19}F NMR (471 MHz, CDCl_3) δ = -62.39

FTIR (ATR): $\tilde{\nu}$ [cm^{-1}] = 2951 (w, $\nu_{\text{as}}(\text{CH}_3)$), 2920 (w, $\nu_{\text{as}}(\text{CH}_2)$), 2854 (w, $\nu_{\text{sym}}(\text{CH}_2)$), 2162 (w), 1582 (w), 1509 (w), 1500 (w), 1472 (w), 1411 (w), 1326 (m), 1260 (w), 1247 (m), 1164 (w), 1123 (w), 1070 (w), 1017 (w), 882 (w), 855 (w), 836 (m), 826 (m), 812 (w), 787 (w), 752 (w), 729 (w), 720 (w), 702 (w), 694 (w)

ESI (+) HRMS calcd for $\text{C}_{63}\text{H}_{71}\text{F}_3\text{S}_3\text{Si}_3\text{K}$: 1103.3609, $[\text{M} + \text{K}]^+$, found m/z 1103.3764

Ph-Tpd-Rot_{LF}



In an oven dried Schlenk-flask, compound **13** (35 mg, 33 μ mol, 1 eq) was dissolved in dry DCM (3 mL), cooled down to 0 °C and flushed with argon. At these conditions, acetyl chloride (0.3 mL) was added, and the mixture was stirred for 20 min. Then, AgBF₄ (32 mg, 164 μ mol, 5 eq) was added and stirred for 3 h. The reaction mixture was cooled down to 0 °C and quenched with an ice water, separated, and extracted with DCM (3 \times 5mL). The combined organic layer was washed with brine and dried with MgSO₄. After filtration and evaporation of all volatiles at room temperature, the crude product was purified by flash chromatography on silica gel (hexane/DCM = 2:3, R_f = 0.24). After drying, 18 mg (62%) of the desired transprotected **Ph-Tpd-Rot_{LF}** was isolated as a white solid.

M.p. = 40 °C (decomposition)

¹H NMR (500 MHz, CD₂Cl₂) = δ 7.53 (d, ³J = 8.2 Hz, 2H, Ar-H), 7.45 (d, ³J = 8.1 Hz, 2H, Ar-H), 7.42 – 7.33 (m, 14H, Ar-H), 7.31 – 7.18 (m, J = 12.7, 6.7 Hz, 7H, Ar-H), 7.09 (s, 4H, Ar-H), 2.36 (s, 9H, CH₃), 2.32 (s, 3H, CH₃)

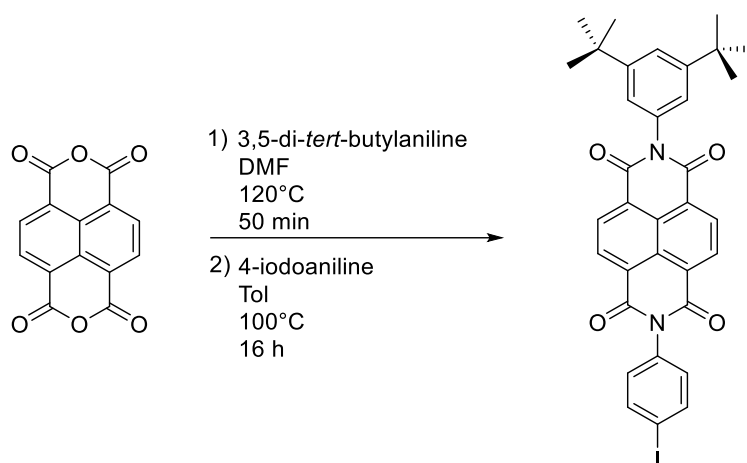
¹³C NMR (126 MHz, CD₂Cl₂) δ = 193.6 (CO), 151.3 (C), 147.3 (C), 146.3 (C), 145.8 (CH), 143.2 (C), 136.5 (C), 135.4 (CH), 133.8 (CH), 131.7 (CH), 131.4 (CH), 131.3 (CH), 131.2 (CH), 131.1 (CH), 130.3 (CH), 129.4 (q, J = 4 Hz, CH), 129.0 (CH), 128.9 (CH), 128.3 (q, J = 30 Hz, C), 126.7 (CH), 124.94 (CH), 124.91 (CH), 124.7 (q, J = 277 Hz, CF₃), 121.0 (C), 94.2 (C), 86.7 (C), 65.1 (C), 56.1 (C), 30.5 (CH₃), 21.0 (CH₃)

¹⁹F NMR (471 MHz, CDCl₃) δ = -62.67.

FTIR (ATR): $\tilde{\nu}$ [cm⁻¹] = 2960 (m), 2924 (m), 2854 (w), 1703 (m), 1585 (w), 1469 (w), 1411 (w), 1326 (m), 1260 (w), 1164 (w), 1113 (m), 1085 (m), 1069 (m), 1035 (m), 1017 (m), 1001 (m), 949 (m), 826 (w), 809 (m), 792 (m), 754 (w), 731 (w), 722 (w), 693 (m), 611 (m)

ESI (+) HRMS calcd for C₅₄H₄₁F₃O₃S₃Na 913.2062 [M + Na]⁺, found m/z 913.2009

***N*-(3,5-Di-*tert*-butylphenyl)-*N'*-(4-iodophenyl)naphthalene-1,4,5,8-tetracarboxdiimide (hNDI)**



Naphthalene-1,4,5,8-tetracarboxylic acid dianhydride **14** (1.0 g, 3.7 mmol, 1.6 eq) was suspended in DMF (15 mL) and heated up to 120 °C. Then, 3,5-di-*tert*-butylaniline (479 mg, 2.3 mmol, 1.0 eq) was added and the suspension was stirred for 50 minutes before it was poured into an ice bath. The crude product was extracted with DCM (3 × 100 mL) and the organic phase was washed with brine to remove most of DMF. After removal of the solvent, the crude product was directly used for the next step. The obtained product was redispersed in toluene (85 mL) and heated up to 100 °C. Then 4-iodoaniline (510 mg, 2.3 mmol, 1.0 eq) was added and the mixture was stirred 16 hours at 100 °C. After cooling down to room temperature, the suspension was filtrated and washed with cold EtOH (100 mL). After evaporation of all volatiles, the crude product was purified by flash chromatography on silica gel (DCM/hexane = 5:1, R_f = 0.23). After drying, 660 mg (43%) of **hNDI** as an off-white solid was isolated.

M.p. = 323 °C

¹H NMR (500 MHz, CDCl₃) δ [ppm] = 8.84 (s, 4H, Ar-H), 7.93 – 7.91 (m, 2H, Ar-H), 7.58 – 7.57 (m, 1H), 7.13 – 7.10 (m, 4H, Ar-H), 1.38 (s, 18H, CH₃)

¹³C NMR (126 MHz, CDCl₃) δ [ppm] = 163.2 (CO), 162.9 (CO), 152.3 (C), 139.0 (CH), 134.4 (C), 134.0 (C), 131.7 (CH), 131.5 (CH), 130.6 (CH), 127.6 (C), 127.33 (C), 127.29 (C), 126.8 (C), 123.5 (CH), 122.6 (CH), 95.2 (C), 35.2 (C), 31.6 (CH₃)

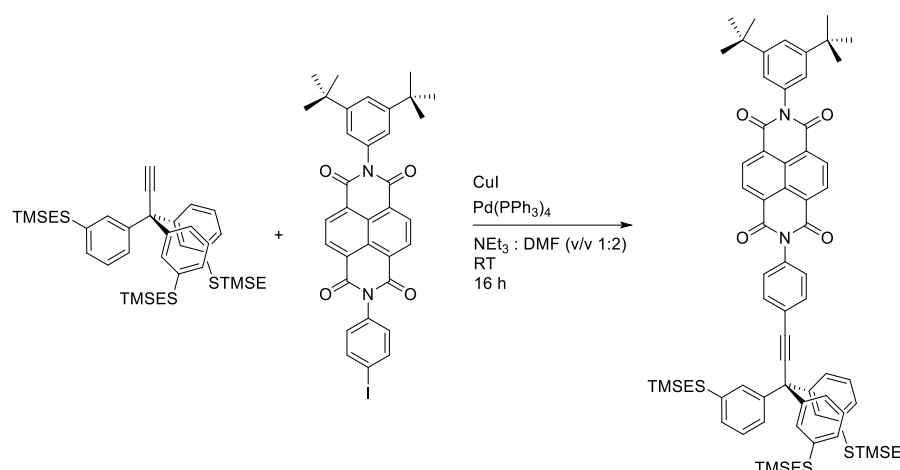
FTIR (ATR): $\tilde{\nu}$ [cm⁻¹] = 2962 (m, ν_{as} (CH₃)), 2867 (w, ν_{sym} (CH₃)), 1714 (m, ν (C=O)), 1674 (m), 1609 (w), 1579 (m), 1483 (m), 1447 (w), 1363 (w), 1343 (m), 1248 (m), 1196 (m), 1147 (w), 1118 (w), 1012 (w), 978 (w), 866 (w), 839 (w), 808 (w), 767 (w), 762 (m), 742 (m), 707 (w), 658 (w), 510 (w), 424 (w);

ESI (+) HRMS calcd for C₃₄H₂₉IN₂O₄H: 657.1245, [M + H]⁺, found m/z 657.1408

Anal calcd. for C₃₄H₂₉IN₂O₄ (656.52): C, 62.20; H, 4.45; N, 4.27; Found: C, 62.27; H, 4.63; N, 4.60

UV-Vis (DCM) (λ_{max} [nm], (ϵ)) = 360 (30347), 381 (33863)

Compound 17



Under inert conditions, in an oven dried Schlenk flask, **hNDI** (50 mg, 76 μmol , 1.0 eq), $\text{Pd}(\text{PPh}_3)_4$ (4 mg, 4 μmol , 0.05 eq) and copper(I)-iodide (2 mg, 8 μmol , 0.1 eq) were dissolved in freshly distilled DMF (2 mL) and purged with argon for 30 min. Then, freshly distilled and degassed triethylamine (1 mL) and compound **6** (61 mg, 91 μmol , 1.2 eq) was added and the reaction mixture was stirred for 16 hours. The reaction mixture was subsequently quenched with NH_4Cl solution (10%, 15 mL) and diluted with ethyl acetate (15 mL). The organic layer was washed with brine and dried over MgSO_4 . After filtration and evaporation of all volatiles, the crude product was purified by flash chromatography on silica gel (hexane/EtOAc = 4:1, R_f = 0.32). After drying, 61 mg (67%) of the desired compound **17** was isolated as an off-white solid.

M.p. = 159 $^\circ\text{C}$ (decomposition)

^1H NMR (500 MHz, CDCl_3) δ [ppm] = 8.85 (s, 4H, Ar-H), 7.71 (d, J = 8.5 Hz, 2H, Ar-H), 7.58 (m, 1H, Ar-H), 7.33 – 7.31 (m, 2H, Ar-H), 7.28 – 7.20 (m, 9H, Ar-H), 7.15 – 7.10 (m, 5H, Ar-H), 2.90 – 2.87 (m, 6H, CH_2), 1.39 (s, 18H, CH_3), 0.90 – 0.87 (m, 6H, CH_2), 0.01 (s, 27H, CH_3)

^{13}C NMR (126 MHz, CDCl_3) δ [ppm] = 163.2 (CO), 163.0 (CO), 152.2 (C), 145.4 (C), 137.6 (C), 134.4 (C), 134.0 (C), 132.9 (CH), 131.6 (CH), 131.5 (CH), 129.1 (CH), 128.8 (CH), 128.6 (CH), 127.5 (C), 127.31 (C), 127.28 (CH), 126.9 (C), 126.5 (CH), 124.6 (C), 123.5 (CH), 122.6 (CH), 96.3 (C), 84.9 (C), 56.1 (C), 35.2 (C), 31.6 (CH_3), 29.3 (CH_2), 16.8 (CH_2), -1.6. (CH_3)

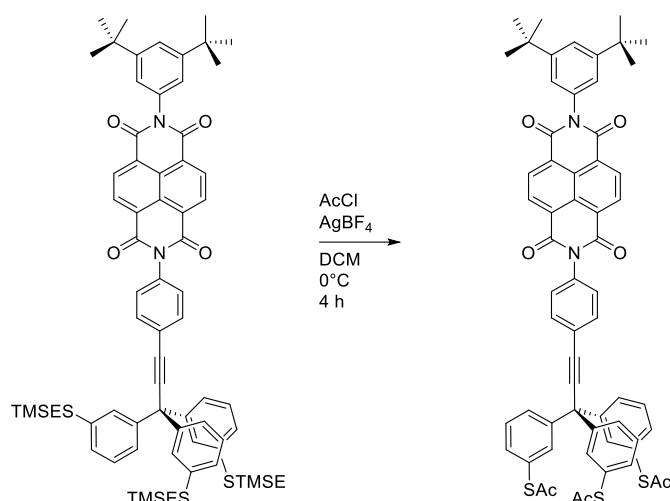
FTIR (ATR): $\tilde{\nu}$ [cm^{-1}] = 2953 (m, $\nu_{\text{as}}(\text{CH}_3)$), 2924 (m, $\nu_{\text{as}}(\text{CH}_2)$), 2858 (w, $\nu_{\text{sym}}(\text{CH}_3)$), 1715 (m, $\nu(\text{C=O})$), 1675 (m), 1580 (m), 1509 (w), 1472 (w), 1449 (w), 1343 (m), 1246 (m), 1196 (m), 1162 (w), 1147 (w), 1119 (w), 839 (m), 763 (w), 748 (w), 727 (w), 712 (w), 704 (w), 692 (w), 676 (w)

ESI (+) HRMS calcd for $\text{C}_{70}\text{H}_{80}\text{N}_2\text{O}_4\text{S}_3\text{Si}_3\text{Na}$: 1215.4480 $[\text{M} + \text{Na}]^+$, found m/z 1215.4308

Anal. calcd for $\text{C}_{70}\text{H}_{80}\text{N}_2\text{O}_4\text{S}_3\text{Si}_3$ (1193.86): C, 70.42; H, 6.75; N, 2.35. Found: C, 70.58; H, 6.83; N, 2.51.

UV-Vis (DCM) (λ_{max} [nm], (ϵ)) = 360 (20515), 381 (25813)

Ph-Tpd-hNDI



Under inert conditions, in an oven dried Schlenk flask, compound **17** (39 mg, 33 μ mol, 1 eq) was dissolved in dry DCM (5.0 mL) and cooled down to 0 °C. At this temperature, AcCl (0.5 mL) was added and the reaction mixture was stirred for 10 min before addition of AgBF₄ (32 mg, 163 μ mol, 5 eq). The reaction mixture was stirred for 4 h to reach room temperature. The reaction mixture was cooled down to 0 °C and quenched with an ice water, separated, and extracted with DCM (3 \times 5mL). The combined organic layer was washed with brine and dried with MgSO₄. After filtration and evaporation of all volatiles, the crude product was purified by flash chromatography on silica gel (hexane/EtOAc = 3:1, R_f = 0.2). After drying, 31 mg (93%) of the target molecule **Ph-Tpd-hNDI** was isolated as an off-white solid.

M.p. = 40 °C (decomposition)

¹H NMR (500 MHz, CDCl₃) δ [ppm] = 8.85 (s, 4H, Ar-H), 7.75 (d, J = 8.5 Hz, 2H, Ar-H), 7.58 – 7.57 (m, 1H, Ar-H), 7.44 – 7.30 (m, 14H, Ar-H), 7.14 (d, J = 1.5 Hz, 2H), 2.40 (s, 9H, CH₃), 1.38 (s, 18H, CH₃)

¹³C NMR (126 MHz, CDCl₃) δ [ppm] = 193.7 (CO), 163.2 (CO), 163.0 (CO), 152.3 (C), 145.4 (C), 135.1 (CH), 134.6 (C), 134.0 (CH), 133.5 (CH), 133.1 (CH), 131.7 (CH), 131.5 (CH), 130.2 (CH), 129.3 (CH), 128.8 (CH), 128.4 (C), 127.5 (C), 127.33 (C), 127.30 (C), 126.9 (C), 124.3 (C), 123.5 (CH), 122.6 (CH), 95.4 (C), 85.8 (C), 55.9 (C), 35.2 (C), 31.6 (CH₃), 30.4 (CH₃)

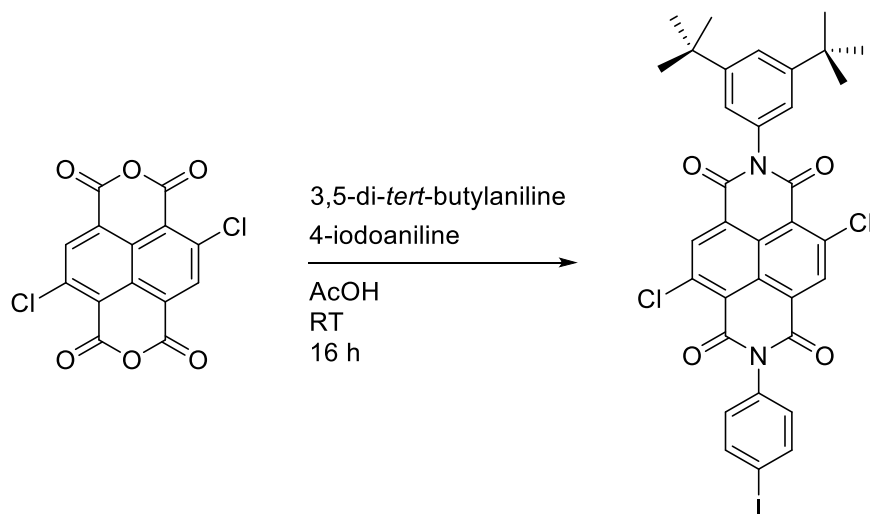
FTIR (ATR): $\tilde{\nu}$ [cm⁻¹] = 2959 (m, $\nu_{\text{as}}(\text{CH}_3)$), 2924 (w, $\nu_{\text{as}}(\text{CH}_3)$), 2865 (w, $\nu_{\text{sym}}(\text{CH}_3)$), 2164 (w), 1713 (m, $\nu(\text{C}=\text{O})$), 1673 (m), 1608 (w), 1579 (m), 1482 (w), 1448 (w), 1428 (w), 1363 (w), 1342 (m), 1246 (m), 1196 (w), 1118 (w), 1011 (w), 979 (w), 838 (w), 767 (w), 763 (w), 742 (w), 729 (w), 707 (w), 422 (w)

ESI (+) HRMS calcd for C₆₁H₅₀N₂O₇S₃Na: 1041.2672 [M + Na]⁺, found m/z 1041.3114

Anal. calcd for C₆₁H₅₀N₂O₇S₃ (1019.26): C, 71.88; H, 4.94; N, 2.75. Found: C, 71.53; H, 5.21; N, 2.65

UV-Vis (DCM) (λ_{max} [nm], (ϵ)) = 360 (24995), 381 (26976)

2,6-Dichloro-*N*-(3,5-di-*tert*-butylphenyl)-*N'*-(4-iodophenyl)naphthalene-1,4,5,8-tetracarboxdiimide **16**



3,5-Di-*tert*-butylaniline (274 mg, 1.3 mmol, 1.5 eq) and *p*-iodoaniline (292 mg, 1.3 mmol, 1.5 eq) were suspended in glacial acetic acid (15 mL) and stirred for 30 minutes. Then, 2,6-dichloronaphthalene-1,4,5,8-tetracarboxylic acid dianhydride **15** (300 mg, 0.9 mmol, 1 eq) was added and the suspension was stirred overnight. The suspension was filtered and washed with acetic acid to remove the residual anilines. After purification by flash chromatography on silica gel (hexane/DCM = 3:2, R_f = 0.37), the purple-reddish solid was suspended in hot acetone (50 mL). After filtration and drying under reduced pressure, 215 mg (39%) of compound **16** was isolated as an off-white powder.

M.p. >380 °C

¹H NMR (500 MHz, CD₂Cl₂) δ [ppm] = 8.82 (s, 2H, Ar-H), 7.93 – 7.91 (m, 2H, Ar-H), 7.60 (s, 1H, Ar-H), 7.11 – 7.08 (m, 4H, Ar-H), 1.36 (s, 18H, CH₃)

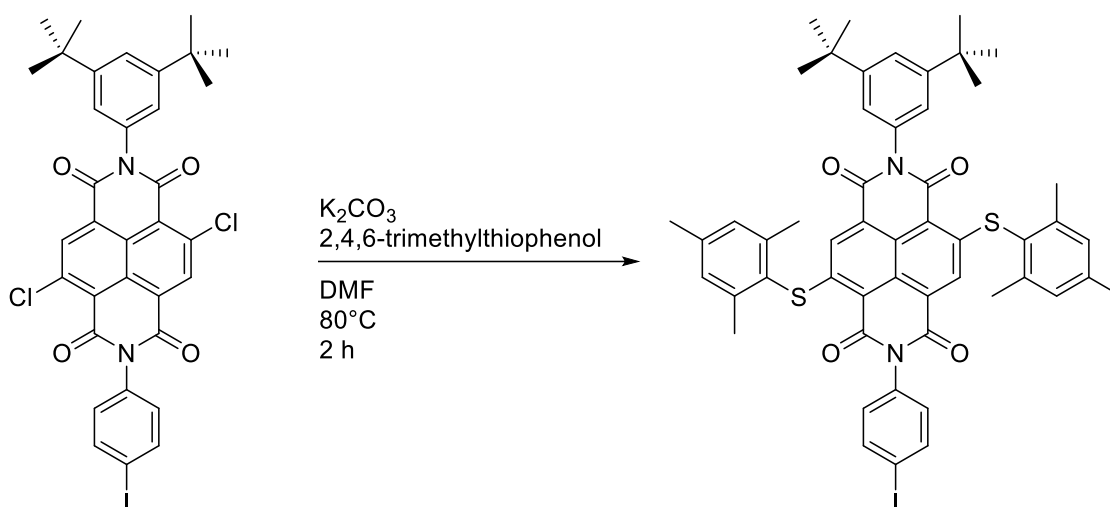
¹³C NMR (126 MHz, CD₂Cl₂) δ [ppm] = 161.6 (CO), 161.4 (CO), 161.1 (CO), 160.9 (CO), 152.9 (C), 140.9 (C), 140.6 (C), 139.2 (CH), 136.6 (CH), 136.4 (CH), 134.9 (C), 134.6 (C), 130.9 (CH), 128.1 (C), 127.2 (C), 126.6 (C), 123.8 (CH), 123.5 (C), 123.0 (C), 122.9 (CH), 95.2 (C), 35.4 (C), 31.5 (CH₃)

FTIR (ATR): $\tilde{\nu}$ [cm⁻¹] = 2959 (m, ν_{as} (CH₃)), 1730 (m, ν (C=O)), 1717 (m), 1686 (m, ν (C=C)), 1671 (s), 1607 (w), 1564 (m), 1482 (m), 1427 (m), 1393 (w), 1357 (m), 1323 (m), 1240 (m), 1221 (m), 1168 (m), 1010 (m), 910 (w), 892 (m), 866 (w), 848 (w), 813 (m), 784 (m), 776 (w), 746 (m), 705 (w), 549 (w), 536 (w), 513 (w)

ESI (+) HRMS Calcd for C₃₄H₂₇N₂O₄ICl₂Na([M + Na]⁺, 747.0285), found m/z 747.4226

Anal. calcd for C₃₄H₂₇Cl₂IN₂O₄ (725.40): C, 56.30; H, 3.75; N, 3.86. Found: C, 55.97; H, 3.41; N, 3.54.

2,6-Bis(1,3,5-trimethylphenylsulfanyl)-*N*-(3,5-di-*tert*-butylphenyl)-*N'*-(4-iodophenyl)naphthalene-1,4,5,8-tetracarboxdiimide (sNDI)



Compound **16** (180 mg, 248 μmol , 1 eq), K_2CO_3 (103 mg, 744 μmol , 3 eq) and 2,4,6-trimethylthiophenol (0.1 mL, 744 μmol , 3 eq) were dissolved in anhydrous DMF (8 mL), heated up to 80 $^{\circ}\text{C}$ and stirred for 2 hours. Afterwards, the reaction mixture was quenched with NH_4Cl solution (10%, 15 mL), diluted with ethyl acetate (15 mL), followed by extracting the aqueous phase with ethyl acetate (3×5 mL). The combined organic layer was washed with brine and dried with MgSO_4 . After filtration and evaporation of all volatiles, the crude product was purified by flash chromatography on silica gel (hexane/DCM = 1:2, R_f = 0.52). After drying, 165 mg (69%) of **sNDI** was isolated as a red solid.

M.p. = 310 $^{\circ}\text{C}$

^1H NMR (500 MHz, CDCl_3) δ [ppm] = 8.04 (s, 1H, Ar-H), 8.01 (s, 1H, Ar-H), 7.88 (d, J = 8.5 Hz, 2H, Ar-H), 7.53 (s, 1H, Ar-H), 7.11–7.07 (m, 8H, Ar-H), 2.36 (s, 12H, CH_3), 2.32 (s, 6H, CH_3), 1.35 (s, 18H, CH_3)

^{13}C NMR (126 MHz, CDCl_3) δ [ppm] = 163.8 (CO), 163.6 (CO), 162.60 (CO), 162.57 (CO), 152.2 (C), 149.9 (C), 149.2 (C), 143.7 (C), 141.2 (C), 141.1 (C), 138.9 (CH), 134.6 (C), 134.1 (C), 130.7 (CH), 130.33 (CH), 130.30 (CH), 129.5 (CH), 129.3 (CH), 126.4 (C), 126.3 (C), 125.3 (C), 125.0 (C), 124.0 (C), 123.7 (CH), 122.4 (CH), 119.9 (C), 118.9 (C), 94.9 (C), 35.1 (C), 31.6 (CH_3), 21.7 (CH_3), 21.44 (CH_3), 21.42 (CH_3)

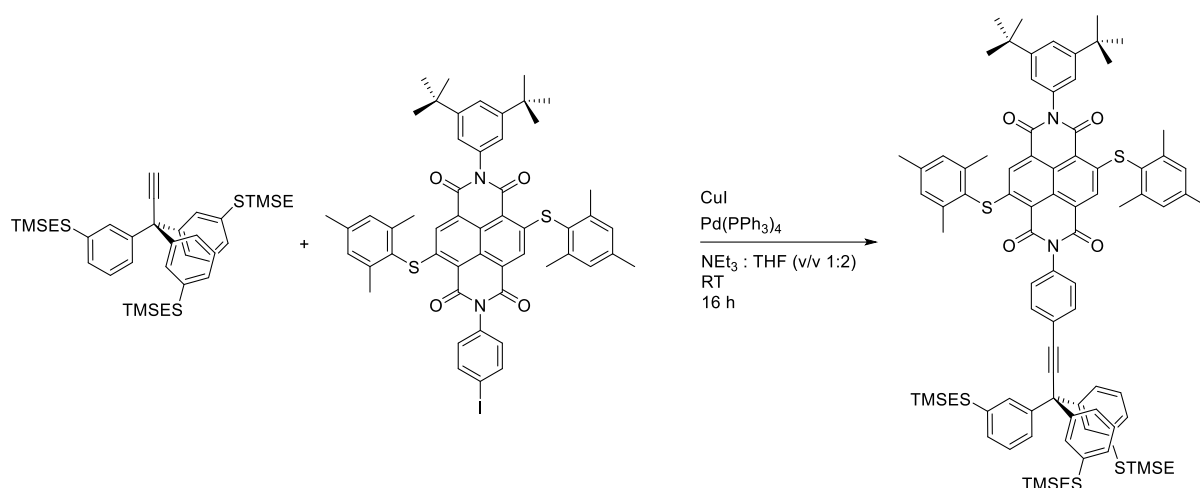
FTIR (ATR): $\tilde{\nu}$ [cm^{-1}] = 2961 (m, $\nu_{\text{as}}(\text{CH}_3)$), 2923 (m, $\nu_{\text{as}}(\text{CH}_3)$), 2858 (w, $\nu_{\text{sym}}(\text{CH}_3)$), 2163 (w), 1705 (m, $\nu(\text{C}=\text{O})$), 1665 (m), 1603 (w), 1549 (m), 1484 (w), 1430 (m), 1362 (w), 1321 (m), 1247 (m), 1223 (m), 1165 (m), 1093 (w), 1059 (w), 1026 (w), 1009 (m), 898 (w), 844 (w), 811 (w), 787 (w), 745 (w), 673 (w), 535 (w)

ESI (+) HRMS calcd for $\text{C}_{52}\text{H}_{49}\text{IN}_2\text{O}_4\text{S}_2\text{Na}$: 979.2071 [$\text{M} + \text{Na}$] $^{+}$, found m/z 979.2099

Anal. calcd for $\text{C}_{52}\text{H}_{49}\text{IN}_2\text{O}_4\text{S}_2$ (957.00): C, 65.26; H, 5.16; N, 2.93. Found: C, 65.09; H, 5.19; N, 2.76

UV-Vis (λ_{max} [nm], (ϵ)) = 297 (50058), 356 (10802), 371 (11398), 525 (21419)

Compound 18



Under inert conditions, in an oven dried Schlenk-flask, **sNDI** (100 mg, 105 μmol , 1.0 eq), Pd(PPh₃)₂Cl₂ (6 mg, 5 μmol , 0.05 eq) and copper(I)-iodide (2 mg, 10 μmol , 0.1 eq) were dissolved in dry THF (8 mL) and purged with argon for 30 min. Then compound **6** (83 mg, 125 μmol , 1.2 eq) dissolved in freshly distilled NEt₃ (4 mL) was added and the reaction mixture was stirred overnight. The reaction mixture was quenched with NH₄Cl solution (10%, 15 mL) and diluted with ethyl acetate (15 mL). The aqueous phase was extracted with ethyl acetate (3 \times 5 mL) and the combined organic layer was washed with brine and dried with MgSO₄. After filtration and evaporation of all volatiles, the crude product was purified by flash chromatography on silica gel (hexane/DCM = 2:3, R_f = 0.37). After drying, 72 mg (46%) of the desired compound **18** was isolated as a red oil.

¹H NMR (500 MHz, CDCl₃) δ [ppm] = 8.04 (s, 1H, Ar-H), 8.01 (s, 1H, Ar-H), 7.67 – 7.65 (m, 2H, Ar-H), 7.53 – 7.52 (m, 1H, Ar-H), 7.31 – 7.19 (m, 11H, Ar-H), 7.11 – 7.01 (m, 9H, Ar-H), 2.89 – 2.84 (m, 6H, CH₂), 2.36 (s, 12H, CH₃), 2.322 (s, 3H, CH₃), 2.318 (s, 3H, CH₃), 1.35 (s, 18H, CH₃), 0.89 – 0.85 (m, 6H, CH₂), 0.03 (s, 27H, CH₃)

¹³C NMR (126 MHz, CDCl₃) δ [ppm] = 163.8 (CO), 163.6 (CO), 162.7 (CO), 162.6 (CO), 152.1, 149.8, 149.2, 145.4, 143.72, 143.70, 141.2, 141.1, 137.6, 134.6, 134.2, 132.8, 130.3, 129.4, 129.3, 129.1, 128.9, 128.6, 127.3, 126.6, 126.4, 126.3, 125.3, 125.1, 124.9, 124.4, 124.1, 123.7, 122.5, 119.8, 119.0, 96.2 (C), 84.9 (C), 56.1 (C), 35.1 (C), 31.6 (CH₃), 29.3 (CH₂), 21.7 (CH₃), 21.44 (CH₃), 21.41, 16.8 (CH₂), -1.6 (CH₃)

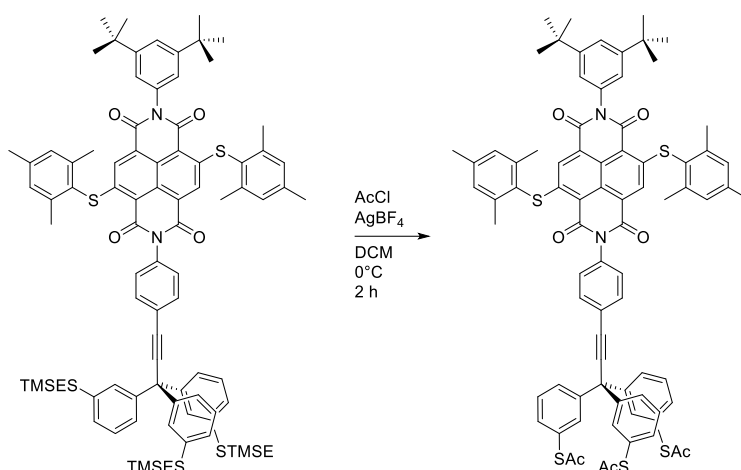
FTIR (ATR): $\tilde{\nu}$ [cm⁻¹] = 2954 (m, $\nu_{\text{as}}(\text{CH}_3)$), 2923 (m, $\nu_{\text{as}}(\text{CH}_2)$), 2853 (m, $\nu_{\text{sym}}(\text{CH}_2)$), 1703 (m, $\nu(\text{C=O})$), 1655 (m), 1585 (w), 1567 (m), 1467 (m), 1453 (m), 1415 (w), 1377 (w), 1355 (w), 1219 (w), 1115 (m), 948 (w), 790 (w), 782 (w), 732 (w), 721 (w), 694 (w), 614 (m)

ESI (+) HRMS calcd for C₈₈H₁₀₀O₄N₂S₅Si₃Na: 1516.5519 [M + Na]⁺, found m/z 1516.5328

Anal. calcd for C₈₈H₁₀₀O₄N₂S₅Si₃ (1494.33): C, 70.73; H, 6.75; N, 1.87. Found: C, 70.32; H, 6.94; N, 1.51

UV-Vis (DCM) (λ_{max} [nm], (ϵ)) = 294 (120830), 357 (11935), 370 (12164), 524 (17485)

Ph-Tpd-sNDI



In an oven dried Schlenk flask, compound **18** (43 mg, 29 μmol , 1 eq) was dissolved in dry DCM (3 mL), cooled down to 0 $^{\circ}\text{C}$ and flushed with argon before acetyl chloride (0.3 mL) was added and the reaction mixture was stirred for 20 min. Then, AgBF_4 (28 mg, 143 μmol , 5 eq) was added and the reaction mixture was stirred for another 2 hours to reach room temperature. Afterwards, the reaction mixture was quenched with crashed ice, diluted with DCM (5 mL) and extracted with DCM (3×5 mL). The combined organic layer was dried with MgSO_4 . After filtration and evaporation of all volatiles at room temperature, the crude product was purified by flash chromatography on silica gel (hexane/EtOAc = 3:1, R_f = 0.31). After drying, 31 mg of **Ph-Tpd-sNDI** was isolated as a red solid in 82% yield.

M.p. = 40 $^{\circ}\text{C}$ (decomposition)

^1H NMR (500 MHz, CDCl_3) δ [ppm] = 8.05 (s, 1H, Ar-H), 8.01 (s, 1H, Ar-H), 7.71 – 7.70 (m, 2H, Ar-H), 7.53 – 7.52 (m, 1H, Ar-H), 7.44 – 7.32 (m, 14H, Ar-H), 7.09 – 7.07 (m, 6H, Ar-H), 2.40 (s, 9H, CH_3), 2.36 (s, 12H, CH_3), 2.33 (s, 3H, CH_3), 2.32 (s, 3H, CH_3), 1.35 (s, 18H, CH_3)

^{13}C NMR (126 MHz, CDCl_3) δ [ppm] = 193.7 (CO), 163.8 (CO), 163.7 (CO), 162.64 (CO), 162.63 (CO), 152.1 (C), 149.8 (C), 149.2 (C), 145.3 (C), 143.7 (C), 143.7 (C), 141.2 (C), 141.1 (C), 135.1 (CH), 134.7 (C), 134.1 (C), 133.5 (CH), 133.0 (CH), 130.3 (CH), 130.2 (CH), 129.4 (CH), 129.2 (CH), 128.9 (CH), 128.4 (C), 126.4 (C), 126.3 (C), 125.3 (C), 125.0 (C), 124.9 (C), 124.10 (C), 124.06 (C), 123.7 (CH), 122.4 (CH), 119.8 (C), 119.0 (C), 95.2 (C), 85.7 (C), 55.8 (C), 35.1 (C), 31.6 (CH_3), 30.4 (CH_3), 21.7 (CH_3), 21.44 (CH_3), 21.42 (CH_3)

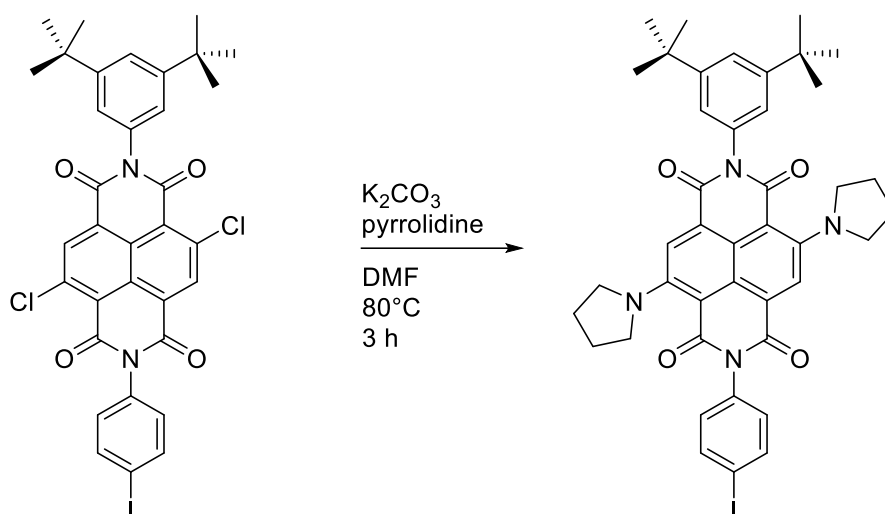
FTIR (ATR): $\tilde{\nu}$ [cm^{-1}] = 2954 (m, $\nu_{\text{as}}(\text{CH}_3)$), 2923 (m), 2854 (m, $\nu_{\text{sym}}(\text{CH}_3)$), 1705 (m, $\nu(\text{C}=\text{O})$), 1665 (m), 1603 (w), 1551 (m), 1509 (w), 1464 (w), 1433 (m), 1376 (w), 1364 (w), 1324 (m), 1247 (m), 1231 (m), 1166 (m), 1115 (m), 1035 (w), 800 (w), 788 (w), 751 (w), 721 (w), 616 (w)

ESI (+) HRMS: calcd for $\text{C}_{79}\text{H}_{70}\text{N}_2\text{O}_7\text{S}_5$ Na: 1341.3679 [$\text{M} + \text{Na}$] $^{+}$, found: 1341.4003

Anal calcd for $\text{C}_{79}\text{H}_{70}\text{N}_2\text{O}_7\text{S}_5$ (1319.74): C, 71.90; H, 5.35; N, 2.12. Found: C, 70.91; H, 5.84; N, 1.86

UV-Vis (DCM): λ_{max} [nm] (ϵ) = 297 (50637), 357 (10053), 370 (10620), 524 (19231)

2,6-Bis(1-pyrrolidinyl)-*N*-(3,5-di-*tert*-butylphenyl)-*N'*-(4-iodophenyl)naphthalene-1,4,5,8-tetracarboxdiimide (nNDI)



Compound **16** (180 mg, 248 μ mol, 1 eq) and pyrrolidine (0.2 mL, 2.5 mmol, 10 eq) were dissolved in DMF (15 mL), heated up to 80 °C and stirred for 3 hours. The dark violet solution was quenched with NH_4Cl solution (10%, 20 mL) and diluted with ethyl acetate (15 mL), followed by separating and extracting the aqueous phase with ethyl acetate (3×5 mL). The combined organic layer was washed with brine and dried with MgSO_4 . After filtration and evaporation of all volatiles, the crude product was purified by flash chromatography on silica gel (hexane/DCM = 1:3, R_f = 0.65). After drying, 195 mg (99%) of **nNDI** was isolated as a blue solid.

M.p. = 260 °C (decomposition)

^1H NMR (500 MHz, CDCl_3) δ [ppm] = 8.43 (s, 1H, Ar-H), 8.40 (s, 1H, Ar-H), 7.88 (d, J = 8.5 Hz, 2H, Ar-H), 7.54 – 7.53 (m, 1H, Ar-H), 7.11 – 7.07 (m, 4H, Ar-H), 3.48 (m, 8H, CH_2), 2.03 (m, 8H, CH_2), 1.37 (s, 18H, CH_3)

^{13}C NMR (126 MHz, CDCl_3) δ [ppm] = 164.0 (CO), 163.9 (CO), 162.1 (CO), 161.6 (CO), 151.7 (C), 147.8 (C), 147.6 (C), 138.7 (CH), 136.0 (C), 135.3 (C), 131.0 (CH), 125.7 (C), 124.9 (C), 123.1 (C), 123.0 (CH), 122.8 (CH), 122.1 (CH), 122.0 (CH), 106.0 (C), 105.0 (C), 94.5 (C), 52.8 (CH_2), 52.7 (CH_2), 35.1 (C), 31.6 (CH_3), 26.1 (CH_2)

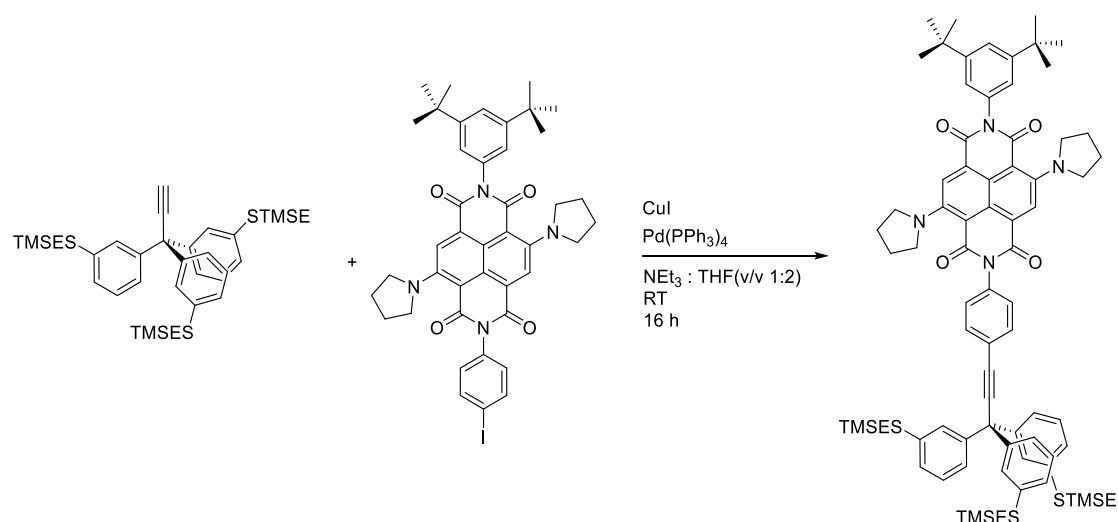
FTIR (ATR): $\tilde{\nu}$ [cm^{-1}] = 2961 (m, $\nu_{\text{as}}(\text{CH}_3)$), 2926 (m, $\nu_{\text{as}}(\text{CH}_3)$), 2869 (m, $\nu_{\text{sym}}(\text{CH}_3)$), 1690 (m, $\nu(\text{C=O})$), 1651 (m), 1568 (m), 1483 (m), 1446 (m), 1422 (m), 1395 (w), 1355 (m), 1329 (m), 1319 (m), 1259 (w), 1211 (m), 1161 (w), 1139 (m), 1118 (w), 1061 (w), 1008 (w), 980 (w), 940 (w), 930 (w), 889 (w), 879 (w), 861 (w), 815 (w), 780 (m), 747 (w), 655 (w), 510 (w)

ESI (+) HRMS calcd for $\text{C}_{42}\text{H}_{43}\text{IN}_4\text{O}_4\text{Na}$: 817.2221 [$\text{M} + \text{Na}$] $^+$, found m/z 817.2101

Anal. calcd for $\text{C}_{42}\text{H}_{43}\text{IN}_4\text{O}_4$ (794.73): C, 63.48; H, 5.45; N, 7.05. Found: C, 63.31; H, 5.42; N, 7.11.

UV-Vis (DCM) (λ_{max} [nm], (ϵ)) = 300 (51390), 349 (13998), 365 (17195), 602 (19247)

Compound 19



Under inert conditions, in an oven dried Schlenk flask, **nNDI** (16 mg, 20 μmol , 1.0 eq), $\text{Pd}(\text{PPh}_3)_4$ (1 mg, 1 μmol , 0.05 eq) and copper(I)-iodide (0.4 mg, 2 μmol , 0.1 eq) were dissolved in dry THF (2 mL) and degassed with argon for 30 min. Then, compound **6** (16 mg, 24 μmol , 1.2 eq) dissolved in distilled NEt_3 (1 mL) was added and the reaction mixture was stirred overnight. Quenching the reaction with water and diluting with ethyl acetate (15 mL) was followed by separating and extracting the aqueous phase with ethyl acetate (3×5 mL). The combined organic layer was washed with brine dried over MgSO_4 . After filtration and evaporation of all volatiles, the crude product was purified by flash chromatography on silica gel (hexane/DCM = 1:3, R_f = 0.3). After drying, 21 mg (78%) of compound **19** was isolated as a blue oil.

^1H NMR (500 MHz, CD_2Cl_2) δ [ppm] = 8.40 (s, 2H, Ar-H), 7.70 – 7.68 (m, 2H, Ar-H), 7.57 (s, 1H, Ar-H), 7.32 – 7.21 (m, 12H, Ar-H), 7.14 – 7.13 (m, 4H, Ar-H), 3.48 (m, 8H, CH_2), 2.92 – 2.89 (m, 6H, CH_2), 2.02 (m, 8H, CH_2), 1.39 (s, 18H, CH_3), 0.90 – 0.87 (m, 6H, CH_2), 0.01 (s, 27H, CH_3)

^{13}C NMR (126 MHz, CD_2Cl_2) δ [ppm] = 164.2 (CO), 164.1 (CO), 162.4 (CO), 162.0 (CO), 152.3 (C), 147.9 (C), 147.7 (C), 145.8 (C), 138.2 (C), 137.0 (C), 136.5 (C), 132.7 (CH), 129.6 (CH), 129.1 (CH), 128.9 (CH), 127.4 (CH), 126.7 (CH), 125.9 (C), 125.5 (C), 123.8 (C), 123.5 (CH), 123.2 (C), 122.8 (CH), 122.0 (CH), 106.1 (C), 105.6 (C), 96.0 (C), 85.5 (C), 56.4 (C), 35.3 (C), 31.6 (CH_3), 30.1 (CH_2), 29.4 (CH_2), 26.3 (CH_2), 17.0 (CH_2), -1.7 (CH_3)

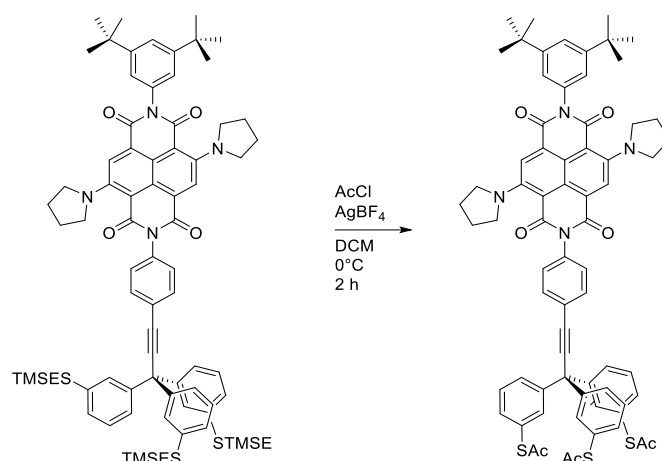
FTIR (ATR): $\tilde{\nu}$ [cm^{-1}] = 2952 (m, $\nu_{\text{as}}(\text{CH}_3)$), 2922 (s, $\nu_{\text{as}}(\text{CH}_2)$), 2852 (m, $\nu_{\text{sym}}(\text{CH}_2)$), 1693 (m, $\nu(\text{C}=\text{O})$), 1656 (m, $\nu(\text{C}=\text{C})$), 1568 (m), 1449 (m), 1425 (m), 1247 (m), 1215 (m), 1140 (m), 856 (m), 838 (m), 781 (m), 751 (m), 720 (m), 693 (m)

ESI (+) HRMS calcd for $\text{C}_{78}\text{H}_{94}\text{N}_4\text{O}_4\text{S}_3\text{Si}_3\text{Cl}$: 1367.5484 [$\text{M} + \text{Cl}$] $^+$, found m/z 1367.4533

Anal. calcd for $\text{C}_{78}\text{H}_{94}\text{N}_4\text{O}_4\text{S}_3\text{Si}_3$ (1332.07): C, 70.33; H, 7.11; N, 4.21. Found: C, 70.91; H, 7.42; N, 3.85

UV-Vis (DCM) (λ_{max} [nm], (ϵ)) = 298 (31642), 349 (7834), 365 (9306), 601 (14460)

Ph-Tpd-nNDI



In an oven dried Schlenk-flask, the compound **19** (25 mg, 19 μ mol, 1 eq) was dissolved in dry DCM (5 mL), cooled down to 0 $^{\circ}$ C and flushed with argon. Then, acetyl chloride (0.5 mL) was added and the mixture was stirred for 20 min before AgBF_4 (28 mg, 143 μ mol, 5 eq) was added. The original blue reaction mixture changed the colour to pink and after \sim 5 min, to a milky suspension, which was stirred for 2 hours to reach room temperature. The reaction mixture was quenched with crashed ice and neutralised with sodium hydrogen carbonate to pH \sim 6. After extraction with DCM, the combined organic layer was dried with MgSO_4 . After filtration and evaporation of all volatiles at room temperature, the crude product was purified by flash chromatography on silica gel (hexane/DCM = 1:2, R_f = 0.22). After drying, 15 mg (69%) of the title compound **Ph-Tpd-nNDI** was isolated as a blue solid.

M.p. = 40 $^{\circ}$ C (decomposition)

^1H NMR (500 MHz, CDCl_3) δ [ppm] = 8.43 (s, 1H, Ar-H), 8.42 (s, 1H, Ar-H), 7.72 – 7.70 (m, 2H, Ar-H), 7.54 – 7.53 (m, 1H, Ar-H), 7.44 - 7.36 (m, 12H, Ar-H), 7.31 – 7.30 (m, 2H, Ar-H), 7.11 (d, J = 1.7 Hz, 2H), 3.48 (m, 8H, CH_2), 2.40 (s, 9H, CH_3), 2.04 (m, 8H, CH_2), 1.37 (s, 18H, CH_3)

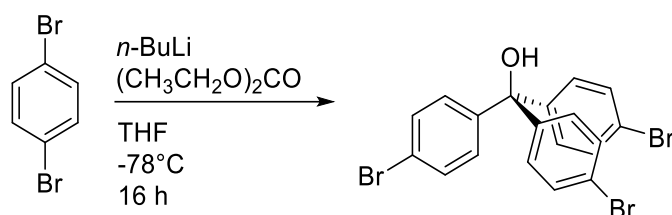
^{13}C NMR (126 MHz, CDCl_3) δ [ppm] = 193.8 (CO), 164.1 (CO), 164.0 (CO), 162.1 (CO), 161.8 (CO), 151.7 (C), 147.8 (C), 147.6 (C), 145.4 (C), 136.3 (C), 135.4 (C), 135.1 (CH), 133.5 (CH), 132.9 (CH), 130.2 (CH), 129.2 (CH), 129.1 (CH), 128.4 (C), 125.7 (C), 125.0 (C), 123.6 (C), 123.1 (C), 123.0 (CH), 122.8 (CH), 122.1 (CH), 122.0 (CH), 106.0 (C), 105.2 (C), 94.8 (C), 86.1 (C), 55.8 (C), 52.79 (CH_2), 52.75 (CH_2), 35.1 (C), 31.6 (CH_3), 30.4 (CH_3), 26.1 (CH_2)

FTIR (ATR): $\tilde{\nu}$ [cm^{-1}] = 2954 (m, $\nu_{\text{as}}(\text{CH}_3)$), 2923 (m, $\nu_{\text{as}}(\text{CH}_2)$), 2853 (m, $\nu_{\text{sym}}(\text{CH}_2)$), 1703 (m), 1655 (m), 1585 (w), 1567 (m), 1467 (m), 1453 (m), 1415 (w), 1377 (w), 1355 (w), 1219 (w), 1115 (m), 948 (w), 790 (w), 782 (w), 732 (w), 721 (w), 694 (w), 614 (m)

ESI (+) HRMS calcd for $\text{C}_{69}\text{H}_{63}\text{N}_4\text{O}_7\text{S}_3\text{H}$: 1157.4010 [$\text{M} + \text{H}$] $^{+}$, found m/z 1157.4117

Anal. calcd for $\text{C}_{69}\text{H}_{63}\text{N}_4\text{O}_7\text{S}_3$ (1156.46): C, 71.66; H, 5.49; N, 4.84. Found: C, 72.01; H, 5.78; N, 4.81

UV-Vis (DCM) (λ_{max} [nm], (ϵ)) = 298 (32790), 349 (9600), 365 (11463), 602 (17376)

Tris(4-bromophenyl)methanol 20^[356]

Under argon, 1,4-dibromobenzene (16.1 g, 68.3 mmol, 1.3 eq) was dissolved in dry THF (270.0 mL). After cooling down to -78 °C, *n*-BuLi (38.4 mL, 61.0 mmol, 0.9 eq) was added dropwise. After 10 minutes, the solution turned into a suspension and was stirred for another 60 min at this temperature. Then, diethyl carbonate (2.1 mL, 17.1 mmol, 0.25 eq) was slowly added and the reaction mixture was stirred overnight to reach room temperature. After quenching the reaction mixture with NH₄Cl (10%, 50 mL), the aqueous phase was extracted with ethyl acetate (3 × 50.0 mL) and the combined organic layer was washed with brine and dried over MgSO₄. After filtration and evaporation of all volatiles, the crude product was purified by flash chromatography on silica gel (hexane/EtOAc = 8:1, R_f = 0.27) to afford 7.80 g (92%) of the title compound as a white solid.

M.p. = 106 °C (decomposition)

¹H NMR (500 MHz, CDCl₃) δ [ppm] = 7.48 – 7.41 (m, 6H, Ar-H), 7.17 – 7.09 (m, 6H, Ar-H), 2.80 (s, 1H, O-H).

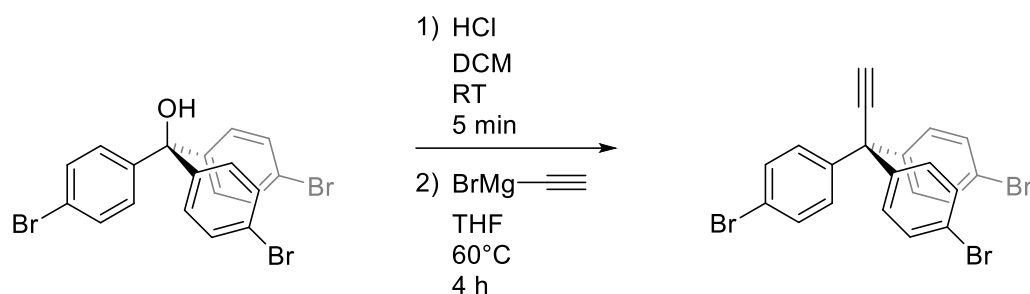
¹³C NMR (126 MHz, CDCl₃) δ [ppm] = 145.0 (C), 131.4 (CH), 129.6 (CH), 122.1 (C), 81.2 (C)

FTIR (ATR): $\tilde{\nu}$ [cm⁻¹] = 3408 (m, ν (OH)), 1589 (w), 1572 (w), 1485 (m), 1393 (m), 1317 (m), 1297 (w), 1270 (w), 1177 (w), 1150 (m, ν (R₃-C-O)), 1073 (m), 1010 (m), 1000 (m), 947 (w), 918 (w), 907 (m), 809 (m), 588 (w), 580 (w), 519 (w), 476 (w)

EI MS *m/z* (%): 340.96 (23), 185 (100), 156.97 (38), 76.03 (54)

The compound was synthesised according to a literature procedure.^[356]

3,3,3-Tris(4-bromophenyl)propyne **21**



In a round-bottom flask, tris(4-bromobenzene)methanol (1.32 g; 2.7 mmol, 1.0 eq) was dissolved in freshly distilled DCM (10.0 mL) and HCl_{aq} (30.0 mL). Then, the two phased mixture was stirred vigorously for 5 minutes while the reaction progress was monitored by GC-MS. After separation of the phases, the organic solvent was evaporated, and the residue was dried under vacuum for 3 hours at 50 °C. The oily crude product was then redissolved in dry THF (15.0 mL) before 0.5 M ethynyl magnesium bromide in THF (21.3 mL, 10.6 mmol, 4.0 eq) was added at 60 °C. The mixture was stirred at this temperature for 4 h. The reaction was quenched with water (10.0 mL), separated and the aqueous phase was extracted with ethyl acetate (3 × 5.0 mL). The combined organic layer was washed with brine and dried over MgSO₄. After filtration and evaporation of all volatiles, the crude product was purified by flash chromatography on silica gel (hexane, R_f = 0.37) to afford 0.47 g (35%) of the title compound **21** as a white powder and 0.51 g (40%) of compound **22** as a side product

M.p. = 180 °C (decomposition)

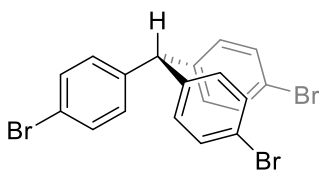
¹H NMR (500 MHz, CDCl₃) δ [ppm] = 7.46 – 7.40 (m, 6H, Ar-H), 7.14 – 7.08 (m, 6H, Ar-H), 2.74 (s, 1H, CH)

¹³C NMR (126 MHz, CDCl₃) δ [ppm] = 143.0 (C), 131.6 (CH), 130.8 (CH), 121.8 (C), 88.2 (C), 74.7 (CH), 54.5 (C)

FTIR (ATR): $\tilde{\nu}$ [cm⁻¹] = 3307 (m, $\nu(\equiv\text{CH})$), 2922 (w), 2851 (w), 1905 (w), 1572 (w), 1486 (m), 1474 (m), 1397 (m), 1076 (m), 1007 (m), 963 (w), 948 (w), 907 (m), 812 (m), 781 (w), 739 (w), 722 (w), 710 (w), 624 (m), 530 (m), 520 (m), 468 (w), 461 (w), 450 (w)

EI MS m/z (%): 424.74 (40), 264.99 (40), 189.01 (100), 131.51 (54)

Tris(4-bromophenyl)methane **22**



M.p. = 116 °C

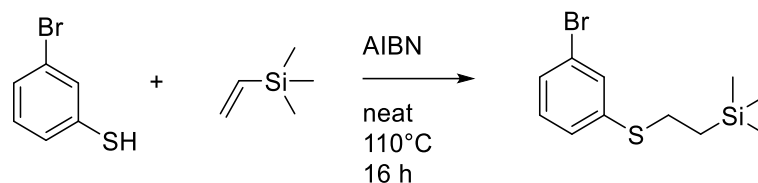
¹H NMR (500 MHz, CDCl₃) δ [ppm] = 7.44 – 7.39 (m, 6H, Ar-H), 6.96 – 6.91 (m, 6H, Ar-H), 5.40 (s, 1H, CH)

¹³C NMR (126 MHz, CDCl₃) δ [ppm] = 141.9 (C), 131.8 (CH), 131.1 (CH), 120.9 (C), 55.2 (CH)

FTIR (ATR): $\tilde{\nu}$ [cm⁻¹] = 3059 (w), 3029 (w), 1917 (w), 1898 (w), 1586 (w), 1574 (w), 1566 (w), 1483 (s), 1437 (w), 1405 (m), 1363 (w), 1315 (w), 1302 (w), 1289 (w), 1253 (w), 1214 (w), 1195 (w), 1178 (w), 1166 (w), 1108 (w), 1071 (m), 1008 (s), 958 (w), 848 (m), 829 (w), 807 (m), 780 (m), 732 (w), 530 (m), 495 (m), 482 (m)

EI MS m/z (%): 481.90 (11), 479.87 (11), 402.99 (21), 400.98 (43), 398.98 (20), 241.16 (37), 165.13 (100)

The analytical data is in accordance with the literature.^[356]

1-Bromo-3-[2-(trimethylsilyl)ethylsulfanyl]benzene 26^[196]

An oven dried pressure tube was charged with *m*-bromothiophenol (2.7 mL, 26.5 mmol, 1.0 eq), vinyltrimethylsilane (8.7 mL, 55.5 mmol, 2.1 eq) and AIBN (0.2 mL, 1.3 mmol, 0.05 eq) and sealed. Then, the mixture was heated up to 110 °C and stirred for 16 hours at this temperature. After cooling down to room temperature, the reaction was quenched with decarbonated water, diluted with DCM (50.0 mL) and separated. The organic layer was washed with brine and dried over MgSO₄. After removal of the solvent, purification by flash chromatography on silica (hexane, R_f = 0.63) gave 7.3 g (95%) of the desired compound as a colourless oil.

¹H NMR (500 MHz, CDCl₃) δ [ppm] = 7.42 – 7.39 (m 1H, Ar-H), 7.29 – 7.26 (m, 1H, Ar-H), 7.21 – 7.18 (m, 1H, Ar-H), 7.16 – 7.11 (m, 1H, Ar-H), 2.99 – 2.91 (m, 2H, CH₂), 0.93 (m, 2H, CH₂), 0.05 (s, 9H, CH₃)

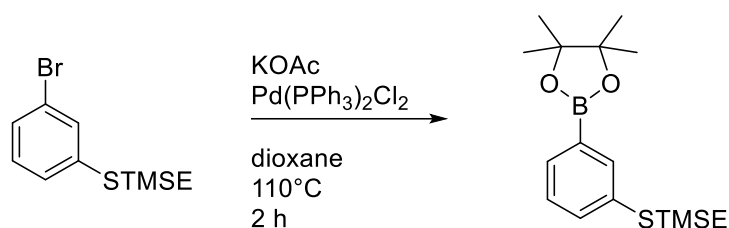
¹³C NMR (126 MHz, CDCl₃) δ [ppm] = 140.1 (C), 130.9 (CH), 130.2 (CH), 128.6 (CH), 127.1 (CH), 122.9 (C), 29.4 (CH₂), 16.8 (CH₂), -1.6 (CH₃)

FTIR (ATR): $\tilde{\nu}$ [cm⁻¹] = 2952 (w, $\nu_{as}(\text{CH}_3)$), 2918 (w, $\nu_{as}(\text{CH}_2)$), 2895 (w), 1730 (w), 1576 (m), 1555 (w), 1459 (m), 1439 (w), 1417 (w), 1400 (w), 1259 (w), 1249 (m), 1164 (w), 1101 (w), 1083 (w), 1068 (w), 1011 (w), 991 (w), 881 (w), 856 (m), 839 (m), 769 (w), 754 (w), 693 (w), 677 (w)

EI MS m/z (%): 260.03 (3), 101.09 (12), 73.04 (100)

The compound was synthesised according to a literature procedure.^[196]

3-[2-(Trimethylsilyl)ethylsulfanyl]phenylboronic acid pinacol ester **27**^[196]



Under inert conditions, in an oven dried Schlenk flask, 1-bromo-3-[2-(trimethylsilyl)ethylsulfanyl]benzene (200 mg, 0.7 mmol, 1 eq), bis(pinacolato)diboron (263 mg, 1.0 mmol, 1.50 eq) and potassium acetate (271 mg, 2.8 mmol, 4.00 eq) were dissolved in dry dioxane (5.0 mL) and purged with argon for 30 minutes. Then, $\text{Pd(PPh}_3)_2\text{Cl}_2$ (24 mg, 55 μmol , 0.08 eq) was added and mixture was stirred at 110°C for 2 hours. Then, the reaction was quenched with NH_4Cl (10%, 8 mL), diluted with ethyl acetate (5 mL) and separated. The aqueous phase was extracted with ethyl acetate (3×10.0 mL). The combined organic layer was washed with brine and dried over MgSO_4 . After filtration and evaporation of all volatiles, the crude product was purified by flash chromatography on silica gel (hexane/ EtOAc = 40:1, R_f = 0.4) to isolate 221 mg (96%) of the desired title compound as a colourless oil.

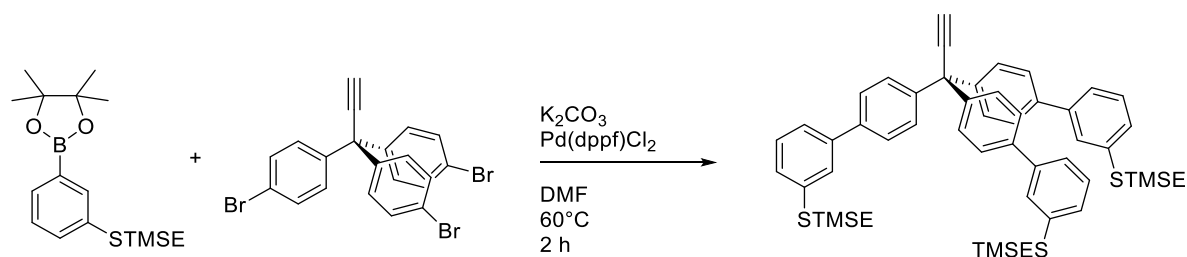
^1H NMR (500 MHz, CDCl_3) δ [ppm] = 7.75 (s, 1H, Ar-H), 7.62 – 7.57 (m, 1H, Ar-H), 7.42 – 7.38 (m, 1H, Ar-H), 7.32 – 7.27 (m, 1H, Ar-H), 3.00 – 2.93 (m, 2H, CH_2), 1.35 – 1.33 (m, 12H, CH_3), 0.97 – 0.90 (m, 2H, CH_2), 0.04 (s, 9H, CH_3)

^{13}C NMR (126 MHz, CDCl_3) δ [ppm] = 136.7 (C), 135.3 (CH), 132.1 (CH), 132.0 (CH), 128.3 (CH), 84.0 (C), 29.6 (CH_2), 25.0 (CH_3), 17.0 (CH_2), -1.60 (CH_3)

FTIR (ATR): $\tilde{\nu}$ [cm^{-1}] = 2978 (m, $\nu_{\text{as}}(\text{CH}_2)$), 2952 (m, $\nu_{\text{as}}(\text{CH}_3)$), 2924 (m), 1701 (w), 1592 (w), 1475 (w), 1400 (m), 1380 (m), 1371 (m), 1351 (s), 1314 (m), 1259 (m), 1249 (m), 1164 (w), 1143 (m), 1111 (m), 1089 (w), 1073 (w), 963 (m), 884 (w), 858 (m), 838 (m), 790 (w), 723 (w), 702 (m), 669 (w), 665 (w)

EI MS m/z (%): 336.3 (M^+ , 9), 308.2 (22), 166.1 (38), 151.1 (30), 73.1 (100)

Compound 28



In an oven dried Schlenk-flask, compound **27** (176 mg, 0.5 mmol, 3.30 eq), compound **21** (80 mg, 158 μ mol, 1.00 eq) and $Pd(dppf)Cl_2$ (6 mg, 8 μ mol, 0.05 eq) were dissolved in dry DMF (2.0 mL) and purged with argon for 60 minutes. Then potassium carbonate (271 mg, 2.8 mmol, 4.00 eq) dissolved in Milli-Q water (0.6 mL) was added and mixture was heated up to $40^\circ C$ and stirred for 2 hours at this temperature. The reaction was then quenched with NH_4Cl (10%, 15 mL) and separated. The aqueous phase was extracted with DCM (3×10.0 mL) and the combined organic layer was washed with brine and dried over $MgSO_4$. After filtration and evaporation of all volatiles, the crude product was purified by flash chromatography on silica gel (hexane/EtOAc = 80:1, R_f = 0.4) to isolate 67 mg (47%) of the desired title compound as a colourless oil.

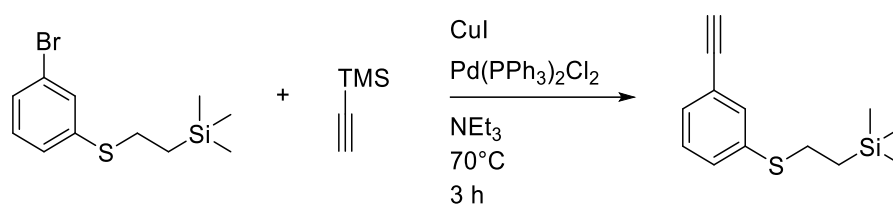
1H NMR (500 MHz, $CDCl_3$) δ [ppm] = 7.56 – 7.55 (m, 9H, Ar-H), 7.44 – 7.43 (m, 6H, Ar-H), 7.42 – 7.34 (m, 6H Ar-H), 7.30 – 7.28 (m, 3H, Ar-H), 3.05 – 2.99 (m, 6H, CH_2), 2.82 (s, 1H, CH), 0.99 – 0.93 (m, 6H, CH_2), 0.07 (s, 27H, CH_3)

^{13}C NMR (126 MHz, $CDCl_3$) δ [ppm] = 144.0 (C), 141.3 (C), 139.6 (C), 138.0 (C), 129.6 (CH), 129.3 (CH), 127.8 (CH), 127.6 (CH), 127.0 (CH), 124.7 (CH), 89.5 (C), 74.2 (CH), 55.0 (C), 29.7 (CH_2), 17.0 (CH_2), -1.6 (CH_3)

FTIR (ATR): $\tilde{\nu}$ [cm^{-1}] = 3294 (w, $\nu(\equiv CH)$), 2950 (m, $\nu_{as}(CH_3)$), 2921 (m, $\nu_{as}(CH_2)$), 2852 (w, $\nu_{sym}(CH_2)$), 1589 (m), 1559 (w), 1511 (w), 1467 (m), 1418 (w), 1388 (w), 1259 (m), 1247 (m), 1162 (w), 1103 (w), 1086 (w), 1015 (w), 882 (w), 855 (m), 829 (m), 780 (m), 763 (m), 752 (m), 693 (m), 634 (w), 588 (w)

ESI (+) HRMS calcd for $C_{54}H_{64}S_3Si_3K$: 931.3115 $[M + K]^+$, found m/z 931.3759

3-[2-(Trimethylsilyl)ethylsulfanyl]phenylacetylene **29**



Under inert conditions, in an oven dried Schlenk-flask, compound **26** (2.12 g, 7.3 mmol, 1.0 eq), $\text{Pd(PPh}_3)_2\text{Cl}_2$ (360 mg, 0.5 mmol, 0.1 eq) and copper(I)-iodide (140 mg, 0.7 mmol, 0.1 eq) were dissolved in freshly distilled triethylamine (7.0 mL) and outgassed with argon for 60 minutes. At 70°C trimethylsilylacetylene (1.4 mL, 10.3 mmol, 1.4 eq) was added and the mixture was stirred for 3 hours at this temperature. Then, the reaction was quenched with NH_4Cl (10%, 10 mL), diluted with diethyl ether (30 mL) and then the layers were separated. The organic phase was washed with decarbonated water (3×20 mL) and brine (20 mL). After removal of the solvent, the crude product was filtered through a silica plug and washed with pure hexane (500 mL). The solvent was evaporated and in a round bottom flask, before the crude product and potassium carbonate (8.0 g) were dispersed in a mixture of DCM (30 mL) and methanol (30 mL) and stirred for 30 minutes. The reaction was quenched with 2M HCl to neutralise. Separating the layers was followed by extracting the aqueous phase with DCM and then, the combined organic layer was washed with brine and dried over MgSO_4 . After filtration and evaporation of all volatiles, the crude product was purified by flash chromatography on silica gel (hexane, $R_f = 0.44$) to afford 1.4 g (82%) of the desired title compound as slightly yellowish oil.

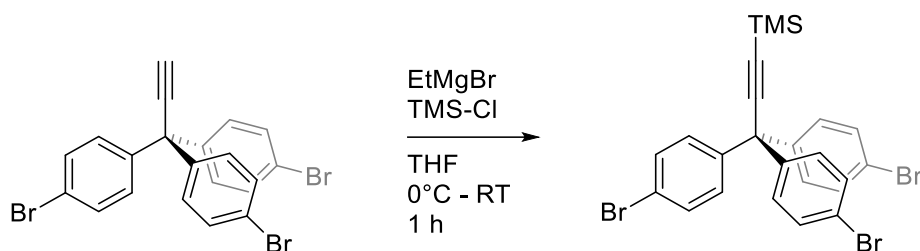
^1H NMR (500 MHz, CDCl_3) δ [ppm] = 7.41 (s, 1H, Ar-H), 7.31 – 7.26 (m, 2H, Ar-H), 7.25 – 7.21 (m, 1H, Ar-H), 3.09 (s, 1H, CH), 3.00 – 2.93 (m, 2H, CH_2), 0.97 – 0.90 (m, 2H, CH_2), 0.06 – 0.04 (m, 9H, CH_3).

^{13}C NMR (126 MHz, CDCl_3) δ [ppm] = 138.0 (C), 131.9 (CH), 129.4 (CH), 129.2 (CH), 128.8 (CH), 83.3 (C), 77.7 (CH), 29.4 (CH_2), 16.8 (CH_2), -1.6 (CH_3)

FTIR (ATR): $\tilde{\nu}$ [cm^{-1}] = 3293 (m, $\nu(\equiv\text{CH})$), 2952 (m, $\nu_{\text{as}}(\text{CH}_3)$), 2919 (w, $\nu_{\text{as}}(\text{CH}_2)$), 2895 (w), 1585 (w), 1562 (m), 1471 (w), 1398 (w), 1260 (m), 1248 (m), 1198 (w), 1163 (w), 1095 (w), 1082 (w), 1010 (w), 884 (w), 855 (m), 837 (m), 783 (m), 752 (w), 727 (w), 685 (m), 647 (m), 616 (m)

EI MS m/z (%): 234.1 (M^+ , 2), 191.1 (11), 73.1 (100)

3-[3,3,3-Tris(4-bromophenyl)]-1-trimethylsilylpropyne **23**



In a Schlenk tube, compound **21** (173.0 mg, 0.3 mmol, 1 eq) was dissolved in dry THF (10 mL) and cooled down to 0°C . Followed by addition of 3 M ethylmagnesium bromide in THF (0.2 mL, 0.4 mmol, 1.2 eq). The reaction mixture was stirred for 10 more minutes after evolving of ethane stopped. Then, trimethylsilylchloride (0.1 mL, 0.9 mmol, 2.5eq) was added dropwise and the mixture was allowed to reach room temperature and stirred for another 60 minutes. The reaction was quenched with ammonium chloride (10%, 5 mL) and the aqueous phase was extracted with ethyl acetate (3×5 mL). The combined organic layer was washed with brine and dried over MgSO_4 . After filtration and removal of all volatiles, purification of the crude product by flash chromatography on silica gel (hexane, $R_f = 0.66$) afforded 118.0 mg (60%) of the title compound as a white powder.

M.p. = 132°C

$^1\text{H NMR}$ (500 MHz, CDCl_3) δ [ppm] = 7.44 - 7.42 (m, 6H, Ar-H), 7.12 – 7.10 (m, 6H, Ar-H), 0.21 (s, 9H, CH_3)

$^{13}\text{C NMR}$ (126 MHz, CDCl_3) δ [ppm] = 143.4 (C), 131.5 (CH), 130.8 (CH), 121.6 (C), 110.1 (C), 90.9 (C), 55.4 (C), 0.0 (CH_3)

FTIR (ATR): $\tilde{\nu}$ [cm^{-1}] = 2960 (w, $\nu_{\text{as}}(\text{CH}_3)$), 2177 (w), 1484 (m), 1474 (w), 1396 (w), 1246 (w), 1076 (m), 1062 (w), 1010 (m), 843 (m), 814 (m), 758 (w), 528 (w), 496 (w)

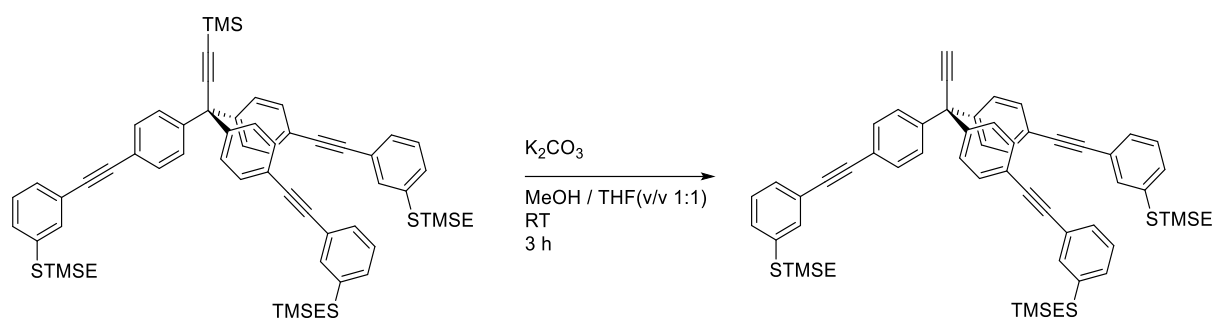
EI MS m/z (%): 496.95 (7), 423.04 (6), 73.05 (100)

M.p. = 122 °C

¹³C NMR (126 MHz, CDCl₃) δ [ppm] = 144.8 (C), 138.0 (C), 131.6 (CH), 131.4 (CH), 129.2 (CH), 128.9 (CH), 128.84 (CH), 128.78 (CH), 124.5 (C), 122.1 (C), 110.4 (C), 90.8 (C), 89.54 (C), 89.48 (C), 56.3 (C), 29.9 (C), 29.5 (CH₂), 16.9 (CH₂), 0.1 (CH₃), -1.6 (CH₃)

ESI (+) HRMS calcd for $\text{C}_{63}\text{H}_{72}\text{S}_3\text{Si}_4\text{K}$: 1075.3511 $[\text{M} + \text{K}]^+$, found m/z 1075.4460

Compound 31



In a round bottom flask compound **30** (439 mg, 0.4 mmol, 1 eq) and potassium carbonate (584 mg, 4.2 mmol, 10 eq) were dispersed in THF (10.0 mL) and methanol (10.0 mL) and stirred for 3 hours. Then, the reaction was diluted with ethyl acetate (10.0 mL) and quenched with 2M HCl to neutralise. The aqueous phase was extracted with DCM (3×10 mL) and the combined organic layer was washed with brine and dried with $MgSO_4$. After filtration and evaporation of all volatiles, the crude product was purified by flash chromatography on silica gel (hexane/ethyl acetate = 60:1, R_f = 0.4) to afford 398 mg (97%) of the desired compound as yellowish oil.

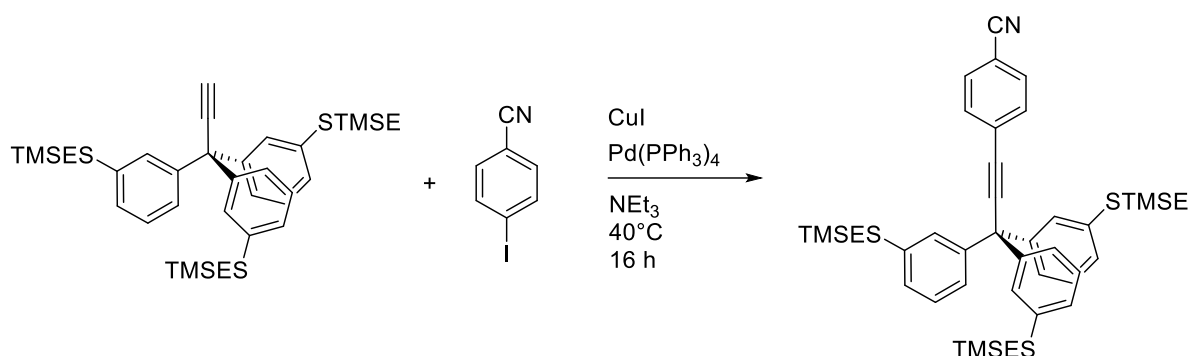
1H NMR (500 MHz, $CDCl_3$) δ [ppm] = 7.50 - 7.46 (m, 9H, Ar-H), 7.35 – 7.31 (m, 3H, Ar-H), 7.29 – 7.25 (m, 12H, Ar-H), 3.04 – 2.97 (m, 6H, CH_2), 2.79 (s, 1H, CH), 0.99 – 0.91 (m, 6H, CH_2), 0.07 (s, 27H, CH_3)

^{13}C NMR (126 MHz, $CDCl_3$) δ [ppm] = 144.3 (C), 138.0 (C), 131.6 (CH), 131.5 (CH), 129.2 (CH), 128.9 (CH), 128.84 (CH), 128.80 (CH), 123.9 (C), 122.3 (C), 89.6 (C), 89.4 (C), 88.5 (C), 74.6 (CH), 55.4 (C), 29.5 (CH_2), 16.9 (CH_2), -1.6 (CH_3)

FTIR (ATR): $\tilde{\nu}$ [cm^{-1}] = 3296 (w, $\nu(\equiv CH)$), 2950 (m, $\nu_{as}(CH_3)$), 2919 (m, $\nu_{as}(CH_2)$), 2895 (w), 2852 (w, $\nu_{sym}(CH_2)$), 1583 (m), 1560 (m), 1501 (m), 1471 (w), 1439 (w), 1403 (m), 1259 (m), 1247 (m), 1162 (w), 1147 (w), 1094 (w), 1080 (w), 1019 (w), 887 (w), 854 (m), 824 (s), 780 (m), 749 (m), 726 (w), 684 (m), 661 (w), 641 (w), 551 (w)

ESI (+) HRMS calcd for $C_{60}H_{63}S_3Si_3$: 964.3478 $[M+H]^+$, found m/z 964.4045

Compound 33



Under inert conditions, in an oven dried Schlenk flask, 4-iodobenzonitrile (44 mg, 120 μmol , 1.1 eq), $\text{Pd(PPh}_3)_4$ (20.1 mg, 17 μmol , 0.1 eq) and copper(I)-iodide (3.32 mg, 17 μmol , 0.1 eq) were dissolved in dry NEt_3 (1.5 mL) and degassed with argon for 30 min. Then, compound **6** (116 mg, 174 μmol , 1.0 eq) dissolved in NEt_3 (3 mL) was added and the reaction mixture was stirred at 40°C overnight. The reaction mixture was quenched with NH_4Cl solution (10%, 5 mL) and diluted with ethyl acetate (15 mL). The aqueous phase was extracted with ethyl acetate (3×5 mL) and the combined organic layer was washed with brine and dried with MgSO_4 . After filtration and evaporation of all volatiles, the crude product was purified by flash chromatography on silica gel (hexane/ EtOAc = 1:40, R_f = 0.32). After drying, 67 mg (50%) of the desired compound **33** was isolated as colourless viscous oil.

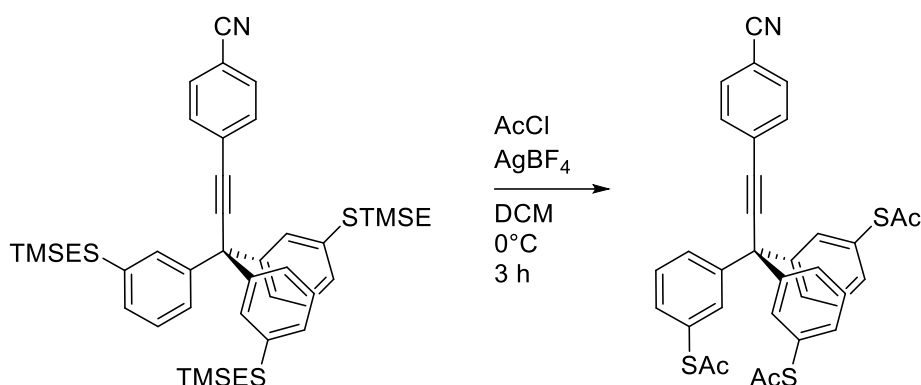
^1H NMR (500 MHz, CDCl_3) δ [ppm] = 7.63 – 7.54 (m, 4H, Ar-H), 7.25 – 7.17 (m, 9H, Ar-H), 7.03 – 6.99 (m, 3H, Ar-H), 2.89 – 2.81 (m, 6H, CH_2), 0.87 – 0.82 (m, 6H, CH_2), 0.02 – -0.06 (m, 27H, CH_3).

^{13}C NMR (126 MHz, CDCl_3) δ [ppm] = 144.9 (C), 137.9 (C), 132.3 (CH), 132.2 (CH), 128.9 (CH), 128.7 (CH), 128.3 (C), 127.3 (CH), 126.4 (CH), 118.6 (C), 111.7 (CN), 99.7 (C), 84.1 (C), 56.2 (C), 29.2 (CH_2), 16.7 (CH_2), -1.7 CH_3

FTIR (ATR): $\tilde{\nu}$ [cm^{-1}] = 2951 (m, $\nu_{\text{as}}(\text{CH}_3)$), 2920 (m), $\nu_{\text{as}}(\text{CH}_2)$, 2852 (w, $\nu_{\text{sym}}(\text{CH}_2)$), 2227 (w, $\nu(\text{C}\equiv\text{N})$), 1604 (w), 1582 (m), 1571 (w), 1501 (w), 1473 (m), 1406 (w), 1260 (m), 1247 (m), 1162 (w), 1010 (w), 882 (w), 856 (m), 835 (m), 786 (m), 771 (w), 752 (w), 720 (m), 701 (m), 694 (m), 554 (w)

ESI (+) HRMS calcd for $\text{C}_{43}\text{H}_{55}\text{NS}_3\text{Si}_3\text{K}$: 804.2441 [$\text{M} + \text{K}$] $^+$, found m/z 804.3104

Ph-Tpd-CN



In an oven dried Schlenk-flask, the compound **33** (50 mg, 65 μ mol, 1 eq) was dissolved in dry DCM (5 mL), cooled down to 0 °C and flushed with argon. Then, acetyl chloride (0.5 mL) was added, and the mixture was stirred for 20 min before AgBF₄ (50.8 mg, 261 μ mol, 4 eq) was added. The reaction mixture changed to a milky suspension, which was stirred for 3 hours to reach room temperature. The reaction mixture was quenched with crashed ice. After extraction with DCM, the combined organic layer was dried with MgSO₄. After filtration and evaporation of all volatiles at room temperature, the crude product was purified by flash chromatography on silica gel (hexane/DCM = 1:2, R_f = 0.29). After drying, 37 mg (96%) of the title compound **Ph-Tpd-CN** was isolated as a white solid.

M.p. = 40 °C (decomposition)

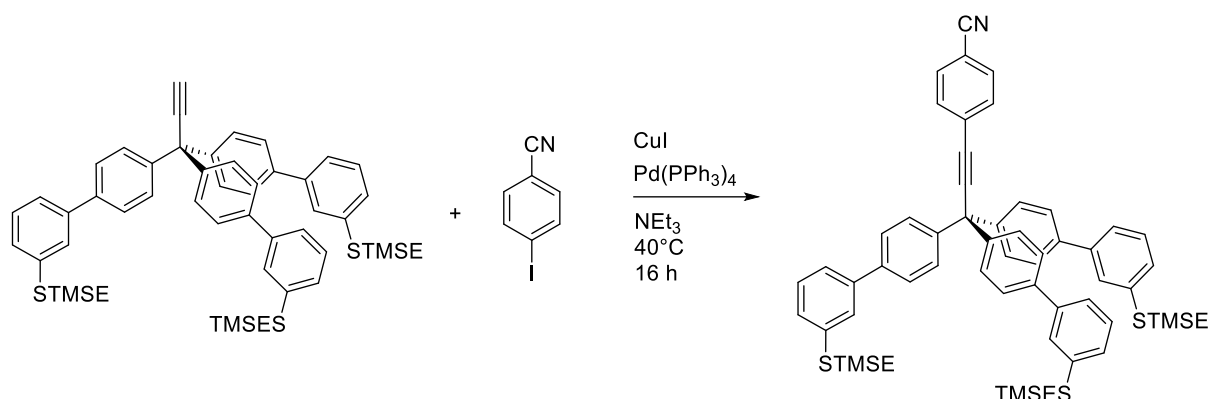
¹H NMR (500 MHz, CDCl₃) δ [ppm] = 7.62 (s, 4H, Ar-H), 7.41 – 7.34 (m, 9H, Ar-H), 7.32 – 7.29 (m, 3H, Ar-H), 2.38 (s, 9H, CH₃)

¹³C NMR (126 MHz, CDCl₃) δ [ppm] = 193.6 (CO), 144.9 (C), 135.1 (CH), 133.6 (CH), 132.5 (CH), 132.2 (CH), 130.1 (CH), 129.3 (CH), 128.5 (C), 128.0 (C), 111.9 (CN), 98.5 (C), 84.9 (C), 55.9 (C), 30.4 (CH₃)

FTIR (ATR): $\tilde{\nu}$ [cm⁻¹] = 2954 (m, ν_{as} (CH₃)), 2921 (m), 2851 (m), 2227 (m, ν (C \equiv N)), 1699 (s, ν (C=O)), 1603 (m), 1585 (m), 1501 (w), 1470 (m), 1406 (m), 1351 (m), 1117 (m), 1100 (m), 1085 (m), 999 (w), 947 (m), 839 (m), 791 (m), 777 (w), 722 (m), 699 (m), 611 (m), 555 (m)

ESI (+) HRMS calcd for C₃₄H₂₅NO₃S₃Na: 614.0894 [M + Na]⁺, found m/z 614.1321

Compound 34



Under inert conditions, in an oven dried Schlenk flask, 4-iodobenzonitrile (32.7 mg, 143 μ mol, 1.1 eq), Pd(PPh₃)₄ (15 mg, 13 μ mol, 0.1 eq) and copper(I)-iodide (2.47 mg, 13 μ mol, 0.1 eq) were dissolved in dry NEt₃ (2 mL) and degassed with argon for 30 min. Then, compound **28** (116 mg, 130 μ mol, 1.0 eq) dissolved in NEt₃ (4 mL) was added and the reaction mixture was stirred at 40 °C overnight. The reaction mixture was quenched with NH₄Cl solution (10%, 5 mL) and diluted with ethyl acetate (15 mL). The aqueous phase was extracted with ethyl acetate (3 \times 5 mL) and the combined organic layer was washed with brine and dried with MgSO₄. After filtration and evaporation of all volatiles, the crude product was purified by flash chromatography on silica gel (hexane/EtOAc = 1:60, R_f = 0.14). After drying, 118 mg (91%) of the desired compound **34** was isolated as a viscous oil.

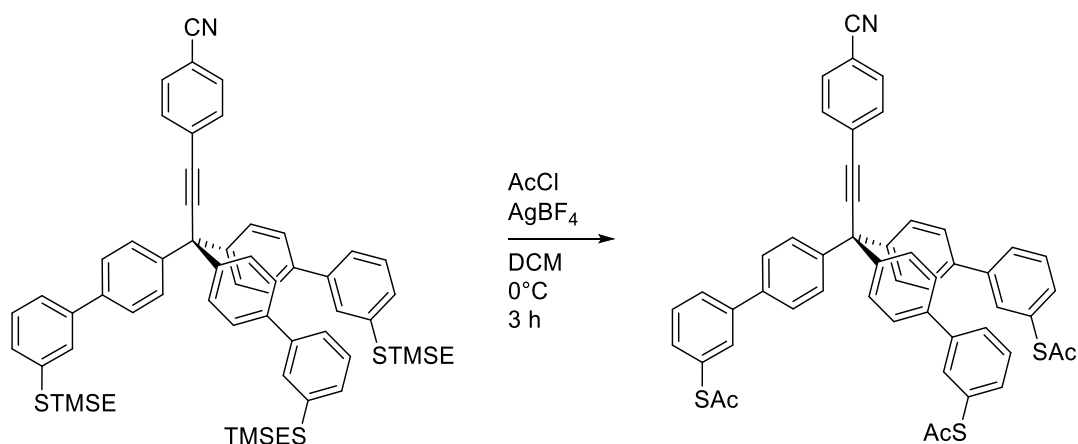
¹H NMR (500 MHz, CDCl₃) δ [ppm] = 7.64 (s, 4H, Ar-H), 7.59 – 7.53 (m, 9H, Ar-H), 7.46 – 7.33 (m, 12H, Ar-H), 7.31 – 7.27 (m, 3H, Ar-H), 3.07 – 2.95 (m, 6H, CH₂), 0.98 – 0.93 (m, 6H, CH₂), 0.08 – 0.01 (m, 27H, CH₃)

¹³C NMR (126 MHz, CDCl₃) δ [ppm] = 144.0 (C), 141.2 (C), 139.8 (C), 138.1 (C), 132.4 (CH), 132.2 (CH), 129.7 (CH), 129.4 (CH), 128.4 (C), 127.8 (CH), 127.7 (CH), 127.2 (CH), 124.7 (CH), 118.7 (C), 111.7 (CN), 100.1 (C), 84.2 (C), 55.7 (C), 29.9 (CH₂), 17.0 (CH₂), -1.6 (CH₃)

FTIR (ATR): $\tilde{\nu}$ [cm⁻¹] = 2951 (m, ν_{as} (CH₃)), 2922 (s, ν_{as} (CH₂)), 2852 (m, ν_{sym} (CH₂)), 2227 (w, ν (C \equiv N)), 2161 (w), 1603 (w), 1588 (w), 1559 (w), 1510 (w), 1501 (w), 1467 (m), 1417 (w), 1388 (w), 1260 (m), 1247 (m), 1162 (w), 1104 (w), 1015 (w), 882 (w), 856 (m), 832 (m), 780 (m), 763 (w), 751 (m), 721 (w), 693 (m), 554 (w)

ESI (+) HRMS calcd for C₆₁H₆₇NS₃Si₃K: 1032.3380 [M + K]⁺, found m/z 1032.5107

Bp-Tpd-CN



In an oven dried Schlenk flask, the compound **34** (79 mg, 79 μmol , 1 eq) was dissolved in dry DCM (5 mL), cooled down to 0 °C and flushed with argon. Then, acetyl chloride (0.5 mL) was added, and the mixture was stirred for 20 min before AgBF₄ (108 mg, 556 μmol , 7 eq) was added. The reaction mixture changed to a milky suspension, which was stirred for 3 hours to reach room temperature. The reaction mixture was quenched with crashed iced. After extraction with DCM, the combined organic layer was dried with MgSO₄. After filtration and evaporation of all volatiles at room temperature, the crude product was purified by flash chromatography on silica gel (hexane/DCM = 1:2, R_f = 0.17). After drying, 51 mg (79%) of the title compound **Bp-Tpd-CN** was obtained as a white solid.

M.p. = 40 °C (decomposition)

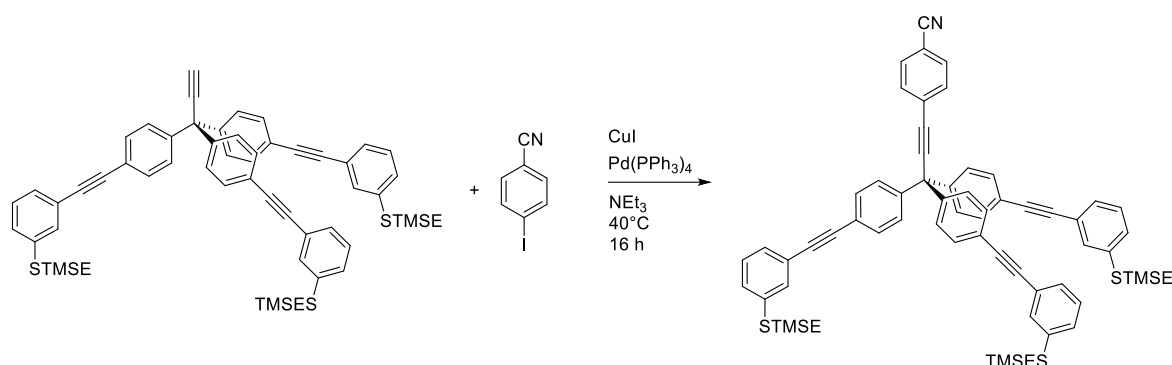
¹H NMR (500 MHz, CDCl₃) δ [ppm] = 7.69 – 7.61 (m, 9H, Ar-H), 7.58 (d, J = 8.2 Hz, 6H, Ar-H), 7.52 – 7.46 (m, 3H, Ar-H), 7.46 – 7.38 (m, 8H, Ar-H), 2.45 (s, 9H, CH₃).

¹³C NMR (126 MHz, CDCl₃) δ [ppm] = 194.0 (CO), 144.1 (C), 141.7 (C), 139.2 (C), 133.4 (CH), 133.2 (CH), 132.4 (CH), 132.2 (CH), 129.8 (CH), 129.7 (CH), 128.7 (C), 128.4 (C), 128.2 (CH), 127.2 (CH), 111.7 (CN), 99.9 (C), 84.3 (C), 55.7 (C), 30.4 (CH₃)

FTIR (ATR): $\tilde{\nu}$ [cm⁻¹] = 2920 (m, $\nu_{\text{as}}(\text{CH}_3)$), 2850 (m, $\nu_{\text{sym}}(\text{CH}_3)$), 2226 (m, $\nu(\text{C}\equiv\text{N})$), 1699 (s), 1603 (m), 1591 (m), 1511 (m), 1501 (m), 1468 (m), 1421 (m), 1390 (m), 1351 (m), 1100 (m), 1015 (m), 948 (m), 836 (m), 784 (s), 693 (m), 613 (m), 592 (m), 555 (m)

ESI (+) HRMS calcd for C₅₂H₃₇NO₃S₃H: 819.1935 [M + H]⁺, found m/z 819.2639

Compound 35



Under inert conditions, in an oven dried Schlenk flask, 4-iodobenzonitrile (25.3 mg, 111 μmol , 1.2 eq), Pd(PPh₃)₄ (11 mg, 9 μmol , 0.1 eq) and copper(I)-iodide (1.7 mg, 9 μmol , 0.1 eq) were dissolved in dry NEt₃ (1.5 mL) and degassed with argon for 30 min. Then, compound **31** (89 mg, 92 μmol , 1.0 eq) dissolved in NEt₃ (4 mL) was added and the reaction mixture was stirred at 40 °C overnight. The reaction mixture was quenched with NH₄Cl solution (10%, 5 mL) and diluted with ethyl acetate (15 mL). The aqueous phase was extracted with ethyl acetate (3 \times 5 mL) and the combined organic layer was washed with brine and dried with MgSO₄. After filtration and evaporation of all volatiles, the crude product was purified by flash chromatography on silica gel (hexane/EtOAc = 1:40, R_f = 0.27). After drying, 91 mg (92%) of the desired compound **35** was isolated as a white solid.

M.p. = 49 °C

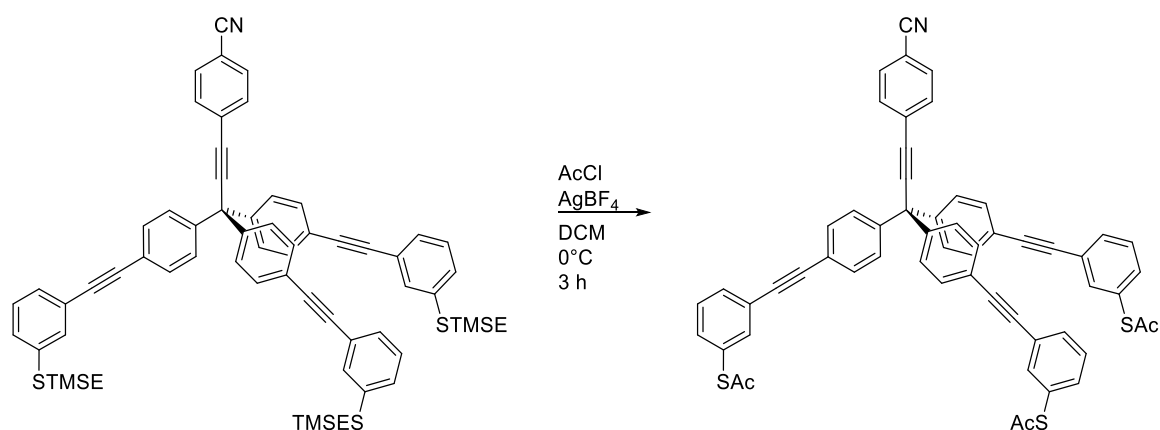
¹H NMR (500 MHz, CDCl₃) δ [ppm] = 7.66 – 7.58 (m, 4H, Ar-H), 7.53 – 7.48 (m, J = 8.3 Hz, 7H, Ar-H), 7.45 (s, 3H, Ar-H), 7.34 – 7.26 (m, 14H, Ar-H), 3.01 – 2.95 (m, 6H, CH₂), 0.97 – 0.91 (m, 6H, CH₂), 0.06 (s, 27H, CH₃)

¹³C NMR (126 MHz, CDCl₃) δ [ppm] = 144.3 (C), 138.0 (C), 132.4 (CH), 132.2 (CH), 131.8 (CH), 131.5 (CH), 129.2 (CH), 128.92 (CH), 128.88 (CH), 128.83 (CH), 128.0 (C), 123.8 (C), 122.5 (C), 118.6 (C), 111.9 (CN), 98.9 (C), 89.8 (C), 89.3 (C), 84.6 (C), 56.2 (C), 29.5 (CH₂), 16.9 (CH₂), -1.6 (CH₃)

FTIR (ATR): $\tilde{\nu}$ [cm⁻¹] = 2950 (m, $\nu_{\text{as}}(\text{CH}_3)$), 2920 (m, $\nu_{\text{as}}(\text{CH}_2)$), 2851 (w, $\nu_{\text{sym}}(\text{CH}_2)$), 2227 (w, $\nu(\text{C}\equiv\text{N})$), 2187 (w), 2161 (w), 1603 (w), 1583 (m), 1560 (w), 1501 (m), 1470 (w), 1438 (w), 1404 (w), 1259 (w), 1247 (m), 1162 (w), 1018 (w), 886 (w), 854 (m), 826 (m), 781 (m), 749 (w), 721 (w), 684 (m), 552 (w)

ESI (+) HRMS calcd for C₆₇H₆₇NS₃Si₃K: 1104.3380 [M + K]⁺, found m/z 1103.8252

Tol-Tpd-CN



In an oven dried Schlenk flask, compound **35** (50 mg, 47 μmol , 1 eq) was dissolved in dry DCM (5 mL), cooled down to 0 °C and flushed with argon. Then, acetyl chloride (0.5 mL) was added, and the mixture was stirred for 20 min before AgBF₄ (36.5 mg, 187 μmol , 4 eq) was added. The reaction mixture changed to a milky suspension, which was stirred for 3 hours to reach room temperature. The reaction mixture was quenched with crashed ice. After extraction with DCM, the combined organic layer was dried with MgSO₄. After filtration and evaporation of all volatiles at room temperature, the crude product was purified by flash chromatography on silica gel (hexane/DCM = 1:3, R_f = 0.43). After drying, 23 mg (56%) of the title compound **Tol-Tpd-CN** was isolated as a white solid.

M.p. = 40 °C (decomposition)

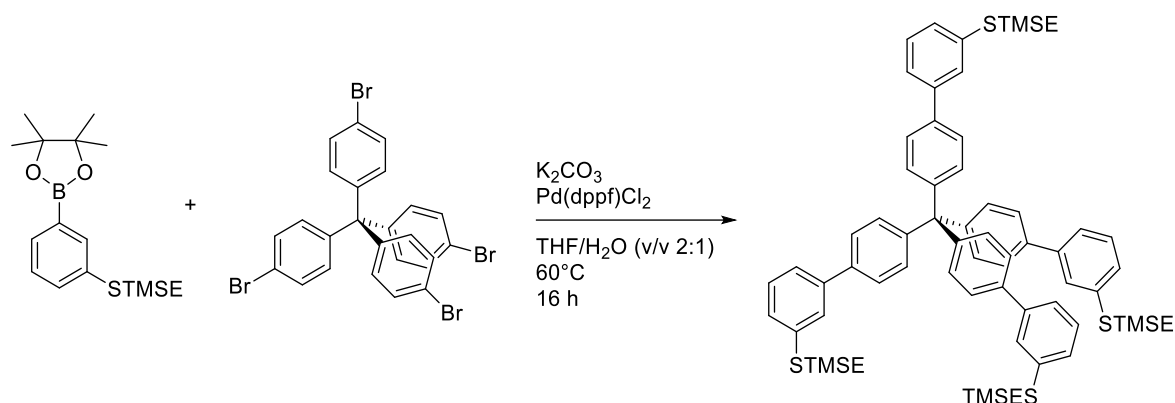
¹H NMR (500 MHz, CDCl₃) δ [ppm] = 7.66 – 7.54 (m, 10H, Ar-H), 7.50 (d, J = 8.5 Hz, 6H, Ar-H), 7.44 – 7.35 (m, 6H, Ar-H), 7.29 (d, J = 8.5 Hz, 6H, Ar-H), 2.44 (s, 9H, CH₃)

¹³C NMR (126 MHz, CDCl₃) δ [ppm] = 193.6 (CO), 144.3 (C), 137.5 (CH), 134.5 (CH), 132.7 (CH), 132.4 (CH), 132.2 (CH), 131.8 (CH), 129.3 (CH), 129.2 (CH), 128.4 (C), 128.0 (C), 124.5 (C), 122.3 (C), 111.9 (CN), 98.8 (C), 90.0 (C), 89.2 (C), 84.7 (C), 56.2 (C), 30.4 (CH₃)

FTIR (ATR): $\tilde{\nu}$ [cm⁻¹] = 2953 (w, $\nu_{\text{as}}(\text{CH}_3)$), 2921 (m), 2851 (m, $\nu_{\text{sym}}(\text{CH}_3)$), 2226 (w, $\nu(\text{C}\equiv\text{N})$), 2168 (w), 2146 (w), 1702 (m), 1603 (w), 1587 (w), 1560 (w), 1501 (m), 1466 (w), 1403 (w), 1351 (w), 1108 (m), 1078 (w), 1018 (w), 948 (w), 885 (w), 825 (m), 787 (m), 752 (w), 684 (m), 612 (m), 553 (w)

ESI (+) HRMS calcd for C₅₈H₃₇NO₃S₃H: 891.1935 [M + H]⁺, found m/z 891.2677

Compound 37



In an oven dried Schlenk-flask, compound **27** (272 mg, 0.8 mmol, 4.60 eq), tetrakis(*p*-bromobenzene)methane (112 mg, 189 μ mol, 1.00 eq), **Pd(dppf)Cl₂** (6 mg, 9 μ mol, 0.05 eq) and Xphos (8 mg, 17 μ mol, 0.1 eq) were dissolved in dry THF (3.0 mL) and purged with argon for 60 min. Then potassium carbonate (130 mg, 0.9 mmol, 5.00 eq) - dissolved in decarbonated water (1.5 mL) - was added and mixture was heated up to 60 °C and stirred overnight at this temperature. The reaction mixture was quenched with NH₄Cl solution (10%, 5 mL) and diluted with ethyl acetate (15 mL). The aqueous phase was extracted with ethyl acetate (3 \times 5 mL) and the combined organic layer was washed with brine and dried with MgSO₄. After filtration and evaporation of all volatiles, the crude product was purified by flash chromatography on silica gel (hexane/EtOAc 25:1, *R_f* = 0.2) to isolate 35 mg (17 %) of the desired compound as a white solid.

M.p. = 127 °C

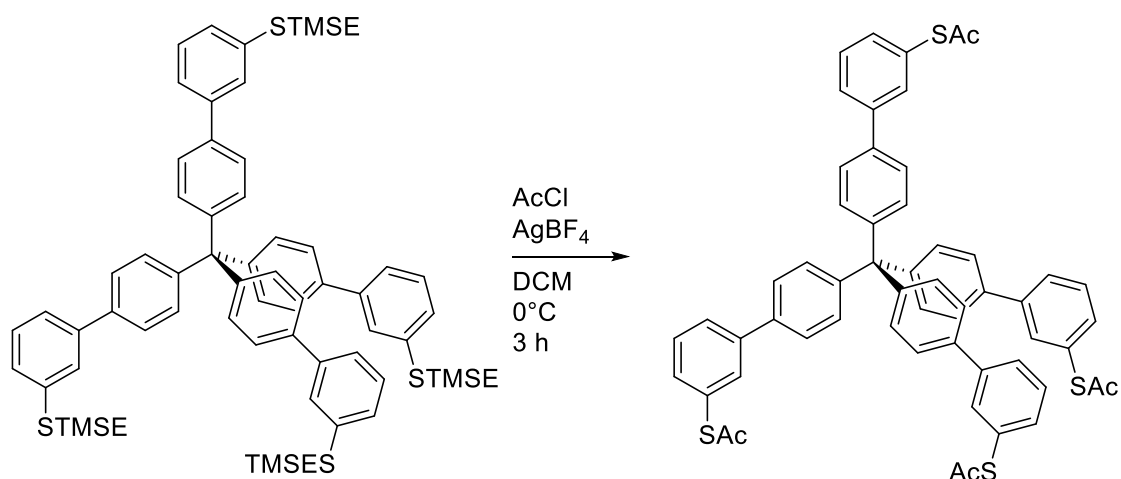
¹H NMR (500 MHz, CDCl₃) δ [ppm] = 7.58 – 7.55 (m, 12H, Ar-H), 7.44 – 7.42 (m, 12H, Ar-H), 7.38 - 7.30 (m, 8H, Ar-H), 3.06 – 2.98 (m, 8H, CH₂), 1.03 – 0.94 (m, 8H, CH₂), 0.06 (s, 36H, CH₃).

¹³C NMR (126 MHz, CDCl₃) δ [ppm] = 146.1 (C), 141.3 (C), 138.4 (C), 137.9 (C), 131.6 (CH), 129.3 (CH), 127.7 (CH), 127.6 (CH), 126.4 (CH), 124.6 (CH), 64.3 (C), 29.7 (CH₂), 17.0 (CH₂), -1.6 (CH₃)

FTIR (ATR): $\tilde{\nu}$ [cm⁻¹] = 2949 (m, *v*_{as}(CH₃)), 2920 (m, *v*_{as}(CH₂)), 2851 (m, *v*_{sym}(CH₂)), 1590 (m), 1573 (w), 1556 (w), 1510 (w), 1467 (m), 1418 (w), 1389 (w), 1259 (m), 1246 (m), 1161 (w), 1103 (w), 1087 (w), 1014 (m), 1007 (w), 880 (w), 855 (m), 826 (m), 797 (m), 775 (m), 752 (m), 696 (m), 586 (w)

ESI (+) HRMS calcd for C₆₉H₈₄O₄S₄K: 1191.4170 [M + K]⁺, found *m/z* 1191.4814

Compound 38



In an oven dried Schlenk-flask, compound **37** (39 mg, 34 μ mol, 1.00 eq) was dissolved in dry DCM (5 mL), cooled down to 0 °C and flushed with argon. Then, acetyl chloride (2.0 mL) was added, and the mixture was stirred for 20 min before AgBF₄ (46 mg, 237 μ mol, 7.00 eq) was added. The reaction mixture changed to a milky suspension, which was stirred for 3 hours to reach room temperature. The reaction mixture was quenched with crashed ice. After extraction with DCM, the combined organic layer was dried with MgSO₄. After filtration and evaporation of all volatiles at room temperature, the crude product was purified by flash chromatography on silica gel (hexane/DCM = 1:2, R_f = 0.44). After drying, 29 mg (93%) of the title compound **38** was as a white solid.

M.p. = 40 °C (decomposition)

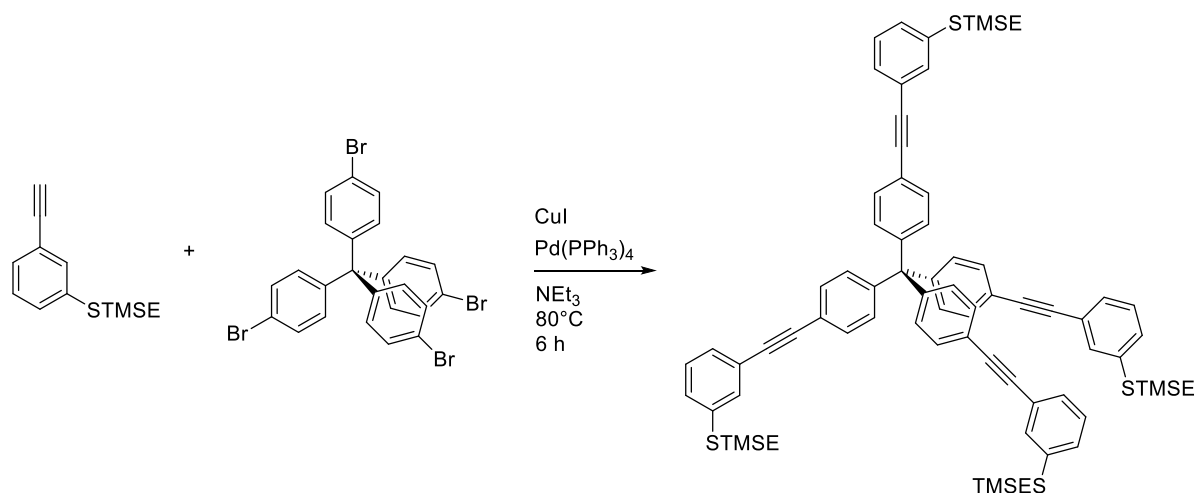
¹H NMR (500 MHz, CD₂Cl₂) δ [ppm] = 7.69 -7.67 (m, 8H, Ar-H), 7.58 – 7.56 (m, 8H, Ar-H), 7.50 - 7.39 (m, 16H, Ar-H), 2.42 (s, 12H, CH₃).

¹³C NMR (126 MHz, CD₂Cl₂) δ [ppm] = 194.1 (CO), 146.6 (C), 142.0 (C), 138.1 (C), 133.6 (C), 133.4 (CH), 131.9 (CH), 129.9 (CH), 129.2 (CH), 128.4 (CH), 126.8 (CH), 64.7 (C), 30.5 (CH₃).

FTIR (ATR): $\tilde{\nu}$ [cm⁻¹] = 2920 (w, ν_{as} (CH₃)), 1700 (m), 1590 (m), 1555 (w), 1508 (w), 1468 (m), 1421 (w), 1390 (w), 1351 (w), 1119 (m), 1097 (m), 1041 (w), 1014 (m), 997 (w), 949 (m), 826 (m), 784 (m), 747 (w), 693 (m), 610 (m), 592 (m)

ESI (+) HRMS calcd for C₅₇H₄₄O₄S₄Na: 943.2015 [M + Na]⁺, found m/z 943.2170

Compound 39



Under inert conditions, in an oven dried Schlenk-flask, tetrakis(*p*-bromobenzene)methane (100 mg, 0.2 mmol, 1.00 eq), Pd(PPh₃)₄ (29 mg, 25 μmol, 0.16 eq) and copper(I)-iodide (6 mg, 31 μmol, 0.1 eq) were dissolved in freshly distilled triethylamine (0.5 mL) and outgassed with argon for 60 minutes. At 80 °C, compound **29** (184 mg, 0.8 mmol, 5.00 eq) - dissolved in freshly distilled and outgassed triethylamine (1 mL) - was added and mixture was stirred for 6 hours at this temperature. The reaction mixture was quenched with NH₄Cl solution (10%, 5 mL) and diluted with ethyl acetate (15 mL). The aqueous phase was extracted with ethyl acetate (3 × 5 mL) and the combined organic layer was washed with brine and dried with MgSO₄. After filtration and evaporation of all volatiles, the crude product was purified by flash chromatography on silica gel (hexane/DCM = 12:1, R_f = 0.14) yielded 100 mg (51%) of the title compound **39** and 33 mg (19%) of three times reacted compound **41**.

M.p. = 145 °C

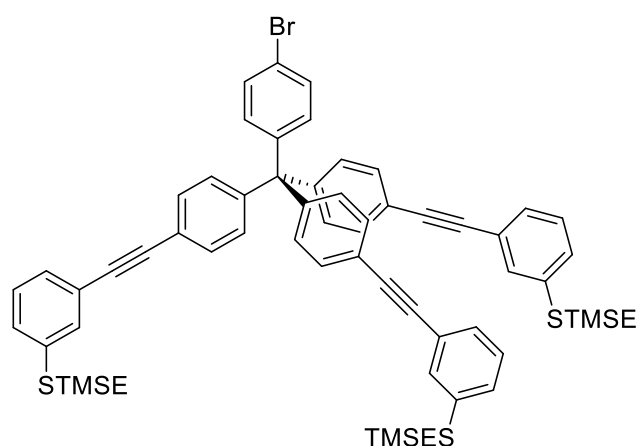
¹H NMR (500 MHz, CDCl₃) δ [ppm] = 7.49 – 7.47 (m, 12H, Ar-H), 7.34 – 7.30 (m, 4H, Ar-H), 7.29 – 7.25 (m, 8H, Ar-H), 7.23 – 7.21 (m, 8H, Ar-H), 3.04 – 2.96 (m, 8H, CH₂), 0.99 – 0.93 (m, 8H, CH₂), 0.07 (s, 36H, CH₃).

¹³C NMR (126 MHz, CDCl₃) δ [ppm] = 146.1 (C), 138.0 (C), 131.4 (CH), 131.3 (CH), 131.0 (CH), 128.9 (CH), 128.8 (CH), 128.8 (CH), 124.9 (C), 121.4 (C), 89.6 (C), 89.5 (C), 65.0 (C), 29.5 (CH₂), 16.9(CH₂), -1.6 (CH₃)

FTIR (ATR): $\tilde{\nu}$ [cm⁻¹] = 2949 (m, ν_{as} (CH₂)), 2920 (m), 2884 (w, ν_{sym} (CH₃)), 2851 (w), 1584 (m), 1559 (w), 1502 (m), 1473 (w), 1440 (w), 1403 (w), 1267 (w), 1258 (w), 1244 (m), 1164 (w), 1108 (w), 1094 (w), 1085 (w), 1019 (w), 1008 (w), 897 (w), 889 (w), 854 (m), 823 (m), 779 (m), 751 (w), 720 (w), 683 (w), 527 (w)

ESI (+) HRMS calcd for C₇₇H₈₄S₄Si₄: 1248.4532 [M + Na]⁺, found *m/z* 1248.5166

Compound 41



M.p. = 45 °C

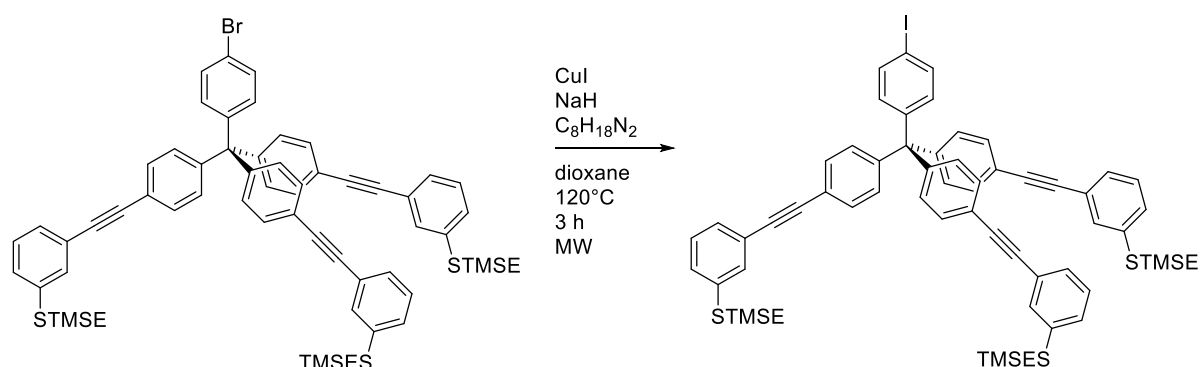
¹H NMR (500 MHz, CDCl₃) δ [ppm] = 7.47 -7.26 (m, 20H, Ar-H), 7.21 – 7.19 (m, 6H, Ar-H), 7.10 (m, 2H, Ar-H), 3.04 – 2.96 (m, 6H, CH₂), 1.00 – 0.92 (m, 6H, CH₂), 0.07 (s, 27H, CH₃)

¹³C NMR (126 MHz, CDCl₃) δ [ppm] = 146.0 (C), 144.9 (C), 138.0 (C), 132.7 (CH), 131.4 (CH), 131.3 (CH), 131.2 (CH), 131.0 (CH), 128.9 (CH), 128.9 (CH), 128.8 (CH), 123.9 (C), 121.4 (C), 120.8 (C), 89.6 (C), 89.4 (C), 64.7 (C), 29.5 (CH₂), 16.9 CH₂, -1.6 (CH₃)

FTIR (ATR): $\tilde{\nu}$ [cm⁻¹] = 2950 (m, $\nu_{as}(\text{CH}_3)$), 2920 (m, $\nu_{as}(\text{CH}_2)$), 2852 (w, $\nu_{sym}(\text{CH}_2)$), 2166 (w), 1583 (m), 1560 (w), 1502 (m), 1486 (m), 1471 (w), 1439 (w), 1398 (w), 1259 (m), 1247 (m), 1162 (w), 1148 (w), 1094 (w), 1079 (w), 1018 (w), 1009 (m), 888 (w), 854 (m), 837 (m), 821 (m), 780 (m), 750 (m), 684 (m), 576 (w), 545 (w), 507 (w)

ESI (+) HRMS calcd for C₆₄H₆₇BrS₃Si₃Na: 1119.2771 [M + Na]⁺, found m/z 1119.2756

Compound 42



Under inert conditions, in an oven dried microwave tube, compound **41** (53 mg, 48 μ mol, 1.00 eq), copper(I)-iodide (0.9 mg, 5 μ mol, 0.10 eq), sodium iodide (15 mg, 97 μ mol, 2 eq) and 1,2-cyclohexanediylmethanamine (1.5 μ l; 10 μ mol, 0.20 eq) were dissolved in dry dioxane (2.0 mL). The reaction was carried out in a microwave system at 230 W at 120 °C for 3 hours. The reaction mixture was quenched with NH₄Cl solution (10%, 5 mL) and diluted with ethyl acetate (15 mL). The aqueous phase was extracted with ethyl acetate (3 \times 5 mL) and the combined organic layer was washed with brine and dried with MgSO₄. After filtration and evaporation of all volatiles, the crude product was purified by flash chromatography on silica gel (hexane/DCM = 5:2, R_f = 0.28) yielded 47 mg (97%) of the desired title compound.

M.p. = 45-50 °C

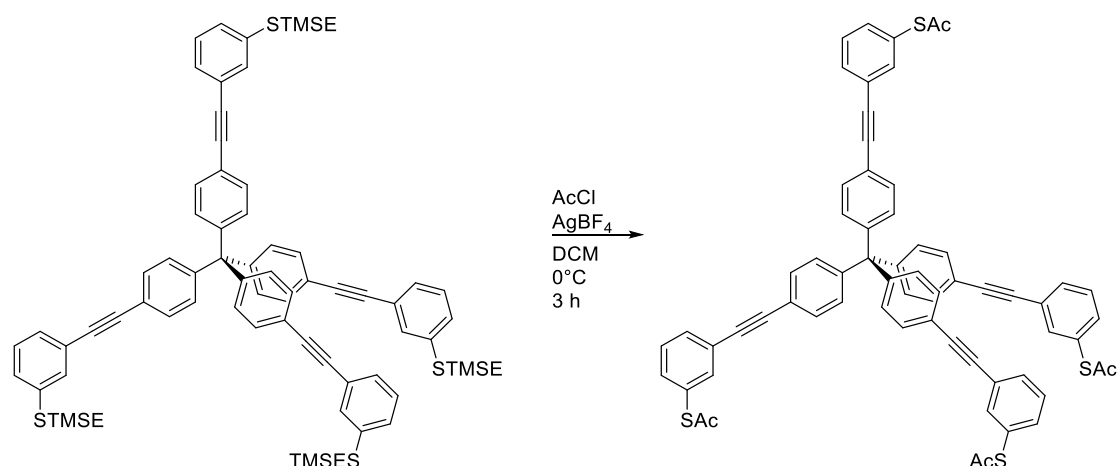
¹H NMR (500 MHz, CDCl₃) δ [ppm] = 7.63 -7.61 (d, ³J = 8.6 Hz, 2H, Ar-H), 7.47- 7.44 (m, 9H, Ar-H), 7.33 – 7.29 (m, 3H, Ar-H), 7.28 – 7.25 (m, 6H, Ar-H), 7.20 -7.18 (m, 6H), 6.97 (d, ³J = 8.6 Hz, 2H, Ar-H), 3.02 – 2.95 (m, 6H, CH₂), 0.99 – 0.91 (m, 6H, CH₂), 0.06 (s, 27H, CH₃).

¹³C NMR (126 MHz, CDCl₃) δ [ppm] = 146.0 (C), 145.6 (C), 138.0 (C), 137.1 (CH), 133.0 (CH), 131.4 (CH), 131.3 (CH), 131.0 (CH), 128.9 (CH), 128.9 (CH), 128.8 (CH), 123.9 (C), 121.4 (C), 92.5 (C), 89.6 (C), 89.4 (C), 64.8 (C), 29.5 (CH₂), 16.9 (CH₂), -1.6 (CH₃)

FTIR (ATR): $\tilde{\nu}$ [cm⁻¹] = 2949 (m, ν_{as} (CH₃)), 2920 (m, ν_{as} (CH₂)), 2851 (w, ν_{sym} (CH₂)), 2167 (w), 1583 (m), 1560 (w), 1502 (m), 1483 (w), 1471 (w), 1439 (w), 1398 (w), 1259 (w), 1247 (m), 1162 (w), 1094 (w), 1079 (w), 1018 (w), 1004 (m), 888 (w), 854 (m), 836 (m), 821 (m), 812 (m), 780 (m), 763 (w), 750 (m), 684 (m), 576 (w), 544 (w), 532 (w), 505 (w)

ESI (+) HRMS calcd for C₆₄H₆₇IS₃Si₃H: 1142.2758 [M + H]⁺, found m/z 1142.3373

Compound 40



In an oven dried Schlenk-flask, compound **39** (60 mg, 48 μ mol, 1 eq) was dissolved in dry DCM (2 mL), cooled down to 0 °C and flushed with argon. Then, acetyl chloride (0.2 mL) was added, and the mixture was stirred for 20 min before AgBF₄ (65 mg, 336 μ mol, 7.0 eq) was added. The reaction mixture changed to a milky suspension, which was stirred for 3 hours to reach room temperature. The reaction mixture was quenched with crashed ice. After extraction with DCM, the combined organic layer was dried with MgSO₄. After filtration and evaporation of all volatiles at room temperature, the crude product was purified by flash chromatography on silica gel (hexane/DCM = 2:3, R_f = 0.14). After drying, 31 mg (63%) of the title compound **40** was isolated as a white solid.

M.p. = 40 °C (decomposition)

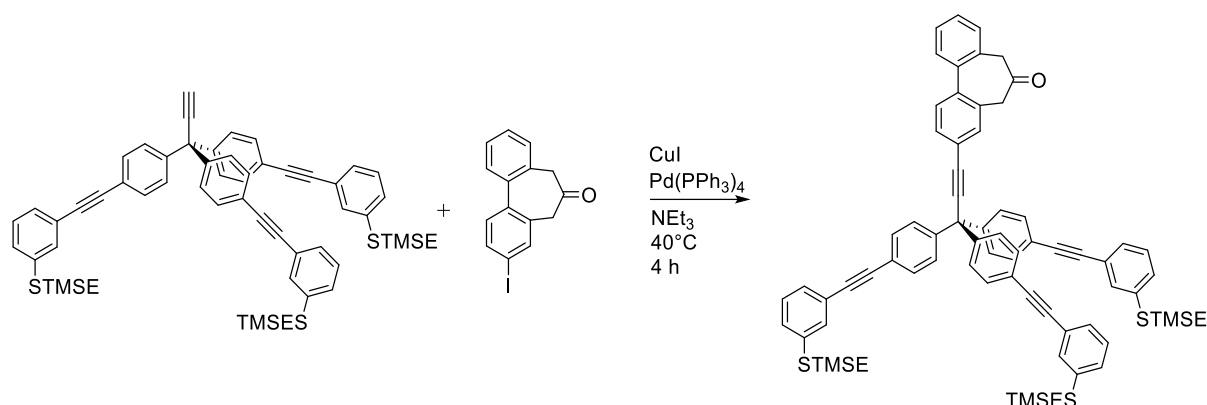
¹H NMR (500 MHz, CD₂Cl₂) δ [ppm] = 7.60 – 7.58 (m, 8H, Ar-H), 7.50- 7.48 (m, 8H, Ar-H), 7.44 -7.40 (m, 8H, Ar-H), 7.26-7.23 (m, 8H, Ar-H), 2.43 (s, 12H, CH₃).

¹³C NMR (126 MHz, CD₂Cl₂) δ [ppm] = 193.7 (CO), 146.6 (C), 137.7 (C), 134.8 (CH), 132.8 (CH), 131.6 (CH), 131.4 (CH), 129.6 (CH), 129.0 (CH), 124.7 (C), 121.4(C), 90.4 (C), 88.9 (C), 65.4 (C), 30.5 (CH₃)

FTIR (ATR): $\tilde{\nu}$ [cm⁻¹] = 2920 (w, ν_{as} (CH₃)), 2850 (w), 1701 (m, ν (C=O)), 1586 (w), 1501 (w), 1467 (w), 1401 (w), 1350 (w), 1108 (w), 1078 (w), 1018 (w), 947 (w), 885 (w), 822 (w), 786 (w), 754 (w), 718 (w), 684 (w), 612 (w), 582 (w)

ESI (+) HRMS calcd for C₆₅H₄₄O₄S₄Na: 1039.2015 [M + Na]⁺, found m/z 1039.1858

Compound 44



Under inert conditions, in an oven dried Schlenk flask, compound **43** (50 mg, 150 μ mol, 1.1 eq), Pd(PPh₃)₄ (9 mg, 8 μ mol, 0.05 eq) and copper(I)-iodide (3 mg, 15 μ mol, 0.1 eq) was dissolved in freshly distilled triethylamine (1.0 mL) and purged with argon for 30 minutes. At 40 °C, compound **31** (160 mg, 165 μ mol, 1.1 eq) - dissolved in freshly distilled and outgassed triethylamine (1.7 mL) - was added and the mixture was stirred for 4 hours at this temperature. The reaction mixture was quenched with NH₄Cl solution (10%, 5 mL) and diluted with ethyl acetate (15 mL). The aqueous phase was extracted with ethyl acetate (3 \times 5 mL) and the combined organic layer was washed with brine and dried with MgSO₄. After filtration and evaporation of all volatiles, the crude product was purified by flash chromatography on silica gel (hexane/EtOAc = 40:1, R_f = 0.24) yielded 147 mg (83%) of the desired compound.

M.p. = 61 °C

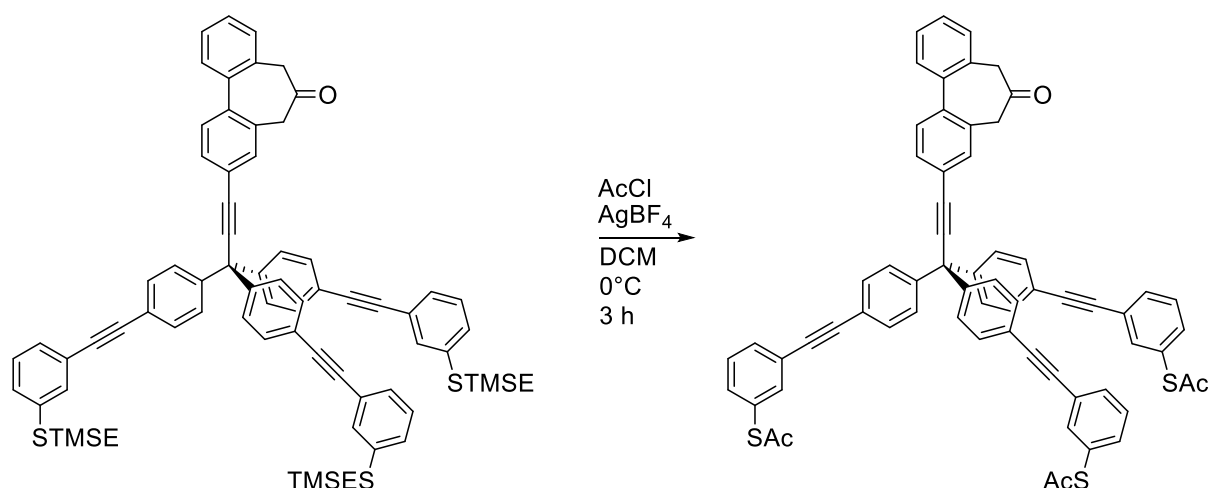
¹H NMR (500 MHz, CDCl₃) δ [ppm] = 7.58 – 7.54 (m, 4H, Ar-H), 7.52– 7.50 (m, 6H, Ar-H), 7.46 – 7.42 (m, 5H, Ar-H), 7.39 – 7.30 (m, 10H, Ar-H), 7.28 – 7.23 (m, 8H, Ar-H), 3.61 – 3.51 (m, 4H, CH₂), 3.03 – 2.94 (m, 6H, CH₂), 0.97 – 0.92 (m, 6H, CH₂), 0.06 (s, 27H, CH₃)

¹³C NMR (126 MHz, CDCl₃) δ [ppm] = 209.7 (CO), 144.8 (C), 139.6 (C), 138.8 (C), 138.0 (C), 133.2 (C), 133.1 (C), 132.6 (CH), 131.7 (CH), 131.5 (CH), 131.0 (CH), 129.7 (CH), 129.5 (CH), 129.4 (CH), 129.2 (CH), 128.9 (CH), 128.9 (CH), 128.8 (CH), 128.6 (CH), 128.0 (CH), 123.9 (C), 122.9 (C), 122.3 (C), 95.4 (C), 89.7 (C), 89.4 (C), 85.7 (C), 56.1 (C), 49.4 (CH₂), 49.1 (CH₂), 29.5 (CH₂), 16.9 (CH₂), -1.6 (CH₃).

FTIR (ATR): $\tilde{\nu}$ [cm⁻¹] = 3060 (w), 2950 (w, $\nu_{as}(\text{CH}_3)$), 2919 (w, $\nu_{as}(\text{CH}_2)$), 2895 (w, $\nu_{sym}(\text{CH}_3)$), 2852 (w, $\nu_{sym}(\text{CH}_2)$), 2161 (w), 1718 (m, $\nu(\text{C}=\text{O})$), 1583 (m), 1560 (w), 1502 (m), 1479 (w), 1446 (w), 1401 (w), 1259 (w), 1247 (m), 1161 (w), 1148 (w), 1108 (w), 1094 (w), 1079 (w), 1018 (w), 1007 (w), 888 (w), 854 (m), 824 (m), 781 (m), 764 (w), 750 (m), 729 (w), 684 (m), 578 (w), 560 (w)

ESI (+) HRMS calcd for C₇₅H₇₄OS₃Si₃Na: 1193.4108 [M + Na]⁺, found m/z 1193.4415

Tol-Tpd-Rotc



In an oven dried Schlenk-flask, compound **44** (77 mg, 66 μ mol, 1.0 eq) was dissolved in dry DCM (3.0 mL), cooled down to 0 °C and flushed with argon. At these conditions, acetyl chloride (0.30 mL) was added, and the reaction mixture was stirred for 20 minutes. Then, AgBF₄ (90 mg, 460 μ mol, 7.0 eq) was added. The reaction mixture was stirred for 3 hours to reach room temperature. After that, the reaction was quenched with crashed ice and diluted with DCM (5.0 mL), separated, and extracted with (3 \times 5 mL) DCM. After evaporation of all solvents at room temperature, the crude product was purified by flash chromatography on silica (hexane/DCM = 5:1, R_f = 0.26). 35 mg (53%) of the desired transprotected **Tol-Tpd-Rotc** was isolated as a white solid.

M.p. = 40 °C (decomposition)

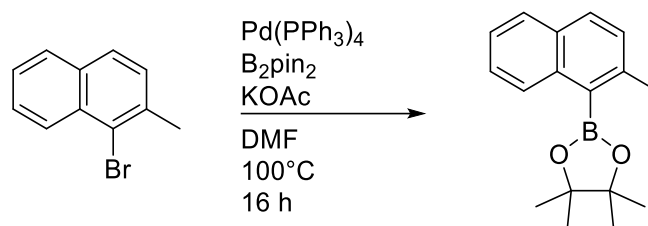
¹H NMR (500 MHz, CDCl₃) δ [ppm] = 7.62 – 7.54 (m, 9H, Ar-H), 7.50 (m, 6H, Ar-H), 7.47 – 7.36 (m, 9H, Ar-H), 7.33 – 7.29 (m, 7H, Ar-H), 3.57 (m, 4H, CH₂), 2.44 (s, 9H, CH₃)

¹³C NMR (126 MHz, CDCl₃) δ [ppm] = 209.7 (CO), 193.7 (CO), 144.9 (C), 139.6 (C), 138.8 (C), 137.5 (CH), 134.4 (CH), 133.2 (C), 133.1 (C), 132.68 (CH), 132.65 (CH), 131.7 (CH), 131.0 (CH), 129.7 (CH), 129.5 (CH), 129.4 (CH), 129.29 (CH), 129.26 (CH), 128.6 (CH), 128.4 (C), 128.0 (C), 124.6 (C), 122.9 (C), 122.1 (C), 95.3 (C), 90.2 (C), 89.0 (C), 85.7 (C), 56.1 (C), 49.4 (CH₂), 49.1 (CH₂), 30.4 (CH₃)

FTIR (ATR): $\tilde{\nu}$ [cm⁻¹] = 2957 (w, ν_{as} (CH₃)), 2921 (w), 2852 (w), 2162 (w), 1713 (w, ν (C=O)), 1586 (w), 1502 (w), 1465 (w), 1401 (w), 1243 (w), 1108 (w), 824 (w), 787 (w), 766 (w), 752 (w), 684 (w), 612 (w)

ESI (+) HRMS calcd for C₆₆H₄₄O₄S₃Na: 1019.2299 [M + Na]⁺, found m/z 1019.2527

4,4,5,5-Tetramethyl-2-(2-methylnaphthalen-1-yl)-1,3,2-dioxaborolane **46**



Under inert conditions, in an oven dried Schlenk-flask, 1-bromo-2-methylnaphthalene (500 mg, 0.7 mmol, 1 eq), bis(pinacolato)diboron (1.15 g, 4.5 mmol, 2.0 eq) and potassium acetate (1.33 g, 2.8 mmol, 6.0 eq) were dissolved in dry DMF (10.0 mL) and purged with argon for 30 minutes. Then, $\text{Pd(PPh}_3)_4$ (131 mg, 113 μmol , 0.05 eq) was added and mixture was stirred at 100°C and for 16 hours. The reaction mixture was quenched with NH_4Cl solution (10%, 5 mL) and diluted with ethyl acetate (15 mL). The aqueous phase was extracted with ethyl acetate (3×5 mL) and the combined organic layer was washed with brine and dried with MgSO_4 . After filtration and evaporation of all volatiles, the crude product was purified by flash chromatography on silica gel (hexane/DCM = 4:1, $R_f = 0.22$) to afford 519 mg (86%) of **46** as a white solid.

M.p. = 100°C

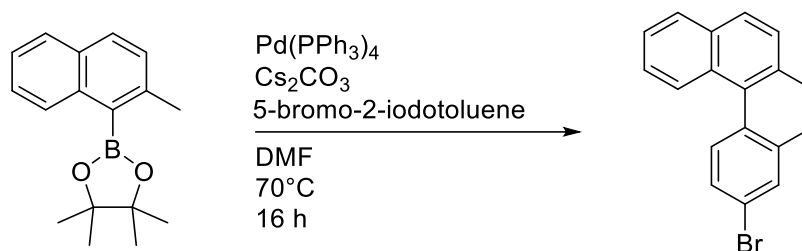
^1H NMR (500 MHz, CDCl_3) δ [ppm] = 8.16 (d, $^3J = 8.5$ Hz, 1H, Ar-H), 7.83 – 7.78 (m, 2H, Ar-H), 7.52 – 7.47 (m, 1H, Ar-H), 7.45 – 7.40 (m, 1H, Ar-H), 7.35 – 7.31 (m, 1H, Ar-H), 2.67 (s, 3H, CH_3), 1.53 (s, 12H, CH_3).

^{13}C NMR (126 MHz, CDCl_3) δ [ppm] = 141.5 (C), 136.8 (C), 131.5 (C), 129.7 (CH), 128.6 (CH), 128.3 (CH), 127.6 (CH), 126.1 (CH), 124.7 (CH), 84.1 (C), 25.2 (CH_3), 22.8 (CH_3)

FTIR (ATR): $\tilde{\nu}$ [cm^{-1}] = 3053 (w), 2990 (m, $\nu_{\text{as}}(\text{CH}_3)$), 2976 (m), 2928 (m), 2865 (w), 1595 (w), 1509 (m), 1468 (w), 1428 (m), 1412 (w), 1397 (m), 1390 (m), 1379 (w), 1370 (m), 1338 (m), 1294 (m), 1274 (m), 1257 (m), 1215 (m), 1164 (m), 1144 (m), 1128 (s), 1105 (m), 1034 (w), 1024 (m), 989 (w), 958 (m), 857 (m), 843 (m), 815 (m), 782 (m), 767 (w), 742 (m), 712 (w), 671 (w), 646 (w), 631 (w), 501 (w)

EI MS m/z (%): 268.3 (M^+ , 34), 211.2 (51), 168.2 (100), 167.2 (78), 141.2 (39), 115.0 (30)

1-(4-Bromo-2-methylphenyl)-2-methylnaphthalene **47**



Under inert conditions, in an oven dried Schlenk flask, compound **46** (40.0 mg, 149 μ mol, 1.0 eq), Pd(PPh₃)₄ (8mg, 7 μ mol, 0.05 eq) and Cs₂CO₃ (243 mg, 1 mmol, 5 eq) and 5-bromo-2-iodotoluene (43 μ L, 298 μ mol, 2 eq) were dissolved in dry DMF (5 mL) and degassed with argon for 30 min. The reaction mixture was stirred at 70 °C overnight. The reaction mixture was quenched with NH₄Cl solution (10%, 5 mL) and diluted with ethyl acetate (15 mL). The aqueous phase was extracted with ethyl acetate (3 \times 5 mL) and the combined organic layer was washed with brine and dried with MgSO₄. After filtration and evaporation of all volatiles, the crude product was purified by flash chromatography on silica gel (hexane/DCM = 5:1, R_f = 0.23). After drying, 39 mg (84%) of the desired compound **47** was isolated as a white solid.

M.p.= 86 °C

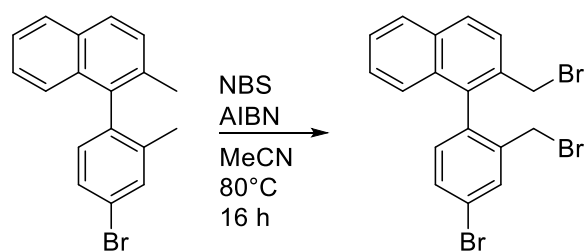
¹H NMR (500 MHz, CDCl₃) δ [ppm] = 7.89 (d, ³J = 8.1 Hz, 1H, Ar-H), 7.84 (d, ³J = 8.4 Hz, 1H, Ar-H), 7.58 (s, 1H, Ar-H), 7.52 – 7.42 (m, 3H, Ar-H), 7.39- 7.37 (m, 1H, Ar-H), 7.26 (d, ³J = 8.5 Hz, 1H, Ar-H), 7.04 (d, ³J = 8.0 Hz, 1H, Ar-H), 2.20 (s, 3H, CH₃), 1.94 (s, 3H, CH₃)

¹³C NMR (126 MHz, CDCl₃) δ [ppm] = 139.4 (C), 138.3 (C), 136.3 (C), 133.3 (C), 133.0 (CH), 132.4 (C), 132.1 (C), 131.8 (CH), 129.3 (CH), 128.7 (CH), 128.1 (CH), 127.6 (CH), 126.3 (CH), 125.5 (CH), 125.0 (CH), 121.3 (C), 20.4 (CH₃), 19.5 (CH₃)

FTIR (ATR): $\tilde{\nu}$ [cm⁻¹] = 3044 (w), 2949 (w, *v*_{as}(CH₃)), 2917 (w), 2855 (w, *v*_{sym}(CH₃)), 1587 (w), 1507 (m), 1482 (m), 1468 (w), 1435 (w), 1391 (w), 1379 (m), 1367 (w), 1193 (m), 1108 (w), 1086 (w), 1029 (w), 967 (w), 909 (w), 872 (m), 856 (m), 826 (m), 811 (m), 788 (m), 745 (m), 673 (w), 640 (w), 568 (w), 455 (w), 445 (w)

EI MS *m/z* (%): 312.0 (M⁺, 48), 310.0 (M⁺, 49), 216.1(100), 215.1 (79), 107.5 (32)

Compound 48



Under inert conditions, in an oven dried Schlenk flask, compound **47** (1.04 g, 3.3 mmol, 1.0 eq), NBS (1.25 g, 7.0 mmol, 2.1 eq) and AIBN (54.9 mg, 0.3 mmol, 0.1 eq) were suspended in acetonitrile (19 mL). The reaction mixture was heated up to 80 °C and the progress was monitored by GC-MS. After 5 hours, the reaction mixture was quenched with NH₄Cl solution (10%, 25 mL) and diluted with ethyl acetate (60 mL). The aqueous phase was extracted with ethyl acetate (3 × 30 mL) and the combined organic layer was washed with brine and dried with MgSO₄. After filtration and evaporation of all volatiles, the crude product was purified by flash chromatography on silica gel (hexane, R_f = 0.28). After drying, 673 mg (43%) of the desired compound **48** was isolated as a colourless oil.

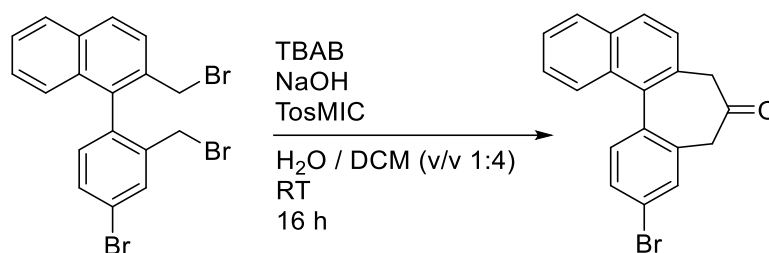
¹H NMR (500 MHz, CDCl₃) δ [ppm] = 7.94 (d, ³J = 8.5 Hz, 1H, Ar-H), 7.89 (d, ³J = 8.1 Hz, 1H, Ar-H), 7.83-7.81 (m, 1H, Ar-H), 7.66 – 7.59 (m, 2H, Ar-H), 7.54 – 7.48 (m, 1H, Ar-H), 7.42 – 7.37 (m, 1H, Ar-H), 7.24 – 7.17 (m, 2H, Ar-H), 4.47 (d, ³J = 10.1 Hz, 1H, CH₂), 4.28 (d, ³J = 10.1 Hz, 1H, CH₂), 4.10 (d, ³J = 10.5 Hz, 1H, CH₂), 3.98 (d, ³J = 10.5 Hz, 1H, CH₂).

¹³C NMR (126 MHz, CDCl₃) δ [ppm] = 138.9 (C), 136.1 (C), 135.1 (C), 133.8 (CH), 133.89 (C), 133.3 (C), 132.4 (CH), 132.3 (C), 132.1 (CH), 129.5 (CH), 128.3 (CH), 127.7 (CH), 127.1 (CH), 126.9 (CH), 126.3 (CH), 122.9 (C), 32.8 (CH₂), 30.5 (CH₂)

FTIR (ATR): $\tilde{\nu}$ [cm⁻¹] = 3051 (w), 1588 (w), 1509 (w), 1483 (m), 1463 (w), 1437 (w), 1382 (w), 1334 (w), 1267 (w), 1216 (m), 1203 (m), 1190 (m), 1162 (w), 1144 (w), 1095 (m), 1077 (w), 1028 (w), 978 (w), 935 (w), 886 (w), 870 (m), 819 (m), 793 (w), 749 (m), 723 (w), 695 (w), 686 (m), 625 (w), 615 (w), 574 (m), 561 (m)

EI MS *m/z* (%): 468.9 (M⁺, 4), 466.8 (M⁺, 4), 390.0 (8), 388.0 (14), 386.0 (8), 309.1 (16), 307.1 (15), 228.1 (40), 226.1 (40), 207.1 (37) 113.1 (100)

Compound 49



1-(Isocyanomethanesulfonyl)-4-methylbenzene (TosMIC) (96 mg, 492 μmol , 1.1 eq), tetrabutylammonium bromide (34 mg, 107 μmol , 0.2 eq) and compound **48** (210 mg, 447 μmol , 1.0 eq) were dissolved in dry DCM (4 mL). Then, NaOH (91 mg, 2.3 mmol, 5.1 eq) was dissolved in 1 mL H₂O and added to the solution. The two-phase reaction mixture was stirred at room temperature for 16 hours. The aqueous phase was extracted with DCM (3 \times 8 mL). After evaporation of all volatiles, the crude product was redissolved in the mixture of methyl *tert*-butyl ether (10 mL) and HCl_(aq) (15 mL) and stirred for 3 hours. Then, the reaction mixture was quenched with NH₄Cl solution (10%, 25 mL) and diluted with ethyl acetate (60 mL). The aqueous phase was extracted with ethyl acetate (3 \times 30 mL) and the combined organic layer was washed with satd. NaHCO₃ (15 mL), brine and dried with MgSO₄. After filtration and evaporation of all volatiles, the crude product was purified by flash chromatography on silica gel (DCM/hexane = 1:1, R_f = 0.31). After drying, 106 mg (70%) of the desired compound **49** was isolated as a white solid.

M.p. = 170 °C

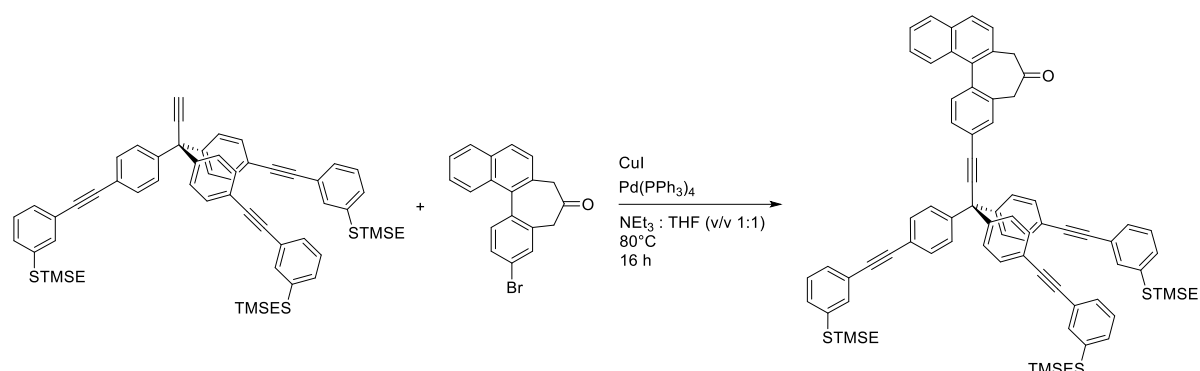
¹H NMR (500 MHz, CDCl₃) δ [ppm] = 8.05 – 8.00 (m, 1H, Ar-H), 7.93 (m, 1H, Ar-H), 7.87 (d, ³J = 8.4 Hz, 1H, Ar-H), 7.62 -7.59 (m, 1H, Ar-H), 7.57 – 7.47 (m, 4H, Ar-H), 7.38 (d, ³J = 8.4 Hz, 1H, Ar-H), 3.68 – 3.57 (m, 3H, CH₂), 3.46 (m, 1H, CH₂)

¹³C NMR (126 MHz, CDCl₃) δ [ppm] = 209.6 (CO), 136.7 (C), 135.6 (C), 134.0 (C), 133.6 (C), 133.4 (CH), 132.5 (CH), 131.4 (C), 130.8 (C), 129.9 (CH), 129.0 (CH), 128.6 (CH), 127.5 (CH), 127.0 (CH), 126.0 (CH), 125.9 (CH), 122.1 (C), 49.7 (CH₂), 48.5 (CH₂)

FTIR (ATR): $\tilde{\nu}$ [cm⁻¹] = 3065 (w), 3056 (w), 1738 (w), 1714 (s, ν (C=O)), 1593 (m), 1553 (w), 1508 (w), 1480 (m), 1419 (m), 1397 (w), 1378 (m), 1227 (m), 1209 (w), 1199 (m), 1181 (w), 1164 (m), 1147 (w), 1136 (m), 1118 (m), 1098 (m), 1077 (m), 962 (w), 943 (m), 904 (m), 876 (w), 867 (w), 858 (m), 825 (m), 815 (m), 795 (m), 780 (w), 756 (m), 735 (m), 671 (m), 641 (w), 582 (w), 570 (w), 548 (m), 536 (w), 509 (w), 500 (w), 454 (w), 430 (w), 407 (w)

EI MS m/z (%): 338.1 (M⁺, 27), 336.1 (M⁺, 27), 310.1 (18), 308.1 (18), 229.2 (84), 228.1 (84), 113.1 (100)

Compound 50



Under inert conditions, in an oven dried Schlenk flask, compound **49** (40 mg, 119 μ mol, 1.0 eq), Pd(PPh₃)₄ (7 mg, 6 μ mol, 0.05 eq) and copper(I)-iodide (2 mg, 12 μ mol, 0.1 eq) were dissolved in freshly distilled THF (2.0 mL) and outgassed with argon for 30 minutes. At 80 °C compound **31** (114 mg, 117 μ mol, 1.0 eq) dissolved in freshly distilled and outgassed triethylamine (2.0 mL) was added and the mixture was stirred for 16 hours at this temperature. Quenching the reaction with NH₄Cl and diluting with ethyl acetate (15 mL) was followed by separating and extracting the aqueous phase with (3 \times 5 mL) ethyl acetate. The combined organic layers were washed with brine and dried over MgSO₄. Purification by flash chromatography (hexanes/EtOAc 60:1 R_f = 0.25) yielded 71 mg (49%) of the desired compound as an off-white solid.

M.p. = 115 °C

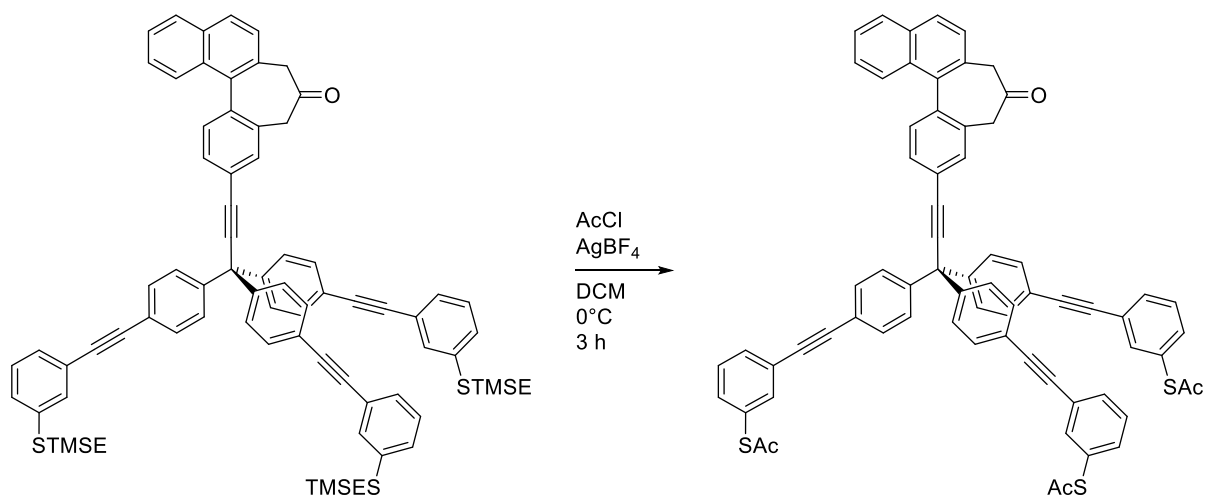
¹H NMR (500 MHz, CDCl₃) δ [ppm] = 8.08 – 8.04 (m, 1H, Ar-H), 7.94 – 7.93 (m, 1H, Ar-H), 7.87 (d, ³J = 8.4 Hz, 1H, Ar-H), 7.67 - 7.62 (m, 2H, Ar-H), 7.58 – 7.44 (m, 12H, Ar-H), 7.42 – 7.29 (m, 10H, Ar-H), 7.27 (m, 6H, Ar-H), 3.64 (m, 3H, CH₂), 3.52 (m, 1H, CH₂), 3.03 – 2.95 (m, 6H, CH₂), 0.99 – 0.92 (m, 6H, CH₂), 0.06 (s, 27H, CH₃).

¹³C NMR (126 MHz, CDCl₃) δ [ppm] = 209.9 (CO), 144.8 (C), 138.0 (C), 136.9 (C), 134.9 (C), 134.5 (C), 133.6 (C), 132.8 (CH), 132.1 (CH), 131.7 (CH), 131.48 (C), 131.45 (CH), 130.9 (C), 129.9 (CH), 129.3 (CH), 129.0 (CH), 128.94 (CH), 128.86 (CH), 128.80 (CH), 128.6 (CH), 127.5 (CH), 126.9 (CH), 126.1 (CH), 126.0 (CH), 123.9 (C), 122.9 (C), 122.3 (C), 95.4 (C), 89.7 (C), 89.4 (C), 85.8 (C), 56.1 (C), 49.8 (CH₂), 48.7 (CH₂), 29.5 (CH₂), 16.9 (CH₂), -1.6 (CH₃)

FTIR (ATR): $\tilde{\nu}$ [cm⁻¹] = 2950 (m, ν_{as} (CH₃)), 2921 (m, ν_{as} (CH₂)), 2851 (m, ν_{sym} (CH₂)), 1718 (m, ν (C=O)), 1584 (m), 1560 (w), 1502 (m), 1470 (w), 1403 (w), 1259 (m), 1247 (m), 1162 (w), 1018 (w), 887 (w), 854 (m), 823 (m), 780 (m), 749 (m), 728 (w), 684 (m), 667 (w), 661 (w), 579 (w)

ESI (+) HRMS calcd for C₇₉H₇₆OSi₃S₃Na: 1243.4264 [M + Na]⁺, found m/z 1243.4921

Tol-Tpd-Rot_eC



In an oven dried Schlenk flask, compound **50** (104 mg, 85 μ mol, 1.00 eq) was dissolved in dry DCM (4.0 mL), cooled down to 0 °C and flushed with argon. At these conditions, acetyl chloride (0.40 mL) was added, and the mixture was stirred for 20 minutes. Then, AgBF₄ (116 mg, 596 μ mol, 7.0 eq) was added. The reaction mixture was stirred for 3 hours to reach room temperature. After that, the reaction was quenched with crashed ice and diluted with DCM (5.0 mL), separated, and extracted with (3 \times 5 mL) DCM. After evaporation of the solvent at room temperature, the crude product was purified by flash chromatography on silica (hexane/DCM = 1:3, R_f = 0.33). 53 mg (60%) of the desired transprotected Tol-Tpd-Rot_eC was isolated as a white solid.

M.p. = 40 °C (decomposition)

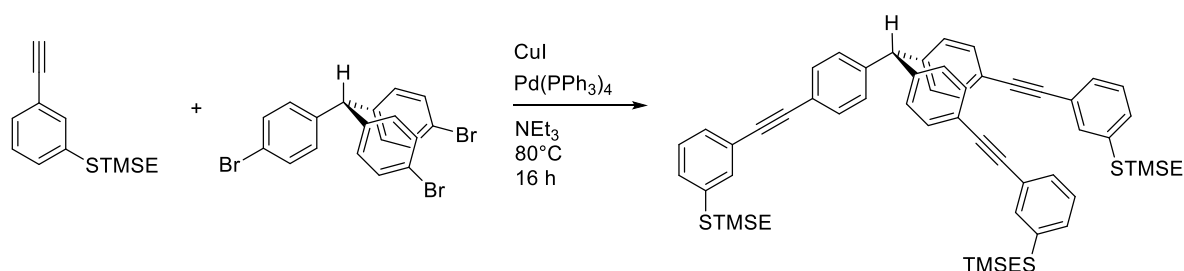
¹H NMR (500 MHz, CDCl₃) δ [ppm] = 8.06 (d, ³J = 7.8 Hz, 1H, Ar-H), 7.94 – 7.90 (m, 1H, Ar-H), 7.87 (d, ³J = 8.4 Hz, 1H, Ar-H), 7.67 - 7.47 (m, 17H, Ar-H), 7.39 (m, 13H, Ar-H), 3.64 (m, 3H, CH₂), 3.53 (m, 1H, CH₂), 2.44 (s, 9H, CH₃).

¹³C NMR (126 MHz, CDCl₃) δ [ppm] = 209.9 (CO), 193.6 (CO), 144.9 (C), 137.5 (CH), 136.9 (C), 134.9 (C), 134.5 (C), 134.4 (CH), 133.6 (C), 132.8 (CH), 132.7 (CH), 132.0 (CH), 131.8 (CH), 131.5 (C), 130.9 (C), 129.9 (CH), 129.28 (CH), 129.26 (CH), 129.0 (CH), 128.6 (C), 128.4 (CH), 127.5 (CH), 126.9 (CH), 126.1 (CH), 126.0 (CH), 124.6 (C), 122.9 (C), 122.1 (C), 95.3 (C), 90.2 (C), 89.0 (C), 85.8 (C), 56.1 (C), 49.8 (CH₂), 48.6 (CH₂), 30.4 (CH₃)

FTIR (ATR): $\tilde{\nu}$ [cm⁻¹] = 2922 (w, ν_{as} (CH₂)), 2852 (w, ν_{sym} (CH₂)), 1704 (m, ν (C=O)), 1587 (m), 1501 (m), 1467 (w), 1403 (w), 1351 (w), 1108 (m), 1079 (m), 1018 (w), 948 (m), 885 (w), 820 (m), 787 (m), 751 (m), 684 (m), 612 (m), 579 (w)

ESI (+) HRMS calcd for C₇₀H₄₆O₄S₃Na: 1069.2450 [M + Na]⁺, found m/z 1069.2402

Compound **51**



Under inert conditions, in an oven dried Schlenk flask, compound **22** (120 mg, 249 μmol , 1.0 eq), $\text{Pd}(\text{PPh}_3)_4$ (7 mg, 6 μmol , 0.05 eq) and copper(I)-iodide (2 mg, 12 μmol , 0.1 eq) were dissolved in freshly distilled NEt_3 (2.0 mL) and outgassed with argon for 30 minutes. At 80 $^\circ\text{C}$ compound **29** (181 mg, 773 μmol , 3.1 eq) dissolved in freshly distilled and outgassed triethylamine (2.0 mL) was added and the mixture was stirred for 16 hours at this temperature. Quenching the reaction with NH_4Cl and diluting with ethyl acetate (15 mL) was followed by separating and extracting the aqueous phase with (3×5 mL) ethyl acetate. The combined organic layers were washed with brine and dried over MgSO_4 . Purification by flash chromatography (hexanes/DCM = 9:1, R_f = 0.32) yielded 92 mg (39%) of the desired compound as a colourless oil.

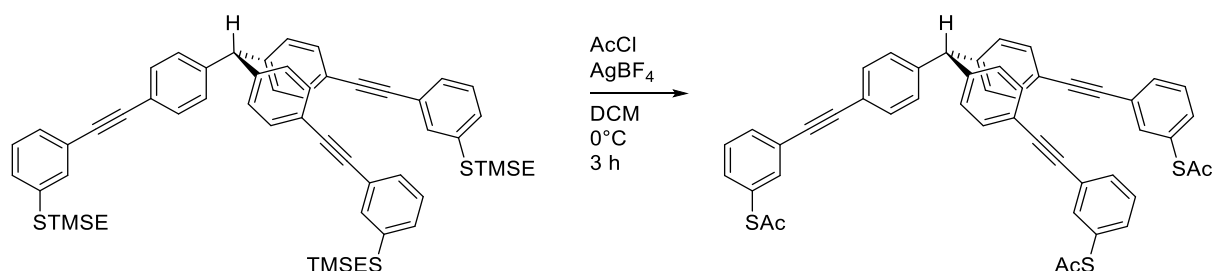
^1H NMR (500 MHz, CDCl_3) δ [ppm] = 7.52 – 7.48 (m, 6H, Ar-H), 7.45 (s, 3H, Ar-H), 7.34 – 7.29 (m, 3H, Ar-H), 7.26 – 7.24 (m, 6H, Ar-H), 7.10 (d, J = 8.2 Hz, 6H, Ar-H), 5.57 (s, 1H, CH), 3.02 – 2.94 (m, 6H, CH_2), 0.98 – 0.92 (m, 6H, CH_2), 0.06 (s, 27H, CH_3).

^{13}C NMR (126 MHz, CDCl_3) δ [ppm] = 143.5 (C), 137.9 (C), 131.9 (CH), 131.4 (CH), 129.6 (CH), 128.9 (CH), 128.8 (CH), 128.7 (CH), 124.0 (C), 121.6 (C), 89.6 (C), 89.3 (C), 56.5 (CH), 29.5 (CH_2), 16.9 (CH_2), -1.6 (CH_3)

FTIR (ATR): $\tilde{\nu}$ [cm^{-1}] = 2951 (m, $\nu_{\text{as}}(\text{CH}_3)$), 2920 (m, $\nu_{\text{as}}(\text{CH}_2)$), 2852 (w, $\nu_{\text{sym}}(\text{CH}_2)$), 1580 (m), 1559 (m), 1470 (w), 1396 (w), 1260 (m), 1248 (m), 1163 (w), 1010 (w), 883 (w), 836 (m), 780 (m), 751 (m), 728 (w), 682 (m)

ESI (+) HRMS calcd for $\text{C}_{58}\text{H}_{64}\text{S}_3\text{Si}_3\text{Na}$: 963.3376 [$\text{M} + \text{Na}$] $^+$, found m/z 965.3674

Tol-Tpd-H



In an oven dried Schlenk flask, compound **51** (68 mg, 72 μ mol, 1.0 eq) was dissolved in dry DCM (2.0 mL), cooled down to 0 °C and flushed with argon. At these conditions, acetyl chloride (0.20 mL) was added, and the mixture was stirred for 20 minutes. Then, AgBF₄ (98 mg, 505 μ mol, 7.0 eq) was added. The reaction mixture was stirred for 3 hours to reach room temperature. After that, the reaction was quenched with crashed ice and diluted with DCM (5.0 mL), separated, and extracted with (3 \times 5 mL) DCM. After evaporation of the solvent at room temperature, the crude product was purified by flash chromatography on silica (hexane/DCM 1:4, R_f = 0.21). 8.3 mg (15%) of the desired transprotected **Tol-Tpd-H** were isolated as a white solid.

M.p. = 40 °C (decomposition)

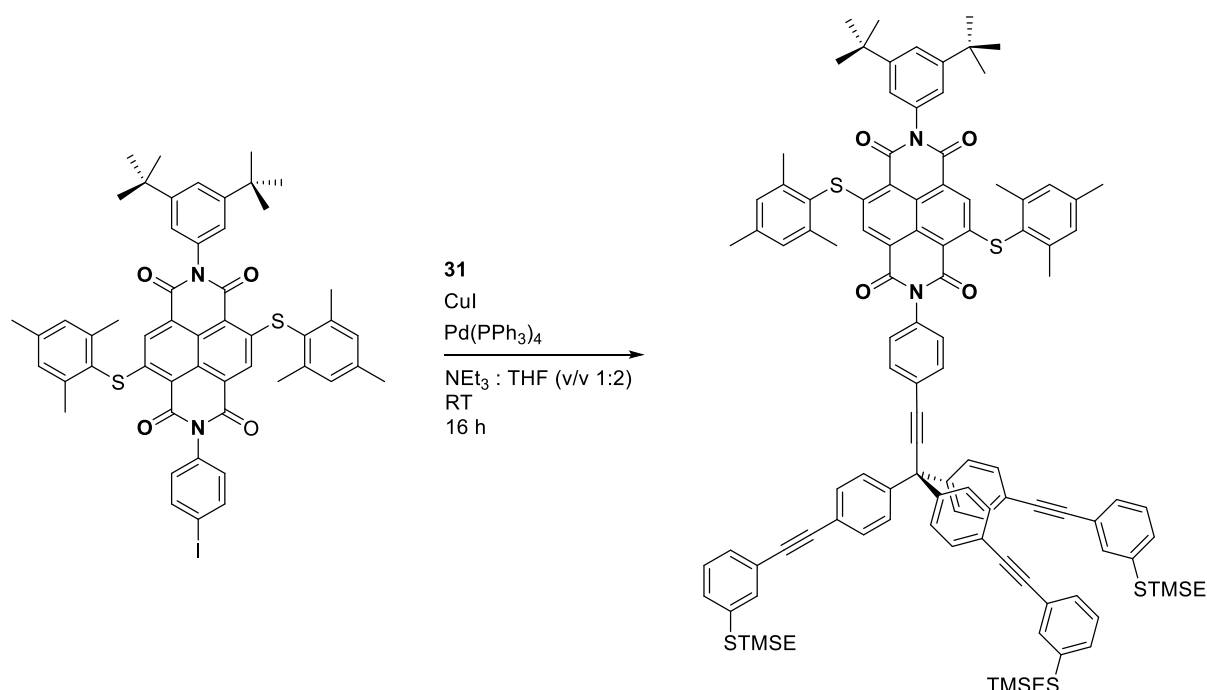
¹H NMR (500 MHz, CDCl₃) δ [ppm] = 7.58 (s, 3H, Ar-H), 7.57 – 7.54 (m, 3H, Ar-H), 7.48 – 7.45 (m, 6H, Ar-H), 7.41 – 7.36 (m, 6H, Ar-H), 7.09 (m, 6H, Ar-H), 5.57 (s, 1H, CH), 2.44 (s, 9H, CH₃).

¹³C NMR (126 MHz, CDCl₃) δ [ppm] = 193.7 (CO), 143.6 (C), 137.4 (CH), 134.3 (CH), 132.6 (CH), 132.0 (CH), 129.6 (CH), 129.3 (CH), 128.4 (C), 124.7 (C), 121.5 (C), 90.4 (C), 88.6 (C), 56.6 (CH), 30.4 (CH₃)

FTIR (ATR): $\tilde{\nu}$ [cm⁻¹] = 1505 (m), 1466 (m), 1402 (w), 1351 (m), 1108 (m), 1078 (m), 1018 (w), 947 (m), 886 (w), 858 (w), 821 (m), 787 (m), 747 (w), 684 (m), 612 (m), 588 (w), 571 (w)

ESI (+) HRMS calcd for C₄₉H₃₄O₃S₃Na: 789.1562 [M + Na]⁺, found m/z 789.1466

Compound 52



Under inert conditions, in an oven dried Schlenk-flask, **sNDI** (132 mg, 138 μ mol, 1.0 eq), Pd(PPh₃)₄ (8 mg, 7 μ mol, 0.05 eq) and copper(I)-iodide (3 mg, 14 μ mol, 0.1 eq) were dissolved in dry THF (2 mL) and purged with argon for 30 min. Then compound **31** (140 mg, 145 μ mol, 1.05 eq) dissolved in freshly distilled NEt₃ (4 mL) was added and the reaction mixture was stirred overnight at room temperature. The reaction mixture was quenched with NH₄Cl solution (10%, 5 mL) and diluted with ethyl acetate (15 mL). The aqueous phase was extracted with ethyl acetate (3 \times 5 mL) and the combined organic layer was washed with brine and dried with MgSO₄. After filtration and evaporation of all volatiles, the crude product was purified by flash chromatography on silica gel (hexane/DCM = 2:3, R_f = 0.40). After drying, 182 mg (74%) of the desired compound **52** was isolated as a red solid.

M.p. = 227 °C

¹H NMR (500 MHz, CDCl₃) δ [ppm] = 8.05 (s, 1H, Ar-H), 8.02 (s, 1H, Ar-H), 7.70 (m, 2H, Ar-H), 7.52 (m, 6H, Ar-H), 7.46 (s, 3H, Ar-H), 7.38 – 7.30 (m, 12H, Ar-H), 7.28 – 7.26 (m, 6H, Ar-H), 7.10 – 7.06 (m, 6H, Ar-H), 3.04 – 2.95 (m, 6H, CH₂), 2.36 (s, 12H, CH₃), 2.32 (s, 6H, CH₃), 1.35 (s, 18H, CH₃), 1.01 – 0.92 (m, 6H, CH₂), 0.06 (s, 27H, CH₃).

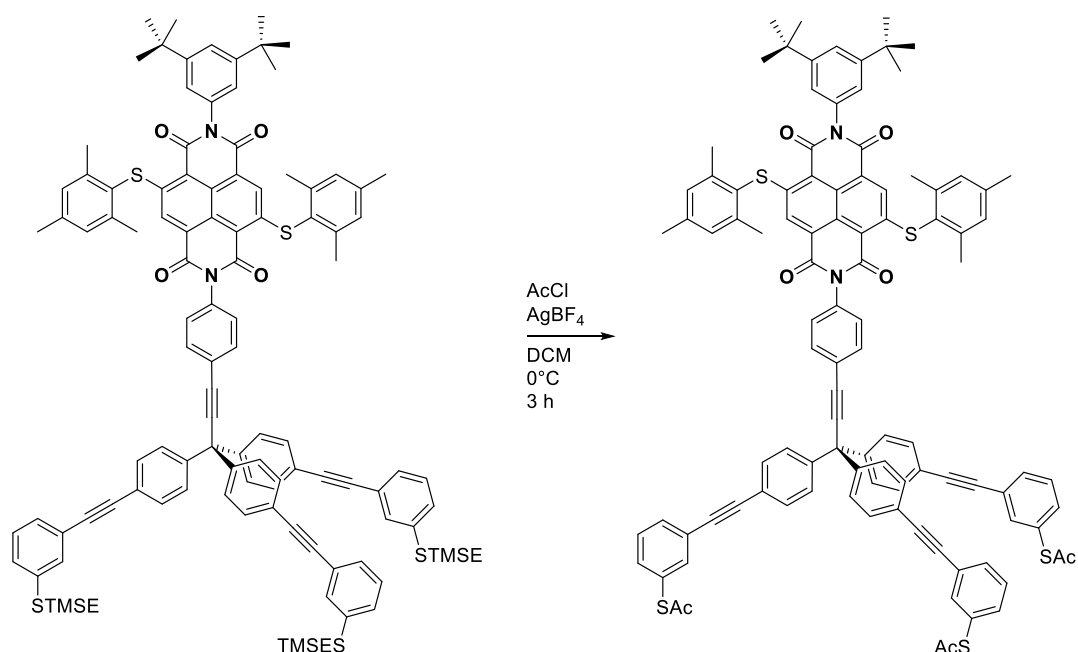
¹³C NMR (126 MHz, CDCl₃) δ [ppm] = 163.8 (CO), 163.7 (CO), 162.6 (CO), 152.1 (CO), 149.8 (C), 149.2 (C), 144.8 (C), 143.7 (C), 141.18 (C), 141.12 (C), 137.9 (C), 134.7 (C), 134.1 (C), 132.9 (CH), 131.7 (CH), 131.4 (CH), 130.3 (CH), 129.4 (CH), 129.3 (CH), 128.9 (CH), 128.84 (CH), 128.79 (CH), 126.36 (C), 126.33 (C), 125.3 (C), 125.0 (C), 124.9 (C), 124.2 (C), 124.1 (C), 124.0 (C), 123.7 (CH), 122.4 (C), 122.3 (CH), 119.9 (C), 119.0 (C), 95.5 (C), 89.6 (C), 89.5 (C), 85.5 (C), 56.1 (C), 35.1 (C), 31.6 (CH₃), 29.5 (CH₂), 21.7 (CH₃), 21.44 (CH₃), 21.42 (CH₃), 16.9 (CH₂), -1.6 (CH₃)

FTIR (ATR): $\tilde{\nu}$ [cm⁻¹] = 2953 (m, $\nu_{\text{as}}(\text{CH}_3)$), 2920 (m), 2866 (w, $\nu_{\text{sym}}(\text{CH}_3)$), 1705 (m, $\nu(\text{C=O})$), 1665 (m), 1584 (w), 1551 (m), 1504 (m), 1431 (m), 1321 (m), 1247 (m), 1224 (m), 1165 (m), 1019 (w), 825 (m), 785 (m), 749 (m), 684 (w)

ESI (+) HRMS calcd for C₁₁₁H₁₁₂N₂O₄S₅Si₃Na: 1816.6465 [M + Na]⁺, found m/z 1816.7222

UV-Vis (DCM) (λ_{max} [nm], (ϵ)) = 295 (144400), 356 (13596), 370 (14327), 523 (24610)

Tol-Tpd-sNDI.



In an oven dried Schlenk flask, **52** (145 mg, 81 μ mol, 1.0 eq) was dissolved in dry DCM (4 mL), cooled down to 0 °C and flushed with argon before acetyl chloride (0.4 mL) was added and the reaction mixture was stirred for 20 min. Then, AgBF₄ (110 mg, 566 μ mol, 7 eq) was added and the reaction mixture was stirred for another 3 hours to reach room temperature. Afterwards, the reaction mixture was quenched with crashed ice, diluted with DCM (5 mL) and extracted with DCM (3 \times 5 mL). The combined organic layer was dried with MgSO₄. After filtration and evaporation of all volatiles at room temperature, the crude product was purified by flash chromatography on silica gel (hexane/DCM = 1:2, R_f = 0.29). After drying, 81 mg of **Tol-Tpd-sNDI** was isolated as a red solid in 62% yield.

M.p. = 40 °C (decomposition)

¹H NMR (500 MHz, CDCl₃) δ [ppm] = 8.05 (s, 1H, Ar-H), 8.02 (s, 1H, Ar-H), 7.73 – 7.68 (m, 2H, Ar-H), 7.62 – 7.56 (m, 6H, Ar-H), 7.53 – 7.50 (m, 6H, Ar-H), 7.43 – 7.31 (m, 15H, Ar-H), 7.12 – 7.06 (m, 6H, CH₂), 2.45 (s, 9H, CH₃), 2.36 (s, 12H, CH₃), 2.33 (s, 6H, CH₃), 1.35 (s, 18H, CH₃).

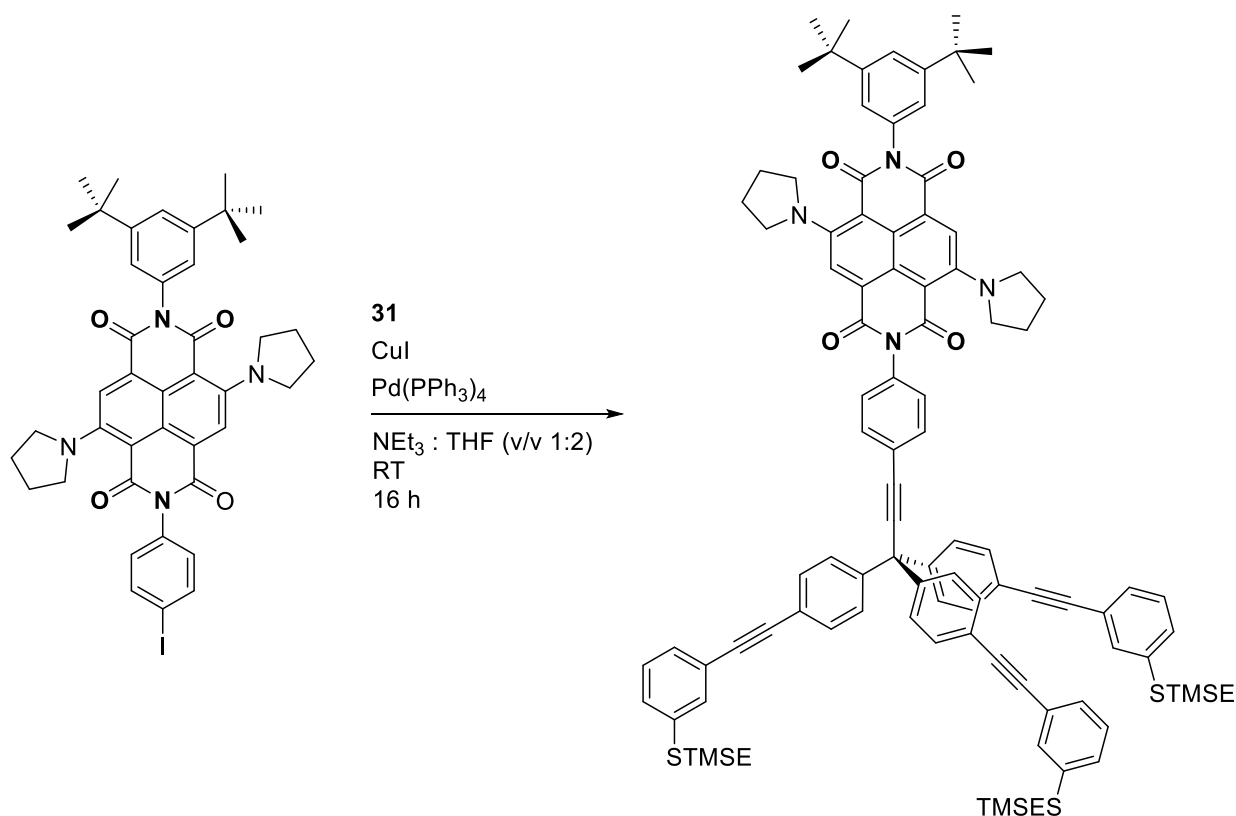
¹³C NMR (126 MHz, CDCl₃) δ [ppm] = 193.7 (CO), 163.8 (CO), 163.7 (CO), 162.6 (CO), 152.1 (CO), 149.8 (C), 149.2 (C), 144.9 (C), 143.7 (C), 141.2 (C), 141.1 (C), 137.5 (C), 134.7 (C), 134.4 (CH), 134.1 (C), 132.9 (CH), 132.7 (CH), 131.7 (CH), 130.3 (CH), 129.4 (CH), 129.28 (CH), 129.26 (CH), 129.0 (CH), 128.4 (C), 126.4 (C), 126.3 (C), 125.3 (C), 125.0 (C), 124.9 (C), 124.56 (C), 124.2 (C), 124.1 (C), 123.7 (CH), 122.4 (CH), 122.1 (C), 119.9 (C), 119.0 (C), 95.5 (C), 90.2 (C), 89.0 (C), 85.5 (C), 56.1 (C), 35.1 (C), 31.6 (CH₃), 30.4 (CH₃), 21.7 (CH₃), 21.44 (CH₃), 21.42 (CH₃)

FTIR (ATR): $\tilde{\nu}$ [cm^{-1}] = 2952 (m, $\nu_{\text{as}}(\text{CH}_3)$), 2921 (m), 2854 (m, $\nu_{\text{sym}}(\text{CH}_3)$), 1704 (m, $\nu(\text{C=O})$), 1665 (m), 1587 (w), 1550 (m), 1503 (m), 1464 (w), 1431 (m), 1403 (w), 1362 (w), 1322 (m), 1248 (m), 1227 (m), 1166 (w), 1110 (m), 1078 (w), 946 (w), 824 (w), 786 (m), 750 (w), 741 (w), 684 (w), 612 (m), 536 (w)

ESI (+) HRMS calcd for $\text{C}_{103}\text{H}_{82}\text{N}_2\text{O}_7\text{S}_5\text{Na}$: 1641.4650 $[\text{M} + \text{Na}]^+$, found m/z 1642.4521

UV-Vis (DCM) ($\lambda_{\text{max}}[\text{nm}]$, (ϵ)) = 294 (121671), 356 (13027), 370 (13647), 524 (21918)

Compound 53



Under inert conditions, in an oven dried Schlenk flask, **nNDI** (105 mg, 132 μ mol, 1.0 eq), Pd(PPh₃)₄ (8 mg, 7 μ mol, 0.05 eq) and copper(I)-iodide (3 mg, 13 μ mol, 0.1 eq) were dissolved in dry THF (2 mL) and purged with argon for 30 min. Then compound **31** (140 mg, 145 μ mol, 1.1 eq) dissolved in freshly distilled NEt₃ (4 mL) was added and the reaction mixture was stirred overnight at room temperature. The reaction mixture was quenched with NH₄Cl solution (10%, 5 mL) and diluted with ethyl acetate (15 mL). The aqueous phase was extracted with ethyl acetate (3 \times 5 mL) and the combined organic layer was washed with brine and dried with MgSO₄. After filtration and evaporation of all volatiles, the crude product was purified by flash chromatography on silica gel (hexane/DCM = 3:1, R_f = 0.4). After drying, 94 mg (71%) of the desired compound **53** was isolated as a blue solid.

M.p. = 133 °C

¹H NMR (500 MHz, CDCl₃) δ [ppm] = 8.44 (s, 1H, Ar-H), 8.43 (s, 1H, Ar-H), 7.72 (d, *J* = 8.2 Hz, 2H, Ar-H), 7.55 – 7.50 (m, 8H, Ar-H), 7.46 (s, 3H, Ar-H), 7.36 – 7.31 (m, 12H, Ar-H), 7.28 – 7.26 (m, 4H, Ar-H), 7.12 (s, 2H, Ar-H), 3.50 (d, *J* = 5.0 Hz, 8H, CH₂), 3.01 – 2.97 (m, 6H, CH₂), 2.04 (s, 8H, CH₂), 1.38 (s, 18H, CH₃), 0.97 – 0.93 (m, 6H, CH₃), 0.06 (s, 27H, CH₃).

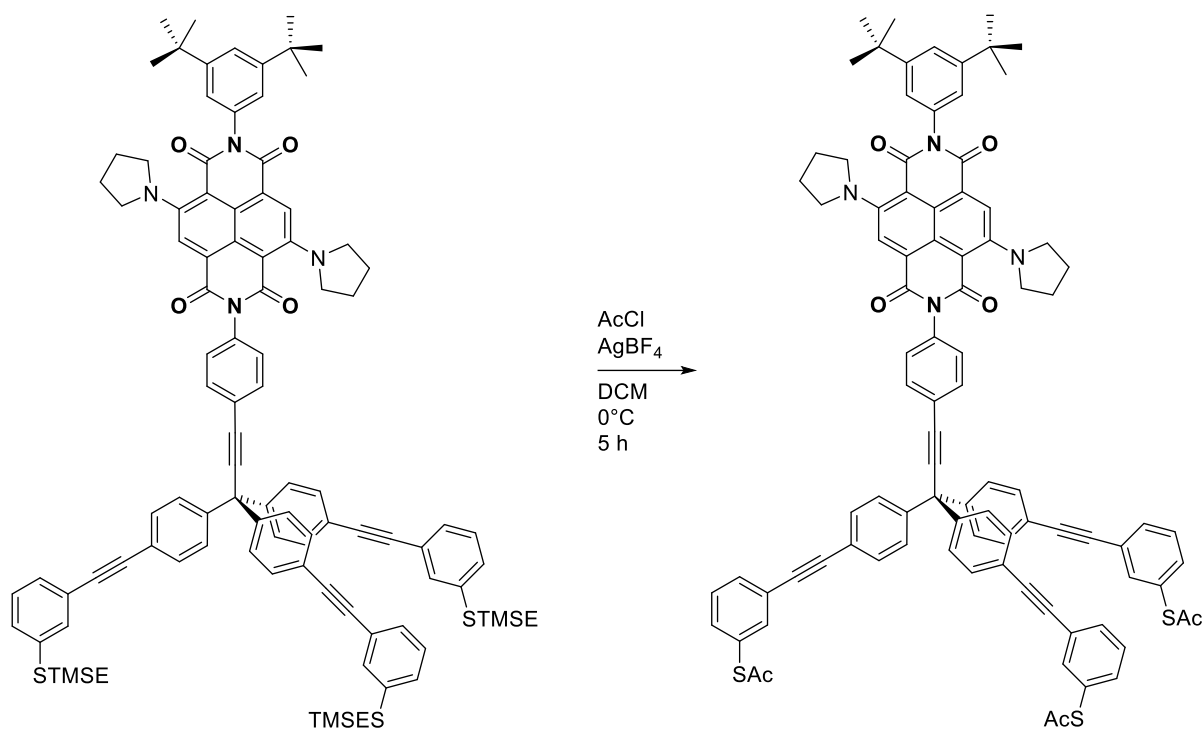
¹³C NMR (126 MHz, CDCl₃) δ [ppm] = 163.9 (CO), 162.4 (CO), 161.8 (CO), 151.7 (CO), 147.7 (C), 147.6 (C), 144.9 (C), 137.9 (C), 136.3 (C), 135.3 (C), 132.8 (CH), 131.7 (CH), 131.4 (CH), 129.3 (CH), 129.2 (CH), 128.9 (CH), 128.84 (CH), 128.78 (CH), 125.7 (C), 125.0 (C), 123.9 (C), 123.6 (C), 123.0 (CH), 122.8 (CH), 122.2 (C), 122.1 (CH), 95.2 (C), 89.6 (C), 89.5 (C), 85.8 (C), 56.1 (C), 52.8 (CH₂), 35.1 (C), 31.6 (CH₃), 29.5 (CH₂), 26.1 (CH₂), 16.9 (CH₂), -1.6 (CH₃).

FTIR (ATR): $\tilde{\nu}$ [cm⁻¹] = 2951 (m, $\nu_{as}(\text{CH}_3)$), 2921 (m, $\nu_{as}(\text{CH}_2)$), 2851 (m, $\nu_{sym}(\text{CH}_2)$), 1693 (m, $\nu(\text{C=O})$), 1656 (m), 1584 (w), 1567 (m), 1503 (m), 1471 (m), 1448 (m), 1425 (m), 1355 (m), 1341 (w), 1330 (m), 1319 (m), 1259 (w), 1247 (m), 1215 (m), 1161 (w), 1141 (m), 1119 (w), 886 (w), 855 (m), 825 (m), 780 (m), 749 (m), 722 (w), 706 (w), 685 (m)

ESI (+) HRMS calcd for C₁₀₂H₁₀₆N₄O₄S₃Si₃H: 1632.6791 [M + Na]⁺, found m/z 1631.7598

UV-Vis (DCM) (λ_{max} [nm], (ϵ)) = 294 (120879), 348 (11720), 365 (13303), 602 (19441)

Tol-Tpd-nNDI



In an oven dried Schlenk flask, the compound **53** (64 mg, 39 μ mol, 1 eq) was dissolved in dry DCM (3 mL), cooled down to 0 °C and flushed with argon. Then, acetyl chloride (0.3 mL) was added, and the mixture was stirred for 20 min before AgBF₄ (38 mg, 196 μ mol, 5 eq) was added. The original blue reaction mixture changed the colour to pink and after ~ 5 min, to a milky suspension, which was stirred for 5 hours to reach room temperature. The reaction mixture was quenched with crashed ice and neutralised with sodium hydrogen carbonate to pH ~ 6. After extraction with DCM, the combined organic layer was dried with MgSO₄. After filtration and evaporation of all volatiles at room temperature, the crude product was purified by flash chromatography on silica gel (hexane/DCM = 1:4, R_f = 0.12). After drying, 43 mg (76%) of the title compound **Tol-Tpd-nNDI** was isolated as a blue solid.

M.p. = 40 °C (decomposition)

¹H NMR (500 MHz, CDCl₃) δ [ppm] = (s, 1H, Ar-H), 8.42 (s, 1H, Ar-H), 7.72 (d, J = 8.2 Hz, 2H, Ar-H), 7.61 (s, 3H, Ar-H), 7.59 – 7.50 (m, 10H, Ar-H), 7.43 – 7.31 (m, 14H, Ar-H), 7.14 – 7.09 (m, 2H, Ar-H), 3.53 – 3.44 (m, 8H, CH₂), 2.44 (s, 9H, CH₃), 2.03 (s, 8H, CH₂), 1.38 (s, 18H, CH₃).

¹³C NMR (126 MHz, CDCl₃) δ [ppm] = 193.7 (CO), 164.1 (CO), 163.9 (CO), 162.1 (CO), 161.8 (CO), 151.7 (C), 147.8 (C), 147.6 (C), 144.9 (C), 137.5 (CH), 136.3 (C), 135.4 (C), 134.4 (CH), 132.8 (CH), 132.7 (CH), 131.7 (CH), 129.3 (CH), 129.2 (CH), 128.4 (C), 125.7 (C), 125.0 (C), 124.6 (C), 123.6 (C), 123.1 (CH), 123.0 (CH), 122.8 (CH), 122.1 (CH), 106.0 (C), 105.2 (C), 95.1 (C), 90.2 (C), 88.9 (C), 85.9 (C), 56.1 (C), 52.8 (CH₂), 35.1 (C), 31.6 (CH₃), 30.4 (CH₃), 26.1 (CH₂)

FTIR (ATR): $\tilde{\nu}$ [cm^{-1}] = 2953 (m), 2923 (m, $\nu_{as}(\text{CH}_2)$), 2855 (m), 1692 (m, $\nu(\text{C=O})$), 1654 (m), 1587 (w), 1566 (m), 1502 (w), 1476 (m), 1448 (m), 1426 (m), 1354 (m), 1342 (w), 1330 (w), 1318 (w), 1213 (m), 1111 (m), 1079 (w), 944 (w), 885 (w), 824 (w), 781 (m), 751 (w), 726 (w), 684 (w), 612 (w)

ESI (+) HRMS calcd for $\text{C}_{93}\text{H}_{76}\text{N}_4\text{O}_7\text{S}_3\text{Na}$: 1480.4800 $[\text{M} + \text{Na}]^+$, found m/z 1480.4989

UV-Vis (DCM) ($\lambda_{\text{max}}[\text{nm}]$, (ϵ)) = 293 (117239), 349 (10031), 365 (11795), 602 (17870)

6 List of Abbreviations

°C	Grad Celsius
A	Absorption
Å	Angstrom
a.u.	Arbitrary unit
AFM	Atomic force microscopy
AIBN	Azobisisobutyronitrile
aq.	Aqueous
b	Broad
Bp	Biphenyl
C-AFM	conducting atomic force microscopy
calcd	calculated
CB	Conduction band
CCM	Constant current mode
CHM	Constant hight mode
CISS	Chiral induced spin selectivity
cm ⁻¹	Wavenumber
CV	Cyclic voltammetry
DCM	Dichloromethane
DMF	<i>N,N</i> -Dimethylformamide
DOS	Density of states
<i>e.g.</i>	Exempli gratia
EA	Elemental analysis
EA	Electron affinity
E _F	Fermie energy
eq.	Equivalent
E _r	Retardation factor
ESI-MS	Electrospray ionization–mass spectrometry
<i>et al</i>	Et alia
Et ₂ O	Diethyl ether
EtOAc	Ethyl acetate
eV	Electron volt

F	Fluorescence
Fc/Fc ⁺	Ferrocene/ferrocenium
g	Gram
GC/MS	Gas chromatography–mass spectrometry
h	Hour
hc	High concentration
HCl	Hydrochloride acid
HOMO	Highest occupied molecular orbital
HR-XPS	High resolution X-ray photoelectron spectroscopy
Hz	Hertz
IC	Internal crossover
IET	Inelastic electron tunnelling
in	minute
IP	Ionisation potential
IR	Infrared
IUPAC	Kelvin
kJ	Kilojoule
LB	Langmuir-Blodgett
LED	Light emitting diode
LUMO	Lowest occupied molecular orbital
m	Medium
m	Multiplet
M	Molar
M.p.	Melting point
m/z	Mass per charge
mbar	Millibar
MeCN	Acetonitrile
MeOH	Methanol
mg	Milligram
MHz	Megahertz
MIP	Memory-in-pixel
mL	Millilitre

mM	Milli molar
mmol	Millimole
MW	Microwave
NBS	<i>N</i> -bromosuccinimide
NDA	naphthalene-1,4,5,8- tetracarboxylic acid dianhydride
NDI	naphthalene-1,4,5,8-tetracarboxdiimides
NEt ₃	Triethylamine
NEXAFS	X-ray absorption near edge structure
nm	Nanometre
NMR	Nuclear magnetic resonance
norm	normalised
OFET	Organic Field-effect transistor
OLED	Organic Light emitting diode
OPE	Oligo- <i>p</i> -phenylenes
OSCs	organic solar cell
P	Phosphorescence
PAH	Polyaromatic hydrocarbons
PDI	Perylene diimide
Ph	Phenyl
PL	Photoluminescence
PPh ₃	Triphenylphosphine
ppm	Parts per million
Ref	Reference
RISC	Reversed intersystem crossing
RT	Room temperature
s	Sharp
s	Singlet
SAM	Self-assembled monolayer
scanning tunnelling microscopy	STM
scanning tunnelling spectroscopy	STS
SOMO	Singly occupied molecular orbital

STML	Scanning tunnelling microscopy induced luminescence
T	Temperature
TADF	Thermally activated delayed fluorescence
TATA	Triazatriangulenium
TBAB	Tetrabutylammonium bromide
THF	Tetrahydrofuran
TLC	Thin-layer chromatography
TMSE	Trimethylsilylethyl
TOF	Time of flight
tol	Toluene
Tol	Tolane
TosMIC	<i>para</i> -tosylmethyl isocyanide
Tpd	Tripod
UHV	Ultra-high vacuum
UV	Ultraviolet
UV-Vis	Ultraviolet-visible
V	Volt
VB	Valence band
vs	versus
XPS	X-ray photoelectron spectroscopy
μg	Microgram
μL	Microliter
μM	Micromolar
μmol	Micromole

7 References

- [1] A. Bernanose, P. Vouaux, *J Chim Phys* **1953**, 50, 261–263.
- [2] A. Bernanose, M. Comte, P. Vouaux, *J Chim Phys* **1953**, 50, 64–68.
- [3] C. W. Tang, S. A. Vanslyke, *Appl. Phys. Lett.* **1987**, 51, 913–915.
- [4] M. Aleksandrova, *Adv. Mater. Sci. Eng.* **2016**, 2016.
- [5] N. Thejo Kalyani, S. J. Dhoble, *Renew. Sustain. Energy Rev.* **2015**, 44, 319–347.
- [6] Ertl, G. *The Nobel Prize in Chemistry*; The Royal Swedish Academy of Sciences: Stockholm, **2007**.
- [7] P. L. Anelli, N. Spencer, J. Fraser Stoddart, *J. Am. Chem. Soc.* **1991**, 113, 5131–5133.
- [8] C. O. Dietrich-Buchecker, J. P. Sauvage, J. M. Kern, *J. Am. Chem. Soc.* **1984**, 106, 3043–3045.
- [9] N. Koumura, R. W. J. Zijlstra, R. A. Van Delden, N. Harada, B. L. Feringa, *Nature* **1999**, 401, 152–155.
- [10] D. Castelvetti, *Nature* **2017**, 544, 278–279.
- [11] 12 Principles of Green Chemistry - American Chemical Society", can be found under <https://www.acs.org/content/acs/en/greenchemistry/principles/12-principles-of-green-chemistry.html>, **2021**.
- [12] G. E. Moore, *Proc. Ieee* **1998**, 86, 82–85.
- [13] G. E. Moore, *Electronics*, **1965**, 38, 82–85.
- [14] R. Kurzweil, *The Singularity Is Near: When Humans Transcend Biology*, Penguin, New York, **2005**.
- [15] Hruska, "Moore's Law is dead, long live Moore's Law - ExtremeTech", can be found under <https://www.extremetech.com/extreme/203490-moores->, **2021**.
- [16] R. M. Metzger, *Chem. Rev.* **2015**, 115, 5056–5115.
- [17] A. Hey, in *Feynman Comput.*, **2018**, p. 464.
- [18] A. Aviram, M. A. Ratner, *Chem. Phys. Lett.* **1974**, 29, 277–283.
- [19] A. Aviram, in *N. Y. Eng. Found.*, New York, **1989**.
- [20] F. Carter, in *Dekker*, New York, **1982**.
- [21] F. Carter, in *Dekker*, New York, **1987**.
- [22] H. Carter, F. L., Siatkowski, R. E., Wohltjen, in *Proc. 3rd. Intl. Symp.*, Amsterdam, **1988**.
- [23] R. M. Metzger, B. Chen, U. Höpfner, M. V. Lakshmikantham, D. Vuillaume, T. Kawai, X. Wu, H. Tachibana, T. V. Hughes, H. Sakurai, J. W. Baldwin, C. Hosch, M. P. Cava, L. Brehmer, G. J. Ashwell, *J. Am. Chem. Soc.* **1997**, 119, 10455–10466.
- [24] K. B. Blodgett, *J. Am. Chem. Soc.* **1935**, 57, 1007–1022.
- [25] K. B. Blodgett, I. Langmuir, *Phys. Rev.* **1937**, 51, 964–982.
- [26] J. Sagiv, *J. Am. Chem. Soc.* **1980**, 102, 92–98.
- [27] W. C. Bigelow, D. L. Pickett, W. A. Zisman, *J. Colloid Sci.* **1946**, 1, 513–538.
- [28] C. D. Bain, E. B. Troughton, Y. T. Tao, J. Evall, G. M. Whitesides, R. G. Nuzzo, *J. Am. Chem. Soc.* **1989**, 111, 321–335.

- [29] Z. J. Donhauser, B. A. Mantooth, K. F. Kelly, L. A. Bumm, J. D. Monnell, J. J. Stapleton, J. Price, A. M. Rawlett, D. L. Allara, J. M. Tour, P. S. Weiss, *Science* **2001**, 292, 2303–2307.
- [30] W. Haiss, H. Van Zalinge, S. J. Higgins, D. Bethell, H. Höbenreich, D. J. Schiffrin, R. J. Nichols, *J. Am. Chem. Soc.* **2003**, 125, 15294–15295.
- [31] T. Dadosh, Y. Gordin, R. Krahne, I. Khivrich, D. Mahalu, V. Frydman, J. Sperling, A. Yacoby, I. Bar-Joseph, *Nature* **2005**, 436, 677–680.
- [32] B. Xu, N. J. Tao, *Science* **2003**, 301, 1221–1223.
- [33] C. Cheng, P. R. McGonigal, S. T. Schneebeli, H. Li, N. A. Vermeulen, C. Ke, J. F. Stoddart, *Nat. Nanotechnol.* **2015**, 10, 547–553.
- [34] S. Erbas-Cakmak, D. A. Leigh, C. T. McTernan, A. L. Nussbaumer, *Artificial Molecular Machines*, **2015**.
- [35] M. M. Pollard, M. Lubomska, P. Rudolf, B. L. Feringa, *Angew. Chem.* **2007**, 119, 1300–1302.
- [36] G. T. Carroll, M. M. Pollard, R. van Delden, B. L. Feringa, *Chem. Sci.* **2010**, 1, 97.
- [37] Bässler H., Köhler A. *Charge Transport in Organic Semiconductors*. In: Metzger R. (eds) Unimolecular and Supramolecular Electronics I. Topics in Current Chemistry, vol 312. Springer, Berlin, Heidelberg, **2011**.
- [38] H. Shirakawa, E. J. Louis, A. G. MacDiarmid, C. K. Chiang, A. J. Heeger, *J. Chem. Soc. Chem. Commun.* **1977**, 578.
- [39] J. H. Burroughes, D. D. C. Bradley, A. R. Brown, R. N. Marks, K. Mackay, R. H. Friend, P. L. Burns, A. B. Holmes, *Nature* **1990**, 347, 539–541.
- [40] C. W. Schlenker, M. E. Thompson, **2011**, pp. 175–212.
- [41] K. Moth-Poulsen, T. Bjørnholm, *Nat. Nanotechnol.* **2009**, 4, 551–556.
- [42] S. V. Aradhya, L. Venkataraman, *Nat. Nanotechnol.* **2013**, 8, 399–410.
- [43] L. Sun, Y. A. Diaz-Fernandez, T. A. Gschneidtnr, F. Westerlund, S. Lara-Avila, K. Moth-Poulsen, *Chem. Soc. Rev.* **2014**, 43, 7378–7411.
- [44] A. W. Adamson, A. P. Gast, *Physical Chemistry of Surfaces*, **1997**.
- [45] D. Bélanger, J. Pinson, *Chem. Soc. Rev.* **2011**, 40, 3995–4048.
- [46] I. Langmuir, *J. Am. Chem. Soc.* **1917**, 39, 1848–1906.
- [47] I. Langmuir, V. J. Schaefer, *J. Am. Chem. Soc.* **1938**, 60, 1351–1360.
- [48] H. Kuhn, D. Möbius, *Angew. Chem. Int. Ed. Engl.* **1971**, 10, 620–637.
- [49] G. M. Whitesides, B. Grzybowski, *Science* **2002**, 295, 2418–2421.
- [50] A. Ulman, *Chem. Rev.* 1996 **1996**, 96, 1533–1554.
- [51] T. Lenz, T. Schmaltz, M. Novak, M. Halik, *Langmuir* **2012**, 28, 13900–13904.
- [52] L. Herrero, S. Martín, P. Cea, *Appl. Sci. Switz.* **2020**, 10.
- [53] C. Vericat, M. E. Vela, G. Benitez, P. Carro, R. C. Salvarezza, *Chem. Soc. Rev.* **2010**, 39, 1805–1834.
- [54] K. A. Peterlinz, R. Georgiadis, *Langmuir* **1996**, 12, 4731–4740.
- [55] R. F. DeBono, G. D. Loucks, D. Della Manna, U. J. Krull, *Can. J. Chem.* **1996**, 74, 677–688.
- [56] G. Hähner, C. Wöll, M. Buck, M. Grunze, *Langmuir* **1993**, 9, 1955–1958.
- [57] C. E. D. Chidsey, C. R. Bertozzi, T. M. Putvinski, A. M. Majsce, *J. Am. Chem. Soc.* **1990**, 112, 4301–4306.

- [58] K. Uosaki, Y. Sato, H. Kita, *Langmuir* **1991**, *7*, 1510–1514.
- [59] Y. Sato, B. L. Frey, R. M. Corn, K. Uosaki, *Bull. Chem. Soc. Jpn.* **1994**, *67*, 21–25.
- [60] N. Patel, M. C. Davies, M. Hartshorne, R. J. Heaton, C. J. Roberts, S. J. B. Tendler, P. M. Williams, *Langmuir* **1997**, *13*, 6485–6490.
- [61] R. G. Chapman, E. Ostuni, L. Yan, G. M. Whitesides, *Langmuir* **2000**, *16*, 6927–6936.
- [62] E. B. Troughton, C. D. Bain, G. M. Whitesides, R. G. Nuzzo, D. L. Allara, M. D. Porter, *Langmuir* **1988**, *4*, 365–385.
- [63] J. M. Seminario, C. E. De La Cruz, P. A. Derosa, *J. Am. Chem. Soc.* **2001**, *123*, 5616–5617.
- [64] J. M. Beebe, V. B. Engelkes, L. L. Miller, C. D. Frisbie, *J. Am. Chem. Soc.* **2002**, *124*, 11268–11269.
- [65] V. B. Engelkes, J. M. Beebe, C. D. Frisbie, *J. Am. Chem. Soc.* **2004**, *126*, 14287–14296.
- [66] M. D. Porter, T. B. Bright, D. L. Allara, C. E. Chidsey, *J. Am. Chem. Soc.* **1987**, *109*, 3559–3568.
- [67] S. Kaneko, T. Nakazumi, M. Kiguchi, *J. Phys. Chem. Lett.* **2010**, *1*, 3520–3523.
- [68] M. Kiguchi, O. Tal, S. Wohlthat, F. Pauly, M. Krieger, D. Djukic, J. C. Cuevas, J. M. Van Ruitenbeek, *Phys. Rev. Lett.* **2008**, *101*, 1–4.
- [69] C. H. Ko, M. J. Huang, M. D. Fu, C. H. Chen, *J. Am. Chem. Soc.* **2010**, *132*, 756–764.
- [70] Z. L. Peng, Z. Bin Chen, X. Y. Zhou, Y. Y. Sun, J. H. Liang, Z. J. Niu, X. S. Zhou, B. W. Mao, *J. Phys. Chem. C* **2012**, *116*, 21699–21705.
- [71] T. Kim, Z. F. Liu, C. Lee, J. B. Neaton, L. Venkataraman, *Proc. Natl. Acad. Sci. U. S. A.* **2014**, *111*, 10928–10932.
- [72] M. Garrido, M. K. Volland, P. W. Münich, L. Rodríguez-Pérez, J. Calbo, E. Ortí, M. Á. Herranz, N. Martín, D. M. Guldi, *J. Am. Chem. Soc.* **2020**, *142*, 1895–1903.
- [73] C. W. Marquardt, S. Grunder, A. Błaszczuk, S. Dehm, F. Hennrich, H. V. Löhneysen, M. Mayor, R. Krupke, *Nat. Nanotechnol.* **2010**, *5*, 863–867.
- [74] P. E. Laibinis, G. M. Whitesides, D. L. Aliara, Y. T. Tao, A. N. Parikh, R. G. Nuzzo, *J. Am. Chem. Soc.* **1991**, *113*, 7152–7167.
- [75] X. Jiang, D. A. Bruzewicz, M. M. Thant, G. M. Whitesides, *Anal. Chem.* **2004**, *76*, 6116–6121.
- [76] A. Carvalho, M. Geissler, H. Schmid, B. Michel, E. Delamarche, *Langmuir* **2002**, *18*, 2406–2412.
- [77] J. C. Love, D. B. Wolfe, M. L. Chabinyc, K. E. Paul, G. M. Whitesides, *J. Am. Chem. Soc.* **2002**, *124*, 1576–1577.
- [78] V. K. M. Poon, A. Burd, *Burns* **2004**, *30*, 140–147.
- [79] D. P. Dowling, K. Donnelly, M. L. McConnell, R. Eloy, M. N. Arnaud, *Thin Solid Films* **2001**, *398*, 602–606.
- [80] A. Vilan, D. Aswal, D. Cahen, *Chem. Rev.* **2017**, *117*, 4248–4286.
- [81] H. Li, T. A. Su, M. Camarasa-Gómez, D. Hernangómez-Pérez, S. E. Henn, V. Pokorný, C. D. Caniglia, M. S. Inkpen, R. Korytár, M. L. Steigerwald, C. Nuckolls, F. Evers, L. Venkataraman, *Angew. Chem. Int. Ed.* **2017**, *56*, 14145–14148.
- [82] X. ZHU, *Surf. Sci. Rep.* **2004**, *56*, 1–83.
- [83] D. Cahen, A. Kahn, *Adv. Mater.* **2003**, *15*, 271–277.
- [84] J. E. Lennard-Jones, *Trans. Faraday Soc.* **1932**, *28*, 333–359.

- [85] F. Huber, J. Berwanger, S. Polesya, S. Mankovsky, H. Ebert, F. J. Giessibl, *Science* **2019**, *366*, 235–238.
- [86] C. M. Crudden, J. H. Horton, I. I. Ebralidze, O. V. Zenkina, A. B. McLean, B. Drevniok, Z. She, H. B. Kraatz, N. J. Mosey, T. Seki, E. C. Keske, J. D. Leake, A. Rousina-Webb, G. Wu, *Nat. Chem.* **2014**, *6*, 409–414.
- [87] B. Xu, X. Xiao, N. J. Tao, *J. Am. Chem. Soc.* **2003**, *125*, 16164–16165.
- [88] A. Mishchenko, L. A. Zotti, D. Vonlanthen, M. Bürkle, F. Pauly, J. C. Cuevas, M. Mayor, T. Wandlowski, *J. Am. Chem. Soc.* **2011**, *133*, 184–187.
- [89] C. A. Martin, D. Ding, J. K. Sørensen, T. Bjørnholm, J. M. Van Ruitenbeek, H. S. J. Van Der Zant, *J. Am. Chem. Soc.* **2008**, *130*, 13198–13199.
- [90] K. Scheil, N. Lorente, M. L. Bocquet, P. C. Hess, M. Mayor, R. Berndt, *J. Phys. Chem. C* **2017**, *121*, 25303–25308.
- [91] D. Bléger, F. Mathevet, D. Kreher, A. J. Attias, A. Bocheux, S. Latil, L. Douillard, C. Fiorini-Debuisschert, F. Charra, *Angew. Chem. Int. Ed.* **2011**, *50*, 6562–6566.
- [92] H. Chen, V. Brasiliense, J. Mo, L. Zhang, Y. Jiao, Z. Chen, L. O. Jones, G. He, Q.-H. Guo, X.-Y. Chen, B. Song, G. C. Schatz, J. F. Stoddart, *J. Am. Chem. Soc.* **2021**, *143*, 2886–2895.
- [93] C. Li, I. Pobelov, T. Wandlowski, A. Bagrets, A. Arnold, F. Evers, *J. Am. Chem. Soc.* **2008**, *130*, 318–326.
- [94] D. Dulić, F. Pump, S. Campidelli, P. Lavie, G. Cuniberti, A. Filoramo, *Angew. Chem.* **2009**, *121*, 8423–8426.
- [95] S. Yasuda, S. Yoshida, J. Sasaki, Y. Okutsu, T. Nakamura, A. Taninaka, O. Takeuchi, H. Shigekawa, *J. Am. Chem. Soc.* **2006**, *128*, 7746–7747.
- [96] B. M. Boardman, J. R. Widawsky, Y. S. Park, C. L. Schenck, L. Venkataraman, M. L. Steigerwald, C. Nuckolls, *J. Am. Chem. Soc.* **2011**, *133*, 8455–8457.
- [97] S. Zhang, K. L. Chandra, C. B. Gorman, *J. Am. Chem. Soc.* **2007**, *6*, 4876–4877.
- [98] F. Chen, X. Li, J. Hihath, Z. Huang, N. Tao, *J. Am. Chem. Soc.* **2006**, *128*, 15874–15881.
- [99] L. Venkataraman, J. E. Klare, C. Nuckolls, M. S. Hybertsen, M. L. Steigerwald, *Nature* **2006**, *442*, 904–907.
- [100] J. Ren, M. Freitag, C. Schwermann, A. Bakker, S. Amirjalayer, A. Rühling, H. Y. Gao, N. L. Doltsinis, F. Glorius, H. Fuchs, *Nano Lett.* **2020**, *20*, 5922–5928.
- [101] M. Lindner, M. Valášek, J. Homberg, K. Edelmann, L. Gerhard, W. Wulfhekel, O. Fuhr, T. Wächter, M. Zharnikov, V. Kolivoška, L. Pospíšil, G. Mészáros, M. Hromadová, M. Mayor, *Chem. - Eur. J.* **2016**, *22*, 13218–13235.
- [102] F. Matino, G. Schull, F. Köhler, S. Gabutti, M. Mayor, R. Berndt, *Proc. Natl. Acad. Sci. U. S. A.* **2011**, *108*, 961–964.
- [103] S. Gabutti, M. Knutzen, M. Neuburger, G. Schull, R. Berndt, M. Mayor, *Chem. Commun.* **2008**, 2370–2372.
- [104] I. L. Herrer, A. K. Ismael, D. C. Milán, A. Vezzoli, S. Martín, A. González-Orive, I. Grace, C. Lambert, J. L. Serrano, R. J. Nichols, P. Cea, *J. Phys. Chem. Lett.* **2018**, *9*, 5364–5372.
- [105] X. Pan, B. Lawson, A. M. Rustad, M. Kamenetska, M. Kamenetska, M. Kamenetska, *Nano Lett.* **2020**, *20*, 4687–4692.

- [106] J. C. Love, L. A. Estroff, J. K. Kriebel, R. G. Nuzzo, G. M. Whitesides, *Self-Assembled Monolayers of Thiolates on Metals as a Form of Nanotechnology*, **2005**.
- [107] M. Valášek, M. Lindner, M. Mayor, *Beilstein J. Nanotechnol.* **2016**, 7, 374–405.
- [108] R. G. Nuzzo, D. L. Allara, *J. Am. Chem. Soc.* **1983**, 105, 4481–4483.
- [109] M. Hasan, D. Bethell, M. Brust, *J. Am. Chem. Soc.* **2002**, 124, 1132–1133.
- [110] M. S. Inkpen, Z. –F Liu, H. Li, L. M. Campos, J. B. Neaton, L. Venkataraman, *Nat. Chem.* **2019**, 11, 351–358.
- [111] P. Maksymovych, D. C. Sorescu, J. T. Yates, *Phys. Rev. Lett.* **2006**, 97, 1–4.
- [112] X. Torrelles, C. Vericat, M. E. Vela, M. H. Fonticelli, M. A. D. Millone, R. Felici, T. L. Lee, J. Zegenhagen, G. Muñoz, J. A. Martín-Gago, R. C. Salvarezza, *J. Phys. Chem. B* **2006**, 110, 5586–5594.
- [113] J. E. Matthiesen, D. Jose, C. M. Sorensen, K. J. Klabunde, *J. Am. Chem. Soc.* **2012**, 134, 9376–9379.
- [114] L. Kankate, A. Turchanin, A. Götzhäuser, *Langmuir* **2009**, 25, 10435–10438.
- [115] I. I. Rzeźnicka, J. Lee, P. Maksymovych, J. T. Yates, *J. Phys. Chem. B* **2005**, 109, 15992–15996.
- [116] Z. Huang, F. Chen, P. A. Bennett, N. Tao, *J. Am. Chem. Soc.* **2007**, 129, 13225–13231.
- [117] L. H. Dubois, B. R. Zegarski, R. G. Nuzzo, *J. Chem. Phys.* **1993**, 98, 678–688.
- [118] Q. Xu, H. Ma, H. Yip, A. K. Y. Jen, *Nanotechnology* **2008**, 19, 135605.
- [119] H. Häkkinen, *Nat. Chem.* **2012**, 4, 443–455.
- [120] P. Maksymovych, D. C. Sorescu, O. Voznyy, J. T. Yates, *J. Am. Chem. Soc.* **2013**, 135, 4922–4925.
- [121] P. Maksymovych, O. Voznyy, D. B. Dougherty, D. C. Sorescu, J. T. Yates, *Prog. Surf. Sci.* **2010**, 85, 206–240.
- [122] H. Grönbeck, M. Walter, H. Häkkinen, *J. Am. Chem. Soc.* **2006**, 128, 10268–10275.
- [123] P. D. Jadzinsky, G. Calero, C. J. Ackerson, D. A. Bushnell, R. D. Kornberg, *Science* **2007**, 318, 430–433.
- [124] R. L. Whetten, R. C. Price, *Science* **2007**, 318, 407–408.
- [125] J. A. Mann, W. R. Dichtel, *ACS Nano* **2013**, 7, 7193–7199.
- [126] J.-F. Morin, Y. Shirai, J. M. Tour, *Org. Lett.* **2006**, 8, 1713–1716.
- [127] B. Baisch, D. Raffa, U. Jung, O. M. Magnussen, C. Nicolas, J. Lacour, J. Kubitschke, R. Herges, *J. Am. Chem. Soc.* **2009**, 131, 442–443.
- [128] T. R. Rusch, A. Schlimm, N. R. Krekieh, T. Tellkamp, Š. Budzák, D. Jacquemin, F. Tuczek, R. Herges, O. M. Magnussen, *Angew. Chem.* **2020**, 132, 17345–17349.
- [129] T. Jasper-Toennies, M. Gruber, S. Johannsen, T. Frederiksen, A. Garcia-Lekue, T. Jäkel, F. Roehricht, R. Herges, R. Berndt, *ACS Nano* **2020**, 14, 3907–3916.
- [130] T. R. Rusch, A. Schlimm, N. R. Krekieh, B. M. Flöser, F. Röhricht, M. Hammerich, I. Lautenschläger, T. Strunskus, R. Herges, F. Tuczek, O. M. Magnussen, *J. Phys. Chem. C* **2019**, 123, 13720–13730.
- [131] F. L. Otte, S. Lemke, C. Schütt, N. R. Krekieh, U. Jung, O. M. Magnussen, R. Herges, *J. Am. Chem. Soc.* **2014**, 136, 11248–11251.
- [132] Z. Wei, X. Wang, A. Borges, M. Santella, T. Li, J. K. Sørensen, M. Vanin, W. Hu, Y. Liu, J. Ulstrup, G. C. Solomon, Q. Chi, T. Bjørnholm, K. Nørsgaard, B. W. Laursen, *Langmuir* **2014**, 30, 14868–14876.

- [133] S. Lemke, S. Ulrich, F. Claußen, A. Bloedorn, U. Jung, R. Herges, O. M. Magnussen, *Surf. Sci.* **2015**, 632, 71–76.
- [134] S. Gabutti, S. Schaffner, M. Neuburger, M. Fischer, G. Schäfer, M. Mayor, *Org. Biomol. Chem.* **2009**, 7, 3222–3229.
- [135] N. L. Schneider, F. Matino, G. Schull, S. Gabutti, M. Mayor, R. Berndt, *Phys. Rev. B* **2011**, 84, 153403.
- [136] P. Du, D. Kreher, F. Mathevet, P. Maldivi, F. Charra, A. J. Attias, *ChemPhysChem* **2015**, 16, 3774–3778.
- [137] P. Du, M. Jaouen, A. Bocheux, C. Bourgogne, Z. Han, V. Bouchiat, D. Kreher, F. Mathevet, C. Fiorini-Debuisschert, F. Charra, A. J. Attias, *Angew. Chem. Int. Ed.* **2014**, 53, 10060–10066.
- [138] S. Le Liepvre, P. Du, D. Kreher, F. Mathevet, A. J. Attias, C. Fiorini-Debuisschert, L. Douillard, F. Charra, *ACS Photonics* **2016**, 3, 2291–2296.
- [139] B. Kim, C. Cho, I. Arfaoui, C. Paris, C. Petit, T. Le Bahers, E. Kim, A. J. Attias, *Mater. Horiz.* **2020**, 7, 2741–2748.
- [140] V. J. Langlais, R. R. Schlittler, H. Tang, A. Gourdon, C. Joachim, J. K. Gimzewski, *Phys. Rev. Lett.* **1999**, 83, 2809–2812.
- [141] S. Fujii, T. Tada, Y. Komoto, T. Osuga, T. Murase, M. Fujita, M. Kiguchi, *J. Am. Chem. Soc.* **2015**, 137, 5939–5947.
- [142] G. S. Kottas, T. Brotin, P. F. H. Schwab, K. Gala, Z. Havlas, J. P. Kirby, J. R. Miller, J. Michl, *Organometallics* **2014**, 33, 3251–3264.
- [143] X. Zheng, M. E. Mulcahy, D. Horinek, F. Galeotti, T. F. Magnera, J. Michl, *J. Am. Chem. Soc.* **2004**, 126, 4540–4542.
- [144] P. Chinwangso, A. C. Jamison, T. R. Lee, *Acc. Chem. Res.* **2011**, 44, 511–519.
- [145] J. K. Whitesell, H. K. Chang, *Science* **1993**, 261, 73–76.
- [146] J. S. Park, A. N. Vo, D. Barriet, Y. S. Shon, T. R. Lee, *Langmuir* **2005**, 21, 2902–2911.
- [147] Y. Ie, T. Hirose, H. Nakamura, M. Kiguchi, N. Takagi, M. Kawai, Y. Aso, *J. Am. Chem. Soc.* **2011**, 133, 3014–3022.
- [148] Y. Ie, T. Hirose, A. Yao, T. Yamada, N. Takagi, M. Kawai, Y. Aso, *Phys. Chem. Chem. Phys.* **2009**, 11, 4949–4951.
- [149] L. Gerhard, K. Edelmann, J. Homberg, M. Valášek, S. G. Bahoosh, M. Lukas, F. Pauly, M. Mayor, W. Wulfhekel, *Nat. Commun.* **2017**, 8, 1–10.
- [150] T. Ohto, A. Tashiro, T. Seo, N. Kawaguchi, Y. Numai, J. Tokumoto, S. Yamaguchi, R. Yamada, H. Tada, Y. Aso, Y. Ie, *Small* **2021**, 17, 1–8.
- [151] K. Nikitin, E. Lestini, M. Lazzari, S. Altobello, D. Fitzmaurice, *Langmuir* **2007**, 23, 12147–12153.
- [152] R. Sakamoto, Y. Ohirabaru, R. Matsuoka, H. Maeda, S. Katagiri, H. Nishihara, *Chem. Commun.* **2013**, 49, 7108–7110.
- [153] Y. Yao, J. M. Tour, *J. Org. Chem.* **1999**, 64, 1968–1971.
- [154] T. Kitagawa, Y. Idomoto, H. Matsubara, D. Hobara, T. Kakiuchi, T. Okazaki, K. Komatsu, *J. Org. Chem.* **2006**, 71, 1362–1369.
- [155] S. Katano, Y. Kim, H. Matsubara, T. Kitagawa, M. Kawai, *J. Am. Chem. Soc.* **2007**, 129, 2511–2515.

- [156] R. Kumar, S. N. Ramakrishna, V. V. Naik, Z. Chu, M. E. Drew, N. D. Spencer, Y. Yamakoshi, *Nanoscale* **2015**, 7, 6599–6606.
- [157] D. Takamatsu, K. Fukui, S. Aroua, Y. Yamakoshi, *Org. Biomol. Chem.* **2010**, 8, 3655.
- [158] F. Ishiwari, G. Nascimbeni, E. Sauter, H. Tago, Y. Shoji, S. Fujii, M. Kiguchi, T. Tada, M. Zharnikov, E. Zojer, T. Fukushima, *J. Am. Chem. Soc.* **2019**, 141, 5995–6005.
- [159] S. Chaunchaiyakul, C. Zhang, H. Imada, E. Kazuma, F. Ishiwari, Y. Shoji, T. Fukushima, Y. Kim, *J. Phys. Chem. C* **2019**, 123, 31272–31278.
- [160] T. Tada, F. Ishiwari, Y. Shoji, T. Fukushima, *J. Phys. Chem. C* **2019**, 123, 4401–4406.
- [161] T. Sakata, S. Maruyama, A. Ueda, H. Otsuka, Y. Miyahara, *Langmuir* **2007**, 23, 2269–2272.
- [162] D. Hirayama, K. Takimiya, Y. Aso, T. Otsubo, T. Hasobe, H. Yamada, H. Imahori, S. Fukuzumi, Y. Sakata, *J. Am. Chem. Soc.* **2002**, 124, 532–533.
- [163] S. E. Zhu, Y. M. Kuang, F. Geng, J. Z. Zhu, C. Z. Wang, Y. J. Yu, Y. Luo, Y. Xiao, K. Q. Liu, Q. S. Meng, L. Zhang, S. Jiang, Y. Zhang, G. W. Wang, Z. C. Dong, J. G. Hou, *J. Am. Chem. Soc.* **2013**, 135, 15794–15800.
- [164] L. Wei, K. Padmaja, W. J. Youngblood, A. B. Lysenko, J. S. Lindsey, D. F. Bocian, *J. Org. Chem.* **2004**, 69, 1461–1469.
- [165] J. A. Mann, J. Rodríguez-López, H. D. Abruña, W. R. Dichtel, *J. Am. Chem. Soc.* **2011**, 133, 17614–17617.
- [166] T. Sebechlebská, J. Šebera, V. Kolivoška, M. Lindner, J. Gasior, G. Mészáros, M. Valášek, M. Mayor, M. Hromadová, *Electrochimica Acta* **2017**, 258, 1191–1200.
- [167] C. B. KC, G. N. Lim, F. D'Souza, *Angew. Chem.* **2015**, 127, 5177–5181.
- [168] A. Schramm, C. Stroh, K. Dössel, M. Lukas, M. Fischer, F. Schramm, O. Fuhr, H. V. Löhneysen, M. Mayor, *Eur. J. Inorg. Chem.* **2013**, 70–79.
- [169] M. Lukas, K. Dössel, A. Schramm, O. Fuhr, C. Stroh, M. Mayor, K. Fink, H. V. Löhneysen, *ACS Nano* **2013**, 7, 6170–6180.
- [170] A. Schramm, C. Stroh, K. Dössel, M. Lukas, O. Fuhr, H. V. Löhneysen, M. Mayor, *Chem. Commun.* **2013**, 49, 1076–1078.
- [171] U. G. E. Perera, F. Ample, H. Kersell, Y. Zhang, G. Vives, J. Echeverria, M. Grisolia, G. Rapenne, C. Joachim, S. W. Hla, *Nat. Nanotechnol.* **2013**, 8, 46–51.
- [172] S. Ramachandra, K. C. Schuermann, F. Edafe, P. Belser, C. A. Nijhuis, W. F. Reus, G. M. Whitesides, L. De Cola, *Inorg. Chem.* **2011**, 50, 1581–1591.
- [173] H. Jian, J. M. Tour, *J. Org. Chem.* **2003**, 68, 5091–5103.
- [174] K. Y. Chen, O. Ivashenko, G. T. Carroll, J. Robertus, J. C. M. Kistemaker, G. London, W. R. Browne, P. Rudolf, B. L. Feringa, *J. Am. Chem. Soc.* **2014**, 136, 3219–3224.
- [175] T. C. Pijper, O. Ivashenko, M. Walko, P. Rudolf, W. R. Browne, B. L. Feringa, *J. Phys. Chem. C* **2015**, 119, 3648–3657.
- [176] Y. Shirai, J. M. Guerrero, T. Sasaki, T. He, H. Ding, G. Vives, B. C. Yu, L. Cheng, A. K. Platt, P. G. Taylor, Y. Gao, J. M. Tour, *J. Org. Chem.* **2009**, 74, 7885–7897.
- [177] J. Homberg, M. Lindner, L. Gerhard, K. Edelmann, T. Frauhammer, Y. Nahas, M. Valášek, M. Mayor, W. Wulfhekel, *Nanoscale* **2019**, 11, 9015–9022.
- [178] G. Yang, G. Liu, *J. Phys. Chem. B* **2003**, 107, 8746–8759.
- [179] M. Mayor, H. B. Weber, J. Reichert, M. Elbing, C. Von Hänisch, D. Beckmann, M. Fischer, *Angew. Chem. Int. Ed.* **2003**, 42, 5834–5838.

- [180] M. Lindner, M. Valášek, M. Mayor, T. Frauhammer, W. Wulfhekel, L. Gerhard, *Angew. Chem. Int. Ed.* **2017**, *56*, 8290–8294.
- [181] F. S. Benneckendorf, V. Rohnacher, E. Sauter, S. Hillebrandt, M. Münch, C. Wang, S. Casalini, K. Ihrig, S. Beck, D. Jänsch, J. Freudenberg, W. Jaegermann, P. Samorì, A. Pucci, U. H. F. Bunz, M. Zharnikov, K. Müllen, *ACS Appl. Mater. Interfaces* **2020**, *12*, 6565–6572.
- [182] V. Rohnacher, F. S. Benneckendorf, M. Münch, E. Sauter, A. Asyuda, M. M. Barf, J. N. Tisserant, S. Hillebrandt, F. Rominger, D. Jänsch, J. Freudenberg, W. Kowalsky, W. Jaegermann, U. H. F. Bunz, A. Pucci, M. Zharnikov, K. Müllen, *Adv. Mater. Technol.* **2021**, *6*.
- [183] J. H. Tang, Z. Cai, D. Yan, K. Tang, J. Y. Shao, C. Zhan, D. Wang, Y. W. Zhong, L. J. Wan, J. Yao, *J. Am. Chem. Soc.* **2018**, *140*, 12337–12340.
- [184] L. J. O'Driscoll, X. Wang, M. Jay, A. S. Batsanov, H. Sadeghi, C. J. Lambert, B. J. Robinson, M. R. Bryce, *Angew. Chem.* **2020**, *132*, 892–899.
- [185] L. A. Bumm, J. J. Arnold, M. T. Cygan, T. D. Dunbar, T. P. Burgin, L. Jones, D. L. Allara, J. M. Tour, P. S. Weiss, *Science* **1996**, *271*, 1705–1707.
- [186] M. A. Reed, *Science* **1997**, *278*, 252–254.
- [187] X. D. Cui, A. Primak, X. Zarate, J. Tomfohr, O. F. Sankey, A. L. Moore, T. A. Moore, D. Gust, G. Harris, S. M. Lindsay, *Science* **2001**, *294*, 571–574.
- [188] Y. S. Park, J. R. Widawsky, M. Kamenetska, M. L. Steigerwald, M. S. Hybertsen, C. Nuckolls, L. Venkataraman, *J. Am. Chem. Soc.* **2009**, *131*, 10820–10821.
- [189] J. Chen, M. A. Reed, A. M. Rawlett, J. M. Tour, *Science* **1999**, *286*, 1550–1552.
- [190] C. Tang, L. Chen, L. Zhang, Z. Chen, G. Li, Z. Yan, L. Lin, J. Liu, L. Huang, Y. Ye, Y. Hua, J. Shi, H. Xia, W. Hong, *Angew. Chem. Int. Ed.* **2019**, *58*, 10601–10605.
- [191] J. Park, A. N. Pasupathy, J. I. Goldsmith, C. Chang, Y. Yaish, J. R. Petta, M. Rinkoski, J. P. Sethna, H. D. Abruña, P. L. McEuen, D. C. Ralph, *Nature* **2002**, *417*, 722–725.
- [192] M. Mayor, C. Von Hänisch, H. B. Weber, J. Reichert, D. Beckmann, *Angew. Chem. Int. Ed.* **2002**, *41*, 1183–1186.
- [193] D. Vonlanthen, A. Mishchenko, M. Elbing, M. Neuburger, T. Wandlowski, M. Mayor, *Angew. Chem. Int. Ed.* **2009**, *48*, 8886–8890.
- [194] V. Pierre, M. Curie, P. Jussieu, P. Cedex, F. Received, *Chem Phys* **1989**, *131*, 481–488.
- [195] A. Schlimm, R. Löw, T. Rusch, F. Röhricht, T. Strunskus, T. Tellkamp, F. Sönnichsen, U. Manthe, O. Magnussen, F. Tuczek, R. Herges, *Angew. Chem. Int. Ed.* **2019**, *58*, 6574–6578.
- [196] M. Valášek, K. Edelmann, L. Gerhard, O. Fuhr, M. Lukas, M. Mayor, *J. Org. Chem.* **2014**, *79*, 7342–7357.
- [197] Y. Ie, K. Tanaka, A. Tashiro, S. K. Lee, H. R. Testai, R. Yamada, H. Tada, Y. Aso, *J. Phys. Chem. Lett.* **2015**, *6*, 3754–3759.
- [198] T. Ijaz, B. Yang, R. Wang, J. Zhu, A. Farrukh, G. Chen, G. Franc, Y. Zhang, A. Gourdon, Z. Dong, *Appl. Phys. Lett.* **2019**, *115*, 1–5.
- [199] S. O. Ann, *Mol. Mot.* **2007**, *422*, 759–765.
- [200] R. T. Abraham, R. S. Tibbetts, *Science* **2005**, *308*, 510–511.
- [201] J. D. Badjic, *Science* **2004**, *303*, 1845–1849.

- [202] B. Lewandowski, G. De Bo, J. W. Ward, M. Papmeyer, S. Kuschel, M. J. Aldegunde, P. M. E. Gramlich, D. Heckmann, S. M. Goldup, D. M. D'Souza, A. E. Fernandes, D. A. Leigh, *Science* **2013**, *339*, 189–193.
- [203] V. Balzani, A. Credi, B. Ferrer, S. Silvi, M. Venturi, in *Mol. Mach.*, Springer-Verlag, Berlin/Heidelberg, **2005**, pp. 1–27.
- [204] R. F. Ismagilov, A. Schwartz, N. Bowden, G. M. Whitesides, *Angew. Chem. Int. Ed.* **2002**, *41*, 652–654.
- [205] T. R. Kline, W. F. Paxton, T. E. Mallouk, A. Sen, *Angew. Chem. Int. Ed.* **2005**, *44*, 744–746.
- [206] R. D. Astumian, *Phys. Chem. Chem. Phys.* **2007**, *9*, 5067–5083.
- [207] D. J. Cárdenas, A. Livoreil, J. P. Sauvage, *J. Am. Chem. Soc.* **1996**, *118*, 11980–11981.
- [208] T. R. Kelly, H. De Silva, R. A. Silva, *Nature* **1999**, *401*, 150–152.
- [209] R. Ballardini, V. Balzani, A. Credi, M. T. Gandolfi, M. Venturi, *Acc. Chem. Res.* **2001**, *34*, 445–455.
- [210] T. Ross Kelly, R. A. Silva, H. De Silva, S. Jasmin, Y. Zhao, *J. Am. Chem. Soc.* **2000**, *122*, 6935–6949.
- [211] A. P. Davis, *Angew. Chem. Int. Ed.* **1998**, *37*, 909–910.
- [212] W. L. Mock, K. J. Ochwat, *J. Phys. Org. Chem.* **2003**, *16*, 175–182.
- [213] G. Haberhauer, *Angew. Chem. Int. Ed.* **2011**, *50*, 6415–6418.
- [214] M. J. Barrell, A. G. Campaña, M. von Delius, E. M. Geertsema, D. A. Leigh, *Angew. Chem.* **2011**, *123*, 299–304.
- [215] T. Kudernac, N. Ruangsapapichat, M. Parschau, B. MacIá, N. Katsonis, S. R. Harutyunyan, K. H. Ernst, B. L. Feringa, *Nature* **2011**, *479*, 208–211.
- [216] G. S. Kottas, L. I. Clarke, D. Horinek, J. Michl, *Chem. Rev.* **2005**, *105*, 1281–1376.
- [217] G. J. Simpson, V. García-López, A. Daniel Boese, J. M. Tour, L. Grill, *Nat. Commun.* **2019**, *10*, 4631.
- [218] H. L. Tierney, C. J. Murphy, A. D. Jewell, A. E. Baber, E. V. Iski, H. Y. Khodaverdian, A. F. McGuire, N. Klebanov, E. C. H. Sykes, *Nat. Nanotechnol.* **2011**, *6*, 625–629.
- [219] H. L. Tierney, C. J. Murphy, E. C. H. Sykes, *Phys. Rev. Lett.* **2011**, *106*, 010801.
- [220] T. A. Balema, Y. Liu, N. A. Wasio, A. M. Larson, D. A. Patel, P. Deshlahra, E. C. H. Sykes, *J. Phys. Chem. C* **2021**, *125*, 3584–3589.
- [221] A. Bauer, M. Maier, W. M. Schosser, J. Diegel, F. Paschke, Y. Dedkov, F. Pauly, R. F. Winter, M. Fonin, *Adv. Mater.* **2020**, *32*.
- [222] T. Wu, L. Liu, Y. Zhang, Y. Wang, Z. Shen, N. Li, R. Berndt, S. Hou, Y. Wang, *Chem. Commun.* **2020**, *56*, 968–971.
- [223] K. H. Au Yeung, T. Kühne, F. Eisenhut, M. Kleinwächter, Y. Gisbert, R. Robles, N. Lorente, G. Cuniberti, C. Joachim, G. Rapenne, C. Kammerer, F. Moresco, *J. Phys. Chem. Lett.* **2020**, *11*, 6892–6899.
- [224] S. Stolz, O. Gröning, J. Prinz, H. Brune, R. Widmer, *Proc. Natl. Acad. Sci.* **2020**, *117*, 14838–14842.
- [225] R. D. Astumian, M. Bier, *Biophys. J.* **1996**, *70*, 637–653.
- [226] Y. Zhang, J. P. Calupitan, T. Rojas, R. Tumbleson, G. Erbland, C. Kammerer, T. M. Ajayi, S. Wang, L. A. Curtiss, A. T. Ngo, S. E. Ulloa, G. Rapenne, S. W. Hla, *Nat. Commun.* **2019**, *10*, 1–9.

- [227] Y. Zhang, H. Kersell, R. Stefak, J. Echeverria, V. Iancu, U. G. E. Perera, Y. Li, A. Deshpande, K.-F. Braun, C. Joachim, G. Rapenne, S.-W. Hla, *Nat. Nanotechnol.* **2016**, *11*, 706–712.
- [228] K. Ray, *Science* **1999**, *283*, 814–816.
- [229] B. Göhler, V. Hamelbeck, T. Z. Markus, M. Kettner, G. F. Hanne, Z. Vager, R. Naaman, H. Zacharias, *Science* **2011**, *331*, 894–897.
- [230] V. Kiran, S. P. Mathew, S. R. Cohen, I. Hernández Delgado, J. Lacour, R. Naaman, *Adv. Mater.* **2016**, *28*, 1957–1962.
- [231] P. C. Mondal, N. Kantor-Uriel, S. P. Mathew, F. Tassinari, C. Fontanesi, R. Naaman, *Adv. Mater.* **2015**, *27*, 1924–1927.
- [232] R. Naaman, Y. Paltiel, D. H. Waldeck, *J. Phys. Chem. Lett.* **2020**, *11*, 3660–3666.
- [233] S. Varela, V. Mujica, E. Medina, *Phys. Rev. B* **2016**, *93*, 155436.
- [234] S. Dalum, P. Hedegård, *Nano Lett.* **2019**, *19*, 5253–5259.
- [235] A. C. Aragonès, E. Medina, M. Ferrer-Huerta, N. Gimeno, M. Teixidó, J. L. Palma, N. Tao, J. M. Ugalde, E. Giralt, I. Díez-Pérez, V. Mujica, *Small* **2017**, *13*, 1602519.
- [236] A.-M. Guo, Q. Sun, *Phys. Rev. Lett.* **2012**, *108*, 218102.
- [237] E. Medina, F. López, M. A. Ratner, V. Mujica, *EPL Europhys. Lett.* **2012**, *99*, 17006.
- [238] J. Gersten, K. Kaasbjerg, A. Nitzan, *J. Chem. Phys.* **2013**, *139*, 114111.
- [239] Z. Xie, T. Z. Markus, S. R. Cohen, Z. Vager, R. Gutierrez, R. Naaman, *Nano Lett.* **2011**, *11*, 4652–4655.
- [240] H. Lu, J. Wang, C. Xiao, X. Pan, X. Chen, R. Brunecky, J. J. Berry, K. Zhu, M. C. Beard, Z. V. Vardeny, *Sci. Adv.* **2019**, *5*, eaay0571.
- [241] A. Kumar, E. Capua, M. K. Kesharwani, J. M. L. Martin, E. Sitbon, D. H. Waldeck, R. Naaman, *Proc. Natl. Acad. Sci.* **2017**, *114*, 2474–2478.
- [242] E. Z. B. Smolinsky, A. Neubauer, A. Kumar, S. Yochelis, E. Capua, R. Carmieli, Y. Paltiel, R. Naaman, K. Michaeli, *J. Phys. Chem. Lett.* **2019**, *10*, 1139–1145.
- [243] G. Bullard, F. Tassinari, C.-H. Ko, A. K. Mondal, R. Wang, S. Mishra, R. Naaman, M. J. Therien, *J. Am. Chem. Soc.* **2019**, *141*, 14707–14711.
- [244] M. Suda, Y. Thathong, V. Promarak, H. Kojima, M. Nakamura, T. Shiraogawa, M. Ehara, H. M. Yamamoto, *Nat. Commun.* **2019**, *10*, 2455.
- [245] B. Valeur, J. C. Brochon, *New Trends in Fluorescence Spectroscopy: Applications to Chemical and Life Sciences*, Springer Berlin Heidelberg, **2012**.
- [246] S. E. Braslavsky, *Pure Appl. Chem.* **2007**, *79*, 293–465.
- [247] "Lumineszenz", can be found under <http://www.chemie.uni-jena.de/institute/oc/weiss/lumineszenz.htm>, **2021**.
- [248] G. Hong, X. Gan, C. Leonhardt, Z. Zhang, J. Seibert, J. M. Busch, S. Bräse, *Adv. Mater.* **2021**, *33*, 2005630.
- [249] G. Destriau, *J. Chim. Phys.* **1936**, *33*, 587–625.
- [250] M. Pope, H. P. Kallmann, P. Magnante, *J. Chem. Phys.* **1963**, *38*, 2042–2043.
- [251] C. Adachi, T. Tsutsui, S. Saito, *Appl. Phys. Lett.* **1990**, *57*, 531–533.
- [252] U. Mitschke, P. Bäuerle, *J. Mater. Chem.* **2000**, *10*, 1471–1507.
- [253] X. K. Chen, D. Kim, J. L. Brédas, *Acc. Chem. Res.* **2018**, *51*, 2215–2224.
- [254] A. Kraft, A. C. Grimsdale, A. B. Holmes, *Angew. Chem. Int. Ed.* **1998**, *37*, 402–428.
- [255] K. Kuhnke, C. Große, P. Merino, K. Kern, *Chem. Rev.* **2017**, *117*, 5174–5222.

- [256] K. Edelmann, L. Gerhard, M. Winkler, L. Wilmes, V. Rai, M. Schumann, C. Kern, M. Meyer, M. Wegener, W. Wulfhekel, *Rev. Sci. Instrum.* **2018**, 89, 123107.
- [257] R. Berndt, J. K. Gimzewski, P. Johansson, *Phys. Rev. Lett.* **1991**, 67, 3796–3799.
- [258] R. D. Young, *Phys. Today* **1971**, 24, 42–49.
- [259] R. Berndt, R. Gaisch, J. K. Gimzewski, B. Reihl, R. R. Schlittler, W. D. Schneider, M. Tschudy, *Science* **1993**, 262, 1425–1427.
- [260] J. K. Gimzewski, B. Reihl, J. H. Coombs, R. R. Schlittler, *Z. Für Phys. B Condens. Matter* **1988**, 72, 497–501.
- [261] X. H. Qiu, G. V. Nazin, W. Hot, *Science* **2003**, 299, 542–546.
- [262] G. Schull, N. Néel, P. Johansson, R. Berndt, *Phys. Rev. Lett.* **2009**, 102, 057401.
- [263] M. Buret, A. V. Uskov, J. Dellinger, N. Cazier, M.-M. Mennemanteuil, J. Berthelot, I. V. Smetanin, I. E. Protsenko, G. Colas-des-Francis, A. Bouhelier, *Nano Lett.* **2015**, 15, 5811–5818.
- [264] B. N. J. Persson, A. Baratoff, *Phys. Rev. Lett.* **1992**, 68, 3224–3227.
- [265] V. M. Agranovich, *Excitations in Organic Solids*, OUP Oxford, **2009**.
- [266] Y. Zhang, Y. Luo, Y. Zhang, Y. J. Yu, Y. M. Kuang, L. Zhang, Q. S. Meng, Y. Luo, J. L. Yang, Z. C. Dong, J. G. Hou, *Nature* **2016**, 531, 623–627.
- [267] H. Imada, K. Miwa, M. Imai-Imada, S. Kawahara, K. Kimura, Y. Kim, *Phys. Rev. Lett.* **2017**, 119, 1–6.
- [268] Z. C. Dong, X. L. Zhang, H. Y. Gao, Y. Luo, C. Zhang, L. G. Chen, R. Zhang, X. Tao, Y. Zhang, J. L. Yang, J. G. Hou, *Nat. Photonics* **2010**, 4, 50–54.
- [269] B. Doppagne, M. C. Chong, H. Bulou, A. Boeglin, F. Scheurer, G. Schull, *Science* **2018**, 361, 251–255.
- [270] Y. M. Kuang, Y. J. Yu, Y. Luo, J. Z. Zhu, Y. Liao, Y. Zhang, Z. C. Dong, *Chin. J. Chem. Phys.* **2016**, 29, 157–160.
- [271] J. Repp, G. Meyer, S. M. Stojković, A. Gourdon, C. Joachim, *Phys. Rev. Lett.* **2005**, 94, 1–4.
- [272] Z. C. Dong, X. L. Guo, A. S. Trifonov, P. S. Dorozhkin, K. Miki, K. Kimura, S. Yokoyama, S. Mashiko, *Phys. Rev. Lett.* **2004**, 92, 1–4.
- [273] M. Valášek, M. Mayor, *Chem. - Eur. J.* **2017**, 23, 13538–13548.
- [274] V. Rai, L. Gerhard, Q. Sun, C. Holzer, T. Repän, M. Krstić, L. Yang, M. Wegener, C. Rockstuhl, W. Wulfhekel, *Nano Lett.* **2020**, 20, 7600–7605.
- [275] N. Sakai, J. Mareda, E. Vauthey, S. Matile, *Chem. Commun.* **2010**, 46, 4225–4237.
- [276] M. Al Kobaisi, S. V. Bhosale, K. Latham, A. M. Raynor, S. V. Bhosale, *Chem. Rev.* **2016**, 116, 11685–11796.
- [277] J. Hak, S. Sabin-Lucian, W. Y. Lee, M. Könemann, H. W. Höffken, C. Röger, R. Schmidt, Y. Chung, W. C. Chen, F. Würthner, Z. Bao, *Adv. Funct. Mater.* **2010**, 20, 2148–2156.
- [278] F. Würthner, M. Stolte, *Chem. Commun.* **2011**, 47, 5109–5115.
- [279] M. Korzec, S. Kotowicz, K. Łaba, M. Łapkowski, J. G. Małecki, K. Smolarek, S. Maćkowski, E. Schab-Balcerzak, *Eur. J. Org. Chem.* **2018**, 2018, 1756–1760.
- [280] H. F. Higginbotham, P. Pander, R. Rybakiewicz, M. K. Etherington, S. Maniam, M. Zagorska, A. Pron, A. P. Monkman, P. Data, *J. Mater. Chem. C* **2018**, 6, 8219–8225.
- [281] H. Vollmann, H. Becker, M. Corell, H. Streeck, *Liebigs Ann* **1937**, 531, 159.

- [282] F. Würthner, S. Ahmed, C. Thalacker, T. Debaerdemaeker, *Chem. - Eur. J.* **2002**, *8*, 4742–4750.
- [283] C. Thalacker, C. Röger, F. Würthner, *J. Org. Chem.* **2006**, *71*, 8098–8105.
- [284] S. Erten, Y. Posokhov, S. Alp, S. İçli, *Dyes Pigments* **2005**, *64*, 171–178.
- [285] D. Shukla, S. F. Nelson, D. C. Freeman, M. Rajeswaran, W. G. Ahearn, D. M. Meyer, J. T. Carey, *Chem. Mater.* **2008**, *20*, 7486–7491.
- [286] F. S. Etheridge, R. Fernando, J. A. Golen, A. L. Rheingold, G. Sauve, *RSC Adv.* **2015**, *5*, 46534–46539.
- [287] M. M. Durban, P. D. Kazarinoff, Y. Segawa, C. K. Luscombe, *Macromolecules* **2011**, *44*, 4721–4728.
- [288] H. Vollmann, H. Becker, M. Corell, H. Streeck, *Justus Liebigs Ann. Chem.* **1937**, *531*, 1–159.
- [289] S. L. Suraru, F. Würthner, *Angew. Chem. Int. Ed.* **2014**, *53*, 7428–7448.
- [290] Y. Zhao, G. Huang, C. Besnard, J. Mareda, N. Sakai, S. Matile, *Chem. - Eur. J.* **2015**, *21*, 6202–6207.
- [291] S. Grunder, D. Muñoz Torres, C. Marquardt, A. Bałaszczczyk, R. Krupke, M. Mayor, *Eur. J. Org. Chem.* **2011**, 478–496.
- [292] A. Błaszczczyk, M. Fischer, C. Von Hänisch, M. Mayor, *Helv. Chim. Acta* **2006**, *89*, 1986–2005.
- [293] C. Vericat, M. E. Vela, G. A. Benitez, J. A. Martin Gago, X. Torrelles, R. C. Salvarezza, *J. Phys. Condens. Matter* **2006**, *18*.
- [294] B. Bhushan, O. Marti, in *Springer Handb. Nanotechnol.*, Springer Berlin Heidelberg, Berlin, Heidelberg, **2010**, pp. 573–617.
- [295] G. Haugstad, *Atomic Force Microscopy: Understanding Basic Modes and Advanced Applications*, Wiley, **2012**.
- [296] G. Binnig, H. Rohrer, *Angew. Chem. Int. Ed. Engl.* **1987**, *26*, 606–614.
- [297] D. A. Bonnell, *Scanning Tunneling Microscopy and Spectroscopy: Theory, Techniques, and Applications*, VCH New York, **1993**.
- [298] P. Parris, M. Passacantando, L. Ottaviano, *Appl. Surf. Sci.* **2006**, *252*, 7469–7472.
- [299] B. J. McIntyre, M. Salmeron, G. A. Somorjai, *Science* **1994**, *265*, 1415–1418.
- [300] F. J. Giessibl, *Rev. Mod. Phys.* **2003**, *75*, 949–983.
- [301] M. H. Schoenfish, J. E. Pemberton, *J. Am. Chem. Soc.* **1998**, *120*, 4502–5413.
- [302] C. Vericat, G. A. Benitez, D. E. Grumelli, M. E. Vela, R. C. Salvarezza, *J. Phys. Condens. Matter* **2008**, *20*.
- [303] C. J. Zhong, R. C. Brush, J. Anderegg, M. D. Porter, *Langmuir* **1999**, *15*, 518–525.
- [304] L. H. Dubois, R. G. Nuzzo, *Annu. Rev. Phys. Chem.* **1992**, *43*, 437–463.
- [305] K. S. Birdi, *Handbook of Surface and Colloid Chemistry*, **2015**.
- [306] D. G. Castner, K. Hinds, D. W. Grainger, *Langmuir* **1996**, *12*, 5083–5086.
- [307] H.-J. Butt, K. Graf, M. Kappl, *Physics and Chemistry of Interfaces*, **2006**.
- [308] E. Lörtscher, J. M. Tour, J. W. Ciszec, H. Riel, *J. Phys. Conf. Ser.* **2007**, *61*, 987–991.
- [309] J. L. Zhang, J. Q. Zhong, J. D. Lin, W. P. Hu, K. Wu, G. Q. Xu, A. T. S. Wee, W. Chen, *Chem. Soc. Rev.* **2015**, *44*, 2998–3022.
- [310] L. Bogani, W. Wernsdorfer, in *Nanosci. Technol.*, Co-Published With Macmillan Publishers Ltd, UK, **2009**, pp. 194–201.

- [311] Visions for a molecular future. *Nat. Nanotechnol.* **2013**, *8*, 385–389.
- [312] J. Rotzler, H. Gsellinger, A. Bihlmeier, M. Gantenbein, D. Vonlanthen, D. Häussinger, W. Kloppe, M. Mayor, *Org. Biomol. Chem.* **2013**, *11*, 110–118.
- [313] R. E. Dawson, A. Hennig, D. P. Weimann, D. Emery, V. Ravikumar, J. Montenegro, T. Takeuchi, S. Gabutti, M. Mayor, J. Mareda, C. A. Schalley, S. Matile, *Nat. Chem.* **2010**, *2*, 533–538.
- [314] S. Guha, F. S. Goodson, L. J. Corson, S. Saha, *J. Am. Chem. Soc.* **2012**, *134*, 13679–13691.
- [315] J. E. Nuñez, T. A. V. Khuong, L. M. Campos, N. Farfán, H. Dang, S. D. Karlen, M. A. Garcia-Garibay, *Cryst. Growth Des.* **2006**, *6*, 866–873.
- [316] J. E. Nuñez, A. Natarajan, S. I. Khan, M. A. Garcia-Garibay, *Org. Lett.* **2007**, *9*, 3559–3561.
- [317] G. I. Feutrill, R. N. Mirring, *Tetrahedron Lett.* **1970**, 1327–1328.
- [318] R. Fernando, Z. Mao, E. Muller, F. Ruan, G. Sauvé, *J. Phys. Chem. C* **2014**, *118*, 3433–3442.
- [319] S. Chopin, F. Chaignon, E. Blart, F. Odobel, *J. Mater. Chem.* **2007**, *17*, 4139–4146.
- [320] J. Pommerehne, H. Vestweber, W. Guss, R. F. Mahrt, H. Bäessler, M. Porsch, J. Daub, *Adv. Mater.* **1995**, *7*, 551–554.
- [321] R. S. K. Kishore, O. Kel, N. Banerji, D. Emery, G. Bollot, J. Mareda, A. Gomez-Casado, P. Jonkheijm, J. Huskens, P. Maroni, M. Borkovec, E. Vauthey, N. Sakai, S. Matile, *J. Am. Chem. Soc.* **2009**, *131*, 11106–11116.
- [322] J. L. Bredas, R. Silbey, D. S. Boudreaux, R. R. Chance, *J. Am. Chem. Soc.* **1983**, *105*, 6555–6559.
- [323] C. Q. Ma, M. Fonrodona, M. C. Schikora, M. M. Wienk, R. A. J. Janssen, P. Bäuerle, *Adv. Funct. Mater.* **2008**, *18*, 3323–3331.
- [324] R. Fernando, F. Etheridge, E. Muller, G. Sauvé, *New J. Chem.* **2015**, *39*, 2506–2514.
- [325] C. Röger, F. Würthner, *J. Org. Chem.* **2007**, *72*, 8070–8075.
- [326] D. Gosztola, M. P. Niemczyk, W. Svec, A. S. Lukas, M. R. Wasielewski, *J. Phys. Chem. A* **2000**, *104*, 6545–6551.
- [327] X. Tao, Z. C. Dong, J. L. Yang, Y. Luo, J. G. Hou, J. Aizpurua, *J. Chem. Phys.* **2009**, *130*, 084706.
- [328] J. Aizpurua, S. P. Apell, R. Berndt, *Phys. Rev. B* **2000**, *62*, 2065–2073.
- [329] B. Doppagne, M. C. Chong, E. Lorchat, S. Berciaud, M. Romeo, H. Bulou, A. Boeglin, F. Scheurer, G. Schull, *Phys. Rev. Lett.* **2017**, *118*, 127401.
- [330] G. Chen, Y. Luo, H. Gao, J. Jiang, Y. Yu, L. Zhang, Y. Zhang, X. Li, Z. Zhang, Z. Dong, *Phys. Rev. Lett.* **2019**, *122*, 177401.
- [331] L. Zhang, Y. J. Yu, L. G. Chen, Y. Luo, B. Yang, F. F. Kong, G. Chen, Y. Zhang, Q. Zhang, Y. Luo, J. L. Yang, Z. C. Dong, J. G. Hou, *Nat. Commun.* **2017**, *8*, 1–7.
- [332] H. Imada, K. Miwa, M. Imai-Imada, S. Kawahara, K. Kimura, Y. Kim, *Nature* **2016**, *538*, 364–367.
- [333] G. Tian, J.-C. Liu, Y. Luo, *Phys. Rev. Lett.* **2011**, *106*, 177401.
- [334] G. Tian, Y. Luo, *Phys. Rev. B* **2011**, *84*, 205419.
- [335] M. C. Chong, G. Reece, H. Bulou, A. Boeglin, F. Scheurer, F. Mathevet, G. Schull, *Phys. Rev. Lett.* **2016**, *116*, 036802.

- [336] P. Nösel, S. Moghimi, C. Hendrich, M. Haupt, M. Rudolph, F. Rominger, A. S. K. Hashmia, *Adv. Synth. Catal.* **2014**, 356, 3755–3760.
- [337] A. Dhara, J. Weinmann, A.-M. Krause, F. Beuerle, *Chem. - Eur. J.* **2016**, 22, 12473–12478.
- [338] S. S. Batsanov, *Inorg. Mater.* **2001**, 37, 871–885.
- [339] B. D. Ratner, D. G. Castner, *Surf. Anal. Princ. Tech.* **2009**, 2, 374–381.
- [340] N. Ballav, B. Schüpbach, S. Neppel, P. Feulner, A. Terfort, M. Zharnikov, *J. Phys. Chem. C* **2010**, 114, 12719–12727.
- [341] J. Stöhr, *NEXAFS Spectroscopy*, Springer Berlin Heidelberg, **2013**.
- [342] S. Frey, V. Stadler, K. Heister, W. Eck, M. Zharnikov, M. Grunze, *Langmuir* **2001**, 17, 2408–2415.
- [343] H. Hamoudi, S. Neppel, P. Kao, B. Schüpbach, P. Feulner, A. Terfort, D. Allara, M. Zharnikov, *Phys. Rev. Lett.* **2011**, 107, 027801.
- [344] S. Rangan, J.-J. Gallet, F. Bournel, S. Kubsky, K. Le Guen, G. Dufour, F. Rochet, F. Sirotti, S. Carniato, V. Ilakovac, *Phys. Rev. B* **2005**, 71, 165318.
- [345] S. Carniato, V. Ilakovac, J.-J. Gallet, E. Kukk, Y. Luo, *Phys. Rev. A* **2005**, 71, 022511.
- [346] A. Klapars, S. L. Buchwald, *J. Am. Chem. Soc.* **2002**, 124, 14844–14845.
- [347] A. Bihlmeier, J. Rotzler, M. Rickhaus, M. Mayor, W. Kloppe, *Phys. Chem. Chem. Phys.* **2015**, 17, 11165–11173.
- [348] Y. Wang, Z. Lin, H. Fan, X. Peng, *Chem. - Eur. J.* **2016**, 22, 10382–10386.
- [349] P. C. Bulman Page, B. R. Buckley, M. M. Farah, A. John Blacker, *Eur. J. Org. Chem.* **2009**, 3413–3426.
- [350] H.-T. Liu, X.-G. Xiong, P. Diem Dau, Y.-L. Wang, D.-L. Huang, J. Li, L.-S. Wang, *Nat. Commun.* **2013**, 4, 2223.
- [351] L. Herrero, A. González-Orive, S. Marqués-González, S. Martín, R. J. Nichols, J. L. Serrano, P. J. Low, P. Cea, *Nanoscale* **2019**, 11, 7976–7985.
- [352] S. Wang, D. P. Goronzy, T. D. Young, N. Wattanatorn, L. Stewart, T. Baše, P. S. Weiss, *J. Phys. Chem. C* **2019**, 123, 1348–1353.
- [353] O. V. Dolomanov, L. J. Bourhis, R. J. Gildea, J. A. K. Howard, H. Puschmann, *J Appl Cryst* **2009**, 42, 339–341.
- [354] G. M. Sheldrick, **2015**, A71, 3–8.
- [355] G. M. Sheldrick, **2015**, C71, 3–8.
- [356] D. N. Bunck, W. R. Dichtel, *Angew. Chem.* **2012**, 124, 1921–1925.

8 Appendix

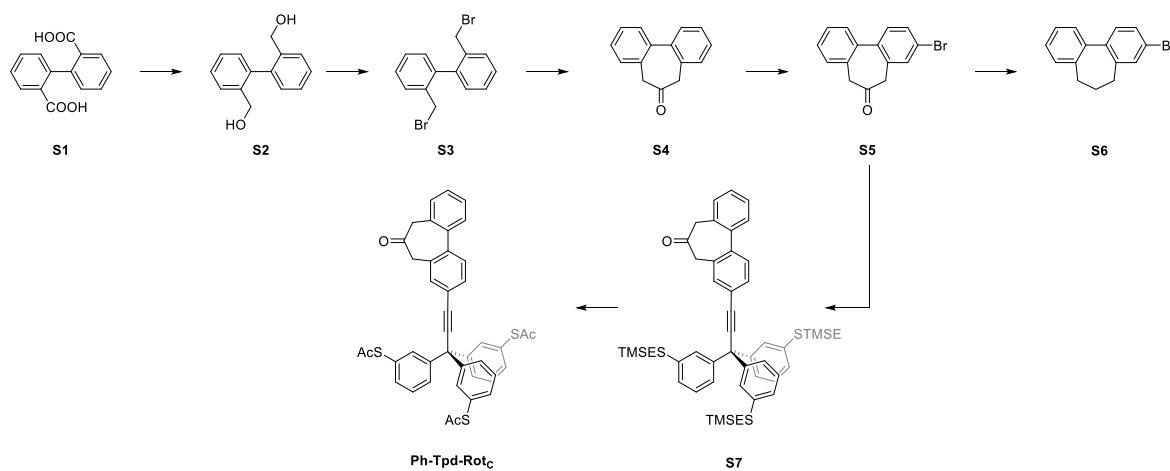


Figure S 1. Synthetic approach to **Ph-Tpd-Rot_{LF}**. Synthesis done by Dr. Jan Lukášek.

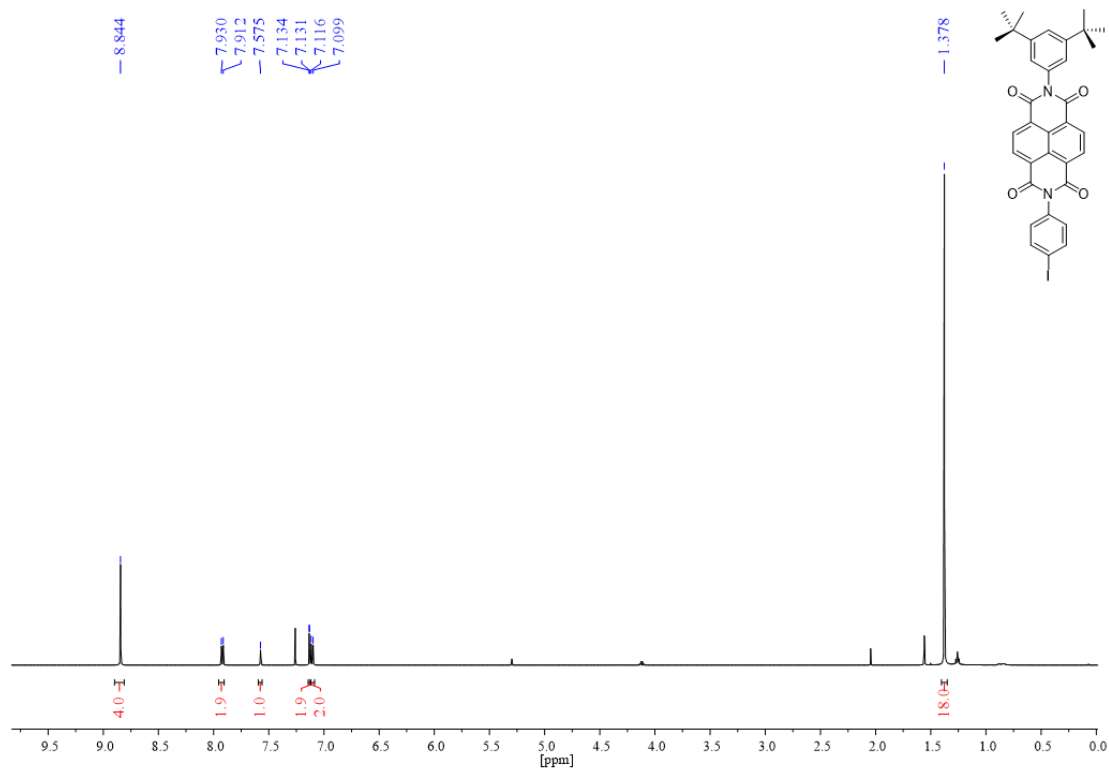


Figure S 2. ¹H NMR (500 MHz, CDCl₃) of hNDI.

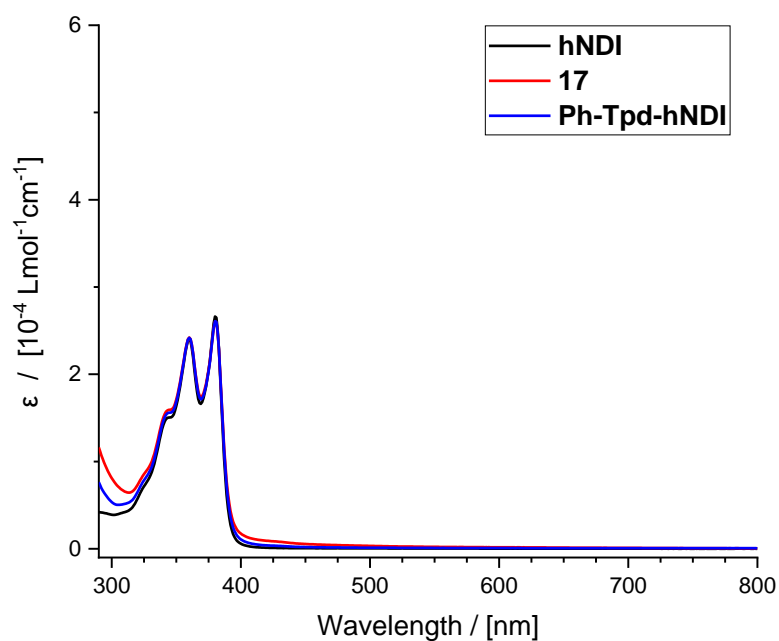


Figure S 5. UV-Vis absorption spectra of **hNDI** (black), compound **17** (red) and **Ph-Tpd-hNDI** (blue) in DCM at room temperature.

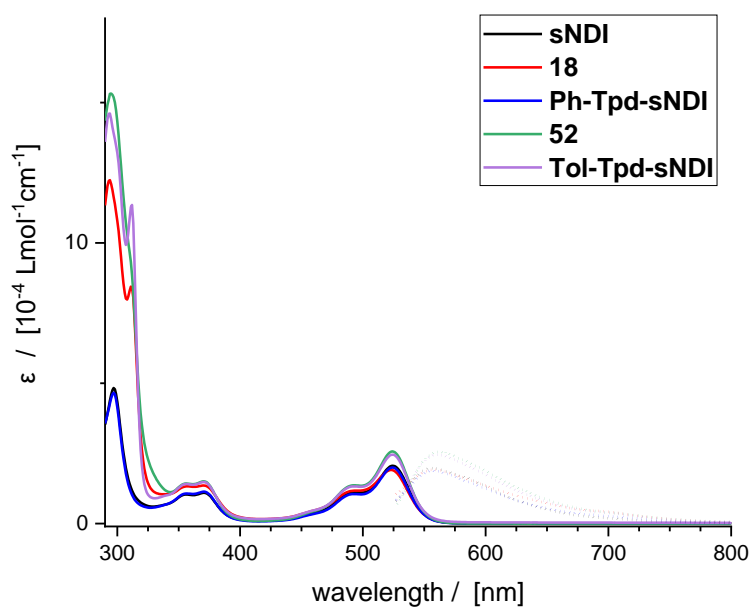


Figure S 6. UV-Vis absorption spectra (solid line) and normalised emission spectra (dotted line) of **sNDI** (black), compound **18** (red), **Ph-Tpd-sNDI** (blue), compound **52** (green) and **Tol-Tpd-sNDI** (purple) in DCM at room temperature.

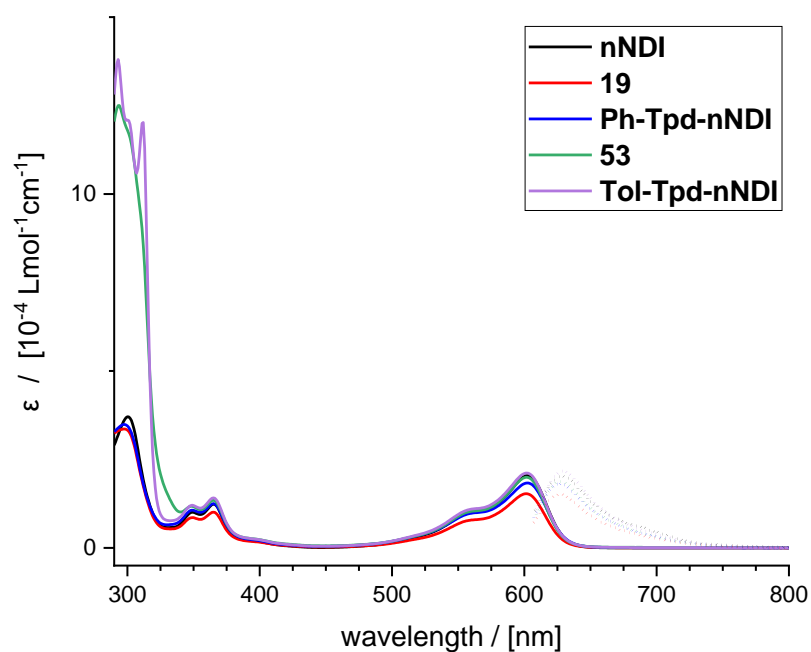


Figure S 7. UV-Vis absorption spectra (solid line) and normalised emission spectra (dotted line) of **nNDI** (black), compound **19** (red), **Ph-Tpd-nNDI** (blue), compound **53** (green) and **Tol-Tpd-nNDI** (purple) in DCM at room temperature.

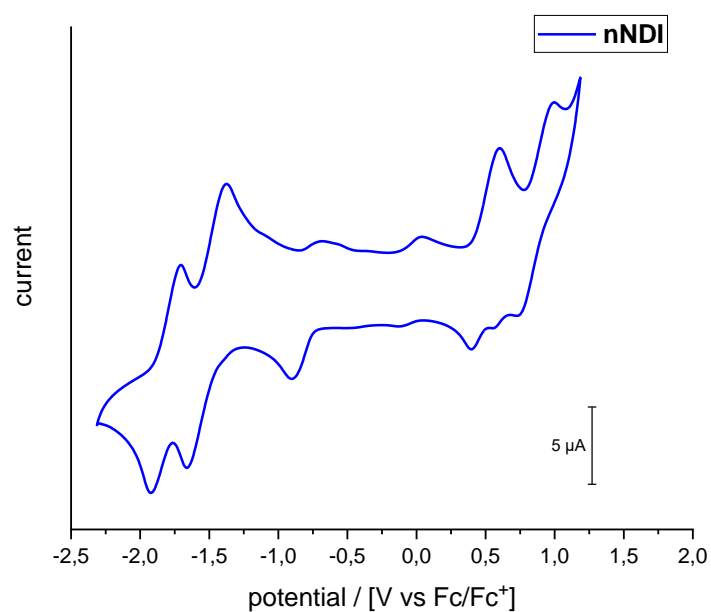


Figure S 8. Cyclic voltammogram of **nNDI** recorded in dichloromethane containing 0.1 M solution of Bu_4NPF_6 as the supporting electrolyte. Fc/Fc^+ was used as an external reference. Scan rate 100 mVs^{-1} .

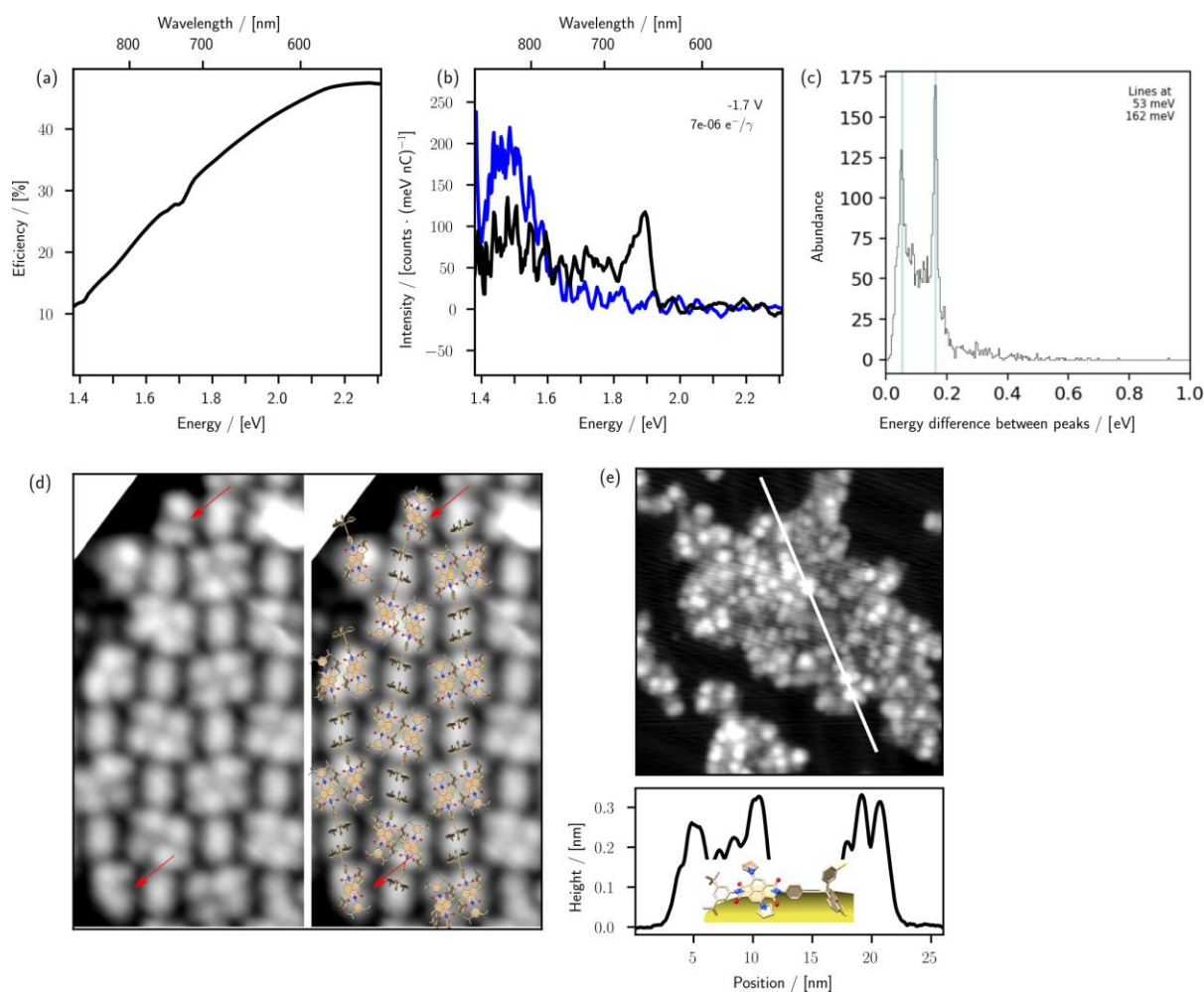


Figure S 9. (a) Efficiency of light collection setup excluding losses in the mirror tip. (b) Over bias emission (black line) of **Ph-Tpd-hNDI** and nearby plasmon spectrum (blue line). Sample bias -1.7 V, tunneling current 130 pA, integration time 2 s. (c) Histogram of energy differences between multiple peaks in photon spectra of **Ph-Tpd-hNDI**. (d) Edges of ordered islands of **Ph-Tpd-sNDI** ending on single molecules (red arrows). Right side shows the same area with molecular models superimposed to scale. Sample bias 2.3 V, tunneling current 2 pA, scan width 7 nm. (e) Unordered island of **Ph-Tpd-nNDI** with cross section along the white line. Molecular model (put model of **Ph-Tpd-nNDI**) not to scale. Sample bias -1.9 V, tunneling current 2 pA, scan width 27 nm.